Towards a unified view of nuclear structure northwest of ^{132}Sn: Systematic studies of high-spin properties in Xe and Ba isotopes

Inaugural-Dissertation

zur
Erlangung des Doktorgrades
der Mathematisch-Naturwissenschaftlichen Fakultät
der Universität zu Köln

vorgelegt von

Levent Kaya
aus Schwäbisch Gmünd

Köln 2020

Berichterstatter:	Prof. Dr. Peter Reiter Prof. Dr. Andreas Zilges Prof. Dr. Thorsten Kröll
Tag der letzten mündlichen Prüfung:	10. Januar 2020

Abstract

This doctoral thesis presents new experimental findings on high-spin states and their theoretical implications to the region of medium-mass ($50 \leq Z, N \leq 82$) transitional nuclei. Detailed experimental data on high-spin structures in $A \approx 130$ nuclei are exploited to benchmark the reliability of shell-model calculations in the area northwest of doubly-magic nucleus ^{132}Sn. The findings are based upon the synergies between different cutting-edge nuclear spectroscopy experiments, relying on multinucleon-transfer reactions using the high-efficient Advanced GAmma Tracking Array (AGATA) coupled in series with the tracking magnetic spectrometer PRISMA located at the Laboratori Nazionali di Legnaro, Italy, and precise fusion-evaporation reactions at the HORUS spectrometer at the FN tandem accelerator of the University of Cologne, Germany. Xe and Ba isotopes near the $50 \leq Z, N \leq 82$ shell closures can not be efficiently populate during fusion-evaporation experiments with reasonable production yields. Weak reaction channels which evaporate charged particles like protons require careful preconditions for a detailed spectroscopy. A new experimental setup consisting of the HORUS array in combination with a double-sided silicon strip detector (DSSSD) was commissioned to allow for detailed particle-gated $\gamma\gamma$-spectroscopy. The existing high-spin level-schemes of ^{137}Nd, ^{137}Ba, ^{136}Ba, ^{135}Ba, ^{134}Ba, ^{133}Ba, ^{133}Xe, ^{131}Xe, and ^{130}I were substantially extended, emphasizing the transitional character of these odd-, and even-mass nuclei. The observation of distinct backbendings in ^{131}Xe and ^{134}Ba establishes an important link in the smooth evolution from spherical to deformed shapes. The identification of new positive- and negative-parity level structures in ^{136}Ba and ^{137}Ba indicates a sudden change of the structure of high-spin states along the $N = 80$ and $N = 81$ chains, only two and one neutrons outside the fully occupied neutron shell. Different high-spin members of the mixed proton-neutron $\pi g_{7/2}/d_{5/2} \otimes \nu h_{11/2}$ and $\pi h_{11/2} \otimes \nu h_{11/2}$ configurations were identified in doubly-odd ^{130}I. Moreover, a millisecond pulsing system at the FN tandem accelerator was commissioned during this thesis. The 2107-, and 2388-keV states in the ^{133}Xe and ^{135}Ba isotones were identified as millisecond $J^\pi = 23/2^+$ isomers, closing the systematic towards the recently investigated $J^\pi = 23/2^+$ isomer in ^{139}Nd. In addition, a comprehensive search for the anticipated $J^\pi = 23/2^+$ isomer in ^{137}Ce was performed using two different experimental approaches. A hitherto tentatively assigned isomer at 1942 keV in the $N = 77$ isotone ^{133}Ba was confirmed as a $J^\pi = 19/2^+$ isomer with a newly measured half-life of $T_{1/2} = 66.6(20)$ ns. Similarly, the half-life value of the $J^\pi = 19/2^+$ isomer at 2222 keV in ^{137}Nd was significantly improved with a new value of $T_{1/2} = 0.38(7)$ ns. The obtained data close systematic gaps along isotopic and isotonic chains and improve the understanding of nuclear configurations nearby the doubly-magic ^{132}Sn. Finally, new developments and recent theoretical advances in shell-model calculations are available for a refined systematic comparison in $A \approx 130$ nuclei. Present-day shell-model interactions like GCN50:82, Realistic SM, and PQM130 are capable to overcome the previous limitations of shell-model calculations. The predictions of these calculations are in good accordance with the new experimental findings and provide access into a detailed microscopic description of high-spin features and the gradual change of nuclear structure towards the shell closure at $N = 82$.

Zusammenfassung

Diese Dissertation umfasst neue experimentelle Ergebnisse über die Hochspin-Strukturen und deren theoretische Implikationen für die Region von Übergangskernen mit mittlerer Massen ($50 \leq Z, N \leq 82$). Detaillierte Informationen über diese Kerne werden genutzt, um die Leistungsfähigkeit von Schalenmodellrechnungen in der Region nordwestlich des doppelt magischen Kern ^{132}Sn zu validieren. Die experimentellen Ergebnisse beruhen auf verschiedenen sich ergänzenden Datensätzen, die zum einen auf Multinukleon-transferreaktion mit dem hochauflösenden Advanced GAmma Tracking Array (AGATA), gekoppelt mit dem Magnetspektrometer PRISMA am Laboratori Nazionali di Legnaro, Italien, und zum anderen auf dedizierten Fusionsverdampfungsreaktionen am HORUS-Spektrometer am FN-Tandembeschleuniger der Universität zu Köln basieren. Die Population leicht neutronenreicher Xe- und Ba-Kerne mit Schwerionenreaktionen erfordert den Nachweis abgedampfter Teilchen, wie geladener Protonen, um detaillierte $\gamma\gamma$-Spektroskopie durchzuführen. Ein neuer Versuchsaufbau, bestehend aus einem doppelseitig segmentierten Siliziumdetektor (DSSSD), welcher zum Nachweis geladener Teilchen in Koinzidenz mit dem Gammaspektrometer HORUS eingesetzt wird, wurde im Rahmen der Arbeit in Betrieb genommen. Die bestehenden Termschemata von ^{137}Nd, ^{137}Ba, ^{136}Ba, ^{135}Ba, ^{134}Ba, ^{133}Ba, ^{133}Xe, ^{131}Xe, und ^{130}I wurden deutlich erweitert. Die Beobachtung verschiedener Backbending-Phänomene in ^{131}Xe und ^{134}Ba stellt ein wichtiges Bindeglied in der Evolution von sphärischen zu deformierten Formen dar. Die Identifizierung neuer Strukturen in den Yrast-Bändern mit positiver und negativer Parität in ^{136}Ba und ^{137}Ba weisen auf eine plötzliche Änderung der Struktur von hoch angeregten Zuständen entlang der $N = 81$ und $N = 80$-Ketten, welche nur ein bzw. zwei Neutronen außerhalb der voll besetzten Neutronenschale liegen, hin. Verschiedene Hochspin-Zustände mit gemischten Protonen-Neutronen $\pi g_{7/2}/d_{5/2} \otimes \nu h_{11/2}$ und $\pi h_{11/2} \otimes \nu h_{11/2}$ Konfigurationen wurden im doppelt ungeraden ^{130}I identifiziert. Darüber hinaus wurde im Rahmen dieser Arbeit ein Millisekunden-Pulssystem am FN-Tandembeschleuniger wieder in Betrieb genommen. Die Zustände bei Anregungsenergien von 2107 und 2388 keV in den Isotonen ^{133}Xe und ^{135}Ba wurden als Millisekunden Isomere mit Spin/Parität $J^\pi = 23/2^+$ identifiziert und schließen die Systematik in Richtung des kürzlich untersuchten $J^\pi = 23/2^+$-Isomers in ^{139}Nd. Darüber hinaus wurde eine detaillierte Suche nach dem letzten fehlenden $J^\pi = 23/2^+$-Isomer entlang der $N = 79$ Kette in ^{137}Ce mit zwei verschiedenen experimentellen Aufbauten durchgeführt. Ein vermutetes Isomer bei einer Anregungsenergie von 1942 keV im $N = 77$ Isotone ^{133}Ba wurde als Isomer mit Spin/Parität $J^\pi = 19/2^+$ mit einer neu gemessenen Halbwertszeit von $T_{1/2} = 66,6(20)$ ns bestätigt. Ebenso wurde die Halbwertszeit des $J^\pi = 19/2^+$ Isomers in ^{137}Nd mit einem neuen Wert von $T_{1/2} = 0,38(7)$ ns entscheidend verbessert. Die neuen Daten, die im Rahmen dieser Arbeit gewonnen wurden, schließen systematische Lücken entlang Isotopen und Isotonenketten. Sie verbessern wesentlich das Verständnis der Kernstruktur in der Umgebung vom doppelt magischen Kern ^{132}Sn. Schließlich motivieren theoretische Fortschritte in den Schalenmodellrechnungen eine verfeinerte systematische Untersuchung dieser Region. Interaktionen wie GCN50:82, Realistic SM und PQM130 sind in der Lage die bisherigen Einschränkungen der Schalenmodellrechnungen in dieser Region zu überwinden. Die Ergebnisse dieser Interaktionen reproduzieren die experimentellen Ergebnisse und liefern eine detaillierte mikroskopische Beschreibung der Hochspin-Eigenschaften und der Evolution der Kernstruktur in Richtung des $N = 82$ Schalenabschlusses.

Contents

1 Introduction . . . 7
1.1 Nuclear structure in the $50 \leq Z, N \leq 82$ region . . . 7
1.1.1 The $gdsh$ valence space and isomeric states in the $50 \leq Z, N \leq 82$ region 8
1.1.2 High-spin features northwest of ^{132}Sn . . . 11
1.1.3 Reaction mechanism to populate nuclei around ^{132}Sn . . . 13
1.2 Shell-model calculations in the $50 \leq Z, N \leq 82$ region . . . 16
1.3 Outline of this thesis . . . 23

2 High-spin structure in the transitional nucleus ^{131}Xe: Competitive neutron and proton alignment in the vicinity of the $N = 82$ shell closure . . . **25**

3 Millisecond $23/2^+$ isomers in the $N = 79$ isotones ^{133}Xe and ^{135}Ba . . . **47**
Addendum: Search for $23/2^+$ isomer in the $N = 79$ isotone ^{137}Ce . . . 65

4 Identification of high-spin proton configurations in ^{136}Ba and ^{137}Ba . . . **69**

5 Isomer spectroscopy in ^{133}Ba and high-spin structure of ^{134}Ba . . . **91**
Addendum: $19/2^+$ isomer in the $N = 77$ isotone ^{137}Nd . . . 111

6 Excited states in doubly-odd ^{130}I . . . **113**

7 Summary . . . **129**

8 Outlook . . . **133**

Bibliography . . . **140**

List of figures . . . **151**

Acknowledgments . . . **157**

Curriculum vitae . . . **161**

Erklärung zur Dissertation . . . **162**

Introduction

1.1 Nuclear structure in the $50 \leq Z, N \leq 82$ region

Comprehensive information on nuclear evolution in the proximity of doubly-magic nuclei are of fundamental interest since they furnish essential information on key ingredients of present-day shell-model interactions like effective charges, one-body operators (single-particle energies), two-body matrix elements (TBMEs), and the tensor part, which is the most ambitious part of the residual interactions. Moreover, experimental data is needed to benchmark theoretical predictions in order to provide improved parameters or even phenomenological corrections to nuclear shell-model calculations and, thus, theory and experiment interact. It is well known that ^{132}Sn and ^{208}Pb exhibit very similar nuclear structures, even though they are very differently located within the nuclei chart [1]. An important signature for this similarity is the almost identical excitation energy of the first excited $J^{\pi} = 2^{+}$ states in ^{132}Sn and ^{208}Pb with respective values of 4.04 and 4.09 MeV [2]. While neutron-rich target materials like $^{206-208}$Pb and ^{209}Bi are available for nuclear structure studies of the proximity of ^{208}Pb, the more exotic region adjacent to ^{132}Sn is far off the line of stability (eight neutrons away from the stable ^{124}Sn). ^{132}Sn is known to exhibit all properties of a strong core due to the double-magic configuration, which is partly seen in the large excitation energies of first $J^{\pi} = 3^{-}$ and 2^{+} states [3]. Reduced transition probabilities along the $Z = 50$ chain of tin isotopes received renewed attention and have been examined in detail from the theoretical as well as from the experimental perspective during the last decade. Significant deviations of $B(E2; 0_1^+ \to 2_1^+)$ values from the expected values of semi-magic Sn isotopes were recognized as a function of the neutron number. A unified theoretical description of these anomalies could not be given until a dedicated Monte-Carlo shell-model calculation with a model space which is extended by single-particle orbits below and above the 50 and 82 shell closures, utilized to reproduce all observed $B(E2; 0_1^+ \to 2_1^+)$ values along the Sn chain [4]. Moreover, the region has a strong impact on nuclear astrophysics, as the r-process approaches the ^{132}Sn waiting point and proceeds subsequently along the tin chain [5].

Nowadays, spectroscopic results for high-lying states are evaluated for nuclei "northeast" [6–10] and "southeast" [11, 12] with respect to ^{132}Sn using multinucleonen-transfer reactions, the ISOL/IGISOL technique, or in-flight fission. Since the N/Z ratio in this regions is large, a detailed knowledge of low-lying states and single-particle excitations exist throughout comprehensive β-decay studies. In addition, sensitive techniques like transfer and knock-out reactions were traditionally used to explore the single-particle nature around ^{132}Sn [13–15]. In contrast, the "northwest" quadrant of ^{132}Sn with $Z \geq 50$ and $N \leq 82$ is under investigation since many decades since it can be populated with sufficiently high statistics in standard nuclear-structure experiments like fusion-evaporation or multinucleon-transfer reactions. The results furnish important information for a phenomenological and systematic understanding of the evolution of the nuclear structure in a medium-mass transitional region. Moreover, the experimental findings can imply predictions for the today unknown nuclear structure of the regions across the $N = 82$ neutron shell with $Z \geq 50$, $N \geq 82$.

1.1.1 The $gdsh$ valence space and isomeric states in the $50 \leq Z, N \leq 82$ region

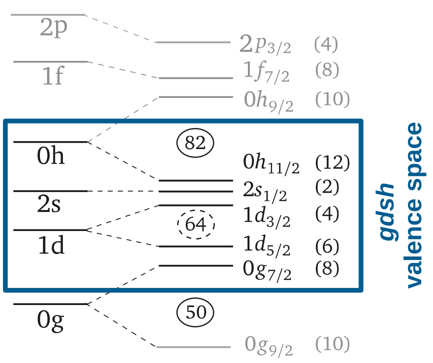

Figure 1: Schematic depiction of single-particle orbitals in the level diagram of the $gdsh$ valence space, arranged by Brown *et al.* [16, 17].

Few-valence-particle nuclei beyond the doubly-magic core-nucleus ^{132}Sn display predominantly single-particle structures in the $gdsh$ valence space, involving the major single-particle orbitals $0g_{7/2}$, $1d_{5/2}$, $1d_{3/2}$, $2s_{1/2}$, and $0h_{11/2}$ [18]. An orbital scheme including single-particle orbitals above and below the $gdsh$ valence space is exemplarily visualized in Fig. 1. The $gdsh$ valence space is governed by the intruder $0h_{11/2}$ orbital. Such high-j intruder orbitals are characterized by large single-particle angular momenta. Proton and neutron single-particle energies, extracted from experimetal level energies of ^{133}Sb and ^{131}Sn, are −9.68/9.74,−8.72/8.97,−7.24/7.31, −7.34/7.62 and −6.88/7.38 MeV for the $0g_{7/2}$, $1d_{5/2}$, $1d_{3/2}$, $2s_{1/2}$, and $0h_{11/2}$ orbitals, respectively [17]. The level energy of the $\pi s_{1/2}$ orbital is fitted to −7.34 MeV since it is not experimentally observed in ^{133}Sb [17]. In the $gdsh$ valence space, the scaling factor of the two-body matrix elements typically follows the nuclear mass as $A^{-1/3}$.

Yrast-trap isomers are constructed from different mixtures of *gdsh* orbitals and, thus, open a gateway for a fundamental understanding of the evolution of the nuclear configurations [21]. Allowing high-spin couplings with large j, the intruder $0h_{11/2}$ neutron orbital is a key ingredient for characteristic yrast spin-gap isomers. Figure 2 shows the distribution of all today measured $J^\pi = 10^+, 19/2^+$ and $23/2^+$ isomers with $T_{1/2} > 10$ ns in the $50 \leq Z, N \leq 82$ range. The negative magnetic moments of the $J^\pi = 10^+$ states in nuclei below gadolinium at $Z = 64$ corroborate a near-spherical, maximally aligned two-neutron-hole $\nu h^{-2}_{11/2}$ configuration [22–24]. Hence, the wide spread of the $J^\pi = 10^+$ isomers throughout this region emphasizes the importance of the intruder $\nu h_{11/2}$ orbital. Half-life values extend from lower nanosecond values up to 198(3) ms in ^{146}Tm [25]. An important signature of the $10^+ \rightarrow 8^+$ transition is the remarkable small transition energy in ^{130}Te and ^{134}Xe [2]. Particularly noteworthy is the long half-life of 8.39(11) ms [26] for the $J^\pi = 10^+$ isomer in ^{132}Xe, decaying via a $E3$ transition to the $J^\pi = 7^-$ state, which is also a nanosecond isomer [27]. Approaching the $Z = 64$ subshell closure, an abrupt reduction of the transition strength of the $10^+ \rightarrow 8^+$ decay is observed [24]. The distinct change of the nuclear structure of the $J^\pi = 10^+$ isomers can be traced back to pair excitations across the $Z = 64$ shell closure, resulting in an increasing contribution of the proton $\pi h^2_{11/2}$ configuration to the overall angular momentum of the $J^\pi = 10^+$ isomers [28].

Similar to the $J^\pi = 10^+$ isomers in even-even nuclei, $J^\pi = 19/2^+$ and $23/2^+$ isomers are characteristic features in even-odd nuclei. The isomers predominantly occur along the Sn, Sb and Te chain and are less abundant in $Z \geq 54$ nuclei. Half-life values are distributed throughout the nano-, micro-, and millisecond range [30, 37]. Figure 3(a) indicates the evolution of negative- and positive-parity states along the $N = 79$ chain. Isomeric $J^\pi = 23/2^+$ states were systematically reported for this chain in ^{129}Sn [29], ^{131}Te [30], and ^{139}Nd [31]. The isomers are members of the seniority $\nu = 3$

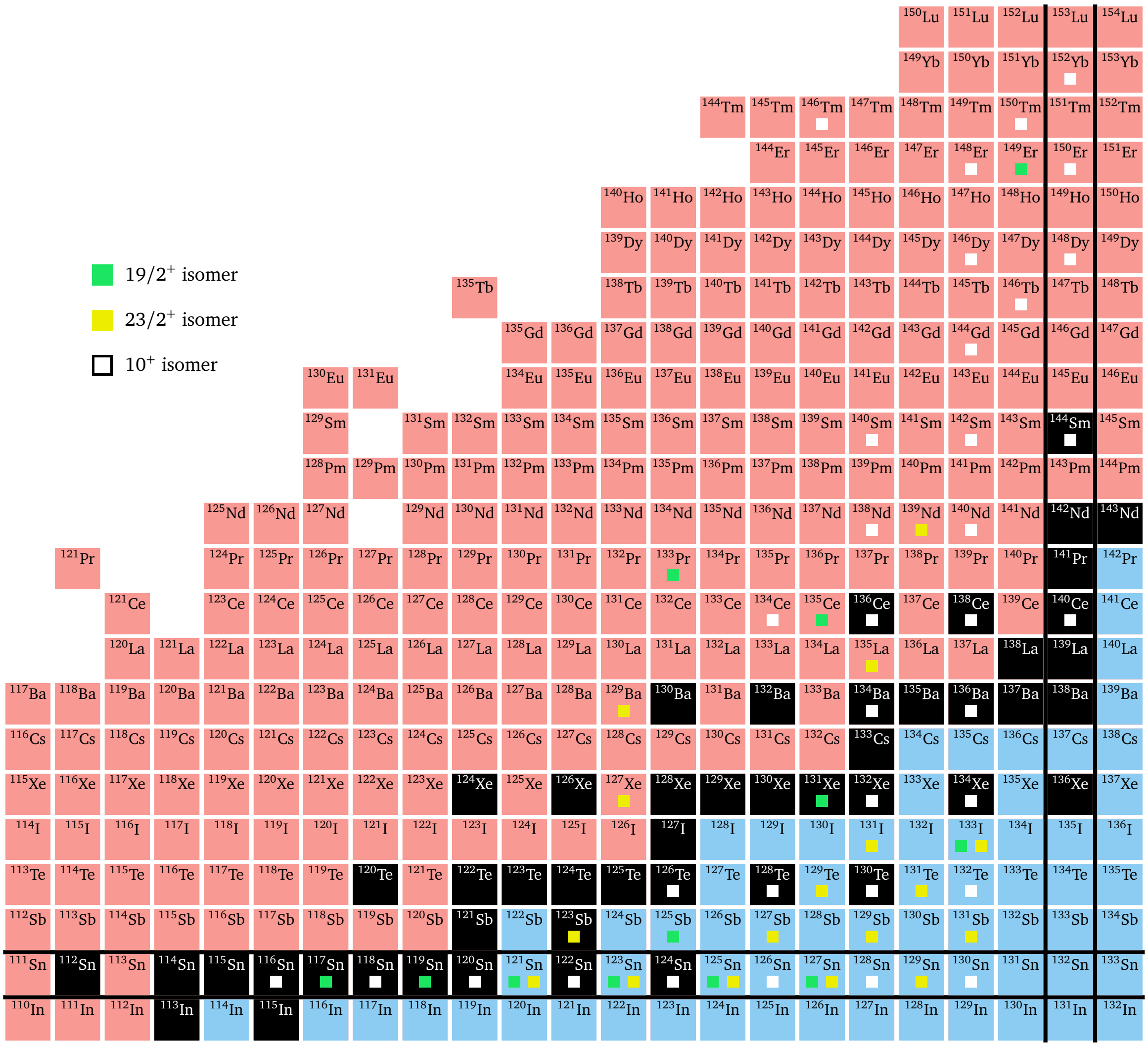

Figure 2: Partial chart of nuclei containing all today measured $J^{\pi} = 19/2^{+}$ (green boxes), $J^{\pi} = 23/2^{+}$ (yellow boxes), and $J^{\pi} = 10^{+}$ (white boxes) isomers with $T_{1/2} > 10$ ns. Data compiled from the Atlas of Nuclear Isomers [19] and Refs. [2, 20].

multiplet and are interpreted to have a predominant $\nu h^{-2}_{11/2} d^{-1}_{3/2}$ configuration. Characteristically, these states are connected to the first or second excited $J^{\pi} = 19/2^{-}$ states. The energy difference between initial $J^{\pi} = 23/2^{+}$ and final $J^{\pi} = 19/2^{-}$ states remains relatively constant with respect to the proton number. However, the half-life values differ by five orders of magnitude between ^{131}Te and ^{139}Nd. Candidates for isomeric counterparts in ^{133}Xe and ^{135}Ba might be anticipated for the 2107-, and 2388-keV states, respectively. In previous works, these states were tentatively assigned to spin and parity of $J^{\pi} = (23/2^{+})$, however, an analysis of delayed γ-ray transitions was not in the scope of these studies [27, 38]. $J^{\pi} = 23/2^{+}$ isomers were also discovered along the $N = 77$ chain in ^{127}Sn ($T_{1/2} = 1.26(15)$ µs [39]) and in ^{129}Te ($T_{1/2} = 33(3)$ ns [40]). From ^{131}Xe onwards, isomeric $J^{\pi} = 19/2^{+}$ states, decaying via $19/2^{+} \rightarrow 19/2^{-}$ $E1$ transitions, prevail along the $N = 77$ chain. Precise half-lives were evaluated in ^{127}Sn [32], ^{131}Xe [33], and ^{135}Ce [34] (c.f. Fig. 3(b)). For

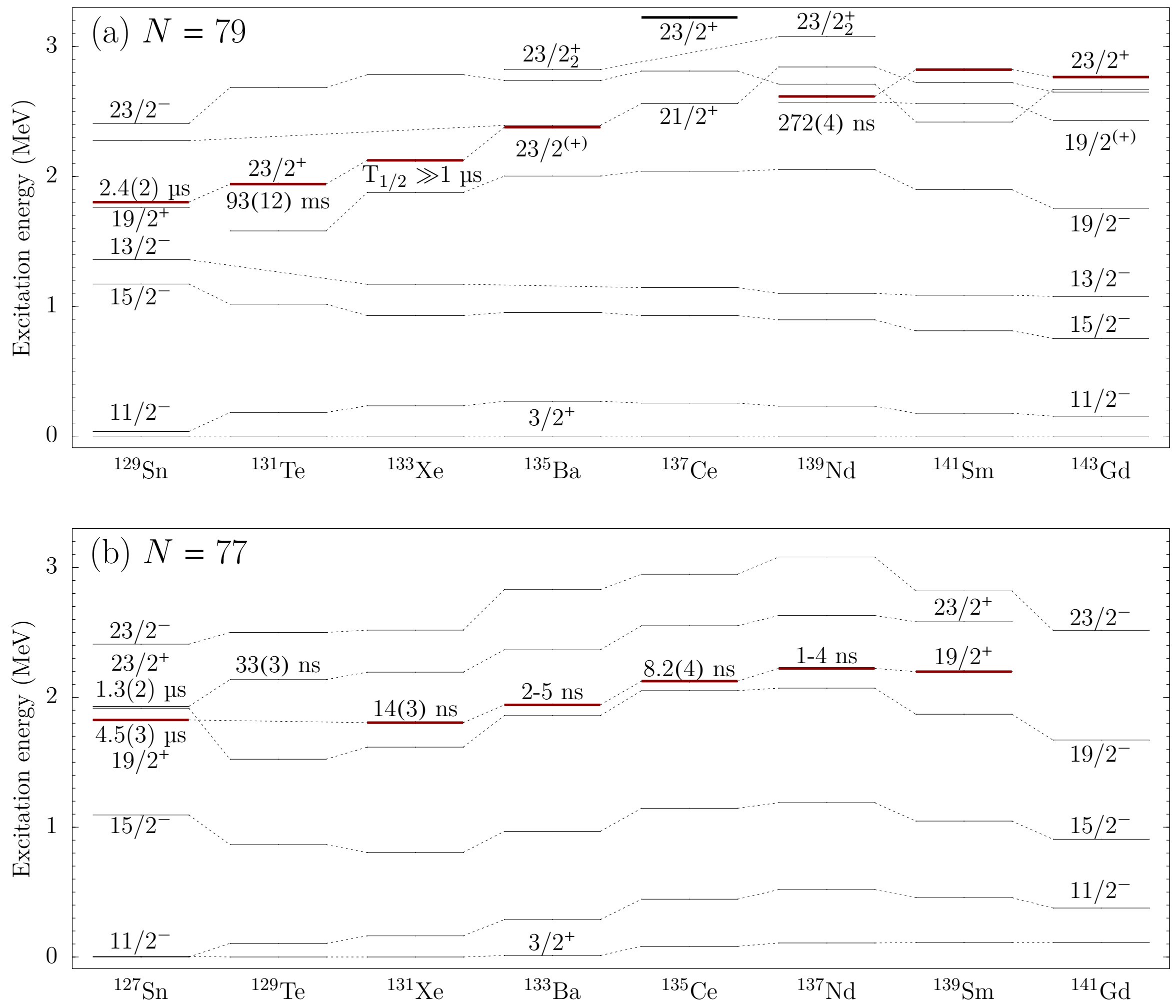

Figure 3: Evolution of excited states throughout the (a) $N = 79$ and (b) $N = 77$ chains. Corresponding $T_{1/2}$ values are given in the figure. Isomeric $J^{\pi} = 23/2^{+}$ states and candidates for this isomer in ^{133}Xe and ^{135}Ba are highlighted with thick red lines. Isomeric $J^{\pi} = 19/2^{+}$ states along $N = 77$ isotones are indicated with thick red lines. Data extracted from ENSDF [2], Refs. [27, 29–31] for the $N = 79$ chain, and Refs. [32–36] for the $N = 77$ chain.

^{133}Ba [36] and ^{137}Nd [35] only estimates of the corresponding half-lives in the lower nanosecond regime are known. $J^{\pi} = 19/2^{+}$ isomers in odd-mass isotopes have a dominating single-particle configuration of $\nu h^{-2}_{11/2} s^{-1}_{1/2}$ and can be interpreted within the particle-plus-rotor model as a coupling of a neutron (hole) to the $J^{\pi} = 5^{-}$ isomer of the neighbouring even-mass partners [32, 35, 36].

Semi-magic nuclei along the $N = 82$ chain received renewed attention with the identification and theoretical interpretation of the neuron $\nu(h^{-1}_{11/2} f^{1}_{7/2})$ cross-shell mixing configuration within the shell-model framework [41, 42]. Hereafter, calculations using an extended $gdsh + \nu(1f_{7/2}, 2p_{3/2})$ cross-shell configuration space were applied to Sb and Te chains [43]. In $^{131-133}$Sb, cross-shell contributions were found to be critical to reproduce the level spacing between low-, and high-spin states as well as $M1$ and higher-multipole $M2$, $E3$, and $E4$ transition strengths between them using the EPQQM interaction [43]. Also the description of parity-changing $E1$ transitions, observed for example in $N = 77$ isotones, requires the consideration of neutron cross-shell configurations [44]. A similar discussion in terms of a so-called $E2$ map and a detailed cross-shell calculation with the EPQQM interaction for the $J^{\pi} = 19/2^{+}$ isomer in ^{133}Ba will be presented in this thesis.

1.1.2 High-spin features northwest of ^{132}Sn

From a certain distance away from the $Z = 50$ and $N = 82$ shell closures, collective features begin to dominate over single-particle excitations due to increasing correlations among valence nucleons. Instead of pure shell-model configurations, the wave functions comprise different linear combinations of couplings of the unique-parity high-j orbital $0h_{11/2}$ with the $2s_{1/2}$, $1d_{3/2}$, $1d_{5/2}$, and $0g_{7/2}$ orbitals [45, 46]. A coarse indicator of structural evolution is given by the ratio between the excitation energies of first $J^{\pi} = 2^{+}$ and 4^{+} states [47]. Figure 4 shows a partial nuclei chart of even-even nuclei with $Z \geq 50$ and $N \leq 82$, whereby the color code illustrates the experimentally determined $R = (E_{4^+}/E_{2^+})$ values, ranging from spherical ^{132}Sn ($R = 1.09$) to deformed rotors like ^{132}Sm ($R = 3.18$). A gradual change between both extreme values is observed throughout a broad near vibration region ($R \approx 2$). In the midshell region, the excitation spectra exhibit the rotational character of a symmetric quantum top ($E \propto J(J+1)$), while the excitation specta of $A \approx 135$ nuclei are well modulated by anharmonic oszillators [48]. A large number of nuclei have R ratios between 2.5 and 3.0, indicating γ-unstable nuclei [49–51]. The γ softness of nuclei in this transitional region originates from the different deformation-driving properties of aligned $0h_{11/2}$ protons (towards prolate shape with $\gamma = 0°$ in the Lund convention) or neutrons (towards oblate shape with $\gamma = -60°$). Studies intended to elucidate high-spin structures are particularly sensitive to mixed configurations involving the intruder $0h_{11/2}$ orbital. The high-spin structure of even-odd nuclei is based on $J^{\pi} = 11/2^{-}$ yrast trap isomers with $\nu h_{11/2}^{-1}$ configuration, which ends up in the $J^{\pi} = 3/2^{+}$ ground state. Similarly, the high-spin structure ($J \geq 10\ \hbar$) of even-even nuclei is build on a $J^{\pi} = 10^{+}$ yrast isomers with a fully spin-aligned two-quasiparticle $\nu h_{11/2}^{-2}$ configuration. In various $A \approx 130$ nuclei collective bands and phenomena involving the $0h_{11/2}$ orbital such as shape coexistence [52], wobbling bands [53], alternating-parity bands [9], and magnetic rotation in dipole bands [54] were established.

Another very characteristic high-spin feature is accompanying by a sudden increase of the total aligned angular momentum, implying a narrow level spacing between high-spin states with respect to the spacing extrapolated from the regular ground-state band [56, 57]. This phenomenon is interpreted as a band crossing between the ground-state band (GS-Band) and a two-quasiparticle band (S-Band), originating from the alignment of a pair of neutrons or protons occupying the intruder $0h_{11/2}$ orbital. In 1972, the crossing of two bands was first observed in ^{162}Er by Johnson *et al.* [58]. In a semi-microscopic model, the fluidity of the nucleus reduces at the alignment frequency, resulting in a sudden increase or bending of the total aligned angular momentum over a small range of rotational frequencies [47]. The alignment process is also manifested in a sudden decrease of $B(E2)$ values between aligning states [59]. Alignment of neutron and proton $0h_{11/2}$ pairs along yrast bands were systematically reported in a series of $A \approx$ 125-136 xenon, barium, and cerium isotopes. Figure 5

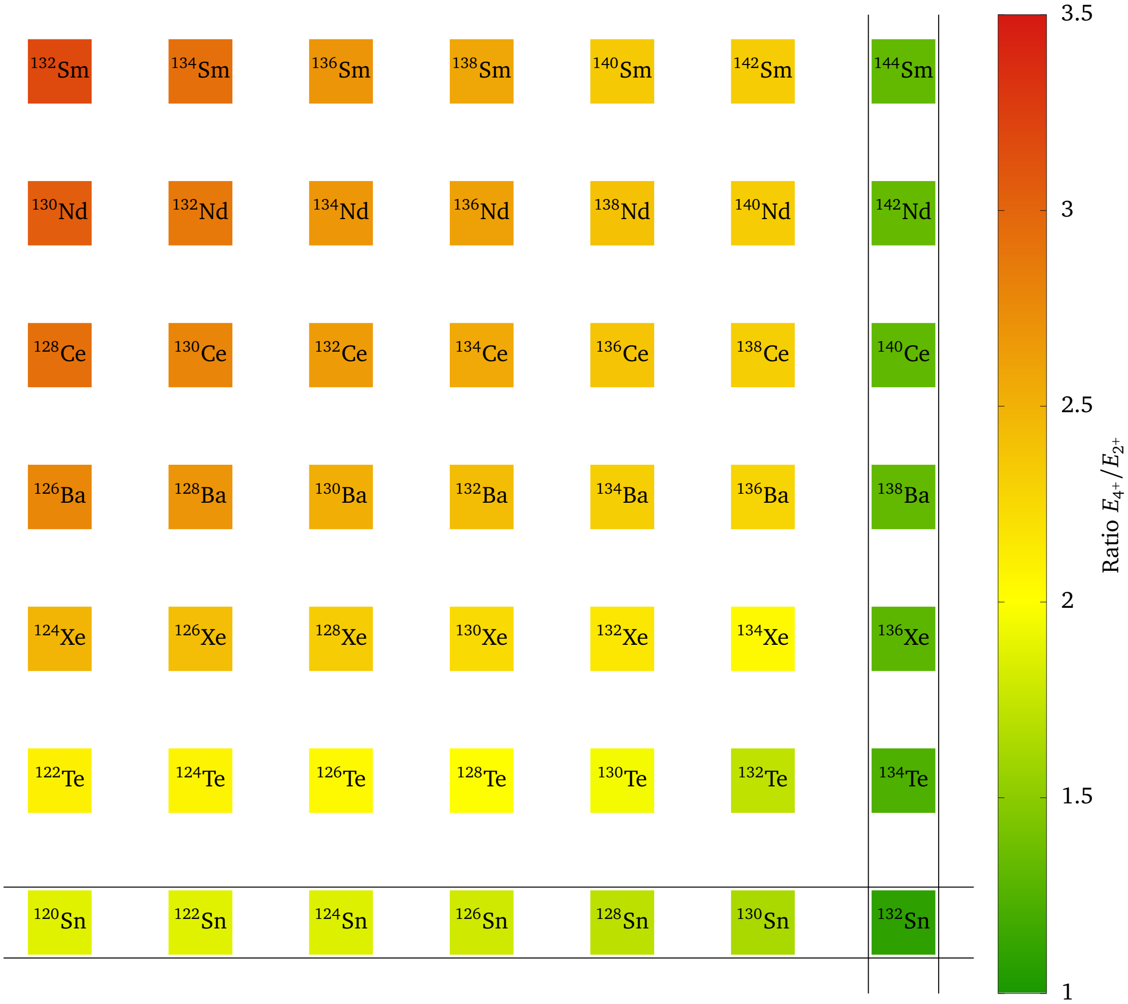

Figure 4: $E_{4_1^+}/E_{2_1^+}$ ratio in even-even nuclei northwest of ^{132}Sn. Ratios range from 1.09 in ^{132}Sn to 3.18 in ^{132}Sm. Solid black lines highlight magic numbers. Data extracted from the NuDat 2.7 database [55].

presents a compilation of the total aligned angular momentum (I_x) of the $E2$ ground-state band for (a)-(h) $^{129-136}$Ce, (i)-(p) $^{127-134}$Ba, and (q)-(x) $^{125-132}$Xe as a function of rotational frequency $\hbar\omega$. Backbending emerges typically at the position of the isomeric $J^\pi = 10^+$ state for even-mass nuclei. In ^{132}Xe, the $J^\pi = 10^+$ isomer (8.39(11) ms [26]) decays though an $E3$ transition to a $J^\pi = 7^-$ state, whereby the $J^\pi = 8^+$ state has not been discovered up to now. Supported by shell-model calculations, it is highly probable that the $J^\pi = 8^+$ state is located very close in energy to the $J^\pi = 10^+$ isomer, implying a remarkable strong backbending character [27]. A characteristic feature of some even-mass nuclei, such as ^{128,130}Ba and ^{132,134,136}Ce, is the presence of two aligned S-bands. The first alignment refers to states above the yrast $J^\pi = 10_1^+$ state, while the second alignment pertains to states in the yrare sequence above the second $J^\pi = 10_2^+$ state. Measured g factors reveal that the alignment of yrast states can be traced back to a pair of neutrons in the $0h_{11/2}$ orbital, whereas the alignment of yrare states corresponds to a proton pair in the $0h_{11/2}$ orbital [22]. Likewise, distinct backbendings and

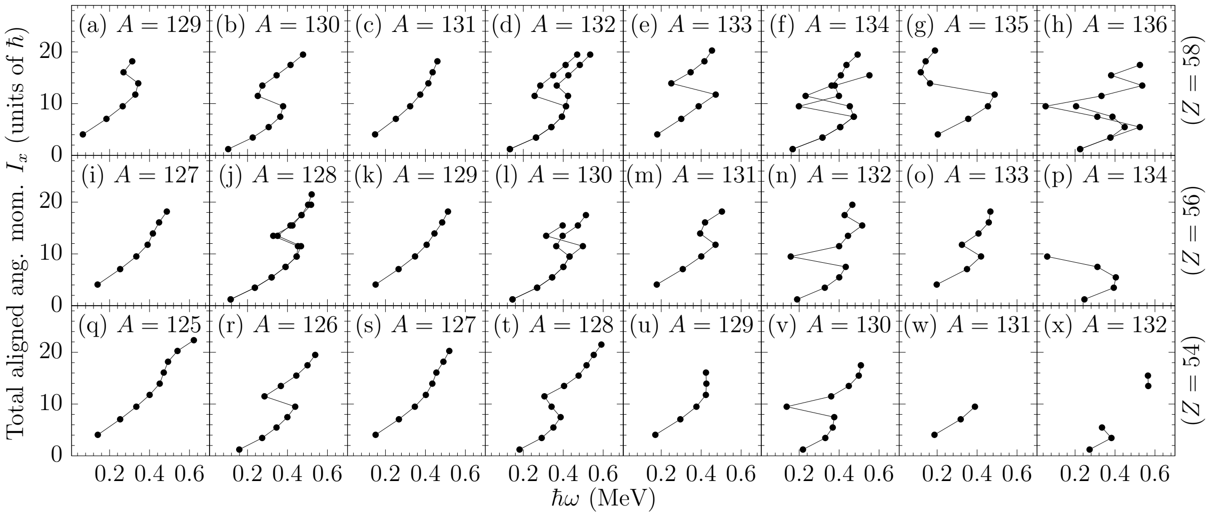

Figure 5: Evolution of total aligned angular momentum against the rotational frequency $\hbar\omega$ for the yrast bands in (a)-(b) Ce ($Z = 58$), (i)-(p) Ba ($Z = 56$), and (q)-(x) Xe ($Z = 54$). See detail in the text. Data extracted from Refs. [2, 53]

upbendings were discovered in various negative-parity ground-state bands of even-odd nuclei in this region. According to cranked-shell-model and total-Routhian-surface calculations, these alignments were solely associated with the breaking of the first neutron $0h_{11/2}$ pairs, except for ^{129}Xe where an alignment of two $0h_{11/2}$ protons was manifested [53]. Reliable information on alignment properties of high-spin states in ^{131}Xe and ^{134}Ba are missing within this systematic.

Furthermore, the nuclear structure of xenon isotopes attracted renewed attention in the field of dark-matter physics. For example, the currently running XENON100 [60] and future XENON1T [61] experiments (located at the Laboratori Nazionali del Gran Sasso (LNGS) in Italy) uses liquid xenon as both target and detection material in the search for weakly interacting massive particles (WIMPS). The xenon used in this dark-matter experiment consists mainly of the isotopes ^{129}Xe and ^{131}Xe, which have high natural isotopic abundances (26.4 % and 21.2 %, respectively). These isotopes exhibit a non-zero ground-state spin and spin-dependent cross sections of inelastic and elastic dark-matter scattering are under discussed. Detailed nuclear shell-model calculations are necessary to calculate structure functions describing the spin content of the proton and neutron groups within the nucleus [62]. Little perceived by the nuclear-structure community, several shell-model studies concentrated on this aspect of WIMP-nucleon coupling involving ^{131}Xe [63–66].

1.1.3 Reaction mechanism to populate nuclei around ^{132}Sn

In the more neutron-deficient part of the $50 \leq Z, N \leq 82$ region, fusion-evaporation reactions between neutron-rich projectiles and neutron-rich target materials are suitable to populate a large amount of excited states in $A \approx 130$ nuclei. Since the 1960s, pioneering studies of high-spin structures in relatively neutron-rich Xe and Ba isotopes were performed with $(\alpha, xn\gamma)$ reactions at typical beam energies of 20-40 MeV with small Ge(Li) detector arrays. Such an experiment restricts the maximum angular momentum of populated states in ^{131,133}Xe to typical values of $21/2\,\hbar$ and excitation energies not higher than 2.5 MeV, as observed in the α+^{130}Te reaction by Kerek *et al.* [33]. Beam ions are required to be heavier than $A = 4$ to enable γ-ray spectroscopy of higher-spin states. However, evaporation cross sections can vary over several orders of magnitude within a narrow range of isotopes. For example, the production cross section of ^{132}Cs can reach the order of 10 barns employing the ^{6}Li + ^{130}Te reaction [67], but drastically decreases to a few microbarns for the population of ^{134}Cs using a ^{11}B + ^{130}Te reaction [68]. γ-ray spectroscopy in such elusive reaction channels require the use of additional detector systems. Especially for a detailed spectroscopy of slightly neutron-rich Xe and Ba isotopes, a gate on evaporated charged particles is crucial to get rid of large background contributions emerging from dominating neutron evaporation channels [69]. In this thesis, γ-ray spectroscopy of ^{131}Xe and ^{130}I considerably benefited from the use of additional silicon detectors inside the target chamber [70] in order to enrich the reaction channel associated with charged particle emission.

Towards the $N = 82$ neutron shell-closure, other reaction techniques are quite common to synthesize neutron-rich nuclei. Multinucleon-transfer reactions (thereafter called MNT) give the possibility for producing neutron-rich nuclei with high yield at standard accelerator facilities. A detailed historical outline of applications of MNT reactions and technological advances, which will be briefly discussed in this part, can be found in Ref. [71]. In these reactions, many nucleons are transferred between beam and target nuclei resulting in a wide range of populated reaction channels. A ^{136}Xe heavy-ion beam allows large energy and angular momentum transfer and is appropriate to populate high-spin states in the neutron-rich Ba, Xe, and Te isotopes. Experimental survival cross sections for MNT reactions employing a ^{136}Xe beam impinging onto ^{238}U [72], ^{209}Bi [73], ^{208}Pb [74], and ^{198}Pt [24] targets are known to be sufficiently high to perform γ-ray spectroscopy for nuclei of interest. Moreover, the availability of recently developed neutron-rich beams like ^{127}I and ^{130}Te opens the door for a systematic investigation of neutron-deficient nuclei in the direction of the neutron drip line [75]. The majority of the previous MNT experiments took advantage of the insignificant Doppler broadening by using thick targets [76]. However, despite the challenging Doppler correction of emitted γ rays, thin target experiments are nowadays feasible in combination with newly developed position-sensitive heavy-ion detector systems. A path-breaking example for such a high-efficiency setup is the combination of the 4π γ-ray spectrometer GAMMASPHERE with the 4π position-sensitive heavy-ion detector CHICO at Lawrence Berkeley National Laboratory (LBNL). Although, the GAMMASPHERE array consists of 103 Compton-suppressed germanium detectors, among them 70 detectors segmented into two halves to reduce the Doppler broadening, the Full Width at Half Maximum (FWHM) of the prompt peaks in the energy spectrum corresponds to typical values of 3.5 keV at low γ-ray energies of approx. 200 keV [24, 71, 77]. Due to many technological advances, the usage of last-generation large solid angle tracking magnetic spectrometers like PRISMA for trajectory reconstruction and ion identification [78–80], in conjunction with next-generation γ-ray tracking spectrometers such as the European Advanced GAmma Tracking Array (AGATA) [81], facilitated a distinct separation of reaction channels and a very careful Doppler correction. In the AGATA physics campaign in 2010 and 2011, the AGATA+PRISMA setup was hosted at the Laboratori Nazionali di Legnaro (INFN LNL Legnaro in Italy)) [71, 82–84].

During two years of the LNL campaign, a number of successful MNT experiments throughout the hole nuclei chart were undertaken, most of them by employing the AGATA+PRISMA setup [85–87]. A series of investigations in the $A \approx 135$ region focused on high-spin states [72]. The level schemes of ^{132}Xe, ^{133}Xe, ^{134}Xe, ^{135}Xe, and ^{137}Ba were successfully extended employing the $^{136}\mathrm{Xe} + ^{238}\mathrm{U}$ and $^{136}\mathrm{Xe} + ^{208}\mathrm{Pb}$ MNT reactions at the AGATA+PRISMA setup. Moreover, data from the $^{136}\mathrm{Xe} + ^{198}\mathrm{Pt}$ MNT reaction performed with the GAMMASPHERE spectrometer coupled to the CHICO array at LBNL could also be analyses within this investigations. Dedicated fusion-evaporation reactions using the HORUS γ-ray array at the University of Cologne were performed to address specific questions [27, 69, 71, 72, 77]. Shell-model calculations employing interactions that are applicable in this mass region reproduced the experimental findings accurately, emphasizing the single-particle nature of the high-spin states in these nuclei [71]. More details on the calculations are briefly described in the following chapter 1.2.

1.2 Shell-model calculations in the $50 \leq Z, N \leq 82$ region

A microscopic attempt to describe nuclear structure properties is given by the nuclear shell-model (SM) theory. Doubly-magic nuclei serve as reference points for all theoretical approaches in this framework, whereby the Hamiltonian comprises the dynamics of valence nucleons in one-body and two-body interaction parts. The quality of an interaction depends crucially upon a precise and systematic description of various nuclear structure properties over a wide range of nuclei. Xenon and Barium isotopes, with $A = 131$-136, are located in a region of the nuclei chart characterized by a variety of (I) single-quasiparticle excitations, (ii) multi-quasiparticle excitations rising from the high coupling $0h_{11/2}$ orbital, and (III) structures arising from the conflation between both (see discussion in Sec. 1.1). Thus, the $50 \leq Z, N \leq 82$ region offers the option for a stringent test of basic ingredients of the spherical shell-model theory and the available effective nuclear interaction Hamiltonians in this region. Especially in the early days, but also at present, a truncation of the SM space is needed to manage the high dimensions in a conventional diagonalization approach using e.g. the Lanczos diagonalization method [88, 89]. However, a truncated SM space may not be sufficient to describe properties of nuclei far outside the inert core [89]. To diagonalize the shell-model Hamiltonian matrices without requiring truncations of the SM space, the present-day shell-model codes ANTOINE [90], NuShellX@MSU [16], and KSHELL [91] are available. In particular, KSHELL was developed for the application on supercomputers like the Post-K computer at RIKEN [92, 93].

The shell-model description of the $N = 82$ isotones attracted attention due to empirical and two-body realistic interactions, which were applied in this mass region. In a pioneering semi-realistic interaction, the two-body part of the shell-model Hamiltonian was derived from modified surface delta interactions in a restricted gds model space [94]. The interaction was a first attempt to analyse excitations originating from proton pairs in the even-mass semi-magic nuclei. It was refined and extended by Kruse *et al.* [95] resulting in the development of the N82 interaction. Later, significant progress was made by using microscopic approaches of nuclear structure calculations utilizing more advanced free nucleon-nucleon potentials. Semi-realistic calculations in the full proton $gdsh$ valence space were carried out along the $N = 82$ nuclei using an effective two-proton interaction obtained from the Brueckner G matrix of the Reid soft-core potential including phenomenological corrections [96]. For almost 15 years, this was the most detailed theoretical description of $N = 82$ nuclei until Andreozzi *et al.* [97] published dedicated calculations employing a realistic effective interaction based on a G-matrix derived from the Bonn-A free nucleon-nucleon potential. The preciseness of the interaction reached a previously unattained precision in the reproduction of the energy spectra and transition probabilities in ^{134}Te and ^{135}I. The authors emphasize that these calculations are the first pure realistic shell-model calculations for $N = 82$ nuclei. Other approaches benefit from the similarities between the nuclear structure of the ^{208}Pb and the ^{132}Sn region. Magnetic moments and energy spectra of nuclei around ^{132}Sn were successfully described by a modified empirical Hamiltonian [98]. The interaction is based on the KH5082 and CW5082 interaction primarily derived for the ^{208}Pb region [99]. The new empirical Hamiltonian is obtained by scaling the TBMEs [98]. The interaction reasonably reproduces quantities like excitation energies, magnetic moments, and transition probabilities of several Sn and Sb nuclei near ^{132}Sn.

Since the coherent interaction between protons and neutrons is mainly responsible for the evolution of the shell structure and the development of collective modes, it is a key ingredient for the description of more complex systems and their excitations beside the $N = 82$ isotones [100, 101]. As stated in Sec. 1.1.2 of this thesis, a prominent feature in nuclei with mass $A \approx 130$ is the backbending phenomena. Since the configuration space reaches an exceptionally order of magnitude for nuclei with a large number of nucleons on top of the closed shells, backbending calculations were traditionally performed on the basis of collective approaches like Hartree-Fock-Bogoliubov calculations [102, 103], Gogny interaction [104, 105], interacting boson model [50, 106, 107], mean-field methods [49, 108], or the cranked-shell-model [53, 109]. Such approaches can be considered as complementary calculations with respect to the shell-model framework [110]. First shell-model calculations, aiming to describe the backbending phenomena, were performed in the pf shell between ^{40}Ca and ^{56}Ni. Caurier *et al.* [110, 111] elucidated the backbending phenomen and the underlying alignment prozess in Cr isotopes with the realistic KB3 interaction. Nowerdays, backbending phenomena of $A \approx 130$ nuclei are in the scope of microscopic studies with untruncated shell-model calculations. Is is noteworthy that only a few studies were performed with the shell-model approach in order to reproduce backbending in the Xe to Ce region [112–114].

Pioneering work in the implementation of realistic large-scale shell-model calculations for nuclei outside the $N = 82$ and $Z = 50$ closed shells was performed by Brown *et al.* [17]. The SN100PN interaction comprises three parts, each dealing with one of the fundamental nucleon-nucleon interaction, plus the Coulomb interaction (Sn100pp+Sn100nn+Sn100pn+Sn100co). The set of TBMEs were evaluated with the G-matrix approach based on the CD-Bonn potential [115]. Single particle energies are chosen to be in line with known experimental levels in ^{133}Sb and ^{131}Sn. The $T = 1$ parts of the of the SN100PN interaction were extensively validated by comprehensive studies along the semi-magic $N = 82$ [41] and $Z = 50$ [116] chains. However, already the limited number of shell-model studies in midshell nuclei revealed that the $T = 0$ proton-neutron monopole part of the SN100PN interaction is insufficient to reproduce experimental data. SN100PN fails to reproduce several nuclear structure properties like isomeric $J^{\pi} = 19/2^{-}$ states in ^{135}Xe and ^{137}Ba [69], which serve as stringent and detailed tests of the proton-neutron part of the interaction since both nuclei exhibit only one valence neutron-hole outside the $N = 82$ shell closure.

In a series of publications, it was pointed out that phenomenological adjustments of the $T = 0$ proton-neutron interaction part in the realistic Hamiltonians, which is the main driver for collective modes, are responsible for an enhanced precision of shell-model predictions [90, 117]. An interaction that implements this approach is the GCN50:82 interaction [118, 119]. Likewise to the SN100PN interaction, it is conducted by applying a realistic G matrix to the CD-Bonn potential [115] by using the method inspired by Hjorth-Jensen *et al.* [120]. In fact, the interaction traced back to the $T = 1$ parts of the SN100PN interaction. The final interaction incorporates corrections obtained by a fit of two-body matrix elements to approx. 400 data points from 80 nuclei with $Z \geq 50$ and $N \leq 82$ [118]. The approach resembles the developed of the GXPF1 interaction in the the pf shell from the early 2000s [121]. Although the main focus of the corrections relates to the monopole part, also modifications of higher order matrix elements were applied, which subsequently slightly improve

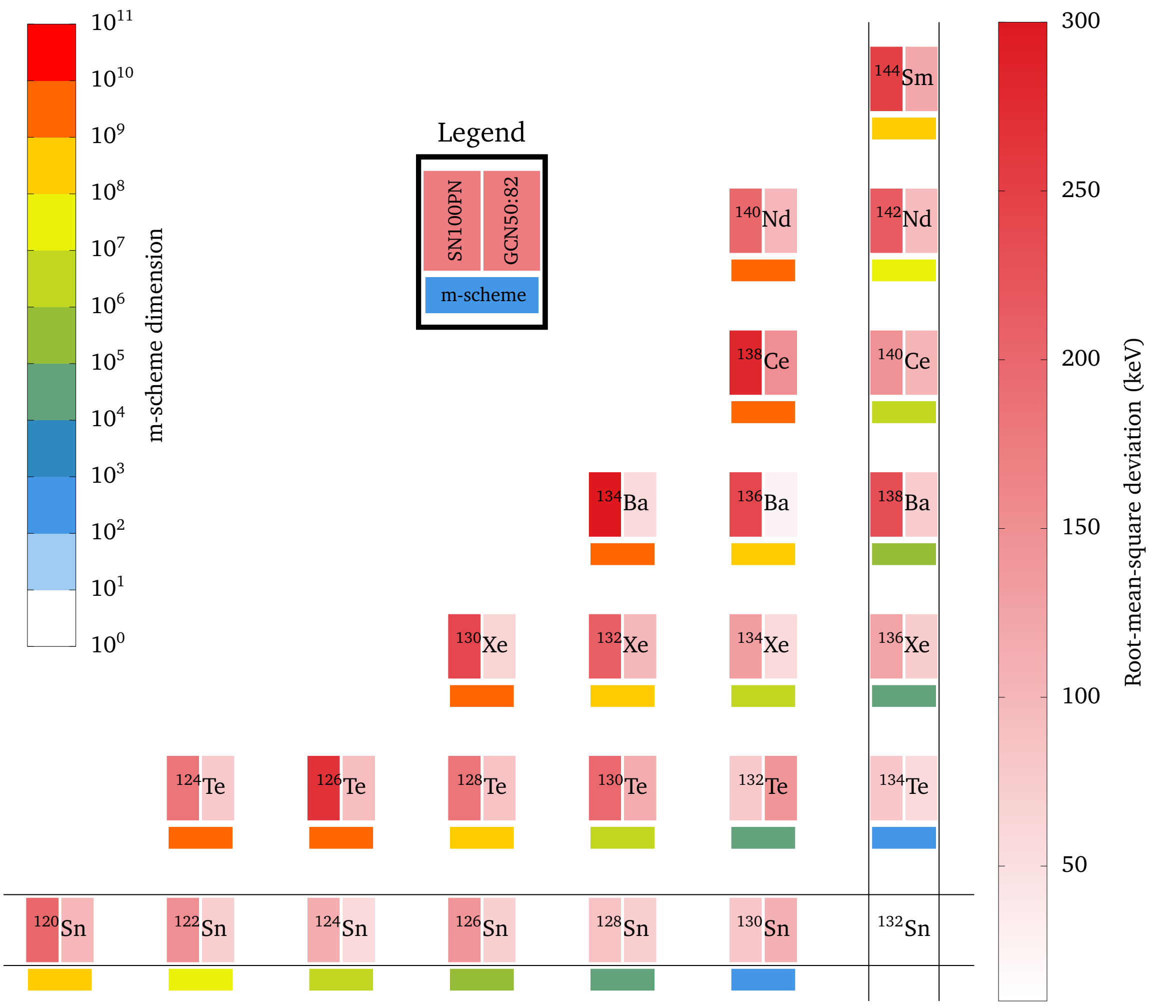

Figure 6: Part of the nuclei chart showing the even-even nuclei in the $50 \leq Z, N \leq 82$ region. Two color codes are shown: (left) The extent of the m-scheme dimension of $J^\pi = 0^+$ states; (right) the root-mean-square (rms) deviation of calculated excitation energies of states in the $E2$ ground-state band ($J^\pi \leq 14^+$), applying the SN100PN and GCN50:82 interactions.

the agreement with experimental data. Caurier *et al.* [118, 122] demonstrated that the GCN50:82 interaction, assuming a bare G matrix, yields a root-mean-square (rms) deviation of 1.35 MeV for a set of several hundred states in this region. A convincing improvement of the absolute rms deviation to 0.25 MeV is gained by correcting the monopole component of the realistic interaction. Moreover, the agreement with respect to the experimental data is further enhanced to a rms deviation of 0.11 MeV by incorporating pairing and multipole components into the fit. The interaction was originally developed in terms of dark matter physics [119, 123]. Meanwhile, the interaction yields convincingly agreement with high-spin states in Te, Xe, Ba, Ce, and Nd nuclei [122, 124].

A more elaborated systematic study of the performance of the GCN50:82 and SN100PN interactions is presented in Fig. 6. The color code arranged on the left-hand side of the figure indicates the m-scheme dimension of the ground states in corresponding nuclei. The color code on the right-hand side refers to the rms deviation of calculated states within the $E2$ ground-state band up to the $J^{\pi} = 14^{+}$ state. Both interactions yield comparable results for the few-valence-particle nuclei along the semi-magic $N = 82$ and $Z = 50$ chains, demonstrating an equivalent performance of the neutron-neutron and proton-proton interaction parts adjacent to ^{132}Sn. However, further depart from the inert core, rms deviations begin to drift apart from each other for $N = 82$ and $Z = 50$ nuclei. For twelve valence particles in ^{120}Sn and ^{144}Nd, the discrepancies between the rms deviations amount to 130 and 100 keV, respectively. Similar results were obtained by approaching the midshell region, whereby the proton-neutron part is gaining importance. The GCN50:82 interaction yields coherently smaller rms deviations for $50 < Z, N < 82$ nuclei, underpinning the assumption of a deficient proton-neutron monopole part of the SN100PN interaction [90, 117]. In the extreme case of highest m-scheme dimension in ^{130}Xe, the rms deviation reaches values of 198 (SN100PN) and 115 keV (GCN50:82). The largest discrepancy between both interactions is observed for ^{134}Ba with rms deviations of 335 (SN100PN) and 59 keV (GCN50:82). The best accordance between theory and experiment is determined for ^{136}Ba, where the rms deviation has a value of 27 keV using the GCN50:82 interaction.

Besides a comparison of calculated and experimental excitation energies, a critical analysis of calculated transition probabilities can provide more reliable information on involved configurations. Effective proton and neutron charges are key ingredients for the description of electric quadrupole transition strengths and moments. For the interactions used in this thesis, effective proton and neutron charges are defined as: $e_{\pi}^{\text{eff}} = 1e + \delta e_{\pi}$ and $e_{\nu}^{\text{eff}} = 0e + \delta e_{\nu}$, where 1 and 0 are bare charges (all in units of e). The proton (δe_{π}) and neutron (δe_{ν}) polarization charges account for the degrees of freedom not explicitly incorporated into the calculations. In particular, polarization effects, where the valence nucleons polarize the underlying inert core, are contributing significantly. Characteristic values are the so-called "standard" effective charges: $e_{\pi}^{\text{eff}} \approx 1.5e$ and $e_{\nu}^{\text{eff}} \approx 0.5e$, which deviate clearly from the free nucleon charges. Considerable effort has been dedicated to determined effective charges in the $gdsh$ valence space. For nuclei around the $N = 82$ chain ($A \approx 138$), deliberately chosen values of $e_{\pi}^{\text{eff}} \approx 1.4e$ and $e_{\nu}^{\text{eff}} \approx 0.7e$ were proposed [125]. Moreover, the neutron charge of $e_{n}^{\text{eff}} \approx 0.7e$ was confirmed for $N = 82$ isotopes in a recent study of the Sn chain, while in the midshell Sn isotopes a neutron charge of $e_{n}^{\text{eff}} \approx 1.0e$ matches the experimental values best [126]. For the nuclei where protons and neutrons are outside closed shells, several sets of effective charges are favored. An analysis of $B(E2; 2^{+} \rightarrow 0^{+})$ transition probabilities in $^{124-127}$Te indicates effective charges of $e_{p}^{\text{eff}} \approx 1.5e$ and $e_{n}^{\text{eff}} \approx 1.0e$ [127]. Otherwise, Teruya *et al.* [128] refers to an empirical set of effective charges which depends on the number of valence protons (N_{π}) and neutrons (N_{ν}): $e_{\pi} = 1.8e - 0.05N_{\pi}e$ and $e_{\nu} = -0.6e - 0.1N_{\nu}e$. The values are parametrized to reproduce experimental $B(E2)$ values in $N = 82$ and $Z = 50$ nuclei. Fully microscopic effective charges were derived by Coraggio *et al.* [129]. Single-particle matrix elements of the microscopic effective electric quadrupole operator (namely effective charges that depend on the specific matrix element) are derived within a many-body perturbative approach, employing an expansion of the $\hat{Q}$ folded diagram of the effective shell-model Hamiltonian [129]. This approach refers to the method developed by Suzuki and Okamoto [130].

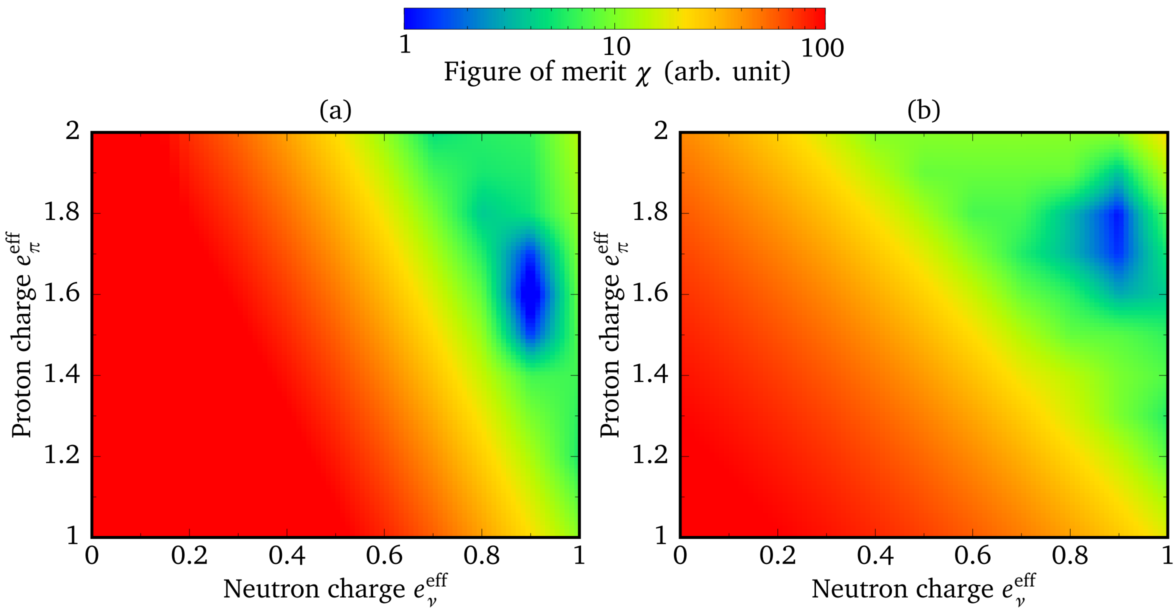

Figure 7: Calculated normalized figure-of-merit scale χ of transition probabilities $B(E2; 10^+ \to 8^+)$ summed over several Sn, Te, Xe, Ba, and Nd isotopes. Landscapes are calculated for different sets of proton and neutron charges (e_π, e_ν) using the (a) SN100PN and (b) GCN50:82 interactions (see text for details).

The landscapes presented in Fig. 7 are aimed to explore the $E2$ effective charges in this region of the nuclei chart using the (a) SN100PN and (b) GCN50:82 interactions. Phenomenological effective charges were determined based upon a comparison of theory with a range of well known $B(E2; 10^+ \to 8^+)$ values for several Sn, Te, Xe, Ba, and Nd isotopes with $T_{1/2} > 10$ ns for the $J^\pi = 10^+$ isomers. The figure of merit $\chi = \sum_{i=0}^{N} \left(\frac{(B(E2)_i^{exp.} - B(E2)_i^{calc.})}{\sigma_i^{exp.}} \right)^2$, summed over the different isotopes, is calculated for the SN100PN and GCN5082 interactions considering different sets of effective proton and neutron charges. The landscapes in Fig. 7 are color-coded with the calculated figure of merits, normalized to the minimum values. The results provide global minima for sets of effective charges (e_π, e_ν): (1.6, 0.9) for SN100PN and (1.75, 0.9) for GCN50:82. Both interactions permit a large acceptance of the proton charge, which is in line with a predominant $\nu h_{11/2}^{-n}$ configuration of the isomeric $J^\pi = 10^+$ states (see discussion in Sec. 1.1.1). Proton components contribute secondarily to the overall configuration of the isomer.

Figure 8 confronts calculated $B(E2)$ transition probabilities from the SN100PN and GCN50:82 interactions with experimentally determined $B(E2)$ values of several transitions in Sn, Te, Xe, Ba, Ce, and Nd nuclei. The compilation is not exhaustive, as only the transitions deexciting isomeric states with $T_{1/2} > 10$ ns in even-mass nuclei were compared. Two sets of effective charges (e_π, e_ν) were used to calculate the theoretical $B(E2)$ values: (a) 1.6, 0.9 (SN100PN), 1.75, 0.9 (GCN50:82), being the above determined values and (b) $e_\pi = 1.8e - 0.05N_\pi e$ and $e_\nu = 0.6e + 0.1N_\nu e$, where N_π and N_ν are the number of valence protons and neutrons with respect to ^{132}Sn, as proposed by Teruya *et al.* [128]. Note that the neutron effective charge is positive in contrast to the definition given in Ref. [128], since SN100PN and GCN50:82 calculations are performed for valence-neutron particles instead of neutron holes.

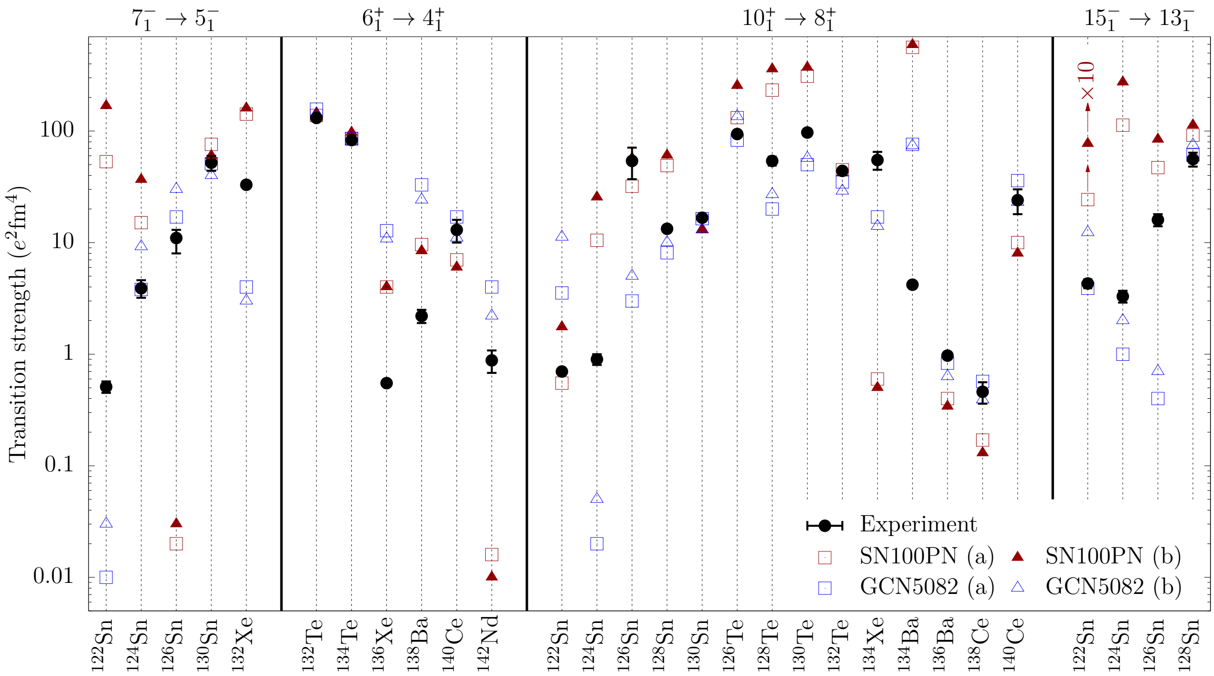

Figure 8: Calculated $B(E2)$ transition probabilities, obtained with an effective proton and neutron charge set (a) of 1.6, 0.9 (SN100PN) and 1.75, 0.9 (GCN50:82), are compared with the experimental values of isomeric states with $T_{1/2} > 10$ ns [2, 19, 131]. Additional calculations with both interactions refer to the effective charge set (b) by Teruya *et al.* [128]: $e_\pi = 1.8e - 0.05N_\pi e$ and $e_\nu = 0.6e + 0.1N_\nu e$. Note the logarithmic scale on the y axis.

For transitions in the two valence-particle nuclei ^{130}Sn and ^{134}Te, all four calculations yield decent agreements with the experimental data. Moreover, the theoretical $B(E2)$ values of the $6_1^+ \to 4_1^+$ transition in the valence alpha-particle nuclei ^{134}Te are compatible with the experimental value. However, notable differences between the calculations were found for $N = 82$ or $Z = 50$ midshell isotopes like ^{136}Xe, ^{138}Ba, ^{142}Nd, and ^{124,122}Sn. Similar conclusions on calculated transition probabilities were also discussed by the authors of Ref. [127]. Further apart from closed shells, the agreement of calculated $B(E2)$ values in adjacent nuclei differs appreciably between different sets of interactions and effective charges. On the one hand, the recently established transition strength of the $10^+ \to 8^+$ decay in ^{136}Ba is well predicted by both interactions. Otherwise, both interactions clearly fail to reproduce the $B(E2)$ values of the $10^+ \to 8^+$ decays in adjacent ^{134}Xe and ^{134}Ba. The small energy gap of 28 keV in ^{134}Xe is predicted at 66 (SN100PN) and 51 keV (GCN50:82), while the 121-keV $10^+ \to 8^+$ transition in ^{134}Ba is predicted to be 10 keV by the GCN50:82 interaction and the SN100PN interaction reverses the ordering of both states. It is notable that the transition strengths of the $15^- \to 13^-$ decays in Sn and Te isotopes are fairly reproduced by the GCN50:82 interaction, although cross-shell contributions were suggested in these isotopes [41–43]. The performance of the different sets of interactions and effective charges is scrutinized by the above introduced figure of merit χ, summed over all isomers. The best agreement is achieved with the GCN50:82 interaction assuming the nuclei dependent effective charge set (b). The figure of merit slightly grows by a factor of 2.9 considering the nucleus-independent effective charge set (a), whereby the calculations are still reproducing the experimental values satisfactorily. In contrast, theoretical transition strengths of the SN100PN interaction with the effective charge set (a) show a significant rise of the figure of merit by a factor of 6.4 relative to the minimal χ value obtained from the GCN50:82 interaction. For the effective charge set (b), this factor enhances up to 14.5. Since $B(E2)$ values are more sensitive to the involved configurations, it can be concluded that the GCN50:82 interaction yields a more accurate description of the different mixed SM configurations of the initial and final states.

Besides the well-established semi-realistic SN100PN and GCN50:82 interactions, the development of the Realistic SM interaction by Coraggio *et al.* [132, 133] made a significant progress in the $A \approx 130$ region. Single-particle energies and TBMEs are derived microscopically by means of the many-body perturbative theory starting from the CD-Bonn potential [115]. To get rid of the repulsive core of the nucleon-nucleon interaction, the high-momentum component are smoothed out using the $V_{\text{low-k}}$ approach with a cutoff momentum of $\Lambda = 2.6$ fm^{-1} [134]. It was chosen carefully to compensate the role of the missing three-nucleon force [129]. The effective shell-model Hamiltonian is derived iteratively by means of the many-body perturbation theory in the $\hat{Q}$- box folded diagram expansion, including all diagrams up to third order in the interaction. More details on the derivation can be found in Ref. [129], where calculations are performed to describe the two-neutrino double-β decay properties of ^{130}Te and ^{136}Xe. The nearly pure microscopic derivation, requiring a minimum set of free parameters, has to be emphasized. This approach aims for a generalized microscopic nuclear structure description.

A further interaction utilizing a monopole-corrected basis is the SNV interaction [44]. The interaction incorporates the N82GYM interaction [135], the SNBG3 interaction [136], and the monopole-based universal force (V_{MU}) for the proton-neutron part introduced by Otsuka *et al.* [137, 138]. The main components of the V_{MU} term are the Gaussian central force and the tensor force. Apart from individual scaling factors, the monopole-based V_{MU} force is intended to serve an universal interaction applicable in different mass regions of the nuclei chart [138]. In the *gdsh* valence space, the strengths of the central and the tensor force from the original V_{MU} interaction are multiplied by factors of 0.84 and 1.3, respectively, to fit the experimental data of one-proton separation energies in Sb isotopes [101]. Very recently, the interaction successfully described the g-factor of the $J^{\pi} = 23/2^{+}$ state in ^{135}La [44].

In the last years, Japanese groups have authored several publications on the theoretical interpretation of nuclei with mass around 130-140 in the light of the pair-truncated shell-model calculations with an extended pairing (monopole and higher order pairing terms) plus quadrupole-quadrupole interaction, employed as an effective interaction [128] (hereafter called PQM130). In order to overcome the large SM space, neutron and proton Hamiltonians are diagonalized one after the other. Afterwards, the total Hamiltonian is diagonalized in a proton and neutron space, which has a maximum number of possible states [128]. This truncation was proven to be sufficient in reproducing several high-spin features of $A \approx 130$ Sn, Sb, Te, I, Xe, Cs, and Ba nuclei [128].

1.3 Outline of this thesis

This cumulative doctoral thesis comprises four peer-reviewed publications published in “Physical Review C” in the years 2018 and 2019. A fifth study is presented in the form of a manuscript. Findings on the search of isomeric states in ^{137}Ce and ^{137}Nd are summarized in addenda attached to two publications. The thesis presents new experimental results on high-spin states of ten nuclei with $A = 133$-138 and their theoretical implementations to a region of medium mass ($50 \leq Z, N \leq 82$) transitional nuclei. The new experimental findings close systematic gaps along isotopic and isotonic chains and improve the understanding of nuclear structure in this region of the nuclei chart. The experimental results are based on dedicated and precise fusion-evaporation reactions at the HORUS spectrometer employed to complement results obtained with the AGATA+PRISMA setup relying on multinucleon-transfer reactions. Finally, recent theoretical advances in latest shell-model interaction theories are included in a refined investigation of high-spin features in $A \approx 135$ nuclei. The thesis contains the following subjects:

The first publication is devoted to new high-spin states in transitional ^{131}Xe. The negative-parity yrast band was extended from 3 to 5 MeV and a distinct backbending along this band was identified. The results are contrasted with the high-spin systematics of $Z = 54$ isotopes and $N = 77$ isotones. Comprehensive truncated and untruncated shell-model calculations in $^{129-132}$Xe elucidate the changing nuclear structure and the observed backbending phenomenon along the Xe chain towards the $N = 82$ shell closure.

The second publication concentrates on millisecond $J^\pi = 23/2^+$ isomers in ^{133}Xe and ^{135}Ba, discovered during a pulsed-beam experiment. The resulting $M2$ and $E3$ reduced transition probabilities are compared with results of shell-model calculations. The isomeric configuration is systematically evaluated along the $N = 79$ chain toward the recently observed $J^\pi = 23/2^+$ isomer in ^{139}Nd. The attached addendum summarizes the results of two independent experiments covering the search of the still pending $J^\pi = 23/2^+$ isomer in ^{137}Ce.

A third publication refers to high-spin states in ^{136}Ba and ^{137}Ba. Besides a revision and an extension of the previously known level scheme above the $J^\pi = 10^+$ isomer in ^{136}Ba, the bandheads of the positive- and negative-parity yrast cascades were established in both isotopes. Based on results of shell-model calculations in lower mass $N = 80$ and $N = 81$ isotones, a fundamental change of the underlying nuclear structure is observed for positive-parity high-spin states.

The fourth publication focuses on a refined investigation of the $J^\pi = 19/2^+$ isomers in ^{133}Ba and the high-spin structure of ^{134}Ba. The isomeric character of the $J^\pi = 19/2^+$ state in ^{133}Ba is interpreted in terms of a calculated $E2$ map and a dedicated cross-shell calculation. The newly observed alignment in ^{134}Ba is discussed within shell-model calculations and a comprehensive systematic analysis of band-crossing frequencies in even-mass Ba isotopes. The attached addendum presents results from a fast-timing measurement on the $J^\pi = 19/2^+$ isomer in ^{137}Nd.

The last study is presented in the form of a manuscript. Results on the first spectroscopy of high-spin states in the odd-odd isotope ^{130}I are presented. Based on theoretical findings from shell-model calculations and systematics along the iodine chain, different mixed proton and neutron configurations are assigned to the new states.

In the last part of this thesis, a summary of outcomes from all five studies will be presented. Finally, the thesis closes with ideas and first results of test measurements for further experiments in the $50 \leq Z, N \leq 82$ region. Suggestions for nuclear-structure studies in neutron-rich nuclei in the vicinity of doubly-magic ^{208}Pb are presented, which will be subject of upcoming beamtimes with the AGATA+PRISMA+NOISE setup at INFN Legnaro.

Publication I: High-spin structure in the transitional nucleus ^{131}Xe: Competitive neutron and proton alignment in the vicinity of the $N = 82$ shell closure

High-spin structure in the transitional nucleus ^{131}Xe: Competitive neutron and proton alignment in the vicinity of the $N = 82$ shell closure

L. Kaya,[1,*] A. Vogt,[1] P. Reiter,[1] M. Siciliano,[2,3] B. Birkenbach,[1] A. Blazhev,[1] L. Coraggio,[4] E. Teruya,[5] N. Yoshinaga,[5] K. Higashiyama,[6] K. Arnswald,[1] D. Bazzacco,[7] A. Bracco,[8] B. Bruyneel,[9] L. Corradi,[3] F. C. L. Crespi,[8] G. de Angelis,[3] J. Eberth,[1] E. Farnea,[7,†] E. Fioretto,[3] C. Fransen,[1] B. Fu,[1] A. Gadea,[10] A. Gargano,[4] A. Giaz,[8] A. Görgen,[11,12,13] A. Gottardo,[3] K. Hadyńska-Klęk,[3] H. Hess,[1] R. Hetzenegger,[1] R. Hirsch,[1] N. Itaco,[4,14] P. R. John,[15] J. Jolie,[1] A. Jungclaus,[16] W. Korten,[17] S. Leoni,[8] L. Lewandowski,[1] S. Lunardi,[2,7] R. Menegazzo,[7] D. Mengoni,[18,2,7] C. Michelagnoli,[19] T. Mijatović,[20] G. Montagnoli,[2,7] D. Montanari,[2,7] C. Müller-Gatermann,[1] D. Napoli,[3] Zs. Podolyák,[21] G. Pollarolo,[22] A. Pullia,[8] M. Queiser,[1] F. Recchia,[2,7] D. Rosiak,[1] N. Saed-Samii,[1] E. Şahin,[11] F. Scarlassara,[2,7] D. Schneiders,[1] M. Seidlitz,[1] B. Siebeck,[1] J. F. Smith,[23] P.-A. Söderström,[24] A. M. Stefanini,[3] T. Steinbach,[1] O. Stezowski,[25] S. Szilner,[20] B. Szpak,[26] C. Ur,[7] J. J. Valiente-Dobón,[3] K. Wolf,[1] and K. O. Zell[1]

[1]*Institut für Kernphysik, Universität zu Köln, D-50937 Köln, Germany*
[2]*Dipartimento di Fisica e Astronomia, Università di Padova, I-35131 Padova, Italy*
[3]*Istituto Nazionale di Fisica Nucleare, Laboratori Nazionali di Legnaro, I-35020 Legnaro, Italy*
[4]*Istituto Nazionale di Fisica Nucleare, Sezione di Napoli, I-80126 Napoli, Italy*
[5]*Department of Physics, Saitama University, Saitama City 338-8570, Japan*
[6]*Department of Physics, Chiba Institute of Technology, Narashino, Chiba 275-0023, Japan*
[7]*Istituto Nazionale di Fisica Nucleare, Sezione di Padova, I-35131 Padova, Italy*
[8]*Dipartimento di Fisica, Università di Milano and INFN Sezione di Milano, I-20133 Milano, Italy*
[9]*CEA Saclay, Service de Physique Nucleaire, F-91191 Gif-sur-Yvette, France*
[10]*Instituto de Física Corpuscular, CSIC-Universidad de Valencia, E-46071 Valencia, Spain*
[11]*Department of Physics, University of Oslo, P.O. Box 1048 Blindern, N-0316 Oslo, Norway*
[12]*Institut de Recherche sur les lois Fondamentales de l'Univers-IRFU, CEA/DSM, Centre CEA de Saclay, F-91191 Gif-sur-Yvette Cedex, France*
[13]*Lawrence Berkeley National Laboratory, Berkeley, California 94720, USA*
[14]*Dipartimento di Matematica e Fisica, Universitá degli Studi della Campania "Luigi Vanvitelli", viale A. Lincoln 5, I-8110 Caserta, Italy*
[15]*Institut für Kernphysik, Technische Universität Darmstadt, D-64289 Darmstadt, Germany*
[16]*Instituto de Estructura de la Materia, CSIC, Madrid, E-28006 Madrid, Spain*
[17]*IRFU, CEA, Universitè Paris-Saclay, F-91191 Gif-sur-Yvette, France*
[18]*Nuclear Physics Research Group, University of the West of Scotland, High Street, Paisley PA1 2BE, Scotland, United Kingdom*
[19]*Institut Laue-Langevin (ILL), 38042 Grenoble Cedex 9, France*
[20]*Ruđer Bošković Institute, HR-10 002 Zagreb, Croatia*
[21]*Department of Physics, University of Surrey, Guildford, Surrey GU2 7XH, United Kingdom*
[22]*Dipartimento di Fisica Teorica dell'Università di Torino and INFN, I-10125 Torino, Italy*
[23]*SUPA, School of Engineering and Computing, University of the West of Scotland, Paisley PA1 2BE, United Kingdom*
[24]*Extreme Light Infrastructure-Nuclear Physics (ELI-NP), 077125 Bucharest-Magurele, Romania*
[25]*Université de Lyon, Université Lyon-1, CNRS/IN2P3, UMR5822, IPNL, F-69622 Villeurbanne Cedex, France*
[26]*Henryk Niewodniczański Institute of Nuclear Physics PAN, PL-31342 Kraków, Poland*

(Received 25 May 2018; published 6 July 2018)

The transitional nucleus ^{131}Xe is investigated after multinucleon transfer in the $^{136}\mathrm{Xe} + {}^{208}\mathrm{Pb}$ and $^{136}\mathrm{Xe} + {}^{238}\mathrm{U}$ reactions employing the high-resolution Advanced γ-Tracking Array (AGATA) coupled to the magnetic spectrometer PRISMA at the Laboratori Nazionali di Legnaro, Italy, and as an elusive reaction product in the fusion-evaporation reaction $^{124}\mathrm{Sn}(^{11}\mathrm{B}, p3n)^{131}\mathrm{Xe}$ employing the High-efficiency Observatory for γ-Ray Unique Spectroscopy (HORUS) γ-ray array coupled to a double-sided silicon strip detector at the University of Cologne, Germany. The level scheme of ^{131}Xe is extended to 5 MeV. A pronounced backbending is observed at $\hbar\omega \approx 0.4$ MeV along the negative-parity one-quasiparticle $\nu h_{11/2}(\alpha = -1/2)$ band. The results are compared to the high-spin systematics of the $Z = 54$ isotopes and the $N = 77$ isotones. Large-scale shell-model calculations employing the PQM130, SN100PN, GCN50:82, SN100-KTH, and a realistic effective interaction reproduce the experimental findings and provide guidance to elucidate the structure of the high-spin states. Further calculations in $^{129-132}$Xe provide insight into the changing nuclear structure along the Xe chain towards the $N = 82$ shell

*Corresponding author: levent.kaya@ikp.uni-koeln.de
†Deceased.

closure. Proton occupancy in the $\pi\, 0h_{11/2}$ orbital is found to be decisive for the description of the observed backbending phenomenon.

DOI: 10.1103/PhysRevC.98.014309

I. INTRODUCTION

The nuclei in the $50 \leqslant Z,N \leqslant 82$ region of the Segrè chart, spanning the nuclei north-west of doubly magic ^{132}Sn, are intriguing systems for the simultaneous investigation of the shell structure as well as for collective degrees of freedom. Couplings of configurations involving the unique-parity high-j orbital $0h_{11/2}$ with configurations in the $2s_{1/2}$, $1d_{3/2}$, $1d_{5/2}$, and $0g_{7/2}$ orbitals give rise to a plethora of high-spin states. The different deformation-driving properties of aligned $h_{11/2}$ proton ($\gamma \approx 0^\circ$ in the Lund convention) or neutron ($\gamma \approx -60^\circ$) configurations cause both collective and noncollective structures [1–5]. Transitional Xe nuclei in the $A \approx 130$ mass region, well described by assuming anharmonic vibrations [6], are known for their softness with respect to γ deformation and form, therefore, an important link in the smooth evolution from spherical to deformed shapes [7–9]. High-j couplings in the high-spin regime form a variety of rotational bands. Their signature splitting ($\alpha = \pm 1/2$) [10] is based on the unique-parity $h_{11/2}$ neutron-hole orbital. Many of the $A \approx 130$ nuclei show irregular yrast sequences in the high-spin regime, accompanied by a sudden increase of moment of inertia along the ground-state band. This phenomenon called backbending [11] is explained as a band crossing of the ground-state band with an aligned two-quasiparticle band, i.e., the quasiparticle level crossing between an unoccupied high-j intruder orbital and the most high-lying occupied orbital.

In the majority of cases, the theoretical investigations of such systems were carried out by means of the interacting boson model (IBM) [9,12,13], mean-field methods [2,14], or the cranked shell model (CSM) [15,16]. However, Xe isotopes have come within reach of advanced untruncated shell-model calculations, providing stringent tests of the predictive power and suitability of various nuclear potentials and models based on modern effective interactions in this region. Is is noteworthy that only a few studies were performed from the shell-model point of view for the description of the backbending [17–19].

The nucleus ^{131}Xe is located in the proton midshell between the $Z = 50$ shell and the $Z = 64$ sub-shell closures and is five neutrons away from the $N = 82$ shell closure. Previous experiments on ^{131}Xe focused primarily on low-spin excitations observed after β decay [20–23], (γ,γ') reactions [24–26], or Coulomb excitation [27]. Like several odd-mass $50 \leqslant Z,N \leqslant 82$ nuclei, ^{131}Xe exhibits a long-lived $J^\pi = 11/2^-_1$ isomer. It has a half-life of 11.84(4) d and an excitation energy of 163.930(8) keV. The isomer has a predominant $\nu h^{-1}_{11/2}$ character and decays via an $M4$ γ ray to the $J^\pi = 3/2^+_1$ ground state [28]. By the end of the 1970s, both Palmer *et al.* [27] and Irving *et al.* [29] studied low-lying positive-parity states in ^{131}Xe utilizing Coulomb excitation and $(\alpha,xn\gamma)$ reactions, respectively. Later, in 1983, Lönnroth *et al.* [30] identified a large number of new low-lying states with one- and three-quasiparticle configurations. Due to a lack of stable beam and target combinations, studies of intermediate and high-spin states were restricted by $(\alpha,xn\gamma)$ reactions [29–31] with small Ge(Li) detector arrays at this time. The most detailed spectroscopy study of the high-spin regime was performed by Kerek *et al.* [31] in 1971, utilizing the ^{130}Te$(\alpha,3n)$ reaction at beam energies of 30 to 40 MeV. Three γ rays with energies of 642.4, 810.6, and 901.5 keV on top of the $J^\pi = 11/2^-_1$ state were found to form a $(21/2^-_1) \xrightarrow{901.5} 19/2^-_1 \xrightarrow{810.6} 15/2^-_1 \xrightarrow{642.4} 11/2^-_1$ negative-parity band. Furthermore, three γ rays with energies of 188.7, 389.0, and 991.6 keV were placed on top of the $J^\pi = 19/2^-_1$ state. The 188.7-keV transition was observed as the $19/2^+_1 \rightarrow 19/2^-_1$ decay of the positive-parity band. The $J^\pi = 19/2^+_1$ state at 1805.7 keV was identified as an isomer with a half-life of 14(3) ns and a three-quasiparticle $\nu(h^{-2}_{11/2}s^{-1}_{1/2})$ configuration. The $J^\pi = 23/2^+_1$ state at 2194.7 keV is explained as a $\nu(h^{-2}_{11/2}d^{-1}_{3/2})$ configuration.

Backbending and upbending phenomena in the yrast bands of even-even Xe isotopes were systematically observed in $^{112-130}$Xe [33–35]. Figure 1 shows the evolution of the total aligned angular momentum for a given transition $I_x = (I^i_x + I^f_x)/2$ with the total angular momenta of the initial and final states $I^{i,f}_x = \sqrt{I^{i,f}(I^{i,f}+1) - K^2}$ versus the rotational frequency $\hbar\omega = (E_i - E_f)/(I^i_x - I^f_x)$ [36] for Xe isotopes with masses ranging from $A = 117$ to $A = 132$ along the yrast bands [32]. The experimental total aligned angular momentum shows a smooth evolution as a function of rotational frequency $\hbar\omega$ for the lighter midshell isotopes. Toward the shell closure, backbending emerges between the $J^\pi = 10^+_1$ and $J^\pi = 12^+_1$ states in ^{122,124,126}Xe and between the $J^\pi = 8^+_1$ and $J^\pi = 10^+_1$ states in ^{128,130}Xe. This behavior is explained by the crossing of a quasiground band and another quasiband with a neutron-aligned $\nu h^{-2}_{11/2}$ configuration [35]. A distinct alignment is observed in the lower-mass neighbor of ^{131}Xe, ^{130}Xe, where the energy difference between the $J^\pi = 10^+_1$ and $J^\pi = 8^+_1$ states is only 276 keV. In the higher-mass neighbor of ^{131}Xe, ^{132}Xe, the $J^\pi = 6^+_1$ state is still tentative and the $J^\pi = 8^+_1$ state is unknown. Compared to the even-mass neighbors of ^{132}Xe, the decay of the $J^\pi = 10^+_1$ state is remarkably hindered ($T_{1/2} = 8.39(11)$ ms [37]). A fully aligned $\nu h^{-2}_{11/2}$ two-neutron-hole configuration was assigned to the state [38]. The $J^\pi = 10^+_1$ state decays predominantly via an $E3$ γ ray to the $J^\pi = (7^-_1)$ state, competitive $E2$ decays were not observed yet. Consequently, it is likely that the $J^\pi = 8^+_1$ state is located very close in energy to the $J^\pi = 10^+_1$ isomer, resulting in a pronounced backbending. This assumption is supported by shell-model calculations [39]. To shade light on the nuclear structure of ^{132}Xe around the $J^\pi = 10^+_1$ state, the high-spin structures of the odd-mass neighboring nuclei can be used to investigate the inert core ^{132}Xe by means of a semiclassical description within the particle-plus-rotor picture. In ^{133}Xe the single-particle character dominates over the collective character [39].

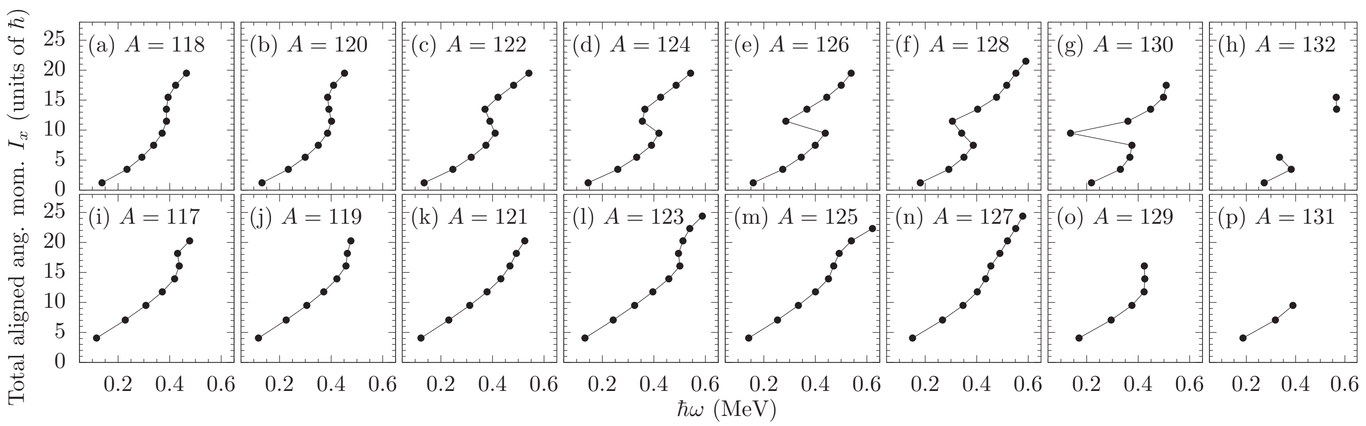

FIG. 1. Total aligned angular momentum against the rotational frequency $\hbar\omega$ for the yrast bands in the Xe isotopes with masses ranging from $A = 117$ to $A = 132$. For definitions see text. Going toward the $N = 82$ shell closure, backbending occurs between the $J^\pi = 10_1^+$ and 12_1^+ states in ^{126}Xe and between the $J^\pi = 8_1^+$ and $J^\pi = 10_1^+$ states in ^{128,130}Xe. In ^{132}Xe the position of the $J^\pi = 8_1^+$ state is not known to date. Data extracted from Ref. [32].

For the lower odd-mass neighbors of ^{131}Xe, ^{125}Xe, and ^{127}Xe, both low-spin structures from ^{3}He- and α-induced reactions [40,41] and elaborate high-spin information from heavy-ion reactions are available. High-spin states of ^{125}Xe were studied at the OSIRIS Compton-suppressed γ-ray spectrometer via the ^{116}Cd(^{13}C,4n) reaction by Granderath *et al.* [42] and via the ^{48}Ca(^{82}Se,5n) reaction by Wiedenhöver *et al.* [43] up to 8.7 MeV. Later, the level scheme and high-spin band structures were significantly extended by Moon *et al.* [15] and Al-Khatib *et al.* [44], respectively. The favored ($\pi = -1, \alpha = -1/2$) negative-parity yrast band built on the $J^\pi = 11/2_1^-$ state is known up to $J^\pi = (47/2^-)$. An alignment at a frequency of $\hbar\omega \approx 0.48$ MeV was observed. Granderath *et al.* [42] proposed a triaxial deformation in the negative-parity band according to calculations in the framework of the triaxial rotor-plus-particle (TRP) model. The crossing in the ($\pi = -1, \alpha = -1/2$) band was assigned to an alignment of a second pair of $h_{11/2}$ neutrons according to theoretical Routhians from CSM calculations. The alignment of the first pair of $h_{11/2}$ neutrons was assumed to be blocked. The findings were reproduced by Moon *et al.* [15] who assigned the negative-parity yrast band a $\nu h_{11/2}[523]7/2$ Nilsson configuration from total Routhian surface (TRS) and CSM calculations.

In ^{127}Xe, high-spin states were thoroughly studied after ^{48}Ca(^{82}Se,3n) reactions at 275 MeV [43]. The negative-parity ground-state band was extended up to 9.5 MeV and a spin of $J^\pi = (51/2^-)$. A band crossing was observed at slightly lower frequencies compared to ^{125}Xe. This observation corroborated a $\nu h_{11/2}^{-3}$ neutron alignment similar to ^{125}Xe [45], however, no theoretical description is available in the literature to date.

Going toward the $N = 82$ shell closure, ^{129}Xe is the last nucleus which can still be sufficiently populated by means of heavy-ion reactions with stable beams heavier than $A = 4$. In 2016, Huang *et al.* [16] extended the level scheme of the negative-parity ground-state band ($\alpha = -1/2$) up to the $J^\pi = 35/2_1^-$ state at 5194 keV utilizing a ^{9}Be-induced fusion-evaporation reaction on a ^{124}Sn target at a beam energy of 36 MeV. The Nilsson configuration for the band was determined to be $\nu h_{11/2}$ [505] 11/2. An alignment in the negative-parity ground-state band was found at a crossing frequency of approx. $\hbar\omega \approx 0.45$ MeV. Cranked shell-model calculations predicted an alignment of two $h_{11/2}$ protons at $\hbar\omega \approx 0.5$ MeV. However, the alignment of two $h_{11/2}$ neutrons was predicted at $\hbar\omega \approx 0.27$ MeV. Since the proton crossing frequency matched the experimental observation, the backbending was explained as an alignment of two $h_{11/2}$ protons. Furthermore, particle-plus-rotor model calculations suggested a triaxial deformation with $\gamma \approx -30^\circ$ in the negative-parity ground-state band.

This work focuses on the hitherto unknown high-spin structures above the 2518-keV state in the negative-parity band in ^{131}Xe. Excited states in ^{131}Xe were populated in three different experiments. Multinucleon-transfer reactions have proved to be an efficient way for the population of intermediate to high-spin states. The combination of the high-resolution position-sensitive Advanced γ-Tracking Array (AGATA) [46] and the PRISMA magnetic mass spectrometer [47–49] at the Laboratori Nazionali di Legnaro (LNL, Italy) was employed to study transitions in ^{131}Xe after ^{136}Xe + ^{208}Pb and ^{136}Xe + ^{238}U multinucleon transfer. Furthermore, ^{131}Xe was populated in a ^{124}Sn(^{11}B, $p3n$)^{131}Xe fusion-evaporation reaction employing the High-efficiency Observatory for γ-Ray Unique Spectroscopy (HORUS) [50] at the Institute of Nuclear Physics, University of Cologne. The γ-ray array was coupled to a double-sided silicon strip detector (DSSSD) [51] for the detection of evaporated protons.

This paper is organized as follows: the experimental setup and data analysis of the three experiments are described in Sec. II, followed by the experimental results in Sec. III. A comparison with results from modern shell-model calculations is presented in Sec. IV before the paper closes with a summary and conclusions in Sec. V.

II. EXPERIMENTAL PROCEDURE AND DATA ANALYSIS

A. ^{136}Xe + ^{208}Pb and ^{136}Xe + ^{238}U multinucleon transfer

Excited states in ^{131}Xe were populated in (i) a ^{136}Xe + ^{208}Pb and (ii) a ^{136}Xe + ^{238}U multinucleon-transfer experiment in the five-neutron stripping channel at the Laboratori Nazionali di Legnaro (LNL), Italy. In the first experiment, a 6.84 MeV/nucleon ^{136}Xe beam, delivered by the PIAVE+ALPI accelerator complex, impinged onto a 1-mg/cm^2 ^{208}Pb target. AGATA [46] was employed in a first demonstrator configuration [52] with nine large-volume electronically segmented high-purity Ge (HPGe) detectors in three triple cryostats [53] to measure γ rays from excited states. The array was placed at a distance of 18.8 cm from the target position. Details on the setup and data analysis are given in Refs. [54,55]. In the second experiment, the PIAVE+ALPI accelerator provided a ^{136}Xe beam with an energy of 7.35 MeV/nucleon and a beam current of 2 pnA to subsequently bombard two different ^{238}U targets with thicknesses of 1 and 2 mg/cm^2. A 0.8-mg/cm^2 Nb backing faced the beam. AGATA was employed in its full demonstrator configuration with 15 HPGe detectors in five triple cryostats placed in the nominal position, 23.5 cm away from the target. Information on the data analysis of this experiment is comprised in Ref. [56]. In both experiments the light projectilelike reaction fragments of interest were identified by the magnetic spectrometer PRISMA [47–49] placed at the reaction's grazing angle of $\theta_{\rm lab} = 42^\circ$ in the ^{136}Xe + ^{208}Pb experiment and $\theta_{\rm lab} = 50^\circ$ in the ^{136}Xe + ^{238}U experiment, respectively. Pulse-shape analysis of the digitized detector signals was applied to determine the individual interaction points within the HPGe shell [57], allowing the Orsay forward-tracking algorithm [58] to reconstruct the individual γ-ray energies, determine the first interaction point of the γ ray in the germanium and, thus, the emission angle. Together with the kinematic information from PRISMA, a precise Doppler correction was performed on a event-by-event basis.

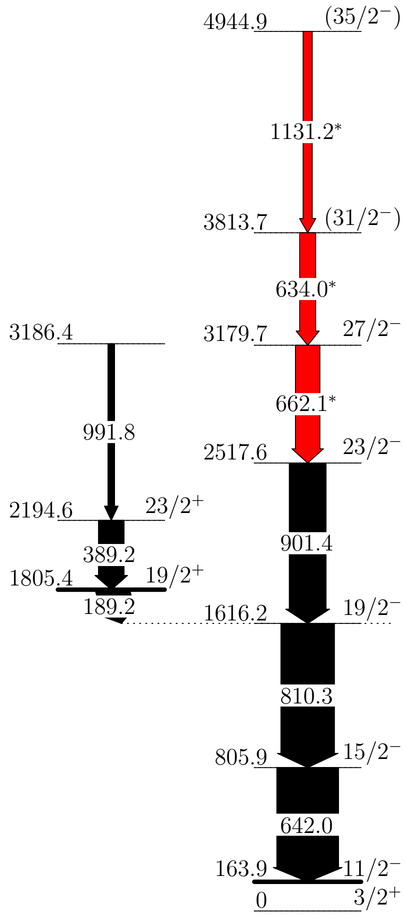

FIG. 2. Level scheme assigned to ^{131}Xe in the present study. Transition and excitation energies are given in keV. Intensities of the cascades above the 164-keV isomer are deduced from the HORUS experiment and normalized to the 642-keV transition. New γ-ray transitions are marked in red with asterisks. See text for details.

B. ^{11}B + ^{124}Sn fusion evaporation

Excited states in ^{131}Xe were populated via the fusion-evaporation reaction ^{124}Sn(^{11}B, $p3n$)^{131}Xe. A 54-MeV ^{11}B beam, delivered by the FN Tandem accelerator located at the Institute for Nuclear Physics, University of Cologne, impinged onto a 3-mg/cm^2 95.3%-enriched ^{124}Sn target, which was evaporated on a 2.7-mg/cm^2 $^{\rm nat.}$Ta backing. All residual reaction products were stopped in the target layers. γ rays from excited states were measured employing the HORUS γ-ray array [50] comprising 14 HPGe detectors, six of them equipped with BGO Compton suppression shields. The detectors are positioned on the eight corners and six faces of a cube geometry. The count rate of the individual HPGe crystals was maintained around 18 kHz during the experiment.

Compared to preceding α-induced reactions [29–31] a ^{11}B beam is better suited for the population of the high-spin regime. Nevertheless, at a beam energy of 54 MeV, several fusion-evaporation codes compute the relative cross section for the population of ^{131}Xe to be in the range of less than 1%. A detection of evaporated charged particles is imperative to cope with the large background emerging from the dominating ^{131,130}Cs neutron evaporation channels. By setting a gate on evaporated charged particles, the peak to background ratio for the $p3n$ channel ^{131}Xe can be enhanced significantly. For this reason, evaporated charged particles were detected with an annular double-sided silicon strip detector (DSSSD) mounted at backward direction covering an angular range from 118° to 163° with respect to the beam axis. The 310-μm-thick silicon disk was produced by RADCON Ltd. (Zelenograd, Russia) and mounted and bonded onto printed circuit boards at the University of Lund, Sweden. The active detector area is divided into 64 radial segments (sectors) on the p-type junction side and into 32 annular segments (rings) on the ohmic n-side facing the target. Each two adjacent ring signals were merged together and read out, to distribute the 32 rings to a total of 16 data acquisition channels. Further information and a detailed characterization of the detector are given in Ref. [51]. The DSSSD was shielded against backscattered beam particles by a 25-μm thick tantalum sheet held in place by a 3-μm Tesa adhesive applied onto a 2-μm polyethylene terephthalate carrier foil [59]. The thickness of the Ta sheet was chosen in such a way that only evaporated protons could reach the Si detector disk.

Coincident events were processed and recorded utilizing the synchronized 80-MHz XIA digital γ finder (DGF) data-acquisition system and stored to disk. The data were analyzed offline using the SOCO-V2 [60] and TV [61] codes. A total number of 1.5×10^{10} prompt $\gamma\gamma$ events and 3×10^6 proton-gated $\gamma\gamma$ events were recorded. Events were sorted into (i)

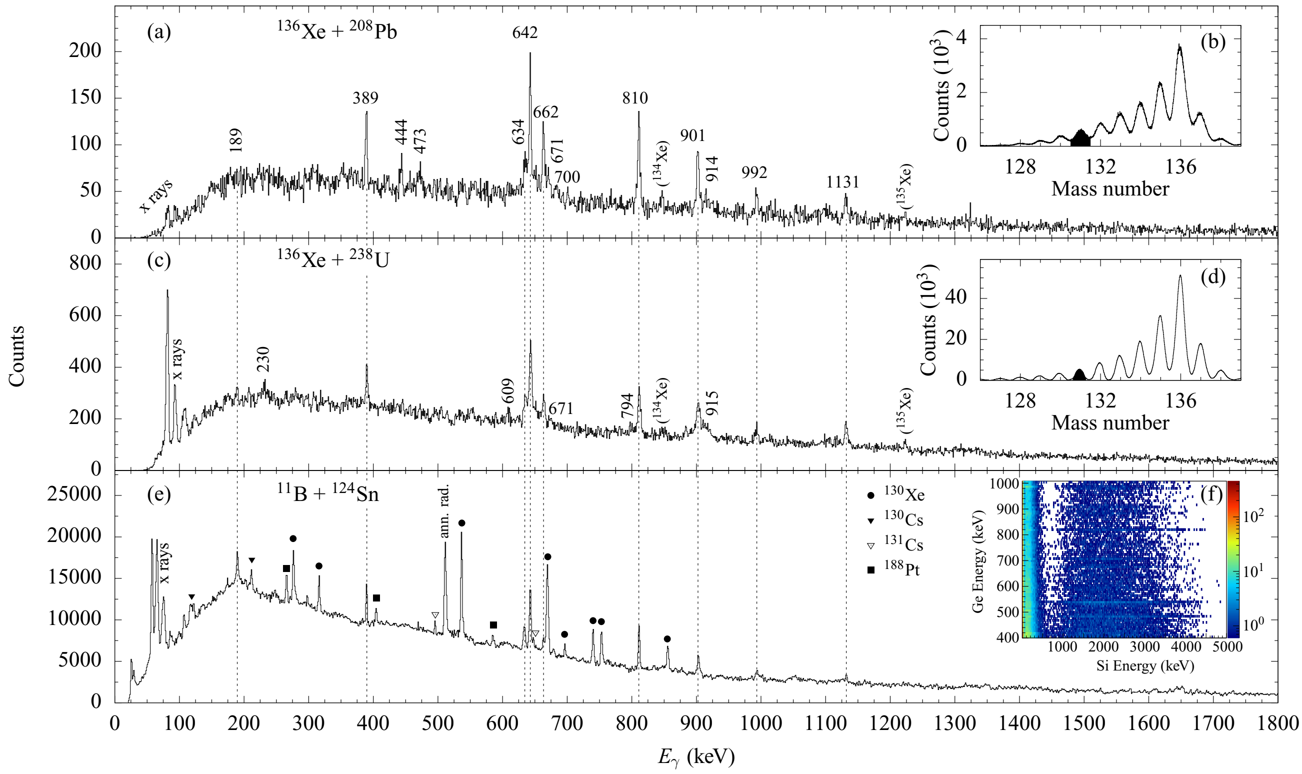

FIG. 3. (a) Doppler-corrected γ-ray spectrum gated on ^{131}Xe identified with PRISMA in the ^{136}Xe + ^{208}Pb experiment. Random background is subtracted with a gate on the prompt peak in the spectrum of time differences between AGATA and PRISMA. (c) Similar data from the ^{136}Xe + ^{238}U experiment. Both insets (b) and (d) represent the mass spectra of the Xe isotopes obtained with PRISMA. The applied mass gates for ^{131}Xe are marked black. (e) Projection of the $\gamma\gamma$ matrix gated on evaporated protons [cf. inset (f)] obtained in the HORUS fusion-evaporation reaction ^{11}B + ^{124}Sn. Remaining contaminant transitions are marked with symbols and dominant transitions from ^{131}Xe are marked with dashed lines to guide the eye.

a general symmetrized two-dimensional matrix to study $\gamma\gamma$ coincidence relations, (ii) two three-dimensional cubes for DSSSD-Ge-Ge and Ge-Ge-Ge coincidences, and (iii) a total of eight group matrices each corresponding to Ge detector pairs with relative angles $\theta_{1,2} \in \{35,45,90,135,145\}$ with respect to the beam axis, and angles $\phi \in \{\pm 270,\pm 215,\pm 180,\pm 55,0\}$ between the planes spanned by the Ge detectors and the beam axis to investigate multipolarities via angular correlations. Spins of populated states are investigated with the $\gamma\gamma$ angular-correlation code CORLEONE [62,63] employing the directional correlation from oriented states (DCO) based on the phase convention by Krane, Steffen, and Wheeler [64,65]. Different hypotheses of involved spins J_1,J_2,J_3 and multipole-mixing ratios δ_1,δ_2 of two coincident γ rays in a cascade $J_1 \xrightarrow{\delta_1} J_2 \xrightarrow{\delta_2} J_3$ are evaluated in χ^2 fits of the correlation function $W(\theta_1,\theta_2,\phi) \equiv W(J_1,J_2,J_3,\delta_1,\delta_2,\sigma)$ on experimental intensities in the different angular-correlation groups. The width of the distribution of the magnetic substates m, i.e., the width of the alignment distribution, was found to be constant at $\sigma = 2.6$. More details on the angular-correlation analysis with CORLEONE are given in Refs. [66,67].

III. RESULTS

The final level scheme of ^{131}Xe deduced from the three experiments is presented in Fig. 2. It is based on $\gamma\gamma$ coincidences, relative transition intensities, and an angular-correlation analysis. Energies of γ-ray transitions and excitation energies are given in keV. Intensities of γ-ray transitions above the $J^\pi = 11/2_1^-$ isomeric state are extracted from the HORUS experiment and normalized to the 642-keV transition. Newly assigned γ-ray transitions are marked with asterisks.

The beam-like Doppler-corrected singles γ-ray spectra of ^{131}Xe from the ^{136}Xe + ^{208}Pb and ^{136}Xe + ^{238}U AGATA experiments are shown in Figs. 3(a) and 3(c), respectively. The corresponding Xe mass distributions are depicted in the insets Figs. 3(b) and 3(d). Random background is significantly suppressed by gating on the prompt peak in the time-difference distribution between AGATA and PRISMA. Prominent transitions are marked with dotted lines to guide the eye. Energies, spin/parity assignments, and relative in-beam intensities of transitions in ^{131}Xe, observed in both AGATA experiments, are summarized in the right-hand side of Table I. Efficiency-corrected relative in-beam intensities in Table I were determined for the ^{136}Xe + ^{208}Pb experiment and normalized to the 642-keV transition. In total, the γ-ray spectra exhibit eight hitherto known peaks and nine new transitions. None of the known low-spin positive-parity excited states below 2 MeV [30,31] were populated. γ rays with energies of 188, 389, 642, 810, 901, and 992 keV depopulating the hitherto known positive- and negative-parity states [31] above the $J^\pi = 11/2_1^-$ isomer are clearly visible in the spectra. In addition, the decays

TABLE I. Energies, spin assignments, and relative in-beam intensities for transitions observed in ^{131}Xe above the $J^\pi = 11/2_1^-$ isomer at 164 keV. Fitted energies and intensities normalized to the 642-keV transition are taken from the ^{11}B + ^{124}Sn fusion-evaporation experiment and the AGATA ^{136}Xe + ^{208}Pb multinucleon-transfer experiment.

HORUS						AGATA	
E_γ (keV)	E_i (keV)	E_f (keV)	I_i^π	I_f^π	I_γ	E_γ (keV)	I_γ
189.2	1805.4	1616.2	$19/2^+$	$19/2^-$	29(2)	189	Weak
389.2	2194.6	1805.4	$23/2^+$	$19/2^+$	30(4)	389	41(4)
634.0	3813.7	3179.7	$27/2^-$	$23/2^-$	24(4)	634	36(3)
642.0	805.9	163.9	$15/2^-$	$11/2^-$	≡100	642	≡100
662.1	3179.7	2517.6	$(31/2^-)$	$27/2^-$	32(3)	662	48(4)
810.3	1616.2	805.9	$19/2^-$	$15/2^-$	87.7(4)	810	78(7)
901.4	2517.6	1616.2	$23/2^-$	$19/2^-$	58.6(6)	901	60(3)
991.8	3186.4	2194.6	–	$23/2^+$	18(3)	992	25(3)
1131.2	4944.9	3813.7	$(35/2^-)$	$(31/2^-)$	15(2)	1131	29(2)
–	–	–	–	–	–	230	Weak
–	2249.3	1805.4	$21/2^+$	$19/2^+$	–	444	25(2)
–	–	–	–	–	–	473	19(2)
–	–	–	–	–	–	609	Weak
–	–	–	–	–	–	671	15(2)
–	–	–	–	–	–	700	12(2
–	1600	805.9	$17/2^-$	$15/2^-$	–	794	Weak
–	–	–	–	–	–	915	12(2)

of the $J^\pi = 21/2_1^+$ and $17/2_1^-$ states at energies of 444 and 794 keV are observed in the MNT experiments. The peaks at 230, 473, 609, 634, 662, 671, 700, 915, and 1131 keV are candidates for new transitions in ^{131}Xe.

In the ^{11}B + ^{124}Sn fusion-evaporation experiment, a particle trigger is crucial to cope with the significant contribution from xn evaporation channels to achieve clean gating conditions for a $\gamma\gamma$ coincidence analysis. The projection of the proton-gated $\gamma\gamma$ matrix is shown in Fig. 3(e). Evaporation residues are identified and selected in the matrix depicted in inset Fig. 3(f), where the energy detected by the DSSSD is plotted versus the HORUS γ-ray energy. Evaporated protons are expected in an energy range of approx. 1 to 6 MeV. Low-energy random coincidences are mainly caused by the detection of low-energy δ electrons and β particles. A gate on proton energies larger than 1 MeV is applied; in the resulting $\gamma\gamma$ projection several transitions of the proton-evaporation channels ^{130,131}Xe are well visible above the background. Remaining contaminant transitions from Cs and Pt isotopes are marked by symbols in Fig. 3(e).

The intensities of the coincident γ rays in the HORUS experiment are summarized in the left-hand side of Table I. All intensities are efficiency corrected and normalized to the intensity of the 642-keV transition. The uncertainties in the transition energies are ±0.5 keV. Spin/parity assignments are supported by systematics, shell-model calculations and angular-correlation measurements. Various HORUS prompt $\gamma\gamma$-coincidence spectra are shown in Figs. 4(a)–4(g). The decay of the $J^\pi = 11/2_1^-$ isomer is not observed due to its long half-life of 11.8 days [28]. Figure 4(a) presents the γ-ray spectrum with a gate on the 642-keV transition. Coincidences are labeled with filled arrow heads. The spectrum exhibits anticipated coincidences at 810, 901, 189, 389, and 992 keV. Beside transitions from ^{130,131}Cs, contaminant peaks are caused by the ground-state band of ^{188}Pt [68] stemming from a dominant fusion-evaporation reaction in the ^{181}Ta backing of the target. All three known γ rays in the positive-parity band with energies of 189, 389, and 992 keV are mutually coincident in the HORUS experiment and were arranged according to their intensity balance as proposed by Kerek *et al.* [31]. Unassigned peaks at 634, 662, and 1131 keV, observed in both AGATA experiments, are coincident to the 642-keV transition. The γ-ray transitions are also in coincidence with the 810-keV transition in Fig. 4(b). Previously, a 901-keV transition was placed parallel to the 3186 keV $\xrightarrow{992\,\text{keV}}$ $23/2_1^+$ $\xrightarrow{389\,\text{keV}}$ $19/2_1^+$ $\xrightarrow{189\,\text{keV}}$ $19/2_1^-$ cascade, depopulating the 2518-keV state. A gate on the 901-keV transition is shown in Fig. 4(c). Coincidences as well as the intensity balance require the newly observed 662-, 634-, and 1131-keV transitions to be placed above the 2518-keV state. Gates on those newly observed transitions are shown in Figs. 4(d)–4(f). All three γ rays are mutually coincident and, thus, form a cascade. The intensity balance in the $\gamma\gamma$ projection gated on the 901-keV transition suggests that the 662-keV transition is directly feeding the 2518-keV state. The intensity of the 634-keV γ-ray peak in the $\gamma\gamma$-coincidence spectrum gated on 901 and 662 keV exceeds the one of the 1131-keV line. In accordance with the intensity balance, the 634-keV transition is placed on top of the newly discovered state at 3180 keV to form the new 3814-keV state. The 1131-keV transition is placed on top of the cascade to establish a new state at 4945 keV. Furthermore, the intensity balance of the three new γ rays determined in the AGATA experiment confirms this assignment. Also, the $\gamma\gamma\gamma$-triple coincidence spectrum with gates on both the 810- and 1131-keV transitions supports a placement of the transitions on top of the 2518-keV state. The maximum excitation energy of approximately

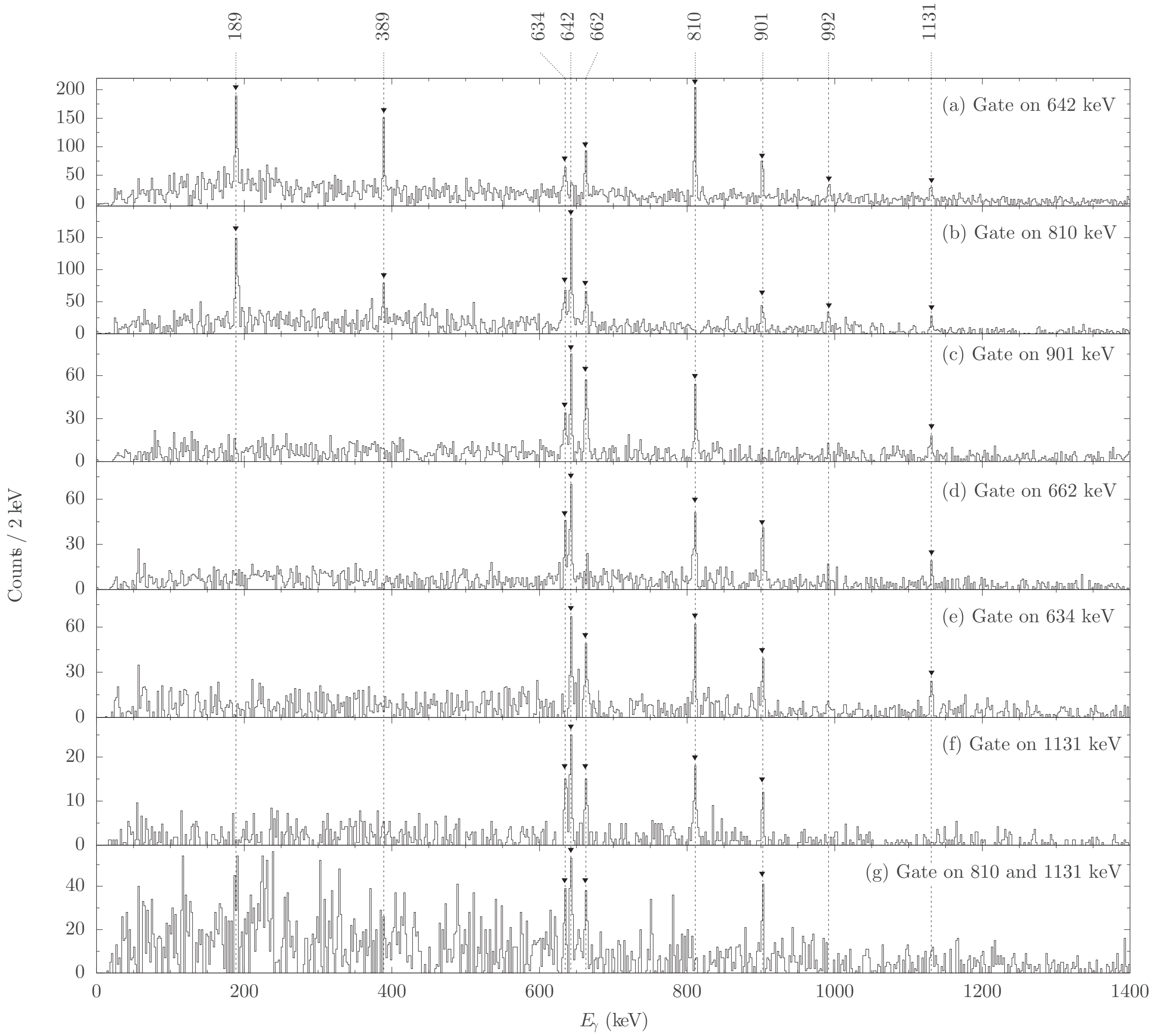

FIG. 4. Prompt HORUS $\gamma\gamma$-double and $\gamma\gamma\gamma$-triple coincidence-spectra with gates on (a) 642, (b) 810, (c) 901, (d) 662, (e) 634, (f) 1131, and (g) 810 and 1131 keV. Thin gray lines mark peak energies identified in both MNT experiments (see Table I). Coincidences are labeled by filled arrow heads.

5 MeV is consistent with other populated reaction channels in both AGATA@LNL experiments [39,69,70]. Unassigned γ-ray transitions observed with AGATA and listed in Table I do not yield meaningful γ-γ coincidences in the HORUS experiment. A placement in the level scheme is not feasible.

In the HORUS experiment spins and parities of excited states are investigated utilizing the angular-correlation analysis described in Sec. II B. A fit of the theoretical angular-distribution function $W(\theta_1,\theta_2,\phi)$ to the experimental intensities of two coincident γ-ray transitions deduced from gates on depopulating transitions in the $\gamma\gamma$ matrices related to the eight angular-correlation groups are performed for each spin hypothesis. To benchmark the validity of the angular correlation analysis, a fit of the $13^+ \rightarrow 12^+$ 417-keV transition in the well populated ^{130}Cs channel is shown in Fig. 5(a). The obtained multipole-mixing ratio $\delta_{\mathrm{exp.}} = -0.11(4)$ reproduces the evaluated value $\delta_{\mathrm{lit.}} = -0.14(6)$ [71]. A further benchmark angular-correlation distribution of the 810-keV transition in ^{131}Xe, gated on the 642-keV transition, is shown in Fig. 5(b). The multipolarity of the 642-keV γ ray is fixed to an $E2$ character, while the spin of the 1616-keV state is tested with values of $J = 15/2$, $17/2$, and $19/2$. Obviously, a pure $E2$ hypothesis yields best results. Figure 5(c) shows the angular-correlation distribution of the 901-810-keV cascade in ^{131}Xe. Spin hypotheses of $J = 19/2$, $21/2$, and $23/2$ were tested for the 2518-keV state. Overall, the $J^\pi = 23/2^-$ hypothesis

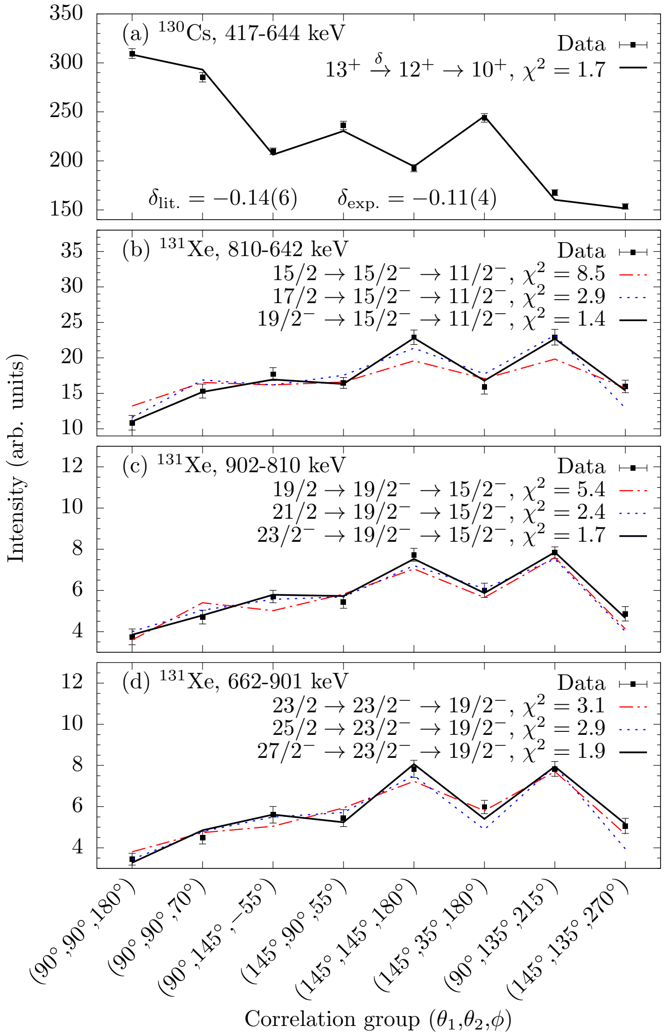

FIG. 5. $\gamma\gamma$ angular correlations. The experimental intensities (data points) are compared to calculated angular-correlation functions (lines). (a) Fit of the 417–644-keV cascade in ^{130}Cs, (b) of the 810–642-keV, (c) of the 901–810-keV, and (d) of the 662–901-keV cascade in ^{131}Xe. See text for details.

matches the experimental values best ($\chi^2 = 1.7$). The previous tentative spin-parity assignment of $J^\pi = 21/2^-$ [31] has to be revised. Using the same method, the spin of the newly established excited state at 3180 keV is determined. The angular distribution of the 662-keV decay is shown in Fig. 5(d). The $J = 23/2$ and 25/2 spin hypotheses show discrepancies between the experimental and the calculated intensities in several correlation groups leading to $\chi^2 = 3.1$ and $\chi^2 = 2.9$, respectively. Based on the experimental data, a $J^\pi = 27/2^-_1$ assignment ($\chi^2 = 1.9$) is most appropriate. Summarizing, there is strong evidence for an $E2$ character of the 662- and 634-keV transitions. No accurate analysis of the $\gamma\gamma$ angular correlations for the weakly populated excited states at 3814 keV and 4945 keV were possible due to insufficient statistics. However, tentative spin assignments of $(31/2^-_1)$ and $(35/2^-_1)$ are most probable due to isotopic systematics discussed in Sec. IV A.

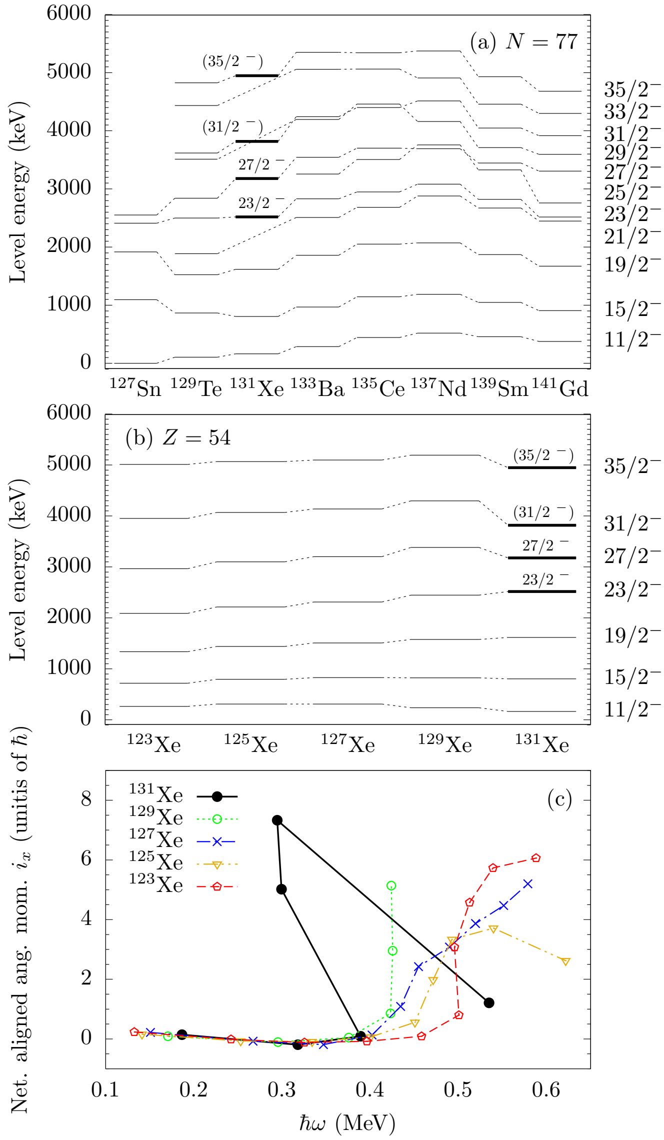

FIG. 6. Evolution of excited states in the negative-parity band along (a) the odd-mass $N = 77$ isotones from $Z = 50$ to $Z = 64$ [72–77] and along (b) the odd-mass $Z = 54$ isotopes from $N = 69$ to $N = 77$ [16,43,78]. Newly discovered states in ^{131}Xe are marked with thick lines. (c) Net aligned angular momenta $i_x(\hbar)$ of favored negative-parity bands in odd-mass $^{123-131}$Xe isotopes as a function of the rotational frequency $\hbar\omega$.

IV. DISCUSSION

A. Systematics along Z = 54

Figure 6(a) shows the evolution of the negative-parity yrast band states along the $N = 77$ isotones from Sn to Gd [72–77]. The newly established states of ^{131}Xe are marked with thicker lines. The reevaluated $J^\pi = 23/2^-_1$ state in ^{131}Xe is 7 keV higher in excitation energy compared to the corresponding state in ^{129}Te, thus, the 2518-keV state in ^{131}Xe fits the systematics of $J^\pi = 23/2^-_1$ states from ^{129}Te to ^{133}Ba. In contrast, the previous $J^\pi = 21/2^-_1$ assignment would disrupt the smooth evolution of the $J^\pi = 21/2^-_1$ states in the $N = 77$ isotones. The newly assigned $J^\pi = 27/2^-_1$ state at 3180 keV is located between the excitation energies of the $J^\pi = 27/2^-_1$ states in both neighboring odd-mass nuclei, which further supports the spin assignment. Also the newly assigned states at 3814 and 4945 keV fit into the systematics. Figure 6(b) compares the levels in the favored negative-parity band in ^{131}Xe from the present work with those in the odd-mass nuclei $^{123-129}$Xe [16,43,78]. The midshell nuclei $^{123-127}$Xe exhibit excitation spectra which are rotational in character. Toward ^{131}Xe a characteristic transition to a vibrational character is observed.

The net aligned angular momentum $i_x(\omega)$ for the favored negative-parity band along the odd-mass Xe isotopes is presented in Fig. 6(c). The parameter i_x is determined by subtracting the collective part from the total aligned angular momentum: $i_x = I_x - I_{x,\mathrm{coll.}}$ where $I_{x,\mathrm{coll.}} = a\omega + c\omega^3$ follows the parametrization by Harris *et al.* [79]. For ^{133}Xe the collective Harris parametrization fails due to a non-rotational single particle character of this isotope. All Xe isotopes exhibit a pronounced upbend. The crossing frequency at which the alignment occurs is mass-dependent and decreases with increasing mass. A delayed upbend in ^{123,125}Xe takes place at a higher frequency compared to the neighboring nuclei. This behavior is explained by the Pauli blocking of the first pair of $h_{11/2}$ neutrons [42,43]. In ^{129}Xe a pronounced upbend is found. Huang *et al.* [16] explained the upbend by an alignment of two $h_{11/2}$ protons according to CSM calculations [16]. The negative-parity band in ^{131}Xe exhibits a large increase of approx. $7\hbar$ in aligned angular momentum, accompanied by a decrease of rotational frequency. Similar to the $-2n$ partner, the alignment takes place at the newly established $J^\pi = 27/2^-_1$ state in ^{131}Xe. Since the bandhead of the favored negative-parity band already shows an initial alignment of $J = 11/2\hbar$, the observed $h^2_{11/2}$ bandcrossing is blocked, i.e. not the fully aligned $10\hbar$ are observed. Following the strong backbending, a remarkable jump back to an alignment of $1\hbar$ is observed with the 1131-keV transition.

B. Shell-model calculations

The extended level scheme of ^{131}Xe is confronted with theoretical predictions from five large-scale shell-model calculations in the *gdsh* valence space outside doubly-magic ^{100}Sn.

The first calculation was carried out in the framework of the pair-truncated shell model using a phenomenological interaction, denoted as PQM130 (Pairing+QQ+Multipole for mass region 130). The approach leverages a pairing-plus-quadrupole interaction that consists of spherical single-particle energies, a monopole-pairing, a quadrupole-pairing, and a quadrupole-quadrupole interaction. The Hamiltonian in each neutron and proton space is diagonalized separately and afterwards the total Hamiltonian is diagonalized in the truncated space. More details on the calculation are given in Refs. [17,80,81].

The second calculation was carried out employing the computer codes NuShellX@MSU [82] and KSHELL [83] in the untruncated *gdsh* model space with the jj55pna Hamiltonian (referred to as the SN100PN interaction) [84]. The Hamiltonian consists of four parts, treating the neutron-neutron, neutron-proton, proton-proton, and Coulomb repulsion between the protons. The realistic two-body residual interaction is based on a renormalized G matrix derived from the CD-Bonn interaction [85]. The neutron-neutron G-matrix elements, written in the hole-hole formalism, are multiplied by a factor 0.9 to improve results for ^{130}Sn. The proton and neutron single-particle energies are based upon the energy levels in ^{133}Sb and ^{131}Sn.

In addition, a calculation with the effective interaction GCN50:82 [86,87] was performed with the program KSHELL. Like the SN100PN interaction, the interaction is derived from a realistic G matrix based on the CD-Bonn potential. However, by fitting different combinations of two-body matrix elements to sets of experimental excitation energies from even-even and even-odd semi-magic nuclei, empirical corrections are added to the original G matrix. By using this approach, mainly the monopole part of the interaction is optimized.

Another calculation was conducted in the framework of the realistic shell model (referred to as realistic SM) [88]. Single-particle energies and the two-body effective interaction are determined via the $V_{\text{low-}k}$ approach from the CD-Bonn free nucleon-nucleon potential [85] with a cutoff momentum of $\Lambda = 2.6\ \mathrm{fm}^{-1}$. The effective shell-model Hamiltonian is derived by means of the many-body perturbation theory in the so-called folded-diagram expansion or $\hat{Q}$-box formalism.

The last calculation, called SN100-KTH, is a monopole-optimized realistic interaction, derived via the Monte Carlo global optimization approach from the G matrix of the CD-Bonn nucleon-nucleon potential [85] by fitting the low-lying states in Sn isotopes. The calculation was performed with the program KSHELL. It was shown that the calculations reproduce well the excitation energies and $E2$ transition probabilities in even-even Te isotopes [89,90].

Figure 7 compares the experimentally determined energies of the first excited states [Fig. 7(a)] with the results of all five shell-model calculations [Figs. 7(b) PQM130, 7(c) SN100PN, 7(d) GCN50:82, 7(e) realistic SM, and 7(f) SN100-KTH]. The states are separated into columns for the (i) negative- and (ii) the positive-parity states. The angular momentum of the $J^\pi = 3/2^+_1$ ground state is reproduced by the PQM130, GCN50:82, SN100-KTH, and realistic SM interactions; however, the SN100PN interaction reverses the first $J^\pi = 3/2^+_1$ and $1/2^+_1$ states. The $J^\pi = 11/2^-_1$ state with a neutron-hole configuration at 164 keV is best reproduced by the SN100PN, GCN50:82, and SN100-KTH interactions with deviations of only 97, 74, and 27 keV, respectively. The realistic SM calculation computes the level energy 157 keV too low, while the PQM130 calculation is the only one which predicts the state 137 keV too high. The excitation energies of the first excited positive-parity states $J^\pi = 5/2^+_1, 7/2^+_1, 9/2^+_1$, and $11/2^+_1$ are fairly reproduced by all five calculations. The experimental $J^\pi = 13/2^-_1$ state is 239 keV higher in energy with respect to the $J^\pi = 15/2^-_1$ state. SN100PN, SN100-KTH, and the realistic SM calculate the energy differences to be 151, 35, and 115 keV, respectively, while PQM130 and GCN50:82 reverse the ordering of both states. Also, the ordering of the first excited $J^\pi = 21/2^+_1$ and $23/2^+_1$ states and of the almost degenerate $J^\pi = 19/2^-_1$ and $17/2^-_1$ states are predicted differently by the five calculations. The experimental energy difference between the $J^\pi = 21/2^+_1$ and $23/2^+_1$ states is 55 keV. This energy difference is predicted slightly larger by the SN100PN, realistic SM, and the GCN50:82 interactions with deviations of 231, 225, and 292 keV, respectively, while PQM130 transposes

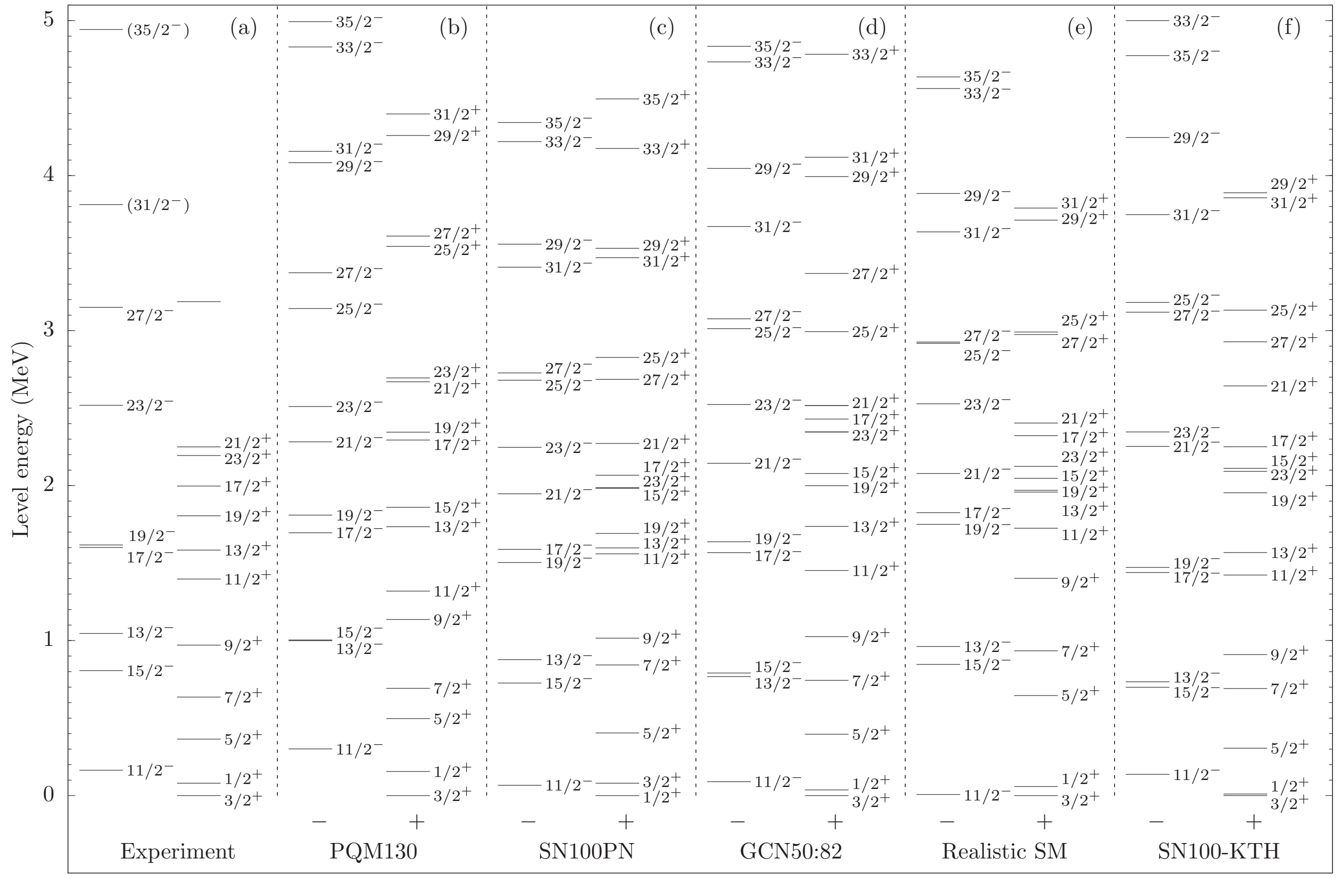

FIG. 7. Comparison of experimental energy spectra with the results of shell-model calculations for ^{131}Xe. (a) Experimental energy spectrum. The results obtained with the different interactions are separated in different columns: (b) PQM130, (c) SN100PN, (d) GCN50:82, (e) realistic SM, and (f) SN100-KTH. For clarity, the states are arranged into two columns for the negative- and the positive-parity states.

both states. The ordering of the $J^\pi = 19/2^-_1$ and $17/2^-_1$ states is predicted correctly by the PQM130, GCN50:82, and SN100-KTH interactions. The calculations suggest that the yet unassigned state on top of the positive-parity band at 3186.4 keV can most likely be interpreted as the first $J^\pi = 25/2^+_1$ or $27/2^+_1$ state. Figure 8 compares the energy

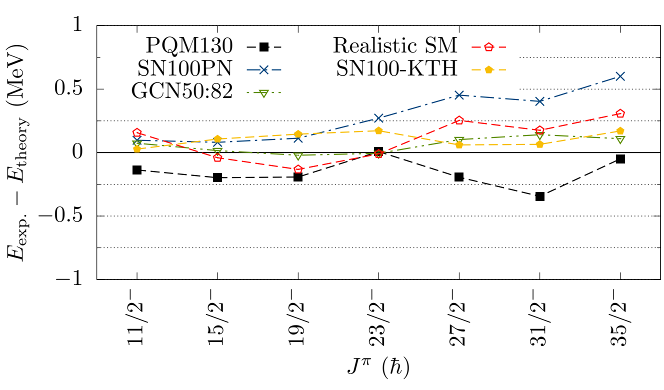

FIG. 8. Energy differences between experimental and calculated excitation energies with different shell-model interactions plotted against the spin of the state.

differences between experimental and predicted level energies of the five calculations along the favored negative-parity band in greater detail. Going to higher spins ($J^\pi \geqslant 23/2^-_1$), the energy differences in the different calculations amount up to 747 keV for the $J^\pi = 31/2^-_1$ state. The high-spin states calculated by the SN100PN interaction are more compressed than in the spectra of the other interactions. All five calculations tend to group pairs of spins ($J^\pi = 25/2^-_1$; $27/2^-_1$), ($J^\pi = 29/2^-_1$; $31/2^-_1$) and ($J^\pi = 33/2^-_1$; $35/2^-_1$). Therefore, spin assignments of the newly observed states at 3813.7 ($J^\pi = 31/2^-_1$) and 4944.9 keV ($J^\pi = 35/2^-_1$) are tentative. The SN100PN, GCN50:82, SN100-KTH, and realistic SM tend to underestimate the excitation energies of states in the high-spin regime, while the PQM130 interaction tends to slightly overestimate the excitation energies.

In addition to the excitation energies, reduced transition probabilities were obtained from in the SN100PN and PQM130 calculations. Kerek *et al.* [31] determined the half-life of the $J^\pi = 19/2^+_1$ state in ^{131}Xe at 1805 keV to be 14(3) ns. Neglecting $M2$ contributions, the experimental $B(E1; 19/2^+_1 \to 19/2^-_1)$ value is $4\times10^{-6} e^2\mathrm{fm}^2$, which is consistent with the result of the SN100PN interaction; however, the lower numerical limit for transition strengths in KSHELL is $10^{-4} e^2\mathrm{fm}^2$. This value fits into the evolution of the half-lives

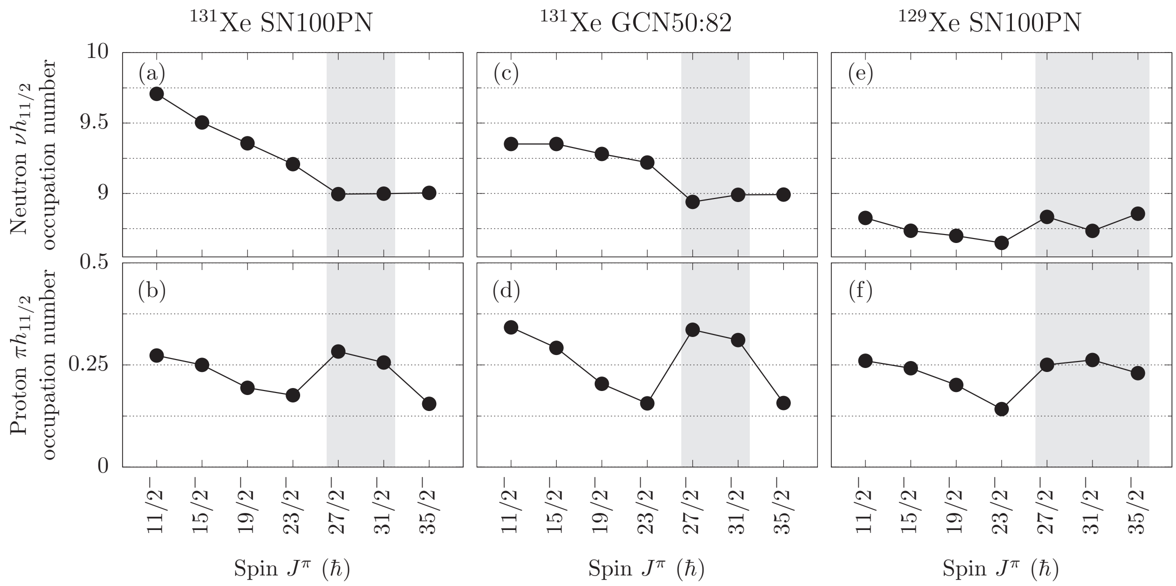

FIG. 9. Average neutron (top row) and proton (bottom row) occupation numbers in the proton and neutron $h_{11/2}$ orbitals in ^{131}Xe, calculated with the (a), (b) SN100PN and (c), (d) GCN50:82 interaction. (e), (f) Similar results for ^{129}Xe calculated with the SN100PN interaction.

of the $J^\pi = 19/2^+_1$ states along the $N = 77$ isotones. In ^{127}Sn the $J^\pi = 19/2^+_1$ state has a long half-life of 4.52(15) µs [72], while in ^{133}Ba and ^{135}Ce the $J^\pi = 19/2^+_1$ states have half-lives between 2 and 5 ns [91] and 8.2(4) ns [92], respectively. In ^{129}Te no corresponding $J^\pi = 19/2^+_1$ state has been discovered so far.

Furthermore, the isotones along the $N = 77$ chain exhibit several $J^\pi = 23/2^+_1$ isomers. In ^{127}Sn the experimental half-life is 1.19(13) µs [72]. The next odd-mass isotone along the $N = 77$ chain, ^{129}Te, has a $J^\pi = 23/2^+_1$ state with a half-life of 33(3) ns [93]. So far, no experimental indication for a long-lived component of the $J^\pi = 23/2^-_1$ state in ^{131}Xe is reported in the literature. Interestingly, the SN100PN interaction computes the $B(E2; 23/2^+_1 \rightarrow 19/2^+_1)$ value to be 6.421 W.u. in ^{131}Xe, corresponding to a lifetime of $\tau \approx 1.4$ ns. Standard effective charges, $e_\pi = 1.5e$ and $e_\nu = 0.5e$, are used in the SN100PN calculation. Furthermore, the PQM130 calculation predicts a $B(E2; 23/2^+_1 \rightarrow 19/2^+_1)$ value of 0.348 W.u., corresponding to a lifetime of ≈ 8 ns. Teruya *et al.* uses effective charges of $e_\nu = -1.1$ (due to the neutron-hole character) and $e_\pi = 1.6$.

To compare the observed backbending in ^{131}Xe with the odd-mass isotopic neighbors, shell-model calculations were performed for negative-parity states above the $J^\pi = 11/2^-_1$ state in ^{129}Xe. These calculations utilizing the SN100PN interaction are computationally demanding with an m-scheme dimension of 2.4×10^9 for the $J^\pi = 11/2^-_1$ state.

The evolution of the average occupation numbers of the proton and neutron single-particle orbits $\pi h_{11/2}$ and $\nu h_{11/2}$ in the favored negative-parity band of ^{131}Xe, calculated by the SN100PN and GCN50:82 interactions, are presented in Figs. 9(a)–9(d). Similar results from a SN100PN calculation for ^{129}Xe are shown in Figs. 9(e) and 9(f). Backbending and upbending states in ^{129}Xe and ^{131}Xe are highlighted gray. In ^{131}Xe, both calculations predict a continuous decrease of occupation in the neutron intruder orbital $\nu h_{11/2}$ until it reaches an occupancy of $N_\nu \approx 9$ in the backbending $J^\pi = 27/2^-_1$ state. The decrease of occupation in the $\nu h_{11/2}$ orbital is mainly balanced by the increase of occupation in the $\nu d_{5/2}$ and $\nu g_{7/2}$ orbitals. For higher-lying states ($J^\pi \geqslant 27/2^-_1$), the $\nu h_{11/2}$ occupation stays constant.

The proton occupancy of the $\pi h_{11/2}$ orbital in ^{131}Xe is predicted to be $N_\pi \approx 0.2$ by both calculations for the $J^\pi = 19/2^-_1$ and $23/2^-_1$ states [Figs. 9(b) and 9(d)]. Going to higher spins along the negative-parity band, the proton $\pi h_{11/2}$ occupancy increases. The occupancy is maximal for the backbending states $J^\pi = 27/2^-_1$ and $31/2^-_1$ and decreases again after the alignment. This observation is also in agreement with the results of the realistic SM calculation were an sharp increase of the $\pi h_{11/2}$ occupancy from 0.14 at the $J^\pi = 23/2^-_1$ state to 0.34 at the $J^\pi = 27/2^-_1$ state is computed. In ^{129}Xe a similar increase of proton occupancy in the $\pi h_{11/2}$ orbital is predicted with the emergence of alignment. The occupation of this configuration persists in the known upbend states with spins $J^\pi \geqslant 27/2^-_1$. This finding agrees with previous investigations within the framework of the cranked shell model where an alignment of two $h_{11/2}$ protons was proposed recently [16]. Supported by the observation in ^{129}Xe, the proton $h_{11/2}$ configuration in ^{131}Xe has a perturbative but decisive role for the description of the structure of alignment states.

The role of the $\pi h_{11/2}$ orbital is also scrutinized by a detailed decomposition of the states along the favored negative-parity band of ^{131}Xe into their proton and neutron configurations in Figs. 10(a)–10(f) for the SN100PN interaction and in Figs. 10(i)–10(n) for the GCN50:82 calculation. All configurations which contribute more than two percent to the overall configuration are shown; the $J^\pi = 15/2^-_1$ state is not visualized for better clarity, nonetheless, the decomposition is very similar to that of the $J^\pi = 11/2^-_1$ state. The percentages of the three most probable configurations are written inside the squares whose areas are proportional to their percentages.

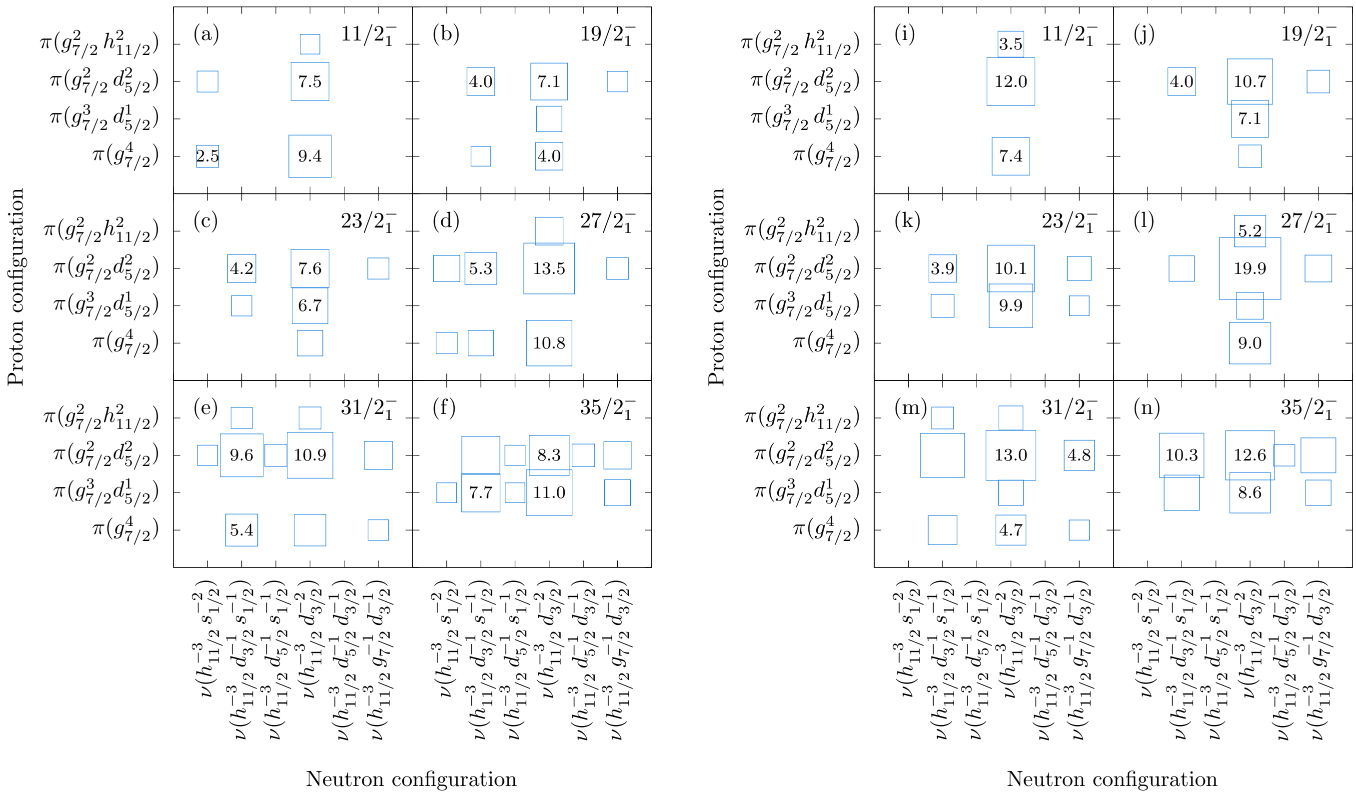

FIG. 10. Decomposition of selected states of ^{131}Xe into their proton and neutron configurations computed by (a$_1$)–(f$_1$) the SN100PN and (a$_2$)–(f$_2$) the GCN50:82 interaction. The three largest percentages are written inside the squares. Percentages below 2% are not visualized.

The decomposition suggests a highly fragmented structure of ^{131}Xe.

In both calculations, the main components of the $J^\pi = 11/2_1^-$ state [cf. Figs. 10(a) and 10(i)] involve the coupling of the neutron configuration $\nu(h_{11/2}^{-3}d_{3/2}^{-2})$ to the leading proton configurations $\pi(g_{7/2}^4)$ and $\pi(g_{7/2}^2d_{5/2}^2)$, respectively. The emergence of the two-proton configurations in the $g_{7/2}$ and $d_{5/2}$ orbitals suggests that these two orbitals are energetically close to each other in the proton space. The configuration $\pi(g_{7/2}^2d_{5/2}^2)$ is the leading proton configuration for both the $J^\pi = 19/2_1^-$ (24.6% SN100PN; 20.5% GCN50:82) and $J^\pi = 23/2_1^-$ (23.4%; 21.1%) states. In addition, the proton configuration $\pi(g_{7/2}^3d_{5/2}^1)$ is gaining significance and is almost equally likely in the $J^\pi = 23/2_1^-$ state (20.0%; 16.9%). In addition to the already mentioned $\nu(h_{11/2}^{-3}d_{3/2}^{-2})$ neutron configurations, a competitive occupation of the $\nu(h_{11/2}^{-3}d_{3/2}^{-1}s_{1/2}^{-1})$ neutron configuration is observed from the $J^\pi = 19/2_1^-$ state onwards.

As discussed and shown in Fig. 6(c), a distinct backbending occurs at rotational frequencies corresponding to the $J^\pi = 27/2_1^-$ and $31/2_1^-$ states. Going from the $J^\pi = 23/2_1^-$ to the $J^\pi = 27/2_1^-$ state, the decomposition matrices of the configurations shown in Figs. 10(d) and 10(l) show once again the emergence of a strong $\pi(g_{7/2}^4)$ proton configuration. Simultaneously, the $\pi(g_{7/2}^3d_{5/2}^1)$ configuration becomes insignificant. The occupation of two protons in the $g_{7/2}$ and $d_{5/2}$ orbitals (31.9%; 31.5%) is slightly favored over the occupation of four protons in a pure $g_{7/2}$ configuration (22.6%; 11.1%). It is also noteworthy that SN100PN and GCN50:82 predict the proton $h_{11/2}$ orbital to contribute pertubatively to the $J^\pi = 27/2_1^-$ configuration as well, which is consistent with the results presented in Figs. 9(b) and 9(d).

For the configurations of the $J^\pi = 31/2_1^-$ state shown in Figs. 10(e) and 10(m), a slight rearrangement of the neutron occupancy from the $\nu(h_{11/2}^{-3}d_{3/2}^{-2})$ (23.4%; 31.3%) to the $\nu(h_{11/2}^{-3}d_{3/2}^{-1}s_{1/2}^{-1})$ (19.8%; 23.2%) is predicted by both interactions. Also the contribution of the proton $h_{11/2}$ orbital persists.

Going to higher spins, the configurations become even more fragmented into configurations with less than 2%. As visible in Fig. 6(c), the backbending is completed at the $J^\pi = 35/2_1^-$ state. The change in the nuclear structure is also observed in Figs. 10(f) and 10(n). Configurations with $\pi(g_{7/2}^4)$ become negligibly small, while the $\pi(g_{7/2}^3d_{5/2}^1)$ configuration, which is negligible small in the backbending region, becomes again a leading configuration. Furthermore, the contribution from the proton $h_{11/2}$ orbital becomes negligibly small after the alignment at $J^\pi = 35/2^-$.

Figure 11 shows a similar decomposition of the $J^\pi = 23/2_1^-, 27/2_1^-, 31/2_1^-$, and $35/2_1^-$ states into their leading proton and neutron configurations, calculated with the SN100PN interaction for ^{129}Xe. Although neutron and proton configurations are more fragmented, the proton configurations before and at the alignment are similar to the ones in ^{131}Xe. Like in ^{131}Xe, the $\pi(g_{7/2}^3d_{5/2}^1)$ configuration becomes less probable, while the $\pi h_{11/2}$ configuration contribute pertubatively to the $J^\pi = 27/2_1^-$ and $31/2_1^-$ state in ^{129}Xe. However, deviations

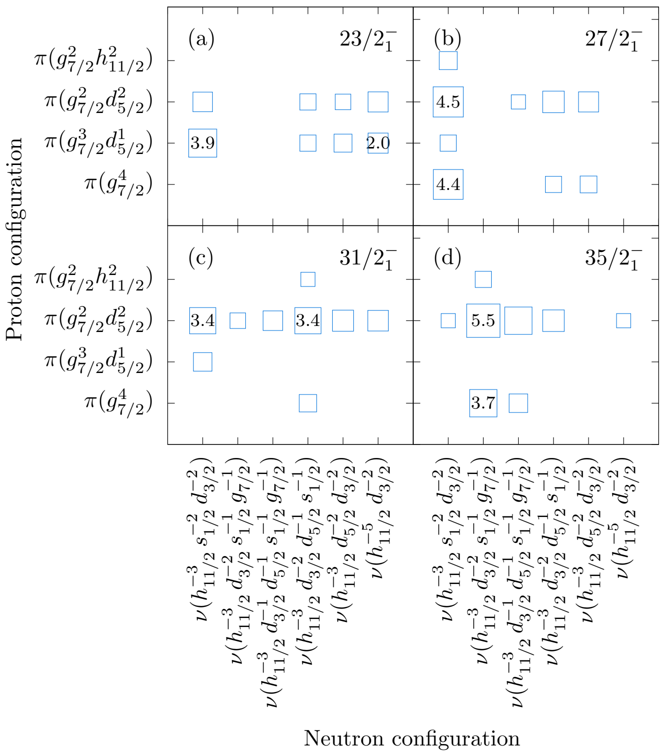

FIG. 11. Decomposition of selected states of ^{129}Xe into their proton and neutron configuration computed by the SN100PN interaction.

occur at the $J^\pi = 35/2_1^-$ state. Unlike in ^{131}Xe [cf. Figs. 10(f) and 10(n)], where a strong $\pi(g_{7/2}^3 d_{5/2}^1)$ character returns to prevail after the backbending, the configurations of the $J^\pi = 35/2_1^-$ state in ^{129}Xe mirror the decompositions observed for the upbend states $J^\pi = 27/2_1^-$ and $31/2_1^-$. In particular, the contributions from the $\pi h_{11/2}$ remain unchanged. This behavior confirms the experimentally observed evolution from upbending in ^{129}Xe to the remarkable backbending in ^{131}Xe.

To inspect the alignment properties and the impact of $\pi h_{11/2}$ protons in ^{131}Xe and ^{129}Xe, the results of the shell-model calculations are reparametrized to the total aligned angular momenta I_x as a function of the rotational frequency $\hbar\omega$. The SN100PN and the GCN50:82 interactions are employed in two separate calculations: (i) permitting excitations into the $\pi h_{11/2}$ orbital and (ii) prohibiting more than one proton in the $\pi h_{11/2}$ orbital. Figure 12(a) compares the extracted theoretical and experimental total aligned angular momenta I_x of ^{131}Xe for calculations without any truncation. The critical frequency at which alignment occurs is slightly underestimated by the realistic SM and the SN100PN interaction, while the GCN50:82 and SN100-KTH interactions predict the alignment frequency in good agreement with the experiment. The experimentally observed refold to the original Harris fit value with the 1131-keV transition after the alignment is predicted correctly by all calculations, particularly by the GCN50:82 calculation. In fact, all four theoretical calculations provide a fair agreement of the experimental backbending pattern in ^{131}Xe. However, PQM130 does not to reproduce the backbending pattern.

Figure 12(b) compares the extracted theoretical and experimental total aligned angular momenta I_x of ^{131}Xe with

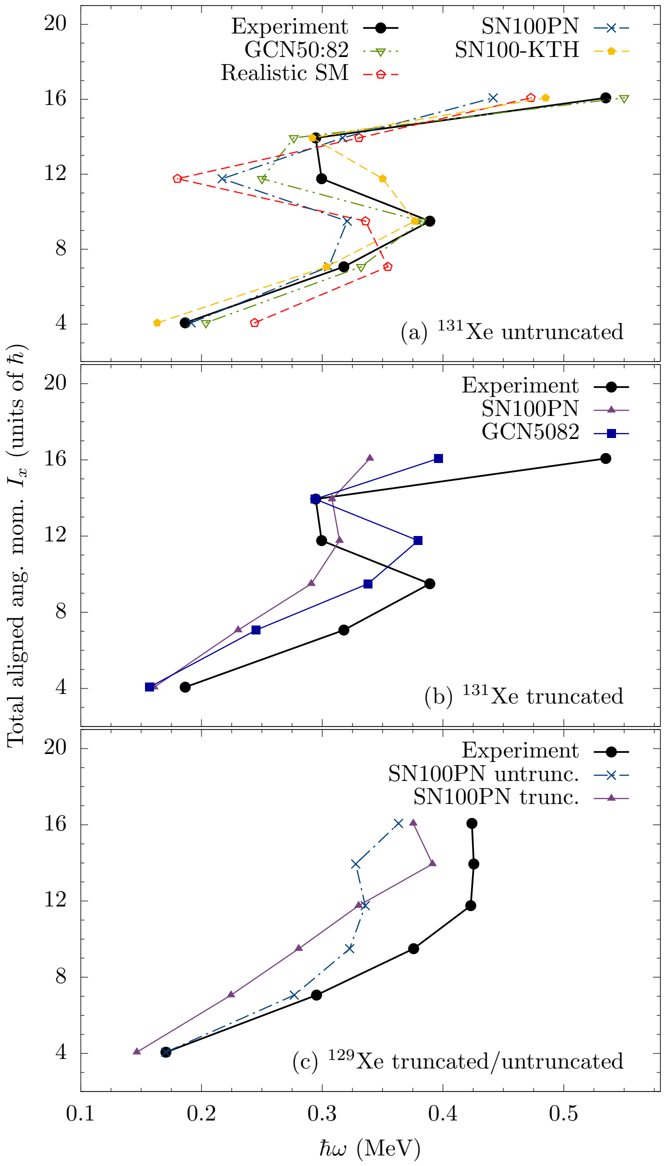

FIG. 12. (a) Comparison between experimental and calculated total aligned angular momenta I_x as a function of the rotational frequency $\hbar\omega$, employing the SN100PN, GCN50:82, SN100-KTH, and realistic SM calculations for ^{131}Xe. (b) Comparison between experimental and calculated total aligned angular momenta I_x as a function of the rotational frequency $\hbar\omega$, employing the SN100PN and GCN50:82 with a truncation of only one allowed proton in the $\pi h_{11/2}$ orbital. (c) Similar comparison for ^{129}Xe employing the SN100PN calculation: (i) untruncated and (ii) truncated with only one proton allowed in the $\pi h_{11/2}$ orbital. Experimental data for ^{129}Xe are taken from Ref. [16].

the truncation of only one proton in the $\pi h_{11/2}$ orbital. The SN100PN calculation with the $\pi h_{11/2}$ truncation exhibits only a weak upbend, while the truncated GCN50:82 calculation predicts a weakened backbend, both at the position of the $J^\pi = 31/2_1^-$ state. Moreover, both calculations do not reproduce the refolding after the alignment at the $J^\pi = (35/2_1^-)$ state. Consequently, the small increase in the average proton occupancy of the $\pi h_{11/2}$ orbital has significant effects beyond small perturbations.

TABLE II. Calculated reduced quadrupole transition strengths $B(E2: J_i \rightarrow J_{i-2})$ of the favored negative-parity band in ^{131}Xe employing the SN100PN/GCN50:82 interaction with standard effective charges $e_\pi = 1.5e$ and $e_\nu = 0.5e$. The first calculation uses the complete $gdsh$ valence space; the second one prohibits more than one proton in the $\pi h_{11/2}$ orbital.

Isotope	Experiment		Theory $B(E2)\downarrow(e^2\,\mathrm{fm}^4)$	
	E_i (keV)	J_i^π	Untruncated	Truncated
^{131}Xe	806	$15/2_1^-$	588/530	559/593
	1616	$19/2_1^-$	821/767	601/748
	2518	$23/2_1^-$	932/929	804/883
	3180	$27/2_1^-$	287/30	782/859
	3814	$(31/2_1^-)$	574/306	444/44
	4945	$(35/2_1^-)$	556/346	568/329

The same approach is applied to ^{129}Xe. Figure 12(c) compares the experimentally determined I_x curve with untruncated and truncated (only one proton allowed in the $\pi h_{11/2}$ orbital) SN100PN calculations. The critical frequency is again slightly underestimated. A satisfactory reproduction of the experimentally observed upbend is achieved by the untruncated calculation. The truncated calculation does not reproduce the upbend pattern for $J^\pi \leqslant 31/2_1^-$ states in the yrast band. The LSSM calculation supports the previous explanation of a $\pi h_{11/2}^2$ proton alignment from cranked shell-model calculations in Ref. [16].

The reduced transition strengths $B(E2; J \rightarrow J-2)$ in the vicinity of the backbending region is of special interest. It is well known that in the neighborhood of the band crossing a minimum in the $B(E2)$ values is caused by the interaction between the bands [94], therefore, a minimum $B(E2)$ value for the $27/2_1^- \rightarrow 23/2_1^-$ decay in ^{131}Xe is expected. The $B(E2)$ values calculated for transitions in the yrast band in ^{131}Xe are shown in Table II employing the SN100PN and the GCN50:82 interaction with standard effective charges $e_\pi = 1.5e$ and $e_\nu = 0.5e$. The theoretical values are arranged into two columns for the untruncated calculation (left) and the truncated calculation where only one proton is allowed in the $\pi h_{11/2}$ orbital (right). The $B(E2)$ values slightly increase towards the $27/2_1^- \rightarrow 23/2_1^-$ transition. The SN100PN calculation yields a reduction of the $E2$ transition strength from 932 e^2 fm^4 for the decay of the $J^\pi = 23/2_1^-$ state to 287 e^2 fm^4 for the decay at the position of the alignment at $J^\pi = 27/2_1^-$. An even more pronounced reduction from 929 to 30 e^2 fm^4 is calculated by the GCN50:82. A similar result is given by the realistic SM, where the $23/2_1^- \rightarrow 19/2_1^-$ transition has $B(E2) = 275\ e^2\,\mathrm{fm}^4$, compared to $B(E2) = 24\ e^2\,\mathrm{fm}^4$ for the $27/2_1^- \rightarrow 23/2_1^-$ transition. Obviously, this result cannot be reproduced by the truncated calculations without pairs in the $\pi h_{11/2}$ orbital. The alignment and the related reduced $B(E2)$ value is observed for the $J^\pi = 31/2_1^-$ state contradicting the experimental findings. In summary, the reduced transition strengths values provide a precise spin dependent confirmation of the significant role of the $\pi h_{11/2}$ orbital.

To obtain a consistent picture also the positive-parity ground state bands in the even-even neighbors ^{130}Xe and ^{132}Xe were investigated and calculations employing the SN100PN interaction were carried out. Like before, the calculations are divided into (i) the full $gdsh$ valence space and (ii) a truncated calculation where only one proton is allowed to occupy the $\pi h_{11/2}$ orbital. A comparison between the calculations and the experimentally obtained total aligned angular momentum I_x for ^{130}Xe is shown in Fig. 13(a). In ^{130}Xe, I_x smoothly follows the Harris curve up to the $J^\pi = 8_1^+$ state at a rotational frequency of approximately $\hbar\omega = 0.38$ MeV. At the position of the $J^\pi = 10_1^+$ state, I_x exhibits a strong backbending down to a frequency of approximately $\hbar\omega = 0.12$ MeV. Similar to ^{131}Xe, a refolding after the alignment is observed for higher-lying states. Both calculations predict an initial alignment at the

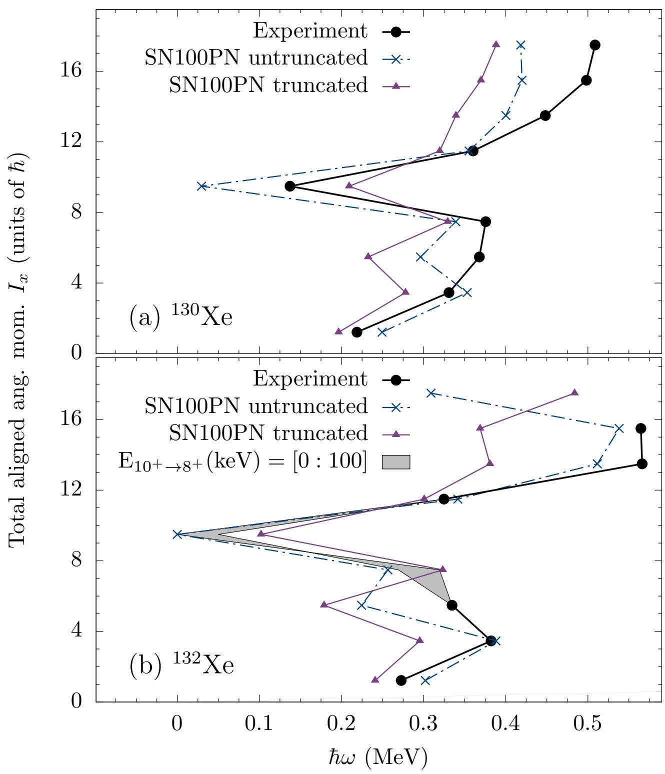

FIG. 13. (a) Comparison between experimental and calculated total aligned angular momenta I_x as a function of the rotational frequency $\hbar\omega$, employing the SN100PN calculation for (a) ^{130}Xe and (b) ^{132}Xe. The SN100PN interaction is employed in two different calculations: (i) untruncated and (ii) truncated with only one proton allowed in the $\pi h_{11/2}$ orbital. Experimental data taken from Refs. [39,95].

position of the $J^\pi = 6_1^+$ state, followed by a strong alignment at the position of the $J^\pi = 10_1^+$ state. The untruncated SN100PN calculation predicts the $J^\pi = 6_1^+$ and 8_1^+ states only 24 keV and 97 keV too low in energy, while the truncated calculation underestimates the energies by 434 keV and 527 keV, respectively. Furthermore, the $J^\pi = 10_1^+$ state at $E_x = 2973$ keV is predicted by the calculations at excitation energies of 2659 keV (untruncated) and 2589 keV (truncated). The occupation of the $\pi h_{11/2}$ orbital decreases from $N_\pi = 0.273$ at the $J^\pi = 0_1^+$ state to $N_\pi = 0.099$ at the $J^\pi = 6_1^+$ state. Subsequently, the occupancy sharply increases to 0.277 at the $J^\pi = 8_1^+$ state and stays almost constant for states with $J^\pi \geqslant 8_1^+$. The increase of the occupancy is not compatible with the experimentally observed alignment. However, the calculated $B(E2)$ values along the $12_1^+ \to 10_1^+ \to 8_1^+ \to 6_1^+$ cascade drop sharply from 548 to 12 e^2 fm^4 and rise back to 1084 e^2 fm^4. Consequently, all experimental observables are well reproduced corroborating a concurrent neutron and proton alignment in ^{130}Xe. A comparable result was obtained by a theoretical study of the even-mass isotopes $^{114-130}$Xe employing the microscopic sdIBM-2 + 2q.p. approach [96]. The alignment along the positive-parity band was proposed to be of caused by the $\pi h_{11/2}^2$ proton pair. Rotational alignment of pair of neutrons in the $\nu h_{11/2}^2$ are given by a calculation obtained with the quadrupole-quadrupole-plus-pairing model [34]. These results are in contradiction to the experimental values in ^{130}Xe.

Approaching the $N = 82$ shell closure, a comparison for total aligned angular momenta I_x for ^{132}Xe is depicted in Fig. 13(b). Since no experimental data is available for the $J^\pi = 8^+$ state, the calculation provides a prediction for this state. To compare theoretical calculations with the experimental data, I_x is plotted for a range from 0 to 100 keV of the expected transition energy of the yet unobserved $10_1^+ \to 8_1^+$ decay. The region is marked gray in Fig. 13(b). Both calculations predict a first alignment at the $J^\pi = 6_1^+$ state followed by a second one at the $J^\pi = 10_1^+$ state. Good agreement is obtained with the untruncated calculation where the $J^\pi = 6_1^+$ and 10_1^+ states are slightly underpredicted by 136 and 262 keV, in contrast to the truncated calculation with a discrepancy of 566 keV for the $J^\pi = 6_1^+$ state. The untruncated calculation predicts the $J^\pi = 8_1^+$ state to be degenerated with the $J^\pi = 10_1^+$ state consistent with experimental searches. The truncated calculations predict an energy difference of 204 keV contradicting the experimental observation. In addition, the $(16_1^+) \to (14_1^+) \to (12_1^+) \to (10_1^+)$ cascade with a tentatively assigned 1130-keV transition [39] is in good agreement with the results by the untruncated SN100PN calculation. In ^{132}Xe the alignment is clearly caused by protons in the $\pi h_{11/2}$ orbital.

V. CONCLUSION

In summary, as a main result of three independent measurements and a detailed spectroscopic investigation the level scheme of ^{131}Xe was extended up to an excitation energy of 4945 keV. A pronounced backbending along the negative-parity band on top of the one-quasiparticle $\nu h_{11/2}(\alpha = -1/2)$ band around $\hbar\omega = 0.4$ MeV was observed. The states of the extended negative-parity band closed the gap of unknown high-spin excitations along the isotopic and isotonic chains close to the shell closure at $N = 82$.

Extended large-scale shell-model calculations were performed for ^{131}Xe and its neighbors employing interactions that are applicable in this mass region. In general, the new experimental results, including the pronounced backbending, are reproduced by the interactions excluding PQM130. A detailed inspection reveals that only interactions with improved and corrected monopole parts, i.e., GCN50:82 and SN100-KTH, describe the backbending curve and the alignment frequency to its full extent. Comparisons between truncated and untruncated shell-model calculations along the Xe chain in $^{129-132}$Xe clearly indicate that alignment of two $0h_{11/2}$ protons is decisive for the backbending. Calculations of the reduced transition strengths reproduce exactly the spin value where the alignment sets in in ^{131}Xe. The microscopic origin of the alignment in ^{131}Xe was traced back via the wave-function decomposition and its development as a function of angular momentum. The occupation number of the proton $0h_{11/2}$ pair changes significantly at the alignment states in ^{131}Xe providing a distinct signature. Similar results were obtained in the $-2n$ isotope ^{129}Xe. The new results together with previous achievements demonstrate convincingly the predictive power of the modern shell-model calculations with its interaction. The interplay between single-particle and collective excitation in this transitional region arise unambiguously from the specific $h_{11/2}$ intruder orbital.

In future, measurements of lifetimes and g factors that serve as sensitive probes for nucleon alignment should be performed to reaffirm the proposed backbending mechanism in transitional Xe isotopes. Specifically, the discovery of the predicted nearly degenerated $J^\pi = 8^+$ state in ^{132}Xe, causing the isomeric $J^\pi = 10^+$ state, is of highest interest. Furthermore, fast-timing measurements are necessary to resolve the possible onset of $J^\pi = 23/2_1^+$ isomerism in ^{131}Xe which is also predicted by shell-model calculations.

ACKNOWLEDGMENTS

We thank the IKP FN Tandem accelerator team for the professional support during the experiment. We also thank Prof. Dr. Alfredo Poves for providing the GCN50:82 interaction. Furthermore, we express our thanks to Prof. Dr. Furong Xu and Prof. Dr. Costel Petrache for valuable discussions. The research leading to these results has received funding from the German BMBF under Contract No. 05P12PKFNE TP4, from the European Union Seventh Framework Programme FP7/2007-2013 under Grant Agreement No. 262010-ENSAR, from the Spanish Ministerio de Ciencia e Innovación under Contract No. FPA2011-29854-C04, from the Spanish Ministerio de Economía y Competitividad under Contract No. FPA2014-57196-C5, and from the U.K. Science and Technology Facilities Council (STFC). L.K. and A.V. thank the Bonn-Cologne Graduate School of Physics and Astronomy (BCGS) for financial support. One of the authors (A. Gadea) has been supported by the Generalitat Valenciana, Spain, under Grant No. PROMETEOII/2014/019 and EU under the FEDER program.

[1] R. Wyss, A. Granderath, R. Bengtsson, P. von Brentano, A. Dewald, A. Gelberg, A. Gizon, J. Gizon, S. Harissopulos, A. Johnson, W. Lieberz, W. Nazarewicz, J. Nyberg, and K. Schiffer, Interplay between proton and neutron S-bands in the Xe-Ba-Ce-region, Nucl. Phys. A **505**, 337 (1989).

[2] A. Granderath, P. F. Mantica, R. Bengtsson, R. Wyss, P. von Brentano, A. Gelberg, and F. Seiffert, Shapes and rotational structures of neutron $h_{11/2}$ configurations in the Xe-Ba-Ce region, Nucl. Phys. A **597**, 427 (1996).

[3] A. Al-Khatib, H. Hübel, P. Bringel, C. Engelhardt, A. Neußer-Neffgen, G. B. Hagemann, C. R. Hansen, B. Herskind, G. Sletten, A. Bracco, F. Camera, G. Benzoni, P. Fallon, R. M. Clark, M. P. Carpenter, R. V. F. Janssens, T. L. Khoo, T. Lauritsen, P. Chowdhury, H. Amro, A. K. Singh, and R. Bengtsson, Transition to non-collective states at high spin in ^{124}Xe, Eur. Phys. J. **36**, 21 (2008).

[4] A. Al-Khatib, A. K. Singh, H. Hübel, P. Bringel, A. Bürger, J. Domscheit, A. Neußer-Neffgen, G. Schönwaßer, G. B. Hagemann, C. Ronn Hansen, B. Herskind, G. Sletten, J. N. Wilson, J. Timár, A. Algora, Zs. Dombrádi, J. Gál, G. Kalinka, J. Molnár, B. M. Nyakó, D. Sohler, L. Zolnai, R. M. Clark, M. Cromaz, P. Fallon, I. Y. Lee, A. O. Macchiavelli, D. Ward, H. Amro, W. C. Ma, M. Kmiecik, A. Maj, J. Styczen, K. Zuber, K. Hauschild, A. Korichi, A. Lopez-Martens, J. Roccaz, S. Siem, F. Hannachi, J. N. Scheurer, P. Bednarczyk, Th. Byrski, D. Curien, O. Dorvaux, G. Duchêne, B. Gall, F. Khalfallah, I. Piqueras, J. Robin, A. Görgen, K. Juhász, S. B. Patel, A. O. Evans, G. Rainovski, G. Benzoni, A. Bracco, F. Camera, S. Leoni, P. Mason, B. Million, A. Paleni, R. Sacchi, O. Wieland, C. M. Petrache, D. Petrache, G. La Rana, R. Moro, G. De Angelis, J. C. Lisle, B. Cederwall, K. Lagergren, R. M. Lieder, E. Podsvirova, W. Gast, H. Jäger, and N. Redon, Competition between collective and noncollective excitation modes at high spin in ^{124}Ba, Phys. Rev. C **74**, 014305 (2006).

[5] A. K. Singh, H. Hübel, J. Domscheit, G. B. Hagemann, B. Herskind, D. R. Jensen, J. N. Wilson, R. Clark, M. Cromaz, P. Fallon, A. Görgen, I. Y. Lee, A. O. Macchiavelli, D. Ward, H. Amro, W. C. Ma, J. Timár, and I. Ragnarsson, Evidence for noncollective oblate structures at high spin in ^{123}Cs, Phys. Rev. C **70**, 034315 (2004).

[6] H. Morinaga and N. L. Lark, Collective excited states in even xenon isotopes, Nucl. Phys. **67**, 315 (1965).

[7] I. Ragnarsson, A. Sobiczewski, R. K. Sheline, S. E. Larsson, and B. Nerlo-Pomorska, Comparison of potential-energy surfaces and moments of inertia with experimental spectroscopic trends for non-spherical $Z = 50-82$ nuclei, Nucl. Phys. A **233**, 329 (1974).

[8] R. Wyss, J. Nyberg, A. Johnson, R. Bengtsson, and W. Nazarewicz, Highly deformed intruder bands in the $A \approx 130$ mass region, Phys. Lett. B **215**, 211 (1988).

[9] R. F. Casten and P. von Brentano, An extensive region of $O(6)$-like nuclei near $A = 130$, Phys. Lett. B **152**, 22 (1985).

[10] Y. S. Chen, S. Frauendorf, and G. A. Leander, Shape of rotating quasiparticle orbits and signature splitting in La, Ce, and Pr nuclei, Phys. Rev. C **28**, 2437 (1983).

[11] R. O. Sayer, J. S. Smith, and W. T. Milner, Rotational and quasirotational bands in even-even nuclei, At. Data Nucl. Data Tables **15**, 85 (1975).

[12] N. Yoshida, A. Arima, and T. Otsuka, Description of high-spin states in the interacting boson model, Phys. Lett. B **114**, 86 (1982).

[13] K. Nomura, T. Nikšić, and D. Vretenar, Shape-phase transitions in odd-mass γ-soft nuclei with mass $A \approx 130$, Phys. Rev. C **96**, 014304 (2017).

[14] L. M. Robledo, R. R. Rodríguez-Guzmán, and P. Sarriguren, Evolution of nuclear shapes in medium mass isotopes from a microscopic perspective, Phys. Rev. C **78**, 034314 (2008).

[15] C.-B. Moon, C. S. Lee, T. Komatsubara, Y. Sasaki, and K. Furuno, Structure of the negative parity bands in ^{125}Xe, Phys. Rev. C **76**, 067301 (2007).

[16] Y. Huang, Z. G. Xiao, S. J. Zhu, C. Qi, Q. Xu, W. J. Cheng, H. J. Li, L. M. Lyu, R. S. Wang, W. H. Yan, H. Yi, Y. Zhang, Q. M. Chen, C. Y. He, S. P. Hu, C. B. Li, H. W. Li, P. W. Luo, X. G. Wu, Y. H. Wu, Y. Zheng, and J. Zhong, High-spin structures in the ^{129}Xe nucleus, Phys. Rev. C **93**, 064315 (2016).

[17] K. Higashiyama, N. Yoshinaga, and K. Tanabe, Shell model study of backbending phenomena in Xe isotopes, Phys. Rev. C **65**, 054317 (2002).

[18] Y. Lei and Z. Y. Xu, $(h_{11/2})^2$ alignments in neutron-rich ^{132}Ba with negative-parity pairs, Phys. Rev. C **92**, 014317 (2015).

[19] T. Takahashi, N. Yoshinaga, and K. Higashiyama, Backbending phenomena in ^{132,134,136}Ce with a pair-truncated shell model, Phys. Rev. C **71**, 014305 (2005).

[20] H. Daniel, O. Mehling, P. Schmidlin, D. Schotte, and E. Thummernicht, Zerfallsschemata, β-Matrixelemente und γ-Multipolordnungen für die Übergänge ^{56}Co $\rightarrow$ ^{56}Fe und ^{131}J $\rightarrow$ ^{131}Xe, Z. Phys **179**, 62 (1964).

[21] R. A. Meyer, F. Momyer, and W. B. Walters, Decay of 8.0-day ^{131}I to levels of ^{131}Xe and 11.77-day ^{131m}Xe, Z. Phys. **268**, 387 (1974).

[22] Chr. Bargholtz, S. Beshai, and L. Gidefeldt, Angular correlation measurements in ^{131}Xe, Nucl. Phys. A **270**, 189 (1976).

[23] M.-C. Lépy, L. Brondeau, Ch. Bobin, V. Lourenço, C. Thiam, and M.-M. Bé, Determination of X- and gamma-ray emission intensities in the decay of ^{131}I, Appl. Radiat. Isot. **109**, 154 (2016).

[24] M. Berman and G. B. Beard, Nuclear Resonance Fluorescence in ^{131}Xe, Phys. Rev. C **2**, 1506 (1970).

[25] H. Langhoff, Lifetime measurements in ^{131}Xe and ^{129}Xe, Nucl. Phys. A **158**, 657 (1970).

[26] D. C. Hoffman, J. W. Barnes, B. J. Dropesky, F. O. Lawrence, G. M. Kelley, and M. A. Ott, Half-lives of ^{129m}Xe, ^{131m}Xe, ^{133m}Xe, ^{133g}Xe and ^{135g}Xe, J. Inorg. Nucl. Chem. **37**, 2336 (1975).

[27] D. C. Palmer, A. D. Irving, P. D. Forsyth, I. Hall, D. G. E. Martin, and M. J. Maynard, Low-lying levels of ^{129}Xe and ^{131}Xe, J. Phys. G **4**, 1143 (1978).

[28] Yu. Khazov, I. Mitropolsky, and A. Rodionov, Nuclear data sheets for $A = 131$, Nucl. Data Sheets **107**, 2715 (2006).

[29] A. D. Irving, P. D. Forsyth, I. Hall, and D. G. E. Martin, The properties of low-lying levels of ^{129}Xe and ^{131}Xe, J. Phys. G **5**, 1595 (1979).

[30] T. Lönnroth, J. Kumpulainen, and C. Tuokko, One- and three-quasiparticle states in ^{127,129,131,133}Xe and their coexistence with band structures, Phys. Scr. **27**, 228 (1983).

[31] A. Kerek, A. Luukko, M. Grecescu, and J. Sztarkier, Two- and three-quasiparticle states in ^{132}Xe and ^{131}Xe, Nucl. Phys. A **172**, 603 (1971).

[32] Evaluated Nuclear Structure Data File (ENSDF) (2017), http://www.nndc.bnl.gov/ensdf/.

[33] J. F. Smith, C. J. Chiara, D. B. Fossan, D. R. LaFosse, G. J. Lane, J. M. Sears, K. Starosta, M. Devlin, F. Lerma, D. G. Sarantites,

S. J. Freeman, M. J. Leddy, J. L. Durell, A. J. Boston, E. S. Paul, A. T. Semple, I. Y. Lee, A. O. Macchiavelli, and P. H. Heenen, Excited states and deformation of ^{112}Xe, Phys. Lett. B **523**, 13 (2001).

[34] S. P. Sarswat, Arun Bharti, and S. K. Khosa, Backbending and breaking of axial symmetry in the yrast bands of $^{114-130}$Xe isotopes, Phys. Rev. C **58**, 2041 (1998).

[35] H. Kusakari, K. Kitao, K. Sato, M. Sugawara, and H. Katsuragawa, High-spin states in even-mass Xe nuclei and backbending phenomena, Nucl. Phys. A **401**, 445 (1983).

[36] C. S. Purry, P. M. Walker, G. D. Dracoulis, T. Kibedi, F. G. Kondev, S. Bayer, A. M. Bruce, A. P. Byrne, W. Gelletly, P. H. Regan, C. Thwaites, O. Burglin, and N. Rowley, Multi-quasiparticle isomers and rotational bands in ^{178}W, Nucl. Phys. A **632**, 229 (1998).

[37] H. F. Brinckmann, C. Heiser, and W. D. Fromm, Ein Hochangeregter isomerer Kernzustand in ^{132}Xe, Nucl. Phys. A **96**, 318 (1967).

[38] M. v. Hartrott, J. Hadijuana, K. Nishiyama, D. Quitmann, D. Riegel, and H. Schweickert, Nuclear spin relaxation of Xe in liquid Te, Z. Phys. A **278**, 303 (1976).

[39] A. Vogt, M. Siciliano, B. Birkenbach, P. Reiter, K. Hadyńska-Klęk, C. Wheldon, J. J. Valiente-Dobón, E. Teruya, N. Yoshinaga, K. Arnswald, D. Bazzacco, A. Blazhev, A. Bracco, B. Bruyneel, R. S. Chakrawarthy, R. Chapman, D. Cline, L. Corradi, F. C. L. Crespi, M. Cromaz, G. de Angelis, J. Eberth, P. Fallon, E. Farnea, E. Fioretto, C. Fransen, S. J. Freeman, B. Fu, A. Gadea, W. Gelletly, A. Giaz, A. Görgen, A. Gottardo, A. B. Hayes, H. Hess, R. Hetzenegger, R. Hirsch, H. Hua, P. R. John, J. Jolie, A. Jungclaus, V. Karayonchev, L. Kaya, W. Korten, I. Y. Lee, S. Leoni, X. Liang, S. Lunardi, A. O. Macchiavelli, R. Menegazzo, D. Mengoni, C. Michelagnoli, T. Mijatović, G. Montagnoli, D. Montanari, C. Müller-Gatermann, D. Napoli, C. J. Pearson, Zs. Podolyák, G. Pollarolo, A. Pullia, M. Queiser, F. Recchia, P. H. Regan, J.-M. Régis, N. Saed-Samii, E. Şahin, F. Scarlassara, M. Seidlitz, B. Siebeck, G. Sletten, J. F. Smith, P.-A. Söderström, A. M. Stefanini, O. Stezowski, S. Szilner, B. Szpak, R. Teng, C. Ur, D. D. Warner, K. Wolf, C. Y. Wu, and K. O. Zell, High-spin structures in ^{132}Xe and ^{133}Xe and evidence for isomers along the $N = 79$ isotones, Phys. Rev. C **96**, 024321 (2017).

[40] H. Helppi, J. Hattula, A. Luukko, M. Jääskeläinen, and F. Dönau, In-beam study of ^{127,129}Xe and collective description of the level structures in odd-A Xe nuclei, Nucl. Phys. A **357**, 333 (1981).

[41] I. Rezanka, A. Kerek, A. Luukko, and C. J. Herrlander, High-spin states in odd Xe nuclei, Nucl. Phys. A **141**, 130 (1970).

[42] A. Granderath, D. Lieberz, A. Gelberg, S. Freund, W. Lieberz, R. Wirowski, P. von Brentano, and R. Wyss, Excited states in ^{125}Xe, Nucl. Phys. A **524**, 153 (1991).

[43] I. Wiedenhöver, U. Neuneyer, C. Kerskens, J. Altmann, O. Stuch, J. Theuerkauf, G. Siems, R. Wirowski, M. Eschenauer, P. von Brentano, R. Schubart, H. Kluge, and K. H. Maier, High spin structure in ^{127}Xe and ^{125}Xe, Z. Phys. **347**, 71 (1993).

[44] A. Al-Khatib, G. B. Hagemann, G. Sletten, A. K. Singh, H. Amro, G. Benzoni, A. Bracco, P. Bringel, F. Camera, M. P. Carpenter, P. Chowdhury, R. M. Clark, C. Engelhardt, P. Fallon, B. Herskind, H. Hübel, R. V. F. Janssens, T. L. Khoo, T. Lauritsen, A. Neußer-Neffgen, and C. R. Hansen, High-spin spectroscopy in ^{125}Xe, Phys. Rev. C **83**, 024306 (2011).

[45] S. Chakraborty, H. P. Sharma, S. S. Tiwary, C. Majumder, P. K. Prajapati, S. Rai, P. Popli, M. Singh, S. S. Bhattacharjee, R. P. Singh, S. Muralithar, P. Banerjee, S. Ganguly, S. Kumar, A. Kumar, and R. Palit, Two-neutron alignment in ^{127}Xe, Braz. J Phys. **47**, 406 (2017).

[46] S. Akkoyun *et al.*, AGATA–Advanced GAmma tracking array, Nucl. Instrum. Meth. Phys. Res. A **668**, 26 (2012).

[47] A. M. Stefanini, L. Corradi, G. Maron, A. Pisent, M. Trotta, A. M. Vinodkumar, S. Beghini, G. Montagnoli, F. Scarlassara, G. F. Segato, A. De Rosa, G. Inglima, D. Pierroutsakou, M. Romoli, M. Sandoli, G. Pollarolo, and A. Latina, The heavy-ion magnetic spectrometer PRISMA, Nucl. Phys. A **701**, 217 (2002).

[48] S. Szilner, C. A. Ur, L. Corradi, N. Marginean, G. Pollarolo, A. M. Stefanini, S. Beghini, B. R. Behera, E. Fioretto, A. Gadea, B. Guiot, A. Latina, P. Mason, G. Montagnoli, F. Scarlassara, M. Trotta, G. de Angelis, F. Della Vedova, E. Farnea, F. Haas, S. Lenzi, S. Lunardi, R. Marginean, R. Menegazzo, D. R. Napoli, M. Nespolo, I. V. Pokrovsky, F. Recchia, M. Romoli, M.-D. Salsac, N. Soić, and J. J. Valiente-Dobón, Multinucleon transfer reactions in closed-shell nuclei, Phys. Rev. C **76**, 024604 (2007).

[49] L. Corradi, S. Szilner, G. Pollarolo, D. Montanari, E. Fioretto, A.M. Stefanini, J. J. Valiente-Dobón, E. Farnea, C. Michelagnoli, G. Montagnoli, F. Scarlassara, C.A. Ur, T. Mijatović, D. Jelavić Malenica, N. Soić, and F. Haas, Multinucleon transfer reactions: Present status and perspectives, Nucl. Instrum. Meth. Phys. Res. B **317**, 743 (2013).

[50] L. Netterdon, V. Derya, J. Endres, C. Fransen, A. Hennig, J. Mayer, C. Müller-Gatermann, A. Sauerwein, P. Scholz, M. Spieker, and A. Zilges, The γ-ray spectrometer HORUS and its applications for nuclear astrophysics, Nucl. Instrum. Meth. Phys. Res. A **754**, 94 (2014).

[51] L. Kaya, A. Vogt, P. Reiter, B. Birkenbach, R. Hirsch, K. Arnswald, H. Hess, M. Seidlitz, T. Steinbach, N. Warr, K. Wolf, C. Stahl, N. Pietralla, T. Limböck, K. Meerholz, and R. Lutter, Characterization and calibration of radiation-damaged double-sided silicon strip detectors, Nucl. Instrum. Meth. Phys. Res. A **855**, 109 (2017).

[52] A. Gadea, E. Farnea, J. J. Valiente-Dobón, B. Million, D. Mengoni, D. Bazzacco, F. Recchia, A. Dewald, Th. Pissulla, W. Rother, G. de Angelis *et al.*, Conceptual design and infrastructure for the installation of the first AGATA sub-array at LNL, Nucl. Instrum. Meth. Phys. Res. A **654**, 88 (2011).

[53] A. Wiens, H. Hess, B. Birkenbach, B. Bruyneel, J. Eberth, D. Lersch, G. Pascovici, P. Reiter, and H.-G. Thomas, The AGATA triple cluster detector, Nucl. Instrum. Meth. Phys. Res. A **618**, 223 (2010).

[54] R.S. Kempley *et al.*, Cross coincidences in the ^{136}Xe + ^{208}Pb deep-inelastic reaction, Acta. Phys. Pol. B **42**, 717 (2011).

[55] M. Siciliano *et al.*, Neutron-rich nuclei in the vicinity of ^{208}Pb, LNL Annual Report 2014 **241**, 63 (2015).

[56] A. Vogt, B. Birkenbach, P. Reiter, L. Corradi, T. Mijatović, D. Montanari, S. Szilner, D. Bazzacco, M. Bowry, A. Bracco, B. Bruyneel, F. C. L. Crespi, G. de Angelis, P. Désesquelles, J. Eberth, E. Farnea, E. Fioretto, A. Gadea, K. Geibel, A. Gengelbach, A. Giaz, A. Görgen, A. Gottardo, J. Grebosz, H. Hess, P. R. John, J. Jolie, D. S. Judson, A. Jungclaus, W. Korten, S. Leoni, S. Lunardi, R. Menegazzo, D. Mengoni, C. Michelagnoli, G. Montagnoli, D. Napoli, L. Pellegri, G. Pollarolo, A. Pullia, B. Quintana, F. Radeck, F. Recchia, D. Rosso, E. Şahin, M. D. Salsac, F. Scarlassara, P.-A. Söderström, A. M. Stefanini, T. Steinbach, O. Stezowski, B. Szpak, Ch.

Theisen, C. Ur, J. J. Valiente-Dobón, V. Vandone, and A. Wiens, Light and heavy transfer products in ^{136}Xe + ^{238}U multinucleon transfer reactions, Phys. Rev. C **92**, 024619 (2015).
[57] B. Bruyneel, B. Birkenbach, and P. Reiter, Pulse shape analysis and position determination in segmented HPGe detectors: The AGATA detector library, Eur. Phys. J. A **52**, 70 (2016).
[58] A. Lopez-Martens, K. Hauschild, A. Korichi, J. Roccaz, and J.-P. Thibaud, γ-ray tracking algorithms: A comparison, Nucl. Instrum. Meth. Phys. Res. A **533**, 454 (2004).
[59] Tesa SE, Tesa adhesive 68556 data sheet.
[60] N. Saed-Samii (unpublished).
[61] J. Theuerkauf, Die Analyse von zwei- und mehrdimensionalen $\gamma\gamma$-Koinzidenzspektren an Beispielen aus Hochspinexperimenten in der Massengegend um ^{146}Gd, Ph.D. thesis, Universität zu Köln (1994).
[62] I. Wiedenhöver (unpublished).
[63] I. Wiedenhöver, O. Vogel, H. Klein, A. Dewald, P. von Brentano, J. Gableske, R. Krücken, N. Nicolay, A. Gelberg, P. Petkov, A. Gizon, J. Gizon, D. Bazzaco, C. Rossi Alvarez, G. de Angelis, S. Lunardi, P. Pavan, D. R. Napoli, S. Frauendorf, F. Dönau, R. V. F. Janssens, and M. P. Carpenter, Detailed angular correlation analysis with 4π spectrometers: Spin determinations and multipolarity mixing measurements in ^{128}Ba, Phys. Rev. C **58**, 721 (1998).
[64] K. S. Krane and R. M. Steffen, Determination of the $E2/M1$ multipole mixing ratios of the gamma transitions in ^{110}Cd, Phys. Rev. C **2**, 724 (1970).
[65] K. S. Krane, R. M. Steffen, and R. M. Wheeler, Directional correlations of gamma radiations emitted from nuclear states oriented by nuclear reactions or cryogenic methods, At. Data Nucl. Data Tables **11**, 351 (1973).
[66] A. Linnemann, Das HORUS-Würfelspektrometer und Multiphononanregungen in ^{106}Cd, Ph.D. thesis, Universität zu Köln, 2006.
[67] L. Bettermann, C. Fransen, S. Heinze, J. Jolie, A. Linnemann, D. Mücher, W. Rother, T. Ahn, A. Costin, N. Pietralla, and Y. Luo, Candidates for the one-phonon mixed-symmetry state in ^{130}Xe, Phys. Rev. C **79**, 034315 (2009).
[68] S. Mukhopadhyay, D. C. Biswas, S. K. Tandel, L. S. Danu, B. N. Joshi, G. K. Prajapati, Somnath Nag, T. Trivedi, S. Saha, J. Sethi, R. Palit, and P. K. Joshi, Coexisting shape- and high-K isomers in the shape transitional nucleus ^{188}Pt, Phys. Lett. B **739**, 462 (2014).
[69] A. Vogt, B. Birkenbach, P. Reiter, A. Blazhev, M. Siciliano, J. J. Valiente-Dobón, C. Wheldon, D. Bazzacco, M. Bowry, A. Bracco, B. Bruyneel, R. S. Chakrawarthy, R. Chapman, D. Cline, L. Corradi, F. C. L. Crespi, M. Cromaz, G. de Angelis, J. Eberth, P. Fallon, E. Farnea, E. Fioretto, S. J. Freeman, A. Gadea, K. Geibel, W. Gelletly, A. Gengelbach, A. Giaz, A. Görgen, A. Gottardo, A. B. Hayes, H. Hess, H. Hua, P. R. John, J. Jolie, A. Jungclaus, W. Korten, I. Y. Lee, S. Leoni, X. Liang, S. Lunardi, A. O. Macchiavelli, R. Menegazzo, D. Mengoni, C. Michelagnoli, T. Mijatović, G. Montagnoli, D. Montanari, D. Napoli, C. J. Pearson, L. Pellegri, Zs. Podolyák, G. Pollarolo, A. Pullia, F. Radeck, F. Recchia, P. H. Regan, E. Şahin, F. Scarlassara, G. Sletten, J. F. Smith, P.-A. Söderström, A. M. Stefanini, T. Steinbach, O. Stezowski, S. Szilner, B. Szpak, R. Teng, C. Ur, V. Vandone, D. Ward, D. D. Warner, A. Wiens, and C. Y. Wu, High-spin structure of ^{134}Xe, Phys. Rev. C **93**, 054325 (2016).
[70] A. Vogt, B. Birkenbach, P. Reiter, A. Blazhev, M. Siciliano, K. Hadyńska-Klęk, J. J. Valiente-Dobón, C. Wheldon, E. Teruya, N. Yoshinaga, K. Arnswald, D. Bazzacco, M. Bowry, A. Bracco, B. Bruyneel, R. S. Chakrawarthy, R. Chapman, D. Cline, L. Corradi, F. C. L Crespi, M. Cromaz, G. de Angelis, J. Eberth, P. Fallon, E. Farnea, E. Fioretto, S. J. Freeman, B. Fu, A. Gadea, K. Geibel, W. Gelletly, A. Gengelbach, A. Giaz, A. Görgen, A. Gottardo, A. B. Hayes, H. Hess, R. Hirsch, H. Hua, P. R. John, J. Jolie, A. Jungclaus, L. Kaya, W. Korten, I. Y. Lee, S. Leoni, L. Lewandowski, X. Liang, S. Lunardi, A. O. Macchiavelli, R. Menegazzo, D. Mengoni, C. Michelagnoli, T. Mijatović, G. Montagnoli, D. Montanari, C. Müller-Gatermann, D. Napoli, C. J. Pearson, L. Pellegri, Zs. Podolyák, G. Pollarolo, A. Pullia, M. Queiser, F. Radeck, F. Recchia, P. H. Regan, D. Rosiak, N. Saed-Samii, E. Şahin, F. Scarlassara, D. Schneiders, M. Seidlitz, B. Siebeck, G. Sletten, J. F. Smith, P.-A. Söderström, A. M. Stefanini, T. Steinbach, O. Stezowski, S. Szilner, B. Szpak, R. Teng, C. Ur, V. Vandone, D. D. Warner, A. Wiens, C. Y. Wu, and K. O. Zell, Isomers and high-spin structures in the $N = 81$ isotones ^{135}Xe and ^{137}Ba, Phys. Rev. C **95**, 024316 (2017).
[71] T. Koike, K. Starosta, C. J. Chiara, D. B. Fossan, and D. R. LaFosse, Systematic search of $\pi h_{11/2} \otimes \nu h_{11/2}$ chiral doublet bands and role of triaxiality in odd-odd $Z = 55$ isotopes: ^{128,130,132,134}Cs, Phys. Rev. C **67**, 044319 (2003).
[72] R. L. Lozeva, G. S. Simpson, H. Grawe, G. Neyens, L. A. Atanasova, D. L. Balabanski, D. Bazzacco, F. Becker, P. Bednarczyk, G. Benzoni, N. Blasi, A. Blazhev, A. Bracco, C. Brandau, L. Cáceres, F. Camera, S. K. Chamoli, F. C. L. Crespi, J.-M. Daugas, P. Detistov, M. De Rydt, P. Doornenbal, C. Fahlander, E. Farnea, G. Georgiev, J. Gerl, K. A. Gladnishki, M. Górska, J. Grębosz, M. Hass, R. Hoischen, G. Ilie, M. Ionescu-Bujor, A. Iordachescu, J. Jolie, A. Jungclaus, M. Kmiecik, I. Kojouharov, N. Kurz, S. P. Lakshmi, G. Lo Bianco, S. Mallion, A. Maj, D. Montanari, O. Perru, M. Pfützner, S. Pietri, J. A. Pinston, Zs. Podolyák, W. Prokopowicz, D. Rudolph, G. Rusev, T. R. Saitoh, A. Saltarelli, H. Schaffner, R. Schwengner, S. Tashenov, K. Turzó, J. J. Valiente-Dobón, N. Vermeulen, J. Walker, E. Werner-Malento, O. Wieland, and H.-J. Wollersheim, New sub-μs isomers in ^{125,127,129}Sn and isomer systematics of $^{124\text{-}130}$Sn, Phys. Rev. C **77**, 064313 (2008).
[73] A. Astier, M. G. Porquet, Ts. Venkova, Ch. Theisen, G. Duchêne, F. Azaiez, G. Barreau, D. Curien, I. Deloncle, O. Dorvaux, B. J. P. Gall, M. Houry, R. Lucas, N. Redon, M. Rousseau, and O. Stézowski, High-spin structures of $^{124-131}$Te: Competition of proton- and neutron-pair breakings, Eur. Phys. J. **50**, 1 (2014).
[74] S. Juutinen, P. Šimeček, P. Ahonen, M. Carpenter, C. Fahlander, J. Gascon, R. Julin, A. Lampinen, T. Lönnroth, J. Nyberg, A. Pakkanen, M. Piiparinen, K. Schiffer, G. Sletten, S. Törmänen, and A. Virtanen, Shape coexistence in the transitional ^{133}Ba nucleus, Phys. Rev. C **51**, 1699 (1995).
[75] R. Ma, E. S. Paul, D. B. Fossan, Y. Liang, N. Xu, R. Wadsworth, I. Jenkins, and P. J. Nolan, Rotational bands in ^{135}Ce: Collective prolate and oblate rotation, Phys. Rev. C **41**, 2624 (1990).
[76] C. M. Petrache, R. Venturelli, D. Vretenar, D. Bazzacco, G. Bonsignori, S. Brant, S. Lunardi, M. A. Rizzutto, C. Rossi Alvarez, G. de Angelis, M. De Poli, and D. R. Napoli, High-spin states in ^{137}Nd: A large variety of collective rotations, Nucl. Phys. A **617**, 228 (1997).

[77] S. M. Mullins, A. Omar, L. Persson, D. Prévost, J. C. Waddington, H. R. Andrews, G. C. Ball, A. Galindo-Uribarri, V. P. Janzen, D. C. Radford, D. Ward, T. E. Drake, D. B. Fossan, D. LaFosse, P. Vaska, M. Waring, and R. Wadsworth, Perturbed alignments within an $i_{13/2}$ neutron intruder band in ^{141}Gd, Phys. Rev. C **47**, R2447 (1993).
[78] A. Schmidt, I. Schneider, H. Meise, I. Wiedenhöver, O. Stuch, K. Jessen, D. Weisshaar, C. Schumacher, P. von Brentano, G. Sletten, B. Herskind, M. Bergström, and J. Wrzesinski, High spin structure in ^{123}Xe, Eur. Phys. J **2**, 21 (1998).
[79] Samuel M. Harris, Higher order corrections to the cranking model, Phys. Rev. **138**, B509 (1965).
[80] E. Teruya, N. Yoshinaga, K. Higashiyama, and A. Odahara, Shell-model calculations of nuclei around mass 130, Phys. Rev. C **92**, 034320 (2015).
[81] K. Higashiyama and N. Yoshinaga, Pair-truncated shell-model analysis of nuclei around mass 130, Phys. Rev. C **83**, 034321 (2011).
[82] B. A. Brown and W. D. M. Rae, The shell-model code NuShellX@MSU, Nucl. Data Sheets **120**, 115 (2014).
[83] N. Shimizu, Nuclear shell-model code for massive parallel computation, KSHELL, arXiv:1310.5431.
[84] B. A. Brown, N. J. Stone, J. R. Stone, I. S. Towner, and M. Hjorth-Jensen, Magnetic moments of the 2_1^+ states around ^{132}Sn, Phys. Rev. C **71**, 044317 (2005).
[85] R. Machleidt, High-precision, charge-dependent bonn nucleon-nucleon potential, Phys. Rev. C **63**, 024001 (2001).
[86] E. Caurier, F. Nowacki, A. Poves, and K. Sieja, Collectivity in the light xenon isotopes: A shell model study, Phys. Rev. C **82**, 064304 (2010).
[87] E. Caurier, F. Nowacki, and A. Poves, Shell model description of the $\beta\beta$ decay of ^{136}Xe, Phys. Lett. B **711**, 62 (2012).
[88] L. Coraggio, L. De Angelis, T. Fukui, A. Gargano, and N. Itaco, Calculation of gamow-teller and two-neutrino double-β decay properties for ^{130}Te and ^{136}Xe with a realistic nucleon-nucleon potential, Phys. Rev. C **95**, 064324 (2017).
[89] C. Qi, Shell-model configuration-interaction description of quadrupole collectivity in te isotopes, Phys. Rev. C **94**, 034310 (2016).
[90] C. Qi and Z. X. Xu, Monopole-optimized effective interaction for tin isotopes, Phys. Rev. C **86**, 044323 (2012).
[91] J. Gizon, A. Gizon, and D. J. Horen, Band structure in ^{131,132,133}Ba observed by (^{12}C,xn) reactions, Nucl. Phys. A **252**, 509 (1975).
[92] A. Zemel, C. Broude, E. Dafni, A. Gelberg, M. B. Goldberg, J. Gerber, G. J. Kumbartzki, and K. H. Speidel, Magnetic moment of the $19/2^+$ isomer in ^{135}ce, Z. Phys. A: At. Nucl. **304**, 269 (1982).
[93] C. T. Zhang, M. Sferrazza, R. H. Mayer, Z. W. Grabowski, P. Bhattacharyya, P. J. Daly, R. Broda, B. Fornal, W. Królas, T. Pawłat, G. de Angelis, D. Bazzacco, S. Lunardi, and C. Rossi-Alvarez, Yrast excitations in ^{129}Te, Z. Phys. A **353**, 11 (1995).
[94] A. Dewald, Transition probabilities in transitional nuclei in the $A = 130$ region, Prog. Part. Nucl. Phys. **28**, 409 (1992).
[95] T. Lönnroth, J. Hattula, H. Helppi, S. Juutinen, K. Honkanen, and A. Kerek, Study of band crossings in ^{130}Xe, Nucl. Phys. A **431**, 256 (1984).
[96] S. Zhu-yi, L. Yong, and S. Jian-ping, The nuclear structure and backbending phenomenon for $^{114-130}$Xe isotopes, Chin. Phys. **10**, 282 (2001).

Publication II: Millisecond $23/2^+$ isomers in the $N = 79$ isotones ^{133}Xe and ^{135}Ba

Millisecond $23/2^+$ isomers in the $N = 79$ isotones ^{133}Xe and ^{135}Ba

L. Kaya,[1,*] A. Vogt,[1] P. Reiter,[1] C. Müller-Gatermann,[1] M. Siciliano,[2,3] L. Coraggio,[4] N. Itaco,[4,5] A. Gargano,[4] K. Arnswald,[1] D. Bazzacco,[6] B. Birkenbach,[1] A. Blazhev,[1] A. Bracco,[7] B. Bruyneel,[8] L. Corradi,[3] F. C. L. Crespi,[7] G. de Angelis,[3] M. Droste,[1] J. Eberth,[1] E. Farnea,[6,†] E. Fioretto,[3] C. Fransen,[1] A. Gadea,[9] A. Giaz,[7] A. Görgen,[10,11,12] A. Gottardo,[3] K. Hadyńska-Klęk,[3] H. Hess,[1] R. Hetzenegger,[1] R. Hirsch,[1] P. R. John,[13] J. Jolie,[1] A. Jungclaus,[14] W. Korten,[11] S. Leoni,[7] L. Lewandowski,[1] S. Lunardi,[2,6] R. Menegazzo,[6] D. Mengoni,[15,2,6] C. Michelagnoli,[16] T. Mijatović,[17] G. Montagnoli,[2,6] D. Montanari,[18] D. Napoli,[3] Zs. Podolyák,[19] G. Pollarolo,[20] F. Recchia,[2,6] D. Rosiak,[1] N. Saed-Samii,[1] E. Şahin,[10] F. Scarlassara,[2,6] M. Seidlitz,[1] P.-A. Söderström,[13] A. M. Stefanini,[3] O. Stezowski,[21] S. Szilner,[17] B. Szpak,[22] C. Ur,[6] J. J. Valiente-Dobón,[3] M. Weinert,[1] K. Wolf,[1] and K. O. Zell[1]

[1]*Institut für Kernphysik, Universität zu Köln, D-50937 Köln, Germany*
[2]*Dipartimento di Fisica e Astronomia, Università di Padova, I-35131 Padova, Italy*
[3]*Istituto Nazionale di Fisica Nucleare, Laboratori Nazionali di Legnaro, I-35020 Legnaro, Italy*
[4]*Istituto Nazionale di Fisica Nucleare, Sezione di Napoli, I-80126 Napoli, Italy*
[5]*Dipartimento di Matematica e Fisica, Università degli Studi della Campania "Luigi Vanvitelli", viale A. Lincoln 5, I-8110 Caserta, Italy*
[6]*Istituto Nazionale di Fisica Nucleare, Sezione di Padova, I-35131 Padova, Italy*
[7]*Dipartimento di Fisica, Università di Milano and INFN Sezione di Milano, I-20133 Milano, Italy*
[8]*CEA Saclay, Service de Physique Nucleaire, F-91191 Gif-sur-Yvette, France*
[9]*Instituto de Física Corpuscular, CSIC-Universidad de Valencia, E-46071 Valencia, Spain*
[10]*Department of Physics, University of Oslo, P. O. Box 1048 Blindern, N-0316 Oslo, Norway*
[11]*Institut de Recherche sur les lois Fondamentales de l'Univers – IRFU, CEA/DSM, Centre CEA de Saclay, F-91191 Gif-sur-Yvette Cedex, France*
[12]*Lawrence Berkeley National Laboratory, Berkeley, California 94720, USA*
[13]*Institut für Kernphysik, Technische Universität Darmstadt, D-64289 Darmstadt, Germany*
[14]*Instituto de Estructura de la Materia, CSIC, Madrid, E-28006 Madrid, Spain*
[15]*Nuclear Physics Research Group, University of the West of Scotland, High Street, Paisley PA1 2BE, Scotland, United Kingdom*
[16]*Institut Laue-Langevin (ILL), 38042 Grenoble Cedex 9, France*
[17]*Ruđer Bošković Institute, HR-10 002 Zagreb, Croatia*
[18]*USIAS - Universite de Strasbourg, IPHC-CNRS, F-67037 Strasbourg Cedex 2, France*
[19]*Department of Physics, University of Surrey, Guildford, Surrey GU2 7XH, United Kingdom*
[20]*Dipartimento di Fisica Teorica dell'Università di Torino and INFN, I-10125 Torino, Italy*
[21]*Université de Lyon, Université Lyon-1, CNRS/IN2P3, UMR5822, IPNL, F-69622 Villeurbanne Cedex, France*
[22]*Henryk Niewodniczański Institute of Nuclear Physics PAN, PL-31342 Kraków, Poland*

(Received 27 July 2018; published 19 November 2018)

Detailed information on isomeric states in $A \approx 135$ nuclei is exploited to benchmark shell-model calculations in the region northwest of doubly magic nucleus ^{132}Sn. The $N = 79$ isotones ^{133}Xe and ^{135}Ba are studied after multinucleon transfer in the ^{136}Xe + ^{208}Pb reaction employing the high-resolution Advanced GAmma Tracking Array (AGATA) coupled to the magnetic spectrometer PRISMA at the Laboratori Nazionali di Legnaro, Italy and in a pulsed-beam experiment at the FN tandem accelerator of the University of Cologne, Germany utilizing a ^{9}Be + ^{130}Te fusion-evaporation reaction at a beam energy of 40 MeV. Isomeric states are identified via delayed γ-ray spectroscopy. Hitherto tentative excitation energy, spin, and parity assignments of the 2107-keV $J^\pi = 23/2^+$ isomer in ^{133}Xe are confirmed and a half-life of $T_{1/2} = 8.64(13)$ ms is measured. The 2388-keV state in ^{135}Ba is identified as a $J^\pi = 23/2^+$ isomer with a half-life of 1.06(4) ms. The new results show a smooth onset of isomeric $J^\pi = 23/2^+$ states along the $N = 79$ isotones and close a gap in the high-spin systematics towards the recently investigated $J^\pi = 23/2^+$ isomer in ^{139}Nd. The resulting systematics of $M2$ reduced transition probabilities is discussed within the framework of the nuclear shell model. Latest large-scale shell-model calculations employing the SN100PN, GCN50:82, SN100-KTH, and a realistic effective interaction reproduce the experimental findings generally well and give insight into the structure of the isomers.

DOI: 10.1103/PhysRevC.98.054312

*Corresponding author: levent.kaya@ikp.uni-koeln.de
†Deceased.

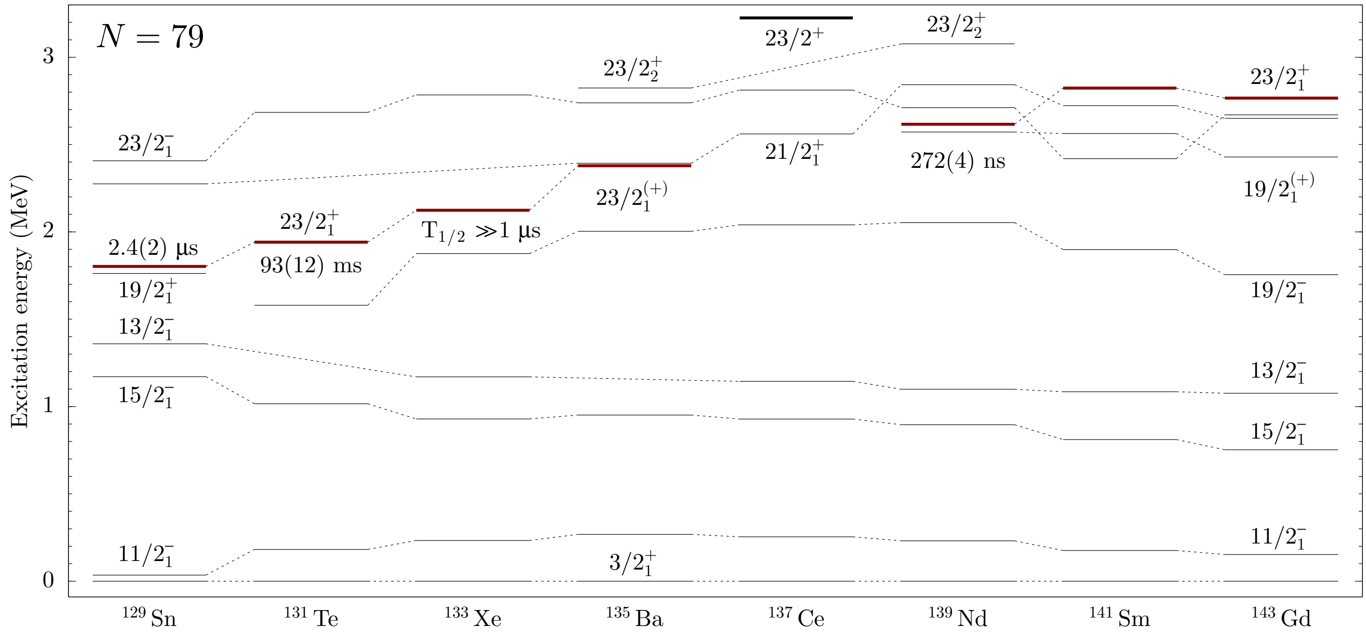

FIG. 1. Evolution of excited states along the $N = 79$ chain. Dashed lines connecting levels of same spin and parity are drawn to guide the eye. The $J^\pi = 23/2_1^+$ states in ^{129}Sn, ^{131}Te, and ^{139}Nd are isomers. A candidate for a $J^\pi = 23/2^+$ isomer at $E_x = 2107 + x$ keV was reported in ^{133}Xe [5]. It is expected that a corresponding long-lived state is also present in ^{135}Ba. Data extracted from the ENSDF database [8] and Refs. [1,5–7].

I. INTRODUCTION

The $N = 79$ isotones ^{133}Xe and ^{135}Ba, only three neutrons away from the $N = 82$ shell closure, are located within the proton midshell between the $Z = 50$ shell and the $Z = 64$ subshell closures. In this region, the evolution of nuclear collectivity competes with the excitation of single-particle states. Enabling high-j couplings, the intruder $h_{11/2}$ neutron orbital is pivotal for high-spin states in this region. ^{133}Xe and ^{135}Ba present an intriguing study ground for the predictive power of the shell model at both low and high spins in the vicinity of the $N = 82$ neutron closed shell. In particular, detailed knowledge of long-lived states—so-called isomers—provide a sensitive probe for the active quasiparticle configurations.

Figure 1 shows the evolution of several negative-, and positive-parity states along the $N = 79$ chain, ranging from semimagic $^{129}_{50}$Sn up to $^{143}_{64}$Gd. Isomeric $J^\pi = 11/2_1^-$ states with neutron-hole $\nu h_{11/2}^{-1}$ configurations were discovered in all odd-mass $N = 79$ isotones. Furthermore, several $J^\pi = 19/2^+$, $23/2^+$, and $27/2^-$ high-spin isomers above the $J^\pi = 11/2_1^-$ states were reported in the literature. These isomeric states are explained as high-spin members of the $\nu(h_{11/2}^{-2} d_{3/2}^{-1})$ and $\nu(h_{11/2}^{-n})$, seniority $\upsilon = 3$ multiplets [1–9].

Information on excited states in ^{129}Sn and ^{131}Te were mainly obtained from β decay and actinide fission studies. In a previous experiment, the semimagic nucleus ^{129}Sn was populated via thermal neutron-induced fission and investigated by means of γ-ray and electron-conversion spectroscopy [1,9]. Two L conversion lines corresponding to transition energies of 41.0 and 19.7 keV were identified as the decay of $J^\pi = 23/2^+$ and $19/2^+$ states, respectively. Based on the decay curves of the two electron-conversion lines and corresponding γ-ray decays, half-lives of $T_{1/2} = 2.4(2)$ μs for the $J^\pi = 23/2^+$ state and $T_{1/2} = 3.6(2)$ μs for the $J^\pi = 19/2^+$ state were determined [1]. In ^{129}Sn the seniority $\upsilon = 3$ multiplet is completed by the $J^\pi = (27/2^-)$ state at $E_x = 2552$ keV [$T_{1/2} = 0.27(7)$ μs], identified by Lozeva *et al.* in 2008 [4].

^{131}Te was populated in a pioneering ^{64}Ni + ^{130}Te multinucleon-transfer experiment at the GASP γ-ray spectrometer [10]. A delayed 361-564-833-keV triple-γ coincidence was identified to form the $(21/2^-) \to (19/2^-) \to (15/2^-) \to 11/2^-$ yrast band. Referring to isotopic systematics, a $J^\pi = 23/2^+$ isomer is proposed that is located slightly above the $J^\pi = (21/2^-)$ state at $E_x = 1941$ keV with a lower half-life limit of $T_{1/2} > 1$ μs. However, no low-energy $E1$ transition was observed in this work. Soon after, ^{131}Te was also populated after thermal fission of U isotopes at the OSIRIS mass separator by Fogelberg *et al.* [6]. In this work, a very long half-life of $T_{1/2} = 93(12)$ ms was determined. Based on conversion-electron measurements, the authors excluded a low-energy $E1$ transition hypothesis and the $E_x = 1941$-keV state was revised to be a $J^\pi = (23/2^+)$ isomer. The 361-keV transition was proposed to be of $E3$ character, connecting the isomer with a $J^\pi = (17/2^-)$ state. Finally, in a later fusion-fission experiment by Astier *et al.* [2] utilizing the EUROBALL array, the negative-parity band on top of the $J^\pi = (19/2^-)$ state was extended to excitation energies of approximately 4.7 MeV and spin $J^\pi = (35/2^-)$. The determined lower limit of the half-life of the $J^\pi = (23/2^+)$ state ($T_{1/2} \gg 10$ μs) is in agreement with the previous experiment. The multipolarity of the 361-keV transition was reevaluated to be mainly of $M2$ character. Based on the OSIRIS result and the reevaluated $M2$ character, a reduced transition strength of $B(M2; 23/2_1^+ \to 19/2_1^-) = 2.0(3) \times 10^{-6}$ W.u. [2] was deduced. Shell-model calculations predict a $\nu(h_{11/2}^{-2}d_{3/2}^{-1})$ configuration for the $J^\pi = (23/2^+)$ state and a predominant $(\nu h_{11/2}^{-1})(\pi g_{7/2}^2)$ configuration for the $J^\pi = (19/2^-)$ state. No feeding transitions for the $J^\pi = (23/2^+)$ isomer were yet discovered in ^{131}Te.

Going to the proton midshell, a first search of high-spin isomers in ^{137}Ce was made using a ^{4}He + ^{138}Ba reaction [11]. No evidence for a long-lived state was found in the off-beam range from 10–300 μs with respect to the beam pulse. Later, a $J = (31/2)$ state at $E_x = 4255$ keV was observed to be isomeric with a half-life of $T_{1/2} = 5(2)$ ns according to the time distribution of the depopulating 552-keV γ ray [12]. The level scheme of ^{137}Ce was extended up to highest spins via ^{18}O + ^{124}Sn [13] and ^{13}C + ^{130}Te [14] reactions. To date, only a $J^\pi = 23/2^+$ state above $E_x = 3$ MeV is reported. It is much higher in excitation energy than in the other $N = 79$ isotones and disrupts the systematics (c.f. Fig. 1).

First spectroscopic data on the elusive $J^\pi = 23/2^+$ isomer in ^{139}Nd were reported by Müller-Veggian *et al.* [15] employing a ^{140}Ce(α, 5n) reaction. The level scheme above the $J^\pi = 11/2_1^-$ isomer was extended to an excitation energy of approximately 4 MeV. Delayed γ rays deexciting the $J^\pi = 19/2_1^+$ state were observed in off-beam $\gamma\gamma$-coincidence spectra. Based on the decay curve, a half-life limit of $T_{1/2} >$ 141 ns was deduced. Later, the isomer's excitation energy was constrained to be above the $J^\pi = 19/2_1^+$ state and a precise half-life of $T_{1/2} = 272(4)$ ns could be obtained [7]. However, the isomer could not unambiguously place in the level scheme. Finally, in 2013, a recoil-decay tagging experiment at the Jyväskylä accelerator facility confirmed the previous half-life measurement [3]. The authors observed feeding transitions from the decay of three higher-lying $J^\pi = (25/2^-)$ states allowing for a placement of the isomeric $J^\pi = (23/2^+)$ state in the level scheme at $E_x = 2616$ keV, only 44 keV above the $J^\pi = 19/2^+$ state. However, that 44-keV transition is still unobserved. Towards the subshell closure at $Z = 64$, detailed high-spin structure information is available for ^{141}Sm [16,17] and ^{143}Gd [17–19]; no high-lying isomeric states were observed.

The onset of isomerism as a function of the proton number along the $N = 79$ chain (see Fig. 1) motivates a refined investigation of isomeric $J^\pi = 23/2^+$ states in ^{133}Xe and ^{135}Ba. The available data on low-spin states in ^{133}Xe mainly originate from β-decay studies of ^{133}I [20]. The $J^\pi = 11/2_1^-$ isomer at 233 keV with a $\nu h_{11/2}^{-1}$ neutron-hole configuration has a half-life of 2.198(13) d [21]. First results on the high-spin structure were obtained by Lönnroth *et al.* [22] via α-induced reactions on ^{130}Te at beam energies of 14.1–18 MeV. Three γ rays with energies of 247.4, 947.8, and 695.2 keV were placed above the $J^\pi = 11/2_1^-$ isomer to form a $(23/2^-) \rightarrow 19/2_1^- \rightarrow 15/2_1^- \rightarrow 11/2_1^-$ cascade.

Recently, the high-spin regime of ^{133}Xe was extended via ^{136}Xe + ^{208}Pb and ^{136}Xe + ^{198}Pt multinucleon-transfer reactions employing the Advanced GAmma Tracking Array (AGATA) coupled to the magnetic spectrometer PRISMA and the GAMMASPHERE spectrometer in combination with the gas-filled detector array CHICO, respectively [5]. A 1253-468-465-keV prompt triple coincidence was observed to form a band unconnected to any known states in ^{133}Xe. According to the time structure in the GAMMASPHERE data set, a long-lived isomer with $T_{1/2} \gg 1$ μs was proposed at $E_x = 2107 + x$ keV.

High-spin states in ^{135}Ba above the $J^\pi = 11/2_1^-$ isomer ($T_{1/2} = 28.7$ h [23]) were investigated by Che *et al.* [24]. Excited states were populated up to excitation energies of 5.8 MeV using a ^{130}Te(^{9}Be, 4n)^{135}Ba reaction at 45 MeV. A 1184-254 keV cascade was observed to feed the $J^\pi = 15/2_1^-$ state at $E_x = 950$ keV. The 2134-keV state was identified as the $J^\pi = 19/2_2^-$ state, while no spin assignment was given for the 2388-keV state. Moreover, no decay from higher-lying states into the 2388-keV state was observed. Later, a first tentative spin assignment of $J^\pi = 21/2^{(-)}$ was proposed for the 2388-keV state [25]. A high-spin investigation by Kumar *et al.* extended the level scheme with 20 new γ rays [26]. Directional correlation measurements confirmed the spin and parity assignments of the $J^\pi = 19/2_2^-$ state and indicated a tentative $J = (23/2)$ spin assignment for the 2388-keV state. Even though detailed data are available up to highest spins and excitation energies, no feeding γ ray to the 2388-keV state was found to date. This observation corroborates the existence of a long-lived $J = 23/2_1^+$ isomer in ^{135}Ba.

In this paper, we report and discuss new results on isomeric $J^\pi = 23/2^+$ states in the $N = 79$ isotones ^{133}Xe and ^{135}Ba obtained in two different experiments. ^{135}Ba was populated in a ^{136}Xe + ^{208}Pb multinucleon-transfer (MNT) experiment employing the high-resolution position-sensitive Advanced GAmma Tracking Array (AGATA) [27] in combination with the magnetic mass spectrometer PRISMA [28–30]. In a fusion-evaporation experiment, both ^{133}Xe and ^{135}Ba were investigated with the HORUS γ-ray array [31] at the Institute of Nuclear Physics, University of Cologne, employing a pulsed 40-MeV ^{9}Be beam impinging onto a ^{130}Te target. This paper is organized as follows: the experimental setup and data analysis of the two experiments are described in Sec. II, followed by the experimental results in Sec. III. A detailed comparison with shell-model calculations is presented in Sec. IV before the paper closes with a summary and conclusions.

II. EXPERIMENTAL PROCEDURE AND DATA ANALYSIS

A. ^{136}Xe + ^{208}Pb multinucleon transfer

^{135}Ba was populated in a ^{136}Xe + ^{208}Pb multinucleon-transfer experiment at the Laboratori Nazionali di Legnaro, Italy. In this experiment, a 6.84 MeV/nucleon ^{136}Xe beam, accelerated by the PIAVE+ALPI accelerator complex, impinged onto a 1-mg/cm^2 ^{208}Pb target. The Advanced GAmma Tracking Array (AGATA) [27] in a first demonstrator configuration [32] was placed at a distance of 18.8 cm from the target position to measure γ rays from excited states. The array consisted of nine large-volume electronically segmented high-purity Ge (HPGe) detectors in three triple cryostats [33]. An isotopic identification of the nuclei of interest was provided by the magnetic spectrometer PRISMA placed at the reaction's grazing angle of $\theta_{\rm lab} = 42^\circ$. An event registered by the PRISMA focal-plane detector in coincidence with an AGATA event was taken as a trigger for the data acquisition.

Pulse-shape analysis of the digitized detector signals was applied to determine the individual interaction points within the HPGe shell [34], enabling the Orsay forward-tracking algorithm [35] to reconstruct the individual emitted γ-ray energies, determine the first interaction point of the γ ray in the germanium and, thus, the emission angle. Together with the kinematic information from PRISMA, a precise Doppler correction was performed. Further details on the analysis can be found in Refs. [36,37].

B. ^{9}Be + ^{130}Te fusion-evaporation reaction

In a second experiment, ^{133}Xe and ^{135}Ba were populated in a ^{130}Te + ^{9}Be fusion-evaporation reaction. The FN Tandem accelerator of the Institute of Nuclear Physics, University of Cologne delivered pulsed 40-MeV ^{9}Be beams with two different repetition rates onto an enriched ^{130}Te target with a thickness of 1.8 mg/cm^2 evaporated onto a 120-mg/cm^2 thick Bi backing plus a 132-mg/cm^2 thick Cu layer for heat dissipation. Approximately 95% of the reaction products were stable nuclei, stopped inside the Bi backing. The pulsing system was placed at the injection line of the FN Tandem accelerator and comprises five deflectors aligned parallel to the beam axis. The electric potential of one side of the deflectors was grounded, while the electrical potential of the opposite side was alternating between ground level and 1.3 kV.

The first pulsed beam had a pulse width of 75 ms and a repetition rate of 3.33 Hz. To exclude the background from β-decay channels and longer-lived isomers, a second pulsed beam was employed with a pulse width of 3.75 s and a repetition rate of 66.66 mHz. γ rays were measured using the HORUS array [31] comprising 14 HPGe detectors, six of them equipped with BGO Compton-suppression shields. The detectors were positioned on the eight corners and six faces of a cube. γ events were processed triggerless and recorded utilizing the synchronized 80-MHz XIA™ Digital Gamma Finder (DGF) data-acquisition system. In addition, a reference signal given by the pulsing system was recorded.

The data were sorted into (i) a two-dimensional γ-γ matrix with a time gate of 250 ns between coincident γ events, (ii) a two-dimensional γ-t matrix to gate on different time windows relative to the reference pulse, and (iii) a total of three group matrices each corresponding to detector pairs with relative angles $\Theta = \{54.7^\circ, 70.4^\circ, 90^\circ\}$ for off-beam angular-correlation measurements using the SOCO-V2 code [38]. In total, 7.1×10^7 $\gamma\gamma$-coincidence events and 1.2×10^9 γ-t events were collected.

Spins and parities of populated states in the HORUS experiment are investigated in the off-beam measurement with the $\gamma\gamma$ angular-correlation code CORLEONE [39,40] based on the phase convention by Krane, Steffen, and Wheeler [41,42]. Different hypotheses of involved spins J_1, J_2, J_3 and multipole-mixing ratios δ_1, δ_2 of two coincident γ rays in a cascade $J_1 \xrightarrow{\delta_1} J_2 \xrightarrow{\delta_2} J_3$ are evaluated by χ^2 fits of the correlation function $W(J_1, \delta_1, J_2, \delta_2, J_3, \Theta, \sigma)$ to experimental correlation intensities for the three angular-correlation groups. θ_1 and θ_2 are the angles between beam axis and detectors; $\Theta = \theta_1 - \theta_2$ denotes the relative angle of a detector pair. A deorientation from the beam axis is taken into account by increasing the value of σ.

III. RESULTS

Partial level schemes of excited states in ^{133}Xe and ^{135}Ba, which are discussed in this paper, are displayed in Figs. 2(a) and 2(b). The determined half-lives of isomeric states in ^{132,133}Xe and ^{135,136}Ba are summarized in Table I.

The Doppler-corrected beamlike singles γ-ray spectrum gated on ^{135}Ba from the ^{136}Xe + ^{208}Pb AGATA experiment is shown in Fig. 3(a). Random background is significantly suppressed by gating on the prompt peak in the time-difference distribution between AGATA and PRISMA. Prominent transitions are marked with labels. The decays of the $J^\pi = 19/2_1^-$ and $15/2_1^-$ states at energies of 1052 and 682 keV are clearly visible as dominant peaks in the spectrum. Transitions in the positive-parity dipole band, on top of the $J^\pi = 21/2_2^+$ state at $E_x = 3083$ keV are observed well above the background. The highest excitation energy identified in the ^{135}Ba reaction channel corresponds to the $J^\pi = 31/2^+$ state at $E_x = 4696$ keV. The insets Figs. 3(b) and 3(c) show magnifications into the measured γ-ray spectrum around the γ-ray energies of the expected decays of the $J^\pi = 23/2^+$ state at 254 keV and around the decay of the $J^\pi = 19/2_2^-$ state at 1184 keV, respectively. The 1184-keV transition is clearly visible in the prompt AGATA spectrum, however, the 254-keV feeding transition is absent. This observation suggests that the half-life of the 2388-keV state is significantly longer compared to the width of the prompt peak in the time-difference spectrum between PRISMA and AGATA, i.e., $\Delta t_{\mathrm{PRISMA-AGATA}} \approx 16$ ns. Consequently, the observation of the 1184-keV transition accompanied by the absence of the 254 keV feeding transition, despite the observation of other high-spin bands, indicates an isomeric character of the $E_x = 2388$ keV state.

In the first part of the HORUS experiment, the beam pulse width was set to 75 ms, followed by a 225-ms time window for off-beam measurements. The recorded reference time at the beginning of the beam flash allows us to gate on different off- and in-beam time windows. In particular, gates within the time window between 75 and 300 ms with respect to the reference pulse restrict the γ-ray spectrum to the off-beam measurement. Figures 3(d) and 3(f) show γ-ray spectra obtained with different time windows. The γ-time matrices with the applied gates are shown in inset Figs. 3(e) and 3(g). In the matrix a distinct separation between in-beam and off-beam γ-ray spectrum is visible at 75 ms relative to the reference pulse.

In order to validate the experimental procedure, several well-known long-lived millisecond isomers were investigated. By gating on the time window $\Delta t = 80$–90 ms [Fig. 3(d)], delayed transitions at energies of 174, 538, 600, 668, and 773 keV, forming a cascade below the $J^\pi = 10_1^+$ isomer in ^{132}Xe, are clearly enhanced in the γ-ray spectrum. Furthermore, the spectrum exhibits the 1048-keV $4_1^+ \rightarrow 2_1^+$ and 819-keV $2_1^+ \rightarrow 0_1^+$ transitions originating from the $J^\pi = 7_1^-$ isomer in ^{136}Ba. The peaks at 231, 948, and 695 keV are mutually coincident and identified as the decay cascade of the $J^\pi = 23/2_1^+$ state in ^{133}Xe. A background-subtracted

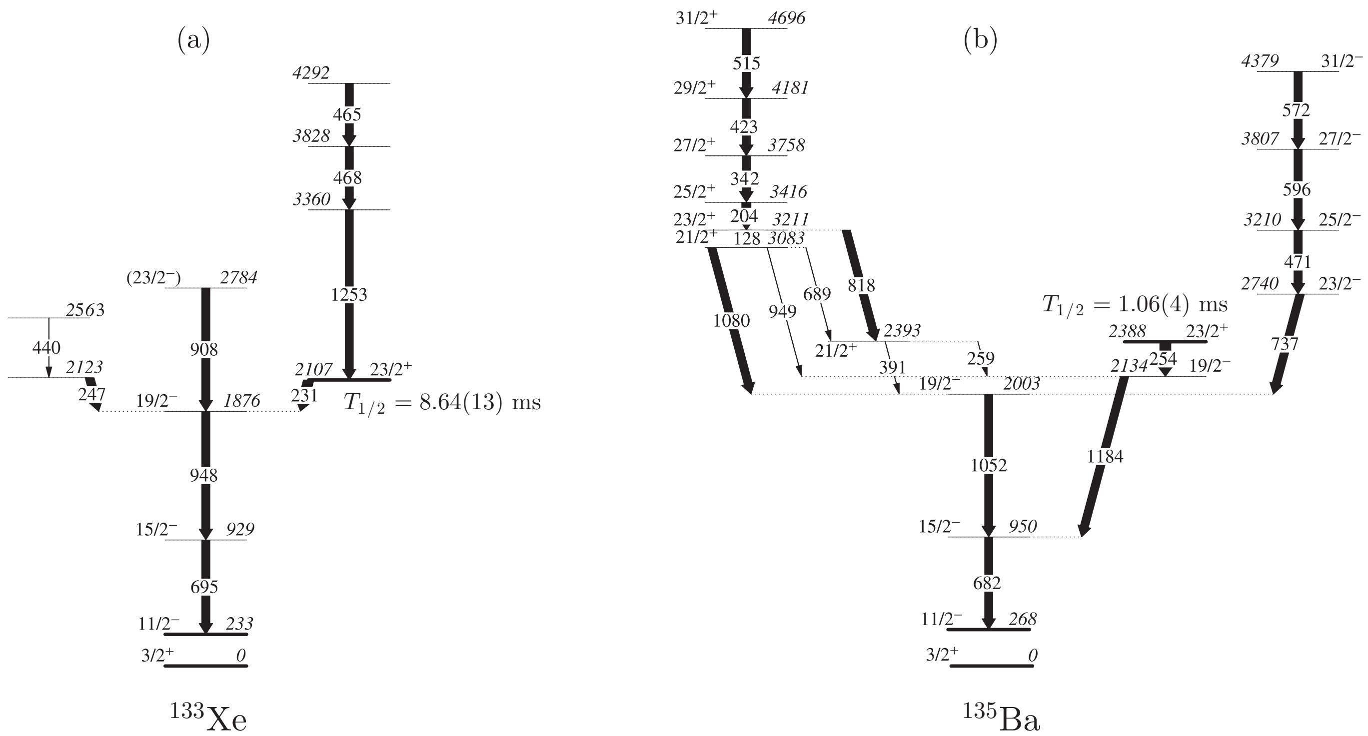

FIG. 2. Partial level schemes of (a) ^{133}Xe and (b) ^{135}Ba. The reduced transition strengths of the 231-keV transition in ^{133}Xe and the 254-keV transition in ^{135}Ba are subject of this paper. Dominating transitions in the HORUS fusion-evaporation experiment are presented with thicker arrows.

in-beam prompt $\gamma\gamma$-coincidence spectrum with a gate on the 1253-keV transition in ^{133}Xe is shown in Fig. 4. Coincident transitions at energies of 465 and 468 keV are forming a 1253-468-465 keV cascade on top of the $J^\pi = 23/2^+$ isomer confirming the observation in Ref. [5]. Other lines at 197, 847, 1039, and 1239 keV originate from the ^{19}F$(n, n'\gamma)$ reactions and the β decay of ^{56}Mn into ^{56}Fe.

The delayed transitions in ^{132,133}Xe and ^{136}Ba are also visible in the spectrum gated on the time window $\Delta t = 75$-80 ms in Fig. 3(f). Based on the AGATA data set, a pronounced delayed 254-1184-682-keV γ-ray cascade in ^{135}Ba is expected. The observation of this cascade in the off-beam spectrum in Fig. 3(f) clearly confirms the presence of an isomer in this nucleus. The absence of the cascade in the spectrum in Fig. 3(d) implies that the isomer in ^{133}Xe has a longer half-life compared to the similar state in ^{135}Ba.

Figures 5($a_{1,2}$)–5($c_{1,2}$) show fits of well-known half-lives of isomeric states in ^{136}Ba and ^{132}Xe. The fit function of the time spectrum $N(t)$ is chosen as $N(t) = a\exp[t\ln(2)/T_{1/2}] + b$ with a and b as free parameters. The decay chain deexciting the $J^\pi = 7^-$ isomer in ^{136}Ba is observed in the seconds-range pulsed-beam experiment. The corresponding background-subtracted time projection of the $2_1^+ \to 0_1^+$ transition at $E_\gamma = 819$ keV and the fitted decay

TABLE I. Measured half-lives of selected isomers observed in the ^{9}Be + ^{130}Te experiment. The different columns indicate the nucleus, repetition rate of the pulsed beam, excitation energy, spin and parity of the isomeric state, the energy of the γ ray used to determine the half-life, the deduced weighted mean half-life, and previous results reported in the literature.

Isotope	Repetition rate (Hz)	E_i (keV)	J_i^π ($\hbar$)	E_γ (keV)	$T_{1/2}$	
					Present work	Literature
^{136}Ba	0.066	2031	7^-	819	0.296(7) s	0.3084(19) s [43]
						0.303(2) s [44]
						0.37(5) s [45]
						0.32(2) s [46]
^{132}Xe	3.33	2752	10^+	174, 538, 600, 668, and 773	8.37(8) ms	8.39(11) ms [47]
						8.4(8) ms [48]
						8.2(6) ms [49,50]
^{133}Xe	3.33	2107	$23/2^+$	231, 695, and 948	8.64(13) ms	–
^{135}Ba	3.33	2388	$23/2^+$	254, 682, and 1184	1.06(4) ms	–

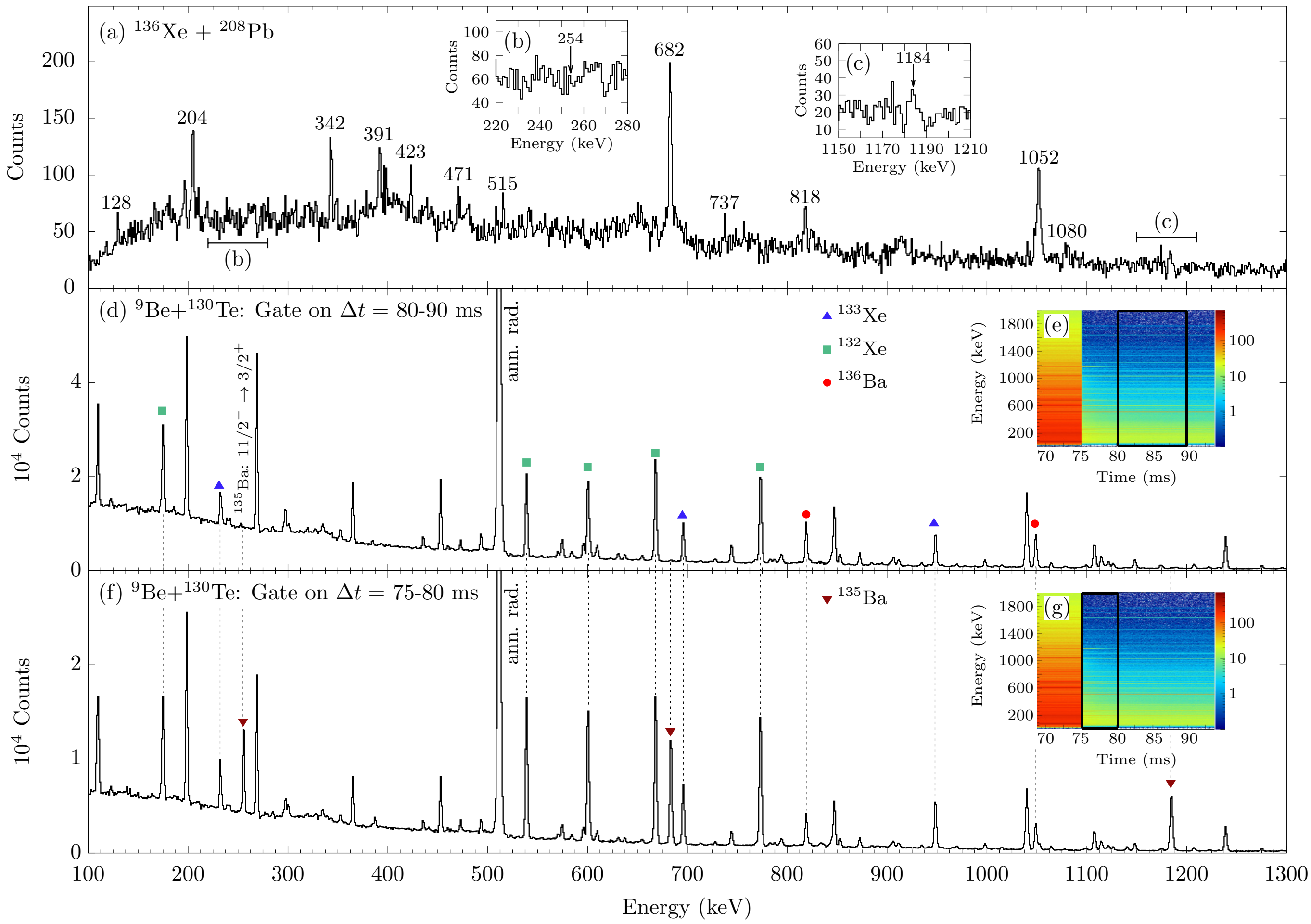

FIG. 3. (a) Doppler-corrected γ-ray spectrum gated on ^{135}Ba identified with PRISMA in the ^{136}Xe+^{208}Pb experiment. Insets show the zoomed spectrum around the expected transitions at (b) 254-keV and (c) 1184-keV. (d) Projection of the γ-t matrix gated on a time window between 80 and 90 ms relative to the reference time at the beginning of the beam flash. (f) Similar data for a gate on a time window between 75 and 80 ms. Delayed transitions below the $J^\pi = 23/2^+_1$ isomers in ^{133}Xe, ^{135}Ba, and below the $J^\pi = 10^+_1$ isomer in ^{132}Xe are marked with symbols and dashed lines to guide the eye. Both insets (e) and (g) present the γ-t matrix relative to the reference time. The applied time gates are surrounded by black boxes.

curve are shown in Fig. 5(a$_1$). For the sake of completeness, a similar plot with a logarithmic scale is shown in the inset Fig. 5(a$_2$). The measured half-life of $T_{1/2} = 0.296(7)$ s is in good agreement with previously measured values [44–46]. The absolute fit residual, defined as difference between absolute experimental value and fit function, is presented in Fig. 5(a$_3$). In addition, fits of the background-subtracted time projections of the 538-keV and 668-keV transitions, depopulating the $J^\pi = 10^+$ isomer in ^{132}Xe, are depicted in Fig. 5(b$_{1,2}$) and Fig. 5(c$_{1,2}$). A small constant background remains after background subtraction in the time distribution of the $2^+_1 \rightarrow 0^+_1$ 668 keV transition due to a weak feeding from β decays of ^{132}I and ^{132}Cs. Both independently determined half-lives are in excellent agreement with the previous values [47–50]. The consistency between the literature values and the current analysis demonstrates the reliability of the analysis.

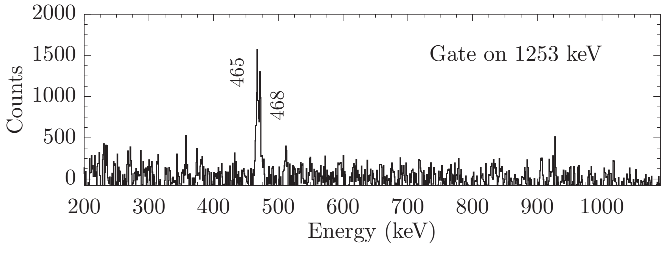

FIG. 4. Prompt in-beam $\gamma\gamma$ coincidence spectrum with a gate on the 1253-keV transition in ^{133}Xe above the $J^\pi = 23/2^+$ isomer. Coincidences at energies of 465 and 468 keV are visible.

The background-subtracted time distributions of the 231-, 947-, and 695-keV transitions in ^{133}Xe are presented in Figs. 5(c$_{1,2}$), 5(d$_{1,2}$), and 5(e$_{1,2}$). Exponential fits of the slope components yield respective half-lives of 8.62(13), 8.60(9), and 8.68(8) ms. The constant random background is determined separately and incorporated into the fit. The independently determined half-lives utilizing the three different gate conditions show excellent agreement. Systematic errors from uncertainties in the determination of the background

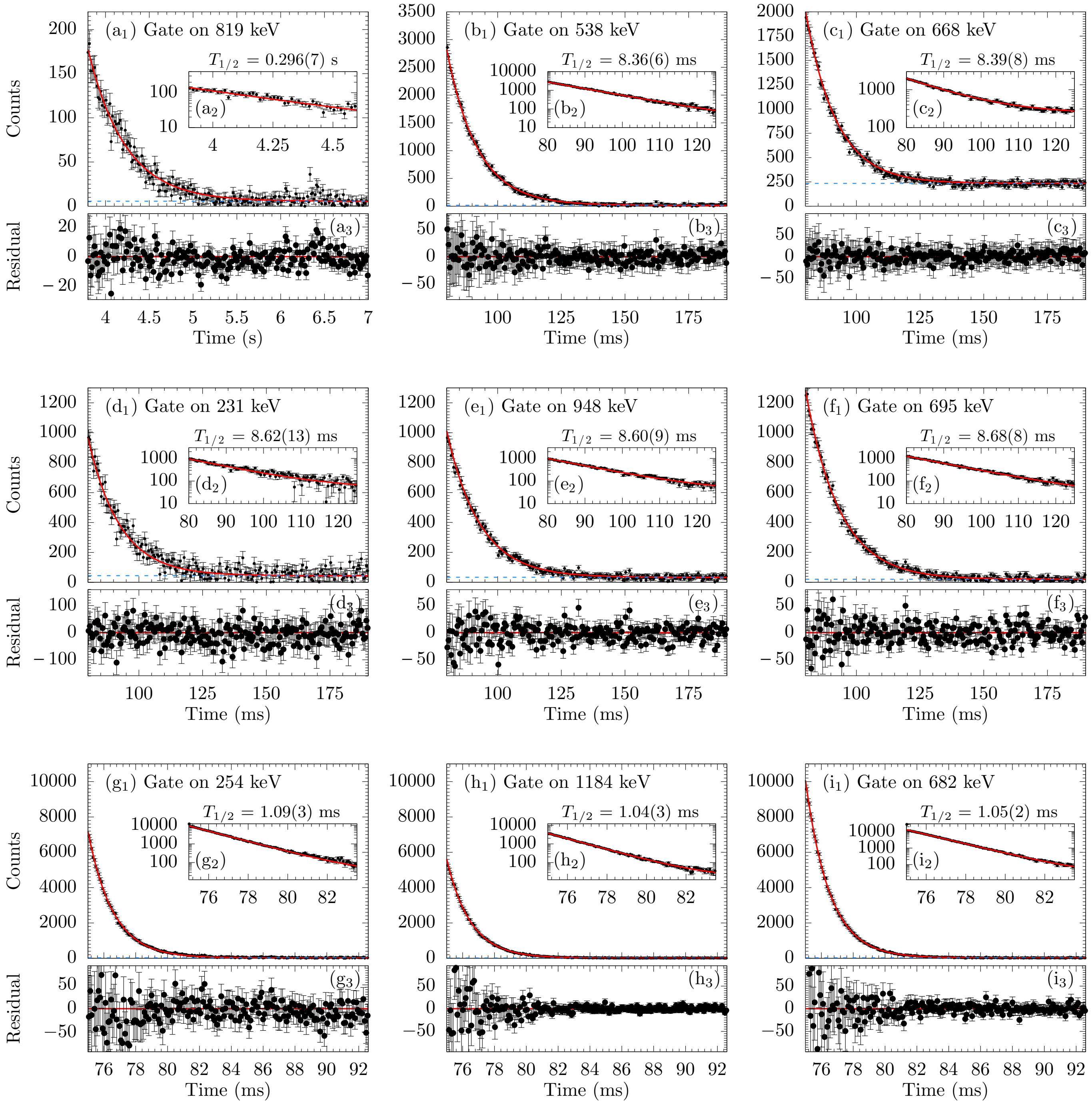

FIG. 5. Gates on background-subtracted γ-time matrices and half-life fits for the gating conditions (a_{1-2}) 819 keV in ^{136}Ba measured in the seconds-pulsing experiment, (b_{1-2}) 538 keV and (c_{1-2}) 668 keV in ^{132}Xe, (d_{1-2}) 231 keV, (e_{1-2}) 947 keV, and (f_{1-2}) 695 keV in ^{133}Xe, (g_{1-2}) 254 keV, (h_{1-2}) 1184 keV, and (i_{1-2}) 682 keV in ^{135}Ba obtained in the milliseconds-pulsing experiment. The corresponding residual, defined as difference between absolute value and fit function, is shown in panels (a_3), (b_3), (c_3), (d_3), (e_3), (f_3), (g_3), (h_3), and (i_3), respectively. Half-lives are determined from exponential fits of the delayed component. The fit is drawn with a solid red line. Random background is determined separately (dashed blue line) and incorporated into the fit model.

are taken into account. The final weighted mean value of $T_{1/2} = 8.64(13)$ ms is newly established for the $J^\pi = 23/2^+$ state in ^{133}Xe.

Background subtracted time spectra of transitions deexciting the state at $E_x = 2388$ keV in ^{135}Ba, fits, and corresponding residuals are presented in Figs. 5(f_1)–5(h_3). The fit for the 254-keV transition yields a half-life of 1.09(3) ms. Independently determined half-lives involving the 1184-keV [1.04(3) ms], and the 682-keV [1.05(2) ms] γ ray are in mutual agreement. The final weighted mean half-life of the $J^\pi = 23/2^+$ state in ^{135}Ba is measured to be $T_{1/2} = 1.06(4)$ ms taking into account systematic errors.

According to systematics and shell-model arguments, a direct single-step decay of the 2107 + x-keV band head of the 465-468-1253-keV cascade in ^{133}Xe via a 231-keV transition was slightly favored in the previous work [5]. However, a decay via an unobserved low-energy transition similar to ^{129}Sn and ^{139}Nd could not be ruled out. Internal conversion coefficients and angular-correlation measurements were carried out to clarify the decay patterns in ^{133}Xe and ^{135}Ba. Since conversion electrons are not directly detected, the internal conversion coefficient α_T is determined via the intensity-balance method described in Ref. [52]. In the off-beam measurement the isomer in ^{133}Xe decays via the 231-948-695 cascade towards the $J^\pi = 11/2^-$ state. Therefore, the intensities of the 231 and 948-keV transitions, corrected for detector efficiency and internal conversion, are equal in the delayed γ-ray spectrum:

$$I_{\gamma_1}(1+\alpha_{\gamma_1}) = I_{\gamma_2}(1+\alpha_{\gamma_2}), \tag{1}$$

where $I_{\gamma_{1,2}}$ are the efficiency-corrected γ-ray intensities and $\alpha_{\gamma_{1,2}}$ are the total internal-conversion coefficients (ICCs). The off-beam intensities $I_{948\ \mathrm{keV}}$ and $I_{231\ \mathrm{keV}}$ are extracted from the γ-ray spectra of the 14 HPGe detectors by gating on the off-beam time window with a time gap of 100 ns from the in-beam part to exclude possible feeding from short-lived components. Using the weighted arithmetic mean of the 14 measurements and the well-established $E2$ character of the 948 keV transition ($\alpha_{948} = 0.00182$ [51]), a value of $\alpha_{231} = 0.49(9)$ is obtained for the 231-keV transition. Based on a comparison with theoretical α_T values [51], presented in Fig. 6(a), the multipolarity of the 231-keV transition can be restricted to an $M2$ or $E3$ character. Applying the same method to the 254-1184-keV cascade in ^{135}Ba, a value of $\alpha_{254} = 0.32(7)$ for the 254 keV transition is computed. Again, a comparison with theoretical values shown in Fig. 6(b) yields a good agreement with $M2$ or $E3$ multipolarities for the 254-keV γ ray.

Angular-correlation measurements provide a complementary approach to the internal conversion coefficient measurement. Figures 6(c)–6(e) show comparisons of theoretical angular-correlation functions $W(J_1, \delta_1, J_2, \delta_2, J_3, \Theta, \sigma)$ (colored lines) with experimentally obtained relative intensities in three different correlation groups. A fit of the $2_2^+ \rightarrow 2_1^+$ 1120-keV transition in ^{214}Po, measured in the energy calibration run with a ^{226}Ra source, is shown in Fig. 6(c). The determined multipole-mixing ratio of $\delta = 0.19(6)$ agrees well with the evaluated multipole-mixing ratio of $\delta_{\mathrm{lit.}} = 0.18(2)$ [53]. The corresponding angular-correlation fit of the 231-keV transition, gated on the 948-keV transition in ^{133}Xe, is presented in Fig. 6(d). The multipolarity of the 948-keV γ ray is fixed to be an $E2$ transition, while different spin hypotheses of the 2107-keV state are tested. Combined with the internal conversion coefficient measurement, a spin assignment of $J^\pi = 23/2^+$ and a multipole-mixing ratio of $\delta_{23/2^+\rightarrow 19/2^-} = -0.021(10)$ is most likely for the 2107-keV state. The small value of the multipole-mixing ratio indicates a dominant $M2$ contribution and a small $E3$ admixture in the $\Delta J = 2$ transition.

Spin hypotheses for the 2388-keV state in ^{135}Ba are tested by employing the same angular-correlation method. In Fig. 6(e) experimentally determined intensities of the 254-keV γ ray in the different correlation groups, gated on the 1184-keV transition, are compared to theoretical intensities.

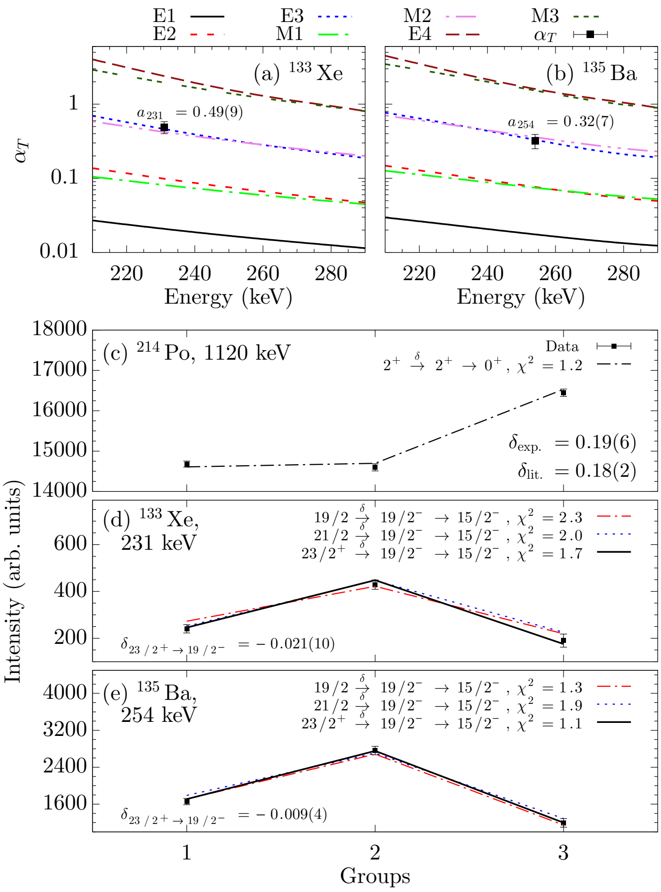

FIG. 6. (a) Total conversion coefficient for the 231-keV transition in ^{133}Xe compared with predicted values from the BrIcc v2.3 database [51]. (b) Similar comparison for the 254-keV transition in ^{135}Ba. The multipolarity of the 231 and 254-keV transition can be restricted to $M2/E3$ character. $\gamma\gamma$ off-beam angular correlations for (c) the known 1120-609-keV cascade in ^{214}Po, (d) the 231-948-keV cascade in ^{133}Xe, and (e) the 254-1184-keV cascade in ^{135}Ba. Experimental values (black points) are compared to calculated angular-correlation functions $W(J_1, \delta_1, J_2, \delta_2, J_3, \Theta, \sigma)$ (lines) for three correlation groups.

Again, the $23/2^+ \xrightarrow{\delta} 19/2^- \rightarrow 15/2^-$ hypothesis (solid line) with $\delta_{23/2^+\rightarrow 19/2^-} = -0.009(4)$ yields the best agreement. The small multipole-mixing ratio indicates a dominating $M2$ character of the 254-keV transition. Nevertheless, based on the fit results of this work, a spin assignment of $J = 19/2$ ($\chi^2 = 1.9$) or $21/2$ ($\chi^2 = 1.3$) cannot be excluded either. However, the internal conversion coefficient measurement shown in Fig. 6(b) suggests a $J^\pi = 23/2^+$ spin assignment. This argument is further supported by the previous results of Ref. [26], where both spin assignments $J = 19/2$ and $J = 21/2$ are excluded.

Internal-conversion coefficients are calculated employing the newly determined multiple-mixing ratios δ via the following expression [54]:

$$\alpha_T = \frac{\alpha_T(M2) + \delta^2 \alpha_T(E3)}{1+\delta^2}, \tag{2}$$

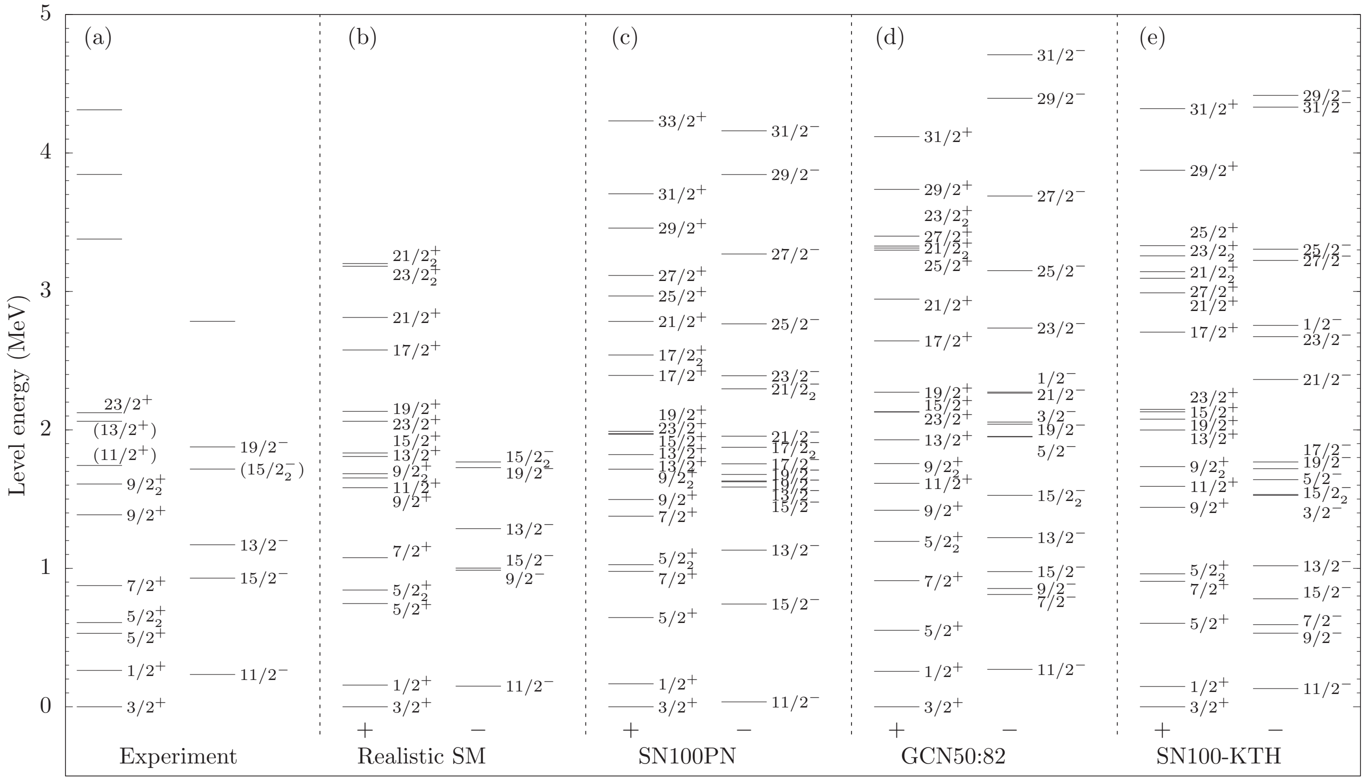

FIG. 7. Comparison of experimental energy spectra of ^{133}Xe [left panel, (a)] with the results of shell-model calculations employing the (b) Realistic SM, (c) SN100PN, (d) GCN50:82, and (e) SN100-KTH interaction. Note that the states are separated into columns for the negative- and the positive-parity states.

where $\alpha_T(M2)$ and $\alpha_T(E3)$ are theoretical ICC values. The calculated values $\alpha_T = 0.421(6)$ for ^{133}Xe and $\alpha_T = 0.364(5)$ for ^{135}Ba are in good agreement with the independently measured ICC values, showing the complementarity between both approaches.

IV. DISCUSSION

The experimentally obtained isomer excitation energies, half-lives and corresponding reduced transition probabilities in ^{133}Xe and ^{135}Ba are compared to shell-model theory. All shell-model calculations were carried out in an untruncated *gdsh* valence space outside doubly magic ^{100}Sn, employing the shell-model code NUSHELLX@MSU [55], the massive-parallelization code KSHELL [56] and the ANTOINE shell-model code [57].

The first calculation is conducted in the framework of the realistic shell model [58,59], denoted as realistic SM. Single-particle energies and two-body effective interaction are determined from the established CD-Bonn free nucleon-nucleon potential using the $V_{\text{low-}k}$ approach with a cutoff momentum of $\Lambda = 2.6$ fm^{-1}, plus the Coulomb force for protons. The effective shell-model Hamiltonian is derived iteratively by means of the many-body perturbation theory in the $\hat{Q}$-box folded diagram expansion, including all diagrams up to third order in the interaction.

Another calculation is carried out with the jj55pn Hamiltonian (referred to as the SN100PN interaction) [60]. The Hamiltonian consists of four terms covering the neutron-neutron, neutron-proton, proton-proton, and Coulomb repulsion between the protons individually. A renormalized G matrix derived from the CD-Bonn interaction [61] was employed to construct the realistic two-body residual interaction. The proton and neutron single-particle energies are based upon the energy levels in ^{133}Sb and ^{131}Sn.

A third calculation is performed utilizing the effective interaction GCN50:82 [62,63]. Similar to the SN100PN interaction, the interaction is derived from a realistic G matrix based on the CD-Bonn potential. Empirical monopole corrections to the original G matrix are introduced by fitting different combinations of two-body matrix elements to sets of experimental excitation energies from even-even and even-odd semimagic nuclei.

The last calculation, hereinafter referred to as SN100-KTH, leverages the realistic CD-Bonn interaction as well. The $T = 1$ part of the monopole interaction was corrected via the Monte Carlo global optimization approach by fitting several low-lying yrast states in Sn isotopes. A renormalization was performed by a perturbative G matrix approach to include core-polarization effects. It was shown that the calculations reproduce well the excitation energies and $E2$ transition probabilities in even-even Te isotopes [64,65].

A comparison of [Fig. 7(a)] experimental energy spectrum of ^{133}Xe with the results of [Fig. 7(b)] realistic SM, [Fig. 7(c)] SN100PN, [Fig. 7(d)] GCN50:82, and [Fig. 7(e)] SN100-KTH shell-model calculations is shown in Fig. 7. The states are separated into columns for the negative- and the positive-parity states. All four calculations reproduce the spin

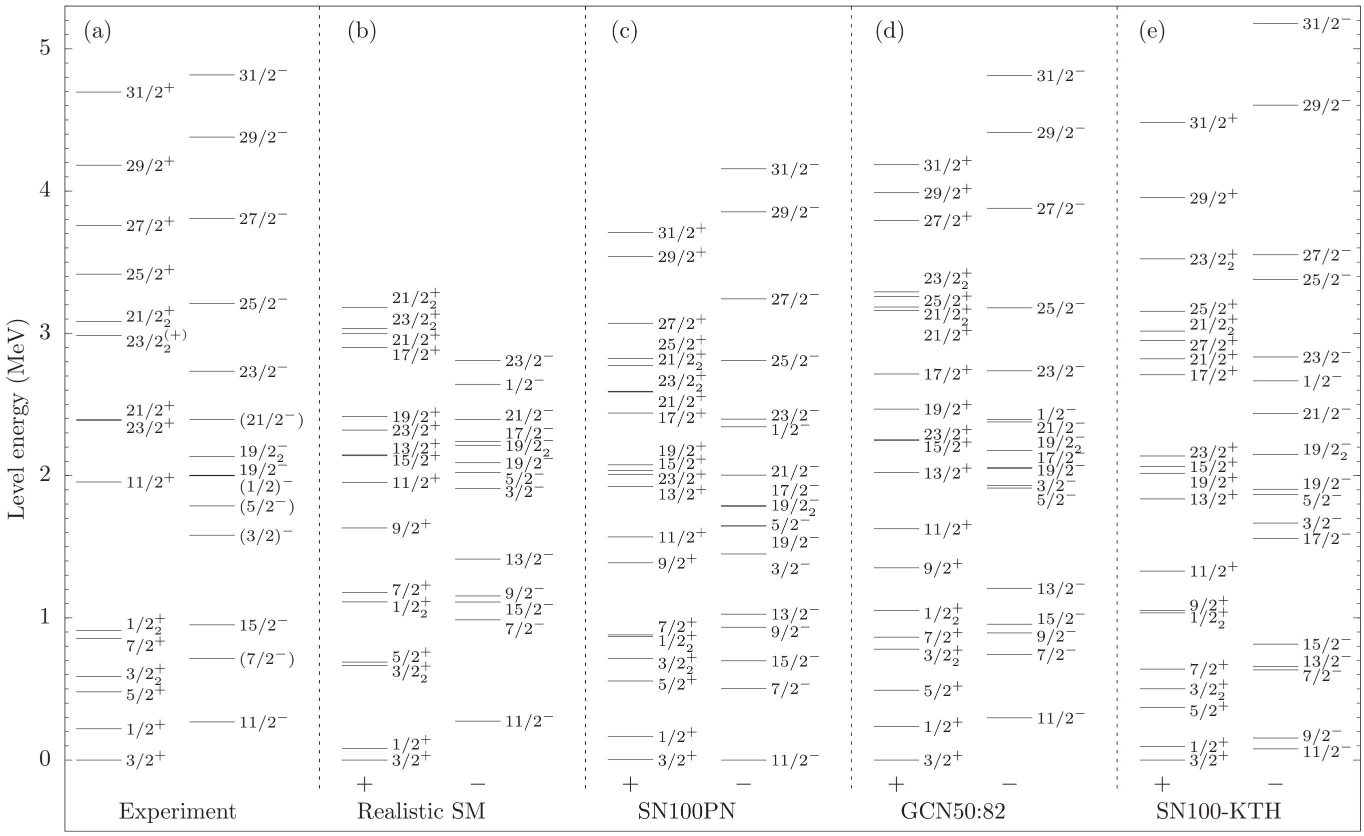

FIG. 8. Comparison of experimental energy spectra of ^{135}Ba [left panel, (a)] with the results of shell-model calculations employing the (b) Realistic SM, (c) SN100PN, (d) GCN50:82, and (e) SN100-KTH interactions. The arrangement of the states mirrors the layout in Fig. 7.

of the $J^\pi = 3/2^+$ ground state. The GCN50:82 interaction slightly overpredicts the $E_x = 233$-keV $J^\pi = 11/2_1^-$ state by 37 keV while the realistic SM, SN100PN, and SN100-KTH interactions place the $J^\pi = 11/2_1^-$ state 84, 198, and 102 keV too low in excitation energy, respectively. All interactions show a good agreement for the low-spin positive-parity states below 1 MeV.

The 948-, and 695-keV γ-ray transitions, forming the $19/2_1^- \to 15/2_1^- \to 11/2_1^-$ cascade, are calculated as 726 and 852 keV using realistic SM, 883 and 707 keV using SN100PN, 977 and 706 keV using GCN50:82, and as 939 and 649 keV using SN100-KTH, respectively. The calculated excitation energy of the isomeric $J^\pi = 23/2_1^+$ state is in excellent agreement with the experimental value exhibiting deviations of only 45 (realistic SM), 134 (SN100PN), 5 (GCN50:82), and 24 keV (SN100-KTH). Additionally, the $23/2_1^+ \to 19/2_1^-$ transition is computed as $E_\gamma = 335$ keV (realistic SM), $E_\gamma = 348$ keV (SN100PN), $E_\gamma = 176$ keV (GCN50:82), and $E_\gamma = 429$ keV (SN100-KTH), compared to the observed 231-keV γ-ray transition in the experiment.

The level structure of the $+2p$ isotone ^{135}Ba is more intricate. A comparison of [Fig. 8(a)] experimental energy spectra of ^{135}Ba with the shell-model results of [Fig. 8(b)] realistic SM, [Fig. 8(c)] SN100PN, [Fig. 8(d)] GCN50:82, and [Fig. 8(e)] SN100-KTH calculations are presented in Fig. 8. Again, the states are separated into columns for negative- and positive-parity states. The $J^\pi = 3/2_1^+$ ground state is well reproduced by the realistic SM, GCN50:82 and SN100-KTH interactions. However, the SN100PN interaction locates the $J^\pi = 3/2_1^+$ state 3 keV above the $J^\pi = 11/2_1^-$ state. The other three interactions compute the $J^\pi = 11/2_1^-$ state ($E_x = 268$ keV) to have excitation energies of 274 (realistic SM), 297 (GCN50:82), and 79 keV (SN100-KTH). The interactions yield a good reproduction of the experimentally determined positive low-spin regime below 1 MeV excitation energy.

The interactions reproduce the $19/2_1^- \to 15/2_1^- \to 11/2_1^-$ cascade with γ-ray energies of 1052 and 682 keV very well. Deviations amount to 73 and 155 keV (Realistic SM), 105 and 16 keV (SN100PN), 43 and 26 keV (GCN50:82), as well as 37 and 54 keV (SN100-KTH). In the experiment the energy difference between the first and second excited $J^\pi = 19/2^-$ states is 131 keV, compared to the calculations of 123 (realistic SM), 139 (SN100PN), 128 (GCN50:82), and 243 keV (SN100-KTH). The calculated excitation energies for the first and second excited $J^\pi = 23/2^+$ states of 2320/3032 (realistic SM), 2007/2668 (SN100PN), 2252/3260 (GCN50:82), and 2138/3523 keV (SN100-KTH) are in good agreement with the experimentally determined $E_x = 2388/2985$ keV. Additionally, the $23/2_1^+ \to 19/2_2^-$ transition is computed as $E_\gamma = 126$ keV (realistic SM), $E_\gamma = 223$ keV (SN100PN), and $E_\gamma = 74$ keV (GCN50:82), compared to the observed 254-keV γ-ray transition in the experiment. Nonetheless, the SN100-KTH interaction is the only interaction, which computes the $J^\pi = 19/2_2^-$ state slightly above the $J^\pi = 23/2_1^+$ state.

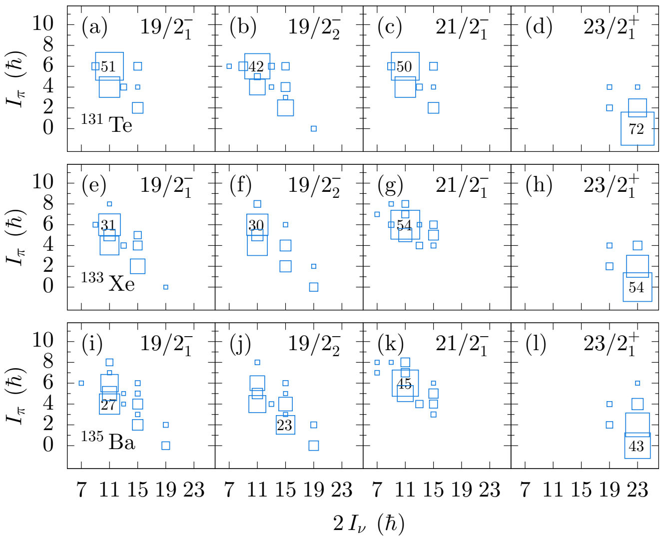

FIG. 9. Decomposition of the total angular momentum $I = I_\pi \otimes I_\nu$ into its proton and neutron components for the $J^\pi = 19/2_1^-$, $19/2_2^-$, $21/2_1^-$, and $23/2_1^-$ states in (a)–(d) ^{131}Te, (e)–(h) ^{133}Xe, and (i)–(l) ^{135}Ba calculated with the GCN50:82 interaction. Strongest components are labeled with corresponding percentages.

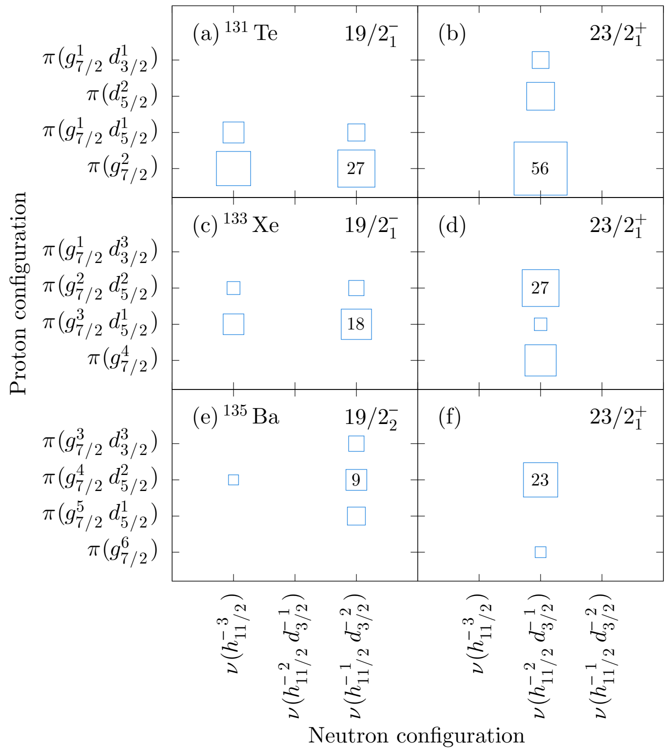

FIG. 10. Decomposition of the $J^\pi = 19/2^-$ and $23/2^+$ states of (a),(b) ^{131}Te, (c),(d) ^{133}Xe, and (e),(f) ^{135}Ba into their proton and neutron configurations computed by the GCN50:82 interaction. Strongest components are labeled with corresponding percentages.

The nuclear structures along the $N = 79$ isotones closely resemble each other. Figures 9(a)–9(l) show the decomposition of the total angular momentum $I = I_\pi \otimes I_\nu$ into its proton and neutron components for selected states using the GCN50:82 interaction. The decompositions are very similar to those computed by the SN100PN and SN100-KTH interactions. Although being more fragmented going from ^{131}Te to ^{135}Ba, the spin decompositions of the high-spin states above the $J^\pi = 11/2_1^-$ state are similar. In ^{131}Te and ^{133}Xe, the $J^\pi = 23/2_1^+$ state decays into the yrast $J^\pi = 19/2_1^-$ state, while in ^{135}Ba it decays into another yrare $J^\pi = 19/2^-$ state. Nevertheless, the spin decomposition of the first and second excited $J^\pi = 19/2^-$ states are almost identical.

The interaction predicts the $J^\pi = 23/2_1^+$ state to predominantly have (54% ^{133}Xe; 43% ^{135}Ba) $\nu\ 23/2^+ \otimes \pi\ 0^+$ and (32%; 37%) $\nu\ 23/2^+ \otimes \pi\ 2^+$ stretched neutron spin configurations. On the other hand, the $J^\pi = 19/2^-$ states in both ^{133}Xe and ^{135}Ba are mostly assigned to configurations with neutron spin $I_\nu = 11/2$ coupled to proton spins of $I_\pi = 4$ and $I_\pi = 6$. These configuration differences provide a microscopic reason of the long-lived $J^\pi = 23/2^+$ states; their decays require a considerable reordering of angular momentum for protons and neutrons, which strongly hinders a transition between both states.

The isomeric character is also scrutinized via a detailed decomposition of the $J^\pi = 19/2^-$, and $23/2^+$ states of the $N = 79$ isotones ^{131}Te, ^{133}Xe, and ^{135}Ba into their proton and neutron configurations computed by the GCN50:82 interaction, presented in Figs. 10(a)–10(f). The wave functions of the $J^\pi = 23/2_1^+$ states are dominated by the neutron $\nu(h_{11/2}^{-2}d_{3/2}^{-1})$ configuration with probabilities of 81.3% (^{131}Te), 60.3% (^{133}Xe), and 44.0% (^{135}Ba). Also the SN100PN and SN100-KTH calculations yield a dominant $\nu(h_{11/2}^{-2}d_{3/2}^{-1})$ neutron configuration.

In contrary, with GCN50:82, the leading neutron configurations of the final $J^\pi = 19/2^-$ state are $\nu h_{11/2}^{-3}$ and $\nu(h_{11/2}^{-1}d_{3/2}^{-2})$ contributing with probabilities of 31.4% and 34.3% in ^{131}Te, 13.7% and 24.8% in ^{133}Xe, as well as 4.9% and 20.3% in ^{135}Ba. The $\nu(h_{11/2}^{-2}d_{3/2}^{-1})$ configuration nearly vanishes in the decomposition of the $J^\pi = 19/2^-$ states. The dominant components of the $J^\pi = 19/2^-$ and $23/2^+$ states can be connected by a $M2$ transition operator, however, the hindrance of the $M2$ transition can be traced back mainly due to the change of the neutron content of the states.

Finally, reduced transition probabilities for the $23/2^+ \rightarrow 19/2^-$ transitions in ^{131}Te, ^{133}Xe and ^{135}Ba are calculated with the realistic SM, SN100PN, GCN50:82, and SN100-KTH interactions. Modified g factors of $g_l = g_{l_{\mathrm{free}}}$ and $g_s = 0.68 g_{s_{\mathrm{free}}}$ for protons and neutrons are used for the SN100PN, GCN50:82, and SN100-KTH interactions. The obtained quenching factor of 0.68 is tuned to reproduce the magnetic moments of the $J^\pi = 11/2_1^-$ states in ^{129}Sn ($\mu = -1.297(5)\mu_n$ [66]) and ^{131}Te ($\mu = -1.123(7)\mu_n$ [67]). In the realistic SM calculation nuclear g factors of $g_l = 1.2$, $g_s = 3.91$ for protons and $g_l = 0.2$, $g_s = -2.678$ for neutrons are employed.

The effective charges for protons and neutrons are selected to reproduce the $E2$ transition strengths of the first excited $J^\pi = 2^+$ state in the $Z = 50$ isotope ^{128}Sn ($B(E2; 2^+ \rightarrow 0^+) = 4.2(3)$ W.u. [68]) and of the $19/2^- \rightarrow 15/2^-$ decay ($B(E2; 19/2^- \rightarrow 15/2^-) = 2.56(14)$ W.u. [69]) in ^{133}Te using the SN100PN, GCN50:82, and SN100-KTH interactions.

TABLE II. Summary of experimental and theoretical results for $E2$, $M2$, and $E3$ reduced transition strengths of the $N = 79$ isotones ^{129}Sn, ^{131}Te, ^{133}Xe, and ^{135}Ba. Transition strengths are given in Weisskopf units. Experimental values of ^{129}Sn and ^{131}Te are taken from Refs. [1,4,6].

Isotope	$J_i^\pi \to J_f^\pi$	E_i (keV)	$T_{1/2}$ (ms)	$\sigma\lambda$	$B(\sigma\lambda)\downarrow$ (W.u.)				
					Experiment	Theory			
						Realistic SM	SN100PN	GCN50:82	SN100-KTH
^{129}Sn	$27/2_1^- \to 23/2_1^-$	2552	$0.27(7) \times 10^{-3}$	$E2$	0.79(36)	–	0.72	0.72	0.72
	$23/2_1^+ \to 19/2_1^+$	1802	$2.4(2) \times 10^{-3}$	$E2$	1.24(10)	–	1.45	0.71	1.44
	$19/2_1^+ \to 15/2_1^+$	1761	$3.6(2) \times 10^{-3}$	$E2$	1.37(8)	–	2.11	1.78	2.14
^{131}Te	$19/2_1^- \to 15/2_1^-$	1581	$71(20) \times 10^{-9}$	$E2$	3.5(10)	–	4.9	2.9	3.5
	$23/2_1^+ \to 19/2_1^-$	1941	93(12)	$M2$	$2.0(3) \times 10^{-6}$	–	404×10^{-6}	197×10^{-6}	305×10^{-6}
^{133}Xe	$23/2_1^+ \to 19/2_1^-$	2107	8.64(13)	$M2$	$0.209(3) \times 10^{-3}$	1.163×10^{-3}	1.613×10^{-3}	0.668×10^{-3}	1.691×10^{-3}
				$E3$	0.0017(16)	0.476	0.124	0.021	0.221
^{135}Ba	$23/2_1^+ \to 19/2_2^-$	2388	1.06(4)	$M2$	$1.053(40) \times 10^{-3}$	4.12×10^{-3}	2.440×10^{-3}	3.878×10^{-3}	2.283×10^{-3}
				$E3$	0.0012(11)	1.161	0.144	0.119	0.164

The adopted effective charges are $e_\nu = 0.81e$ and $e_\pi = 1.52e$. Selected values are in excellent agreement with the effective charges used in a recent study of the $N = 81$ isotonic chain [70] and the previous study of ^{136}Ba [71]. In the realistic SM calculation effective charges of $e_\nu = 0.7e$ and $e_\pi = 1.7e$ are used.

The newly established half-lives are converted into $M2$ and $E3$ reduced transition probabilities using the equations [72,73]:

$$B(M2) = \frac{5.12 \times 10^{-8}}{T_{1/2}E_\gamma^5}\frac{1}{1+\delta^2_{\frac{E3}{M2}}}\ \mu_N^2\mathrm{fm}^2 \tag{3}$$

and

$$B(E3) = \frac{1.21 \times 10^{-3}}{T_{1/2}E_\gamma^7}\frac{\delta^2_{\frac{E3}{M2}}}{1+\delta^2_{\frac{E3}{M2}}}\ e^2\mathrm{fm}^6, \tag{4}$$

where $T_{1/2}$, E_γ and $\delta_{\frac{E3}{M2}}$ correspond to the measured half-life of the initial state in seconds, the γ-ray energy in MeV and the multipole-mixing ratio of the γ ray. The experimentally deduced $B(\sigma\lambda)$ values and the results of the shell-model calculations are summarized in Table II.

To benchmark shell-model calculations, several previously known $B(E2)$ values of ^{129}Sn and ^{131}Te are added. The experimental $E2$ reduced transition strengths of the decay of the seniority $v = 3$ multiplet states $J^\pi = 19/2^+, 23/2^+$, and $27/2^-$ [1,4] in ^{129}Sn are well described within the three shell-model calculations. The discrepancy between the three calculations stays below 50% for the $B(E2; 23/2^+ \to 19/2^+)$ value in ^{129}Sn. Moreover, the calculated $B(E2)$ transition probability of the $19/2^- \to 15/2^-$ decay in ^{131}Te agrees well with the experiment.

Assuming a pure $M2$ transition, the experimental $B(M2; 23/2^+ \to 19/2^-)$ value of the $E_\gamma = 360$-keV transition in ^{131}Te is $2.0(3) \times 10^{-6}$ W.u. [2]. This value is overpredicted by at least two orders of magnitudes by the shell-model calculations. The single-particle Weisskopf estimate for the half-life of the $E_\gamma = 231$ keV transition in ^{133}Xe is 1.8 μs for an $M2$ and 32 ms for an $E3$ transition. In ^{135}Ba the half-life corresponding to one Weisskopf unit is 1.1 μs for an $M2$ and 16 ms for an $E3$ transition. Assuming a pure $M2$ transition, the Weisskopf hindrance factors of the $J^\pi = 23/2^+$ isomers are $F_W = T_{1/2}^{\mathrm{exp}}/T_{1/2}^{\mathrm{W}} = 4800$ in ^{133}Xe and $F_W = 964$ in ^{135}Ba, compared to values of $F_W = 0.27$ and $F_W = 0.066$ for pure $E3$ transitions, respectively.

The experimental $B(M2)$ and $B(E3)$ values of the $23/2_1^+ \to 19/2_1^-$ decay in ^{133}Xe are $209(3) \times 10^{-6}$ and $1.7(16) \times 10^{-3}$ W.u., respectively. Calculations with the four interactions yield $B(M2)$ values, which overpredict the experimental result by factors of 3.2–8.1. The measured $E3$ admixture of the 231-keV transition is predicted at least one to two orders of magnitude too high. Only the $B(E3)$ value computed by the GCN50:82 interaction is in reasonable agreement with the measured one.

The calculations for ^{135}Ba yield 2.2–3.9 times larger $M2$ transition strengths compared to the experimental $M2$ transition strength $B(M2; 23/2^+ \to 19/2^-) = 1.053(40) \times 10^{-3}$ W.u. Moreover, the transition strength to the first excited $J^\pi = 19/2^-$ state is computed to be 2.277×10^{-3}, 1.607×10^{-3}, and 2.627×10^{-3} W.u. by the GCN50:82, SN100-KTH, and SN100PN interactions, respectively. The $B(E3)$ value of the 254-keV transition is overestimated by two orders of magnitude.

The calculated $B(M2)$ values depend on the choice of proton and neutron g factors. Calculations employing $g_l(\pi) = 1.13$, $g_s(\pi) = 4.04$, $g_l(\nu) = 0.02$, and $g_s(\nu) = -2.65$, taking into account core polarization and meson-exchange currents [74,75], change the $B(M2; 23/2^+ \to 19/2^-)$ values slightly to 1.679×10^{-3} W.u (SN100PN), 0.693×10^{-3} W.u (GCN50:82), and 1.771×10^{-3} W.u (SN100-KTH) in ^{133}Xe and similar values of 2.559×10^{-3} W.u (SN100PN), 4.029×10^{-3} W.u (GCN50:82), and 2.406×10^{-3} W.u (SN100-KTH) in ^{135}Ba.

The fact that the $M2$ transition operator is mainly assigned to a change in neutron configuration (cf. Fig 10) is also reflected in the proton A_p and neutron A_n amplitudes which serve as weighting factors for the proton and neutron contribution to the $M2$ matrix elements. For the GCN50:82 interaction, the A_p and A_n amplitudes are 0.032 and 0.251 in ^{133}Xe and 0.057, 0.463 in ^{135}Ba, respectively.

The shell-model calculations support a dominating $M2$ character for the $23/2^+ \to 19/2^-$ transitions. Calculating the ratio $B(M2)/B(E3)$ by using Eqs. (3) and (4) and solving for $|\delta|$ yields multipole-mixing ratios of 0.230, 0.068 (realistic SM), 0.098, 0.055 (SN100PN), 0.032, 0.013 (GCN50:82), and 0.158, 0.003 (SN100-KTH) for ^{133}Xe and ^{135}Ba, respectively. The values derived from the shell-model results are very similar to the experimentally determined $|\delta|$ values of 0.021(10) and 0.009(4). Moreover, the results support the smaller $E3$ admixture in ^{135}Ba compared to ^{133}Xe.

V. CONCLUSIONS

In summary, a detailed study of isomeric $J = 23/2^+$ states was performed in ^{133}Xe and in ^{135}Ba. Their half-lives of $T_{1/2} = 8.64(13)$ ms in ^{133}Xe and $T_{1/2} = 1.06(4)$ ms in ^{135}Ba close a gap along the $N = 79$ isotones. Measurements of the multipole-mixing ratio and internal-conversion coefficient of the 231-keV transition in ^{133}Xe and the 254-keV transition in ^{135}Ba yield a dominant $M2$ character. The experimentally determined $B(M2)$ and $B(E3)$ transition strengths are compared to the results of large-scale shell-model calculations employing the realistic SM, GCN50:82, SN100PN, and SN100-KTH interactions. In particular, interactions with improved and corrected monopole parts, i.e., GCN50:82, show a good agreement with the experimental findings. A detailed inspection of the evolution of proton and neutron decompositions along the $N = 79$ chain provide insight into the changing nuclear structure. The neutron configuration $\nu(h^{-2}_{11/2}d^{-1}_{3/2})$ is responsible for the isomeric character of the $23/2^+$ states. The different shell-model calculations follow the measured $B(M2)$ systematics as function of proton filling in the $gdsh$ orbitals along the $N = 79$ isotones. In particular, the agreement between calculated and experimental $B(M2)$ values improves with increasing proton number.

However, the systematics of the $N = 79$ isotonic chain still lacks some information. In 2013 a recoil-decay tagging experiment reported on three feeding transitions decaying into the isomeric $J^\pi = (23/2^+)$ state at $E_x = 2616$ keV in ^{139}Nd [3]. So far, there are no states observed that populate the $J^\pi = 23/2^+$ isomers in ^{131}Te and ^{135}Ba. In future, a similar measurement in both nuclei is of high interest to resolve those feeding patterns. There is a large disagreement between shell-model theory and experiment for the transition strength of the $23/2^+_1 \to 19/2^-_1$ decay in ^{131}Te, motivating new refined experiments.

Furthermore, despite a detailed knowledge of the high-spin regime in ^{137}Ce, no $J^\pi = 23/2^+_1$ isomer was reported to date. The hitherto known $23/2^+$ state disrupts the isotonic systematics and is unlikely an isomer. However, the 2490-keV state, decaying into the $19/2^-_2$ state, is a possible candidate for the expected isomer [14]. Further experiments should be performed to elucidate a possible onset of $J^\pi = 23/2^+_1$ isomerism in ^{137}Ce.

ACKNOWLEDGMENTS

We thank the IKP FN Tandem accelerator team for the professional support during the experiment. The research leading to these results has received funding from the German BMBF under Contract No. 05P12PKFNE TP4, from the European Union Seventh Framework Programme FP7/2007-2013 under Grant Agreement No. 262010 - ENSAR, from the Spanish Ministerio de Ciencia e Innovación under contract FPA2011-29854-C04, from the Spanish Ministerio de Economía y Competitividad under Contract No. FPA2014-57196-C5, and from the U.K. Science and Technology Facilities Council (STFC). L.K. and A.V. thank the Bonn-Cologne Graduate School of Physics and Astronomy (BCGS) for financial support. One of the authors (A. Gadea) has been supported by the Generalitat Valenciana, Spain, under the grant PROMETEOII/2014/019 and EU under the FEDER program.

[1] J. Genevey, J. A. Pinston, C. Foin, M. Rejmund, H. Faust, and B. Weiss, High spin isomers in ^{129}Sn and ^{130}Sb, Phys. Rev. C **65**, 034322 (2002).

[2] A. Astier, M. G. Porquet, Ts. Venkova, Ch. Theisen, G. Duchêne, F. Azaiez, G. Barreau, D. Curien, I. Deloncle, O. Dorvaux, B. J. P. Gall, M. Houry, R. Lucas, N. Redon, M. Rousseau, and O. Stézowski, High-spin structures of $^{124-131}$Te: Competition of proton- and neutron-pair breakings, Eur. Phys. J. **50**, 1 (2014).

[3] A. Vancraeyenest, C. M. Petrache, D. Guinet, P. T. Greenlees, U. Jakobsson, R. Julin, S. Juutinen, S. Ketelhut, M. Leino, M. Nyman, P. Peura, P. Rahkila, P. Ruotsalainen, J. Saren, C. Scholey, J. Sorri, J. Uusitalo, P. Jones, C. Ducoin, P. Lautesse, C. Mancuso, N. Redon, O. Stezowski, P. Désesquelles, R. Leguillon, A. Korichi, T. Zerrouki, D. Curien, and A. Takashima, Identification of new transitions feeding the high-spin isomers in ^{139}Nd and ^{140}Nd nuclei, Phys. Rev. C **87**, 064303 (2013).

[4] R. L. Lozeva, G. S. Simpson, H. Grawe, G. Neyens, L. A. Atanasova, D. L. Balabanski, D. Bazzacco, F. Becker, P. Bednarczyk, G. Benzoni, N. Blasi, A. Blazhev, A. Bracco, C. Brandau, L. Cáceres, F. Camera, S. K. Chamoli, F. C. L. Crespi, J.-M. Daugas, P. Detistov, M. De Rydt, P. Doornenbal, C. Fahlander, E. Farnea, G. Georgiev, J. Gerl, K. A. Gladnishki, M. Górska, J. Grębosz, M. Hass, R. Hoischen, G. Ilie, M. Ionescu-Bujor, A. Iordachescu, J. Jolie, A. Jungclaus, M. Kmiecik, I. Kojouharov, N. Kurz, S. P. Lakshmi, G. Lo Bianco, S. Mallion, A. Maj, D. Montanari, O. Perru, M. Pfützner, S. Pietri, J. A. Pinston, Zs. Podolyák, W. Prokopowicz, D. Rudolph, G. Rusev, T. R. Saitoh, A. Saltarelli, H. Schaffner, R. Schwengner, S. Tashenov, K. Turzó, J. J. Valiente-Dobón, N. Vermeulen, J. Walker, E. Werner-Malento, O. Wieland, and H.-J. Wollersheim, New sub-μs isomers in ^{125,127,129}Sn and isomer systematics of $^{124\text{-}130}$Sn, Phys. Rev. C **77**, 064313 (2008).

[5] A. Vogt, M. Siciliano, B. Birkenbach, P. Reiter, K. Hadyńska-Klęk, C. Wheldon, J. J. Valiente-Dobón, E. Teruya, N. Yoshinaga, K. Arnswald, D. Bazzacco, A. Blazhev, A. Bracco, B. Bruyneel, R. S. Chakrawarthy, R. Chapman, D. Cline, L. Corradi, F. C. L. Crespi, M. Cromaz, G. de Angelis, J. Eberth, P. Fallon, E. Farnea, E. Fioretto, C. Fransen, S. J. Freeman, B. Fu, A. Gadea, W. Gelletly, A. Giaz, A. Görgen, A. Gottardo, A. B.

Hayes, H. Hess, R. Hetzenegger, R. Hirsch, H. Hua, P. R. John, J. Jolie, A. Jungclaus, V. Karayonchev, L. Kaya, W. Korten, I. Y. Lee, S. Leoni, X. Liang, S. Lunardi, A. O. Macchiavelli, R. Menegazzo, D. Mengoni, C. Michelagnoli, T. Mijatović, G. Montagnoli, D. Montanari, C. Müller-Gatermann, D. Napoli, C. J. Pearson, Zs. Podolyák, G. Pollarolo, A. Pullia, M. Queiser, F. Recchia, P. H. Regan, J.-M. Régis, N. Saed-Samii, E. Şahin, F. Scarlassara, M. Seidlitz, B. Siebeck, G. Sletten, J. F. Smith, P.-A. Söderström, A. M. Stefanini, O. Stezowski, S. Szilner, B. Szpak, R. Teng, C. Ur, D. D. Warner, K. Wolf, C. Y. Wu, and K. O. Zell, High-spin structures in ^{132}Xe and ^{133}Xe and evidence for isomers along the N = 79 isotones, Phys. Rev. C **96**, 024321 (2017).

[6] B. Fogelberg, H. Mach, H. Gausemel, J. P. Omtvedt, and K. A. Mezilev, New high spin isomers obtained in thermal fission, in *The Second International Workshop on Nuclear Fission and Fission-Product Spectroscopy*, edited by G. Fioni, H. Faust, S. Oberstedt, and F.-J. Hambsch, AIP Conf. Proc. No. 447 (AIP, New York, 1998), p. 191.

[7] M. Ferraton, R. Bourgain, C. M. Petrache, D. Verney, F. Ibrahim, N. de Séréville, S. Franchoo, M. Lebois, C. Phan Viet, L. Sagui, I. Stefan, J. F. Clavelin, and M. Vilmay, Lifetime measurement of the six-quasiparticle isomer in ^{140}Nd and evidence for an isomer above the $19/2^+$ state in ^{139}Nd, Eur. Phys. J. A **35**, 167 (2008).

[8] Evaluated Nuclear Structure Data File (ENSDF), http://www.nndc.bnl.gov/ensdf.

[9] J. A. Pinston, C. Foin, J. Genevey, R. Béraud, E. Chabanat, H. Faust, S. Oberstedt, and B. Weiss, Microsecond isomers in ^{125,127,129}Sn, Phys. Rev. C **61**, 024312 (2000).

[10] C. T. Zhang, P. Bhattacharyya, P. J. Daly, Z. W. Grabowski, R. H. Mayer, M. Sferrazza, R. Broda, B. Fornal, W. Królas, T. Pawlat, D. Bazzacco, S. Lunardi, C. Rossi Alvarez, and G. de Angelis, Yrast excitations in $A = 126-131$ Te nuclei from deep inelastic ^{130}Te+^{64}Ni reactions, Nucl. Phys. A **628**, 386 (1998).

[11] J. Ludziejewski and H. Arnold, High-spin levels in ^{137,139}Ce and ^{139,141}Nd evidence for hole-core coupling, Z. Phys. A **281**, 287 (1977).

[12] M. Müller-Veggian, Y. Gono, R. M. Lieder, A. Neskakis, and C. Mayer-Böricke, High-spin states and isomers in ^{136,137,138}Ce, Nucl. Phys. A **304**, 1 (1978).

[13] S. J. Zhu, L. Y. Zhu, M. Li, C. Y. Gan, M. Sakhaee, L. M. Yang, R. Q. Xu, Z. Zhang, Z. Jiang, G. L. Long, S. X. Wen, X. G. Wu, and X. A. Liu, High spin states and a collective oblate band in ^{137}Ce, Phys. Rev. C **62**, 044310 (2000).

[14] T. Bhattacharjee, S. Chanda, A. Mukherjee, S. Bhattacharyya, S. Kumar Basu, S. S. Ghugre, U. D. Pramanik, R. P. Singh, S. Muralithar, N. Madhavan, J. J. Das, and R. K. Bhowmik, Multi-quasiparticle bands in ^{137}Ce, Phys. Rev. C **78**, 024304 (2008).

[15] M. Müller-Veggian, H. Beuscher, D. R. Haenni, R. M. Lieder, A. Neskakis, and C. Mayer-Böricke, Investigation of high-spin states in ^{138,139}Nd, Nucl. Phys. A **344**, 89 (1980).

[16] M. A. Cardona, G. de Angelis, D. Bazzacco, M. De Poli, and S. Lunardi, High spin levels in ^{141}Sm, Z. Phys. A **340**, 345 (1991).

[17] M. Lach, P. Kleinheinz, J. Blomqvist, A. Ercan, H. J. Hähn, D. Wahner, R. Julin, M. Zupancic, F. Cigoroglu, and G. de Angelis, Shell model yrast states in the $N = 79$ nuclei ^{141}Sm and ^{143}Gd, Z. Phys. A **345**, 427 (1993).

[18] M. Sugawara, H. Kusakari, Y. Igari, K. Myojin, D. Nishimiya, S. Mitarai, M. Oshima, T. Hayakawa, M. Kidera, K. Furutaka, and Y. Hatsukawa, Dipole and quadrupole cascades in the yrast region of ^{143}Gd, Eur. Phys. J. A **1**, 123 (1998).

[19] R. M. Lieder, T. Rząca-Urban, H. J. Jensen, W. Gast, A. Georgiev, H.M. Jäger, E. van der Meer, Ch. Droste, T. Morek, D. Bazzacco, S. Lunardi, R. Menegazzo, C. M. Petrache, C. Rossi Alvarez, C. A. Ur, G. de Angelis, D. R. Napoli, Ts. Venkova, and R. Wyss, From highly to superdeformed shapes: Study of ^{143}Gd, Nucl. Phys. A **671**, 52 (2000).

[20] R. A. Meyer, F. F. Momyer, J. H. Landrum, E. A. Henry, R. P. Yaffe, and W. B. Walters, Levels of odd-mass Xe populated in the beta decay of ^{129}Cs, and ^{133}I, Phys. Rev. C **14**, 1152 (1976).

[21] Y. Khazov, A. Rodionov, and F. G. Kondev, Nuclear data sheets for $A = 133$, Nucl. Data Sheets **112**, 855 (2011).

[22] T. Lönnroth, J. Kumpulainen, and C. Tuokko, One- and three-quasiparticle states in ^{127,129,131,133}Xe and their coexistence with band structures, Phys. Scr. **27**, 228 (1983).

[23] R. G. Wille and R. W. Fink, Activation cross sections for 14.8-MeV neutrons and some new radioactive nuclides in the rare earth region, Phys. Rev. **118**, 242 (1960).

[24] X. L. Che, S. J. Zhu, M. L. Li, Y. J. Chen, Y. N. U, H. B. Ding, L. H. Zhu, X. G. Wu, G. S. Li, C. Y. He, and Y. Liu, High-spin levels based on the $11/2^-$ isomer in ^{135}Ba, Eur. Phys. J. A **30**, 347 (2006).

[25] W. T. Cluff, High-Spin Structure of ^{134,135}Ba and ^{120}Te, Ph.D. thesis, Florida State University, 2008.

[26] S. Kumar, A. K. Jain, Alpana Goel, S. S. Malik, R. Palit, H. C. Jain, I. Mazumdar, P. K. Joshi, Z. Naik, A. Dhal, T. Trivedi, I. Mehrotra, S. Appannababu, L. Chaturvedi, V. Kumar, R. Kumar, D. Negi, R. P. Singh, S. Muralithar, R. K. Bhowmik, and S. C. Pancholi, Band structure and shape coexistence in $^{135}_{56}$Ba$_{79}$, Phys. Rev. C **81**, 067304 (2010).

[27] S. Akkoyun *et al.*, AGATA – Advanced GAmma Tracking Array, Nucl. Instrum. Methods Phys. Res. A **668**, 26 (2012).

[28] A. M. Stefanini, L. Corradi, G. Maron, A. Pisent, M. Trotta, A. M. Vinodkumar, S. Beghini, G. Montagnoli, F. Scarlassara, G. F. Segato, A. De Rosa, G. Inglima, D. Pierroutsakou, M. Romoli, M. Sandoli, G. Pollarolo, and A. Latina, The heavy-ion magnetic spectrometer PRISMA, Nucl. Phys. A **701**, 217 (2002).

[29] L. Corradi, S. Szilner, G. Pollarolo, D. Montanari, E. Fioretto, A. M. Stefanini, J. J. Valiente-Dobón, E. Farnea, C. Michelagnoli, G. Montagnoli, F. Scarlassara, C. A. Ur, T. Mijatović, D. Jelavić Malenica, N. Soić, and F. Haas, Multinucleon transfer reactions: Present status and perspectives, Nucl. Instrum. Methods Phys. Res. B **317, Part B**, 743 (2013).

[30] S. Szilner, C. A. Ur, L. Corradi, N. Marginean, G. Pollarolo, A. M. Stefanini, S. Beghini, B. R. Behera, E. Fioretto, A. Gadea, B. Guiot, A. Latina, P. Mason, G. Montagnoli, F. Scarlassara, M. Trotta, G. de Angelis, F. Della Vedova, E. Farnea, F. Haas, S. Lenzi, S. Lunardi, R. Marginean, R. Menegazzo, D. R. Napoli, M. Nespolo, I. V. Pokrovsky, F. Recchia, M. Romoli, M.-D. Salsac, N. Soić, and J. J. Valiente-Dobón, Multinucleon transfer reactions in closed-shell nuclei, Phys. Rev. C **76**, 024604 (2007).

[31] L. Netterdon, V. Derya, J. Endres, C. Fransen, A. Hennig, J. Mayer, C. Müller-Gatermann, A. Sauerwein, P. Scholz, M. Spieker, and A. Zilges, The γ-ray spectrometer HORUS and its applications for nuclear astrophysics, Nucl. Instrum. Methods Phys. Res. A **754**, 94 (2014).

[32] A. Gadea, E. Farnea, J. J. Valiente-Dobón, B. Million, D. Mengoni, D. Bazzacco, F. Recchia, A. Dewald, Th. Pissulla,

W. Rother, G. de Angelis *et al.*, Conceptual design and infrastructure for the installation of the first AGATA sub-array at LNL, Nucl. Instrum. Methods Phys. Res. A **654**, 88 (2011).
[33] A. Wiens, H. Hess, B. Birkenbach, B. Bruyneel, J. Eberth, D. Lersch, G. Pascovici, P. Reiter, and H.-G. Thomas, The AGATA triple cluster detector, Nucl. Instrum. Methods Phys. Res. A **618**, 223 (2010).
[34] B. Bruyneel, B. Birkenbach, and P. Reiter, Pulse shape analysis and position determination in segmented HPGe detectors: The AGATA detector library, Eur. Phys. J. A **52**, 70 (2016).
[35] A. Lopez-Martens, K. Hauschild, A. Korichi, J. Roccaz, and J.-P. Thibaud, γ-ray tracking algorithms: a comparison, Nucl. Instrum. Methods Phys. Res. A **533**, 454 (2004).
[36] R. S. Kempley *et al.*, Cross Coincidences in the ^{136}Xe + ^{208}Pb deep-inelastic reaction, Acta Phys. Pol. B **42**, 717 (2011).
[37] M. Siciliano *et al.*, Neutron-rich nuclei in the vicinity of ^{208}Pb, LNL Annual Report 2014 **241**, 63 (2015), https://www.lnl.infn.it/~annrep/read_ar/2014/contributions/pdfs/063_B_127_B122.pdf.
[38] N. Saed-Samii, Lifetime measurements using the FATIMA array in combination with EXOGAM@ILL, Diplomarbeit, Universität zu Köln, 2013.
[39] I. Wiedenhöver, Computer code CORLEONE, 1997 (unpublished).
[40] I. Wiedenhöver, O. Vogel, H. Klein, A. Dewald, P. von Brentano, J. Gableske, R. Krücken, N. Nicolay, A. Gelberg, P. Petkov, A. Gizon, J. Gizon, D. Bazzaco, C. Rossi Alvarez, G. de Angelis, S. Lunardi, P. Pavan, D. R. Napoli, S. Frauendorf, F. Dönau, R. V. F. Janssens, and M. P. Carpenter, Detailed angular correlation analysis with 4π spectrometers: Spin determinations and multipolarity mixing measurements in ^{128}Ba, Phys. Rev. C **58**, 721 (1998).
[41] K. S. Krane and R. M. Steffen, Determination of the $E2/M1$ Multipole Mixing Ratios of the Gamma Transitions in ^{110}Cd, Phys. Rev. C **2**, 724 (1970).
[42] K. S. Krane, R. M. Steffen, and R.M. Wheeler, Directional correlations of gamma radiations emitted from nuclear states oriented by nuclear reactions or cryogenic methods, At. Data Nucl. Data Tables **11**, 351 (1973).
[43] O. Brandstädter, F. Girsig, F. Grass, and R. Klenk, Eine schnelle Transportautomatik zur Untersuchung kurzlebiger Kernzustände bis in den Millisekunden-Bereich, Nucl. Instrum. Meth. **104**, 45 (1972).
[44] W. G. Winn and D. D. Clark, Half-Life of Ba^{136m}, Bull. Am. Phys. Soc. **11**, 775 (1966).
[45] F. Ruddy and B. D. Pate, The decay of 0.3 sec Ba^{136m}, Nucl. Phys. **69**, 471 (1965).
[46] P. F. Fettweis and E. C. Campbell, Isomères nucléaires produits par les neutrons d'un réacteur, Nucl. Phys. **33**, 272 (1962).
[47] A. Hashizume, H. Kumagai, Y. Tendow, and T. Katou, A mechanical beam chopper system for the measurement of half-lives in the millisecond region, Nucl. Instrum. Meth. **119**, 209 (1974).
[48] H. F. Brinckmann, C. Heiser, and W. D. Fromm, Ein hochangeregter isomerer Kernzustand in ^{132}Xe, Nucl. Phys. A **96**, 318 (1967).
[49] H. R. Hiddleston and C. P. Browne, Nuclear data sheets for A = 132, Nucl. Data Sheets **17**, 225 (1976).
[50] A. G. Demin and Y. P. Kushakevich, New Isomers of Sc^{43}, In^{109}, and Xe^{125}, Sov. J. Nucl. Phys. **1**, 138 (1965).
[51] T. Kibédi, T.W. Burrows, M. B. Trzhaskovskaya, P. M. Davidson, and C. W. Nestor, Jr., Evaluation of theoretical conversion coefficients using BrIcc, Nucl. Instrum. Methods Phys. Res., Sect. A **589**, 202 (2008).
[52] S. Raman, A simple method for accurate measurements of total internal conversion coefficients, Nucl. Instrum. Methods **103**, 407 (1972).
[53] H. W. Taylor, B. Singh, and D. A. Viggars, Mixing parameters of gamma transitions in ^{214}Po, Phys. Rev. C **34**, 2322 (1986).
[54] K. Rezynkina, A. Lopez-Martens, and K. Hauschild, On the graphical extraction of multipole mixing ratios of nuclear transitions, Nucl. Instrum. Methods Phys. Res. A **844**, 96 (2017).
[55] B. A. Brown and W. D. M. Rae, The Shell-Model Code NuShellX@MSU, Nucl. Data Sheets **120**, 115 (2014).
[56] N. Shimizu, Nuclear shell-model code for massive parallel computation, "KSHELL", arXiv:1310.5431 [nucl-ph].
[57] E. Caurier, G. Martínez-Pinedo, F. Nowacki, A. Poves, and A. P. Zuker, The shell model as a unified view of nuclear structure, Rev. Mod. Phys. **77**, 427 (2005).
[58] L. Coraggio, A. Covello, A. Gargano, N. Itaco, and T.T.S. Kuo, Effective shell-model hamiltonians from realistic nucleon-nucleon potentials within a perturbative approach, Ann. Phys. (NY) **327**, 2125 (2012).
[59] L. Coraggio, A. Covello, A. Gargano, N. Itaco, and T. T. S. Kuo, Shell-model calculations and realistic effective interactions, Prog. Part. Nucl. Phys. **62**, 135 (2009).
[60] B. A. Brown, N. J. Stone, J. R. Stone, I. S. Towner, and M. Hjorth-Jensen, Magnetic moments of the 2_1^+ states around ^{132}Sn, Phys. Rev. C **71**, 044317 (2005).
[61] R. Machleidt, F. Sammarruca, and Y. Song, Nonlocal nature of the nuclear force and its impact on nuclear structure, Phys. Rev. C **53**, R1483 (1996).
[62] E. Caurier, F. Nowacki, A. Poves, and K. Sieja, Collectivity in the light xenon isotopes: A shell model study, Phys. Rev. C **82**, 064304 (2010).
[63] E. Caurier, F. Nowacki, and A. Poves, Shell Model description of the $\beta\beta$ decay of ^{136}Xe, Phys. Lett. B **711**, 62 (2012).
[64] C. Qi, Shell-model configuration-interaction description of quadrupole collectivity in Te isotopes, Phys. Rev. C **94**, 034310 (2016).
[65] C. Qi and Z. X. Xu, Monopole-optimized effective interaction for tin isotopes, Phys. Rev. C **86**, 044323 (2012).
[66] F. LeBlanc, L. Cabaret, E. Cottereau, J. E. Crawford, S. Essabaa, J. Genevey, R. Horn, G. Huber, J. Lassen, P. Lee, G. LeScornet, J. Lettry, J. Obert, J. Oms, A. Ouchrif, J. Pinard, H. Ravn, B. Roussiére, J. Sauvage, D. Verney, J. Pinard, L. Cabaret, G. Huber, R. Horn, J. Lassen, J. E. Crawford, J. K. P. Lee, J. Genevey, G. LeScornet, J. Lettry, and H. Ravn, Charge-radius change and nuclear moments in the heavy tin isotopes from laser spectroscopy: Charge radius of ^{132}Sn, Phys. Rev. C **72**, 034305 (2005).
[67] G. White, J. Rikovska, N. J. Stone, J. Copnell, I. S. Towner, A. M. Oros, K. Heyde, B. Fogelberg, L. Jacobsson, and F. Gustavsson, Magnetic dipole moments near ^{132}Sn: Measurement on isomeric $11/2^-$ states in odd-A ^{131}Te and ^{133}Te by NMR/ON, Nucl. Phys. A **640**, 322 (1998).
[68] J. M. Allmond, D. C. Radford, C. Baktash, J. C. Batchelder, A. Galindo-Uribarri, C. J. Gross, P. A. Hausladen, K. Lagergren, Y. Larochelle, E. Padilla-Rodal, and C.-H. Yu, Coulomb excitation of ^{124,126,128}Sn, Phys. Rev. C **84**, 061303 (2011).

[69] J. K. Hwang, A. V. Ramayya, J. H. Hamilton, D. Fong, C. J. Beyer, K. Li, P. M. Gore, E. F. Jones, Y. X. Luo, J. O. Rasmussen, S. J. Zhu, S. C. Wu, I. Y. Lee, M. A. Stoyer, J. D. Cole, G. M. Ter-Akopian, A. Daniel, and R. Donangelo, Half-life measurement of excited states in neutron-rich nuclei, Eur. Phys. J. A **25**, 463 (2005).

[70] A. Vogt, B. Birkenbach, P. Reiter, A. Blazhev, M. Siciliano, K. Hadyńska-Klęk, J. J. Valiente-Dobón, C. Wheldon, E. Teruya, N. Yoshinaga, K. Arnswald, D. Bazzacco, M. Bowry, A. Bracco, B. Bruyneel, R. S. Chakrawarthy, R. Chapman, D. Cline, L. Corradi, F. C. L Crespi, M. Cromaz, G. de Angelis, J. Eberth, P. Fallon, E. Farnea, E. Fioretto, S. J. Freeman, B. Fu, A. Gadea, K. Geibel, W. Gelletly, A. Gengelbach, A. Giaz, A. Görgen, A. Gottardo, A. B. Hayes, H. Hess, R. Hirsch, H. Hua, P. R. John, J. Jolie, A. Jungclaus, L. Kaya, W. Korten, I. Y. Lee, S. Leoni, L. Lewandowski, X. Liang, S. Lunardi, A. O. Macchiavelli, R. Menegazzo, D. Mengoni, C. Michelagnoli, T. Mijatović, G. Montagnoli, D. Montanari, C. Müller-Gatermann, D. Napoli, C. J. Pearson, L. Pellegri, Zs. Podolyák, G. Pollarolo, A. Pullia, M. Queiser, F. Radeck, F. Recchia, P. H. Regan, D. Rosiak, N. Saed-Samii, E. Şahin, F. Scarlassara, D. Schneiders, M. Seidlitz, B. Siebeck, G. Sletten, J. F. Smith, P.-A. Söderström, A. M. Stefanini, T. Steinbach, O. Stezowski, S. Szilner, B. Szpak, R. Teng, C. Ur, V. Vandone, D. D. Warner, A. Wiens, C. Y. Wu, and K. O. Zell, Isomers and high-spin structures in the $N = 81$ isotones ^{135}Xe and ^{137}Ba, Phys. Rev. C **95**, 024316 (2017).

[71] J. J. Valiente-Dobón, P. H. Regan, C. Wheldon, C. Y. Wu, N. Yoshinaga, K. Higashiyama, J. F. Smith, D. Cline, R. S. Chakrawarthy, R. Chapman, M. Cromaz, P. Fallon, S. J. Freeman, A. Görgen, W. Gelletly, A. Hayes, H. Hua, S. D. Langdown, I. Y. Lee, X. Liang, A. O. Macchiavelli, C. J. Pearson, Zs. Podolyák, G. Sletten, R. Teng, D. Ward, D. D. Warner, and A. D. Yamamoto, ^{136}Ba studied via deep-inelastic collisions: Identification of the $(\nu h_{11/2})^{-2}_{10+}$ isomer, Phys. Rev. C **69**, 024316 (2004).

[72] H. C. Pauli, K. Alder, and R. M. Steffen, The Electromagnetic Interaction in Nuclear Spectroscopy in *Advances in Electronics and Electron Physics*, edited by P. W. Hawkes (Academic Press, New York, 1975), chap. 2, p. 39.

[73] O. J. Roberts, C. R. Niţă, A. M. Bruce, N. Mărginean, D. Bucurescu, D. Deleanu, D. Filipescu, N. M. Florea, I. Gheorghe, D. Ghiţă, T. Glodariu, R. Lica, R. Mărginean, C. Mihai, A. Negret, T. Sava, L. Stroe, R. Şuvăilă, S. Toma, T. Alharbi, T. Alexander, S. Aydin, B. A. Brown, F. Browne, R. J. Carroll, K. Mulholland, Zs. Podolyák, P. H. Regan, J. F. Smith, M. Smolen, and C. M. Townsley, $E3$ and $M2$ transition strengths in $^{209}_{83}$Bi, Phys. Rev. C **93**, 014309 (2016).

[74] G. Jakob, N. Benczer-Koller, G. Kumbartzki, J. Holden, T. J. Mertzimekis, K.-H. Speidel, R. Ernst, A. E. Stuchbery, A. Pakou, P. Maier-Komor, A. Macchiavelli, M. McMahan, L. Phair, and I. Y. Lee, Evidence for proton excitations in ^{130,132,134,136}Xe isotopes from measurements of g factors of 2^+_1 and 4^+_1 states, Phys. Rev. C **65**, 024316 (2002).

[75] A. E. Stuchbery, Gyromagnetic ratios of excited states and nuclear structure near ^{132}Sn, in *XXXVI Brazilian Workshop on Nuclear Physics*, edited by M. H. Tabacniks, J. R. B. de Oliveira, and J. Marco, AIP. Conf. Proc. No. 1625 (AIP, New York, 2014), p. 52.

Addendum: Search for $23/2^+$ isomer in the $N = 79$ isotone ^{137}Ce

Millisecond $J^\pi = 23/2^+$ isomers at excitation energies around 2 to 2.5 MeV were systematically reported along $N = 79$ isotones. Typically, these isomers decay into first and second excited $J^\pi = 19/2^-$ states via dominant $M2$ γ-ray transition. Figure 9 shows the evolution of several negative-, and positive-parity states along the $N = 79$ chain, ranging from ^{129}Sn to ^{139}Nd. In addition, calculated excitation energies using the GCN50:82 and SN100PN interactions are shown in the figure. The $J^\pi = 23/2^+$ isomers in ^{133}Xe and ^{135}Ba are subject of the publication "*Millisecond* $23/2^+$ *isomers in the* $N = 79$ *isotones* ^{133}*Xe and* ^{135}*Ba*", presented in this thesis. Considering the results of this article, isomeric $J^\pi = 23/2^+$ states were reported in ^{129}Sn [29], ^{131}Te [30], ^{133}Xe [139], ^{135}Ba [139], and ^{139}Nd [140].

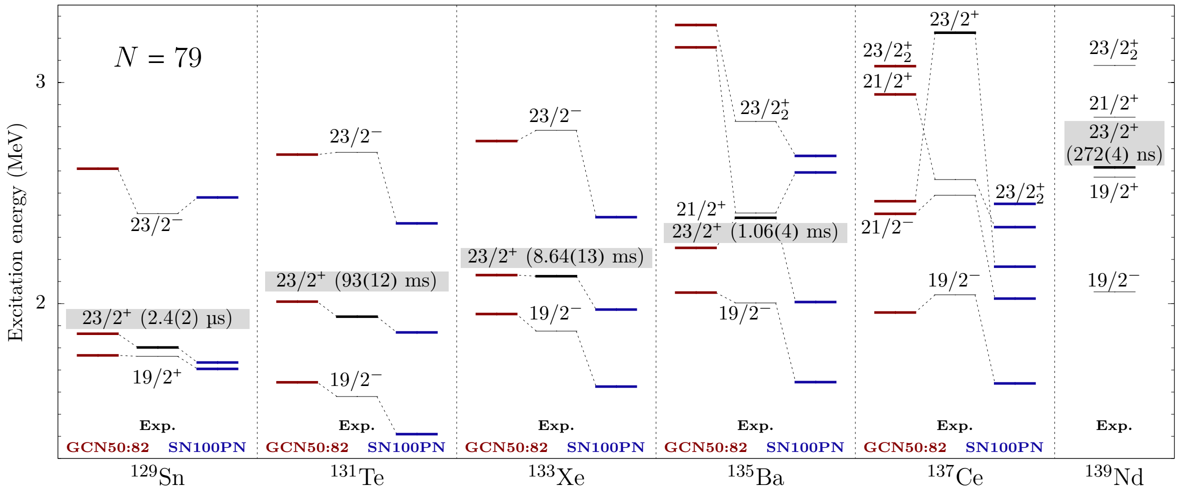

Figure 9: Evolution of excited states along the $N = 79$ chain. Nuclei are arranged in individual panels, separated by dashed vertical lines. Experimental level energies are shown in the mid column of each panel (black). Dashed lines connecting the experimental levels with calculated excitation energies using GCN50:82 (left column in red) and SN100PN (right column in blue) effective interactions. The $23/2^+$ states are isomeric in character except for ^{137}Ce. Half-life values are labeled next to the states.

Despite a detailed knowledge of the high-spin regime, the position of the $J^\pi = 23/2^+$ isomer in ^{137}Ce remains unsolved up to now. A partial level scheme of ^{137}Ce with the important transition used in the present analysis is given in Fig. 10(a). The main part of the nuclear-structure information comes from n, ^{3}He and ^{4}He induced experiments [141–143]. The high-spin level scheme of ^{137}Ce above the $J^\pi = 11/2^-$ isomer ($T_{1/2} = 34.4(3)$ h) at 254 keV [144] was extended up to highest spins via ^{18}O $+^{124}$ Sn [145] and ^{13}C $+^{130}$ Te [146] reactions. A first search for high-spin isomers in ^{137}Ce was based on a ^{4}He $+^{138}$ Ba reaction [147]. No evidence for a long-lived state was found in the off-beam range of 10-300 µs with respect to the beam pulse. Later, a $J = (31/2)$ state at 4255 keV was observed to be isomeric with a half-life of $T_{1/2} = 5(2)$ ns according to the time distribution of the depopulating 552-keV γ-ray [143]. The hitherto known $J^\pi = 23/2^+$ state in ^{137}Ce at $E_x = 3.2$ MeV

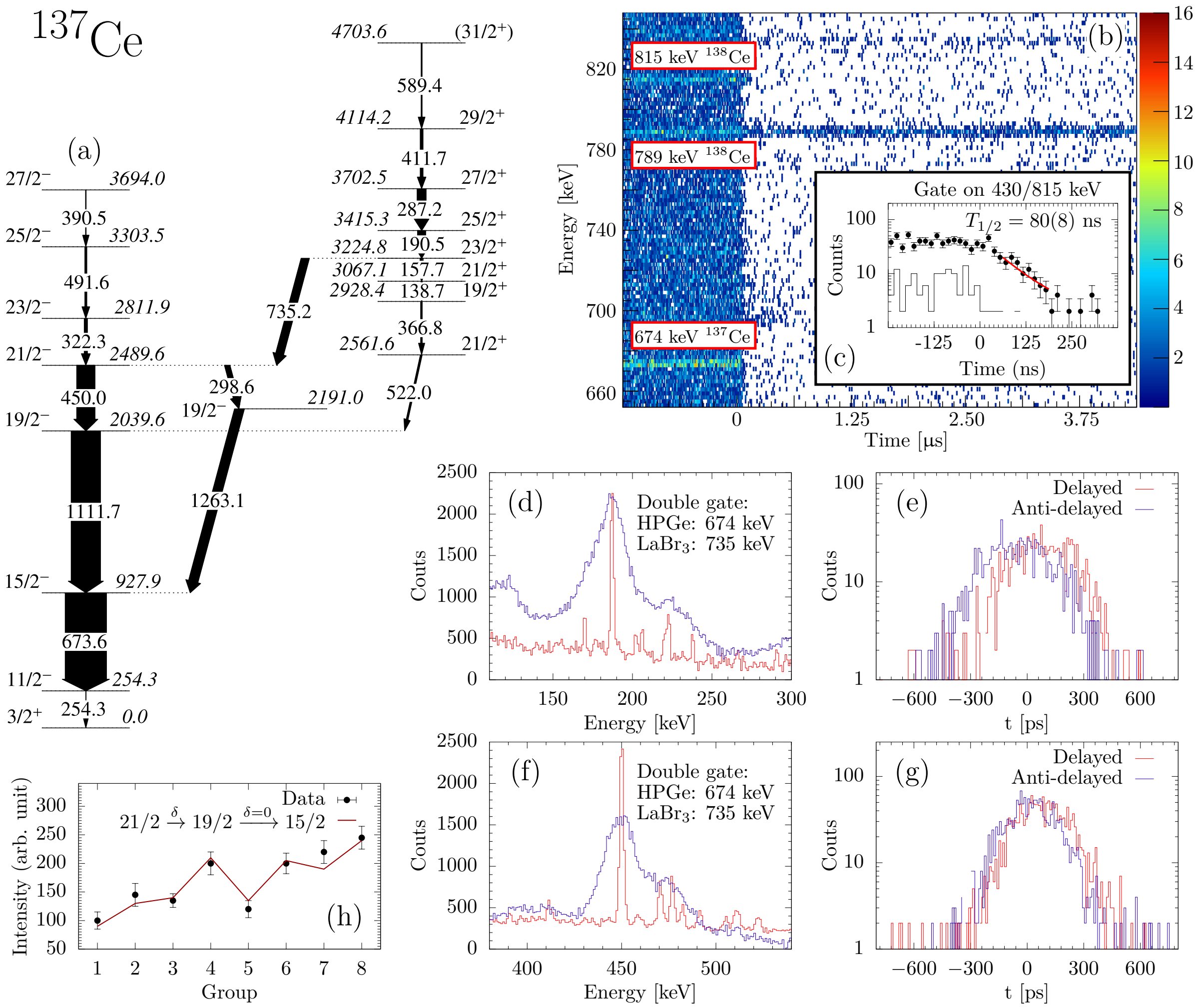

Figure 10: (a) Partial level schemes of ^{137}Ce. (b)-(c) γ-time matrix and summed time distribution of the 430 and 815-keV transitions in ^{138}Ce. (d) and (f) doubly-gated HPGe (red) and LaBr$_3$ (blue) spectra. (e) and (g) obtained delayed (blue) and anti-delayed (red) time distributions for the 3225-keV and 2490-keV states. (h) Angular-correlation distribution for the 450-1112-keV cascade.

does not follow the experimental isotonic systematics (see Fig. 9). In addition, both shell-model calculations predict a yrast $J^\pi = 23/2^+$ state well below 3 MeV excitation energy. Therefore, the discovery of $J^\pi = 23/2^+$ isomers between 2-2.5 MeV excitation energy and the results of shell-model calculations along the $N = 79$ chain suggest the existence of a $J^\pi = 23/2^+$ state considerably below $E_x = 3$ MeV in ^{137}Ce. A possible candidate for the $J^\pi = 23/2^+$ isomer might be anticipated at the 2490-keV state, previously assigned to spin 23/2 $\hbar$ and later revised to $J^\pi = 21/2^-$ [145, 146]. The state decays via a $E_\gamma \approx 300$-keV γ-ray transition toward the $J^\pi = 19/2^-_2$ state, followed by a higher-energy $E_\gamma \approx 1.3$-MeV γ-ray transition feeding the $J^\pi = 15/2^-$ state. The sequence of low- and high-energy transitions is similar to the decay cascade deexciting the $J^\pi = 23/2^+$ isomer in the $-2p$ isotone ^{135}Ba.

A possible onset of $J^{\pi} = 23/2^{+}$ isomerism along the $N = 79$ chain and the half-lives of the 2490-keV and 3225-keV states in ^{137}Ce were subject of two independent experiments at the Cologne 10 MV FN-Tandem accelerator. In the first experiment, ^{137}Ce was populated via a pulsed ^{12}C beam at 65 MeV beam energy impinging onto an enriched ^{130}Te target. The beam pulse had a width of 75 ms and a repetition rate of 3.33 Hz. γ rays were measured using the HORUS array [148] consisting of 14 high-purity germanium (hereafter called HPGe) detectors. Figure 10(b) shows the recorded γ-time matrix with respect to the end of the beam pulse. In the matrix, a distinct separation between the in-beam and off-beam γ-ray spectra is visible. A delayed 789-keV transition deexciting the $J^{\pi} = 7^{-}$ isomer ($T_{1/2}$ = 8.7(2) ms [2]) in ^{138}Ce is observed. Moreover, a delayed 430-815-keV cascade, originating from the decay of the $J^{\pi} = 10^{+}$ isomer ($T_{1/2}$ = 81(2) ns [2]) in ^{138}Ce, emerges well above the background. The inset Fig. 10(c) shows the gated and summed time distribution of the 430-, and 815-keV transitions. An exponential fit of the slope component yields a half-life of 80(8) ns, which is in good agreement with the evaluated value, validating the experimental procedure up to the lower nanosecond regime. However, no delayed transitions from ^{137}Ce were observed in this experiment. In accordance with the measured time resolution of the setup, a half-life of $T_{1/2} \leq 50$ ns is suggested for a possible $J^{\pi} = 23/2^{+}$ isomer in ^{137}Ce.

A second experiment utilizing the electronic fast-timing technique was performed in order to measure lower nano-, and picosecond half-lives. The HORUS array was equipped with eight HPGe detectors and twelve cerium-doped lanthanum-bromide (hereafter called $LaBr_3$) scintillation detectors. Six of the $LaBr_3$ detectors were surrounded by bismuth-germanate (BGO) veto detectors to suppress the Compton background [149]. Time-to-amplitude (TAC) converters were used to measure the time difference between two γ rays, detected in two $LaBr_3$ detectors in HPGe-gated triple-coincidence spectra. Half-lives smaller than the FWHM of the Gaussian prompt response function (PRF) were measured with the generalized centroid difference (GCD) method [150, 151]. The energy dependency of the PRF was determined by a ^{152}Eu source measurement. The analysis procedures for the determination of the half-lives of the 2490-keV and the 3225-keV states are shown in Figs. 10(d)-(g). To illustrate that the transitions of interest are not contaminated by other transitions, doubly-gated spectra are presented in Figs. 10(d) and (f). In both spectra, a HPGe gate on the 674-keV transition and a $LaBr_3$ gate on the 735-keV transition were applied. The gates ensure that the 191-keV (Fig. 10(d)) and the 450-keV (Fig. 10(f)) transitions are well separated from other lines in the $LaBr_3$ spectrum. The delayed and anti-delayed time spectra are generated, using 15-keV wide gates set on the full energy peaks of the doubly-gated $LaBr_3$ spectra (see Figs. 10(e) and (g)). After correcting the centroid difference for background timing response, half-lives of 90(7) ps for the 3225-keV state (Fig. 10(e)) and 38(10) ps for the 2490-keV state (Fig. 10(g)) were obtained. Accordingly, an isomeric $J^{\pi} = 23/2^{+}$ state can be excluded for these states. Moreover, a spin hypothesis of $21/2^{-} \rightarrow 19/2^{-} \rightarrow 15/2^{-}$ for the 450-1112-keV cascade yields an excellent agreement with the experimental angular-correlation distribution, shown in Fig. 10(h).

Publication III: Identification of high-spin proton configurations in ^{136}Ba and ^{137}Ba

Identification of high-spin proton configurations in ^{136}Ba and ^{137}Ba

L. Kaya,[1,*] A. Vogt,[1] P. Reiter,[1] C. Müller-Gatermann,[1] A. Gargano,[2] L. Coraggio,[2] N. Itaco,[2,3] A. Blazhev,[1] K. Arnswald,[1] D. Bazzacco,[4] B. Birkenbach,[1] A. Bracco,[5] B. Bruyneel,[6] L. Corradi,[7] F. C. L. Crespi,[5] G. de Angelis,[7] M. Droste,[1] J. Eberth,[1] E. Farnea,[4,†] E. Fioretto,[7] C. Fransen,[1] A. Gadea,[8] A. Giaz,[5] A. Görgen,[9,10,11] A. Gottardo,[7] K. Hadyńska-Klęk,[7] H. Hess,[1] R. Hetzenegger,[1] R. Hirsch,[1] P. R. John,[12] J. Jolie,[1] A. Jungclaus,[13] W. Korten,[10] S. Leoni,[5] L. Lewandowski,[1] S. Lunardi,[14,4] R. Menegazzo,[4] D. Mengoni,[14,4] C. Michelagnoli,[15] T. Mijatović,[16] G. Montagnoli,[14,4] D. Montanari,[17] D. Napoli,[7] Zs. Podolyák,[18] G. Pollarolo,[19] F. Recchia,[14,4] D. Rosiak,[1] N. Saed-Samii,[1] E. Şahin,[9] M. Siciliano,[14,7] F. Scarlassara,[14,4] M. Seidlitz,[1] P.-A. Söderström,[20] A. M. Stefanini,[7] O. Stezowski,[21] S. Szilner,[16] B. Szpak,[22] C. Ur,[4] J. J. Valiente-Dobón,[7] M. Weinert,[1] K. Wolf,[1] and K. O. Zell[1]

[1] *Institut für Kernphysik, Universität zu Köln, D-50937 Köln, Germany*
[2] *Istituto Nazionale di Fisica Nucleare, Sezione di Napoli, I-80126 Napoli, Italy*
[3] *Dipartimento di Matematica e Fisica, Università degli Studi della Campania "Luigi Vanvitelli", viale A. Lincoln 5, I-8110 Caserta, Italy*
[4] *Istituto Nazionale di Fisica Nucleare, Sezione di Padova, I-35131 Padova, Italy*
[5] *Dipartimento di Fisica, Università di Milano and INFN Sezione di Milano, I-20133 Milano, Italy*
[6] *CEA Saclay, Service de Physique Nucleaire, F-91191 Gif-sur-Yvette, France*
[7] *Istituto Nazionale di Fisica Nucleare, Laboratori Nazionali di Legnaro, I-35020 Legnaro, Italy*
[8] *Instituto de Física Corpuscular, CSIC-Universidad de Valencia, E-46071 Valencia, Spain*
[9] *Department of Physics, University of Oslo, P. O. Box 1048 Blindern, N-0316 Oslo, Norway*
[10] *Institut de Recherche sur les lois Fondamentales de l'Univers – IRFU, CEA/DSM, Centre CEA de Saclay, F-91191 Gif-sur-Yvette Cedex, France*
[11] *Lawrence Berkeley National Laboratory, Berkeley, California 94720, USA*
[12] *Institut für Kernphysik, Technische Universität Darmstadt, D-64289 Darmstadt, Germany*
[13] *Instituto de Estructura de la Materia, CSIC, Madrid, E-28006 Madrid, Spain*
[14] *Dipartimento di Fisica e Astronomia, Università di Padova, I-35131 Padova, Italy*
[15] *Institut Laue-Langevin (ILL), 38042 Grenoble Cedex 9, France*
[16] *Ruđer Bošković Institute, HR-10 002 Zagreb, Croatia*
[17] *USIAS - Universite de Strasbourg, IPHC-CNRS, F-67037 Strasbourg Cedex 2, France*
[18] *Department of Physics, University of Surrey, Guildford, Surrey GU2 7XH, United Kingdom*
[19] *Dipartimento di Fisica Teorica dell'Università di Torino and INFN, I-10125 Torino, Italy*
[20] *Extreme Light Infrastructure-Nuclear Physics (ELI-NP), 077125 Bucharest-Magurele, Romania*
[21] *Université de Lyon, Université Lyon-1, CNRS/IN2P3, UMR5822, IPNL, F-69622 Villeurbanne Cedex, France*
[22] *Henryk Niewodniczański Institute of Nuclear Physics PAN, PL-31342 Kraków, Poland*

(Received 30 October 2018; published 2 January 2019)

The high-spin structures of ^{136}Ba and ^{137}Ba are investigated after multinucleon-transfer (MNT) and fusion-evaporation reactions. ^{136}Ba is populated in a $^{136}\mathrm{Xe} + {}^{238}\mathrm{U}$ MNT reaction employing the high-resolution Advanced GAmma Tracking Array (AGATA) coupled to the magnetic spectrometer PRISMA at the Laboratori Nazionali di Legnaro, Italy, and in two $^{9}\mathrm{Be} + {}^{130}\mathrm{Te}$ fusion-evaporation reactions using the High-efficiency Observatory for γ-Ray Unique Spectroscopy (HORUS) at the FN tandem accelerator of the University of Cologne, Germany. Furthermore, both isotopes are populated in an elusive reaction channel in the $^{11}\mathrm{B} + {}^{130}\mathrm{Te}$ fusion-evaporation reaction utilizing the HORUS γ-ray array. The level scheme above the $J^{\pi} = 10^{+}$ isomer in ^{136}Ba is revised and extended up to an excitation energy of approximately 5.5 MeV. From the results of angular-correlation measurements, the $E_x = 3707$- and $E_x = 4920$-keV states are identified as the bandheads of positive- and negative-parity cascades. While the high-spin regimes of both ^{132}Te and ^{134}Xe are characterized by high-energy $12^{+} \rightarrow 10^{+}$ transitions, the ^{136}Ba $E2$ ground-state band is interrupted by negative-parity states only a few hundred keV above the $J^{\pi} = 10^{+}$ isomer. Furthermore, spins are established for several hitherto unassigned high-spin states in ^{137}Ba. The new results close a gap along the high-spin structure of $N < 82$ Ba isotopes. Experimental results are compared to large-scale shell-model calculations employing the GCN50:82,

*Corresponding author: levent.kaya@ikp.uni-koeln.de
†Deceased.

Realistic SM, PQM130, and SN100PN interactions. The calculations suggest that the bandheads of the positive-parity bands in both isotopes are predominantly of proton character.

DOI: 10.1103/PhysRevC.99.014301

I. INTRODUCTION

The $50 \leqslant Z,\ N \leqslant 82$ nuclei outside the doubly magic nucleus ^{132}Sn are described within the valence space made up by the orbitals $0g_{7/2}$, $1d_{5/2}$, $1d_{3/2}$, $2s_{1/2}$, and $0h_{11/2}$. $A \approx 135$ nuclei near the $N = 82$ shell closure have the Fermi surface in the middle of the proton $d_{5/2}$-$g_{7/2}$ subshell between $Z = 50$ and $Z = 64$ and offer a fertile region to deepen the understanding of the single-particle structure in the framework of the nuclear shell model and to study the evolution of different multiquasiparticle configurations formed by a combined contribution of neutron holes and proton particles.

This work focuses on the high-spin structures of ^{136}Ba and ^{137}Ba with one and two valence neutron holes outside the $N = 82$ closed shell. Isomeric yrast $J^\pi = 10^+$ states accumulate in moderately neutron-rich Xe and Ba isotopes, as well as throughout the $N = 78$, $N = 80$, and $N = 82$ isotones above the $Z = 50$ shell closure. Along the $N = 80$ isotones, between ^{130}Sn and ^{142}Sm, these isomers are predominantly of $\nu h_{11/2}^{-2}$ character and seniority $\upsilon = 2$ [1–6]. The single-particle excitation energy of the $\nu h_{11/2}$ neutron orbital is observed to increase with proton number. This increase in single-particle energy is responsible for an increase of more than 1 MeV in the excitation energy of the yrast $J^\pi = 10^+$ state between ^{130}Sn and ^{140}Nd. From the proton $Z = 64$ subshell closure at ^{144}Gd onwards, $J^\pi = 10^+$ isomers are proposed to have two-proton $\pi h_{11/2}^2$ configurations [6,7]. A compilation of high-spin level schemes above the isomeric $J^\pi = 10^+$ states along $N = 80$ is presented in Fig. 1(a).

The $10^+ \rightarrow 8^+$ isomeric transitions of ^{132}Te and ^{134}Xe have low energies of 22 and 28 keV, respectively [2]. High-spin states in the $N = 80$ isotone ^{132}Te were investigated up to spin $J^\pi = (17^+)$ with an excitation energy of 6.17 MeV [8]. The states along the $(16^+) \rightarrow (15^+) \rightarrow (14^+) \rightarrow (12^+) \rightarrow (10^+)$ cascade above the $J^\pi = 10^+$ isomer are predominantly of $\nu h_{11/2}^{-2}$ character. In ^{134}Xe, the high-spin structure above the isomeric $J^\pi = 10^+$ is known up to spin $J^\pi = (16^+)$ at 5.83 MeV. The high-spin yrast sequence is similar to ^{132}Te, despite an additional tentatively assigned $J^\pi = 13^+$ state between the $J^\pi = 12^+$ and 14^+ levels [9]. States of higher spins built on the $J^\pi = 10^+$ isomers involve the rearrangement of the valence protons since the configuration of the neutrons is already constrained. Therefore, both ^{132}Te and ^{134}Xe are characterized by high-energy $12^+ \rightarrow 10^+$ transitions of 900 and 1323 keV, respectively.

Pioneering work on ^{136}Ba focused on low-spin states up to the $J^\pi = 8^+$ state at $E_x = 2994$ keV, investigated via Coulomb excitation [10], β-decay [11], (n, γ) reactions [12], and ^{9}Be-induced fusion-evaporation reactions [13]. The $J^\pi = 10^+$ state at $E_x = 3357$ keV with a $\nu h_{11/2}^{-2}$ configuration was simultaneously discovered by Shizuma *et al.* [14] employing a ^{82}Se + ^{139}La deep-inelastic reaction at 450 MeV and by Valiente-Dobón *et al.* [3] who populated ^{136}Ba in a ^{136}Xe + ^{198}Pt multinucleon-transfer reaction at a beam energy of 850 MeV. The groups reported half-lives of $T_{1/2} = 94(10)$ ns [14] and $T_{1/2} = 91(2)$ ns [3]. Valiente-Dobón *et al.* employed prompt-delayed correlations to identify seven γ-ray transitions feeding the $J^\pi = 10^+$ state and established a tentative high-spin structure. Contrary to ^{132}Te and ^{134}Xe, the next excited state is located only 349 keV above the 3357-keV isomeric state. According to shell-model calculations and systematics, it was assumed that the excitation pattern above the $J^\pi = 10^+$ state does not correspond to an $E2$ yrast sequence. Instead, a $J^\pi = 10^-$, 11^-, or 12^- assignment was suggested for the $E_x = 3707$-keV state. However, angular-correlation measurements were not in the scope of the experiment [3].

Approaching the proton subshell closure, elaborate high-spin information from heavy-ion fusion-evaporation reactions are available for both ^{138}Ce and ^{140}Nd [15,16]. Measurements of the $J^\pi = 10_1^+$ isomer's g factors in both nuclei corroborated $\nu h_{11/2}^{-2}$ neutron-hole configurations [5]. In ^{138}Ce the $E2$ yrast sequence is interrupted by an intermediate $J^\pi = 11^+$ state, connecting $J = 12$ states of positive and negative parity with the 82(2)-ns $J^\pi = 10^+$ isomer. Going to higher spins, the level structure is significantly fragmented into several band structures dominated by different quasiparticle configurations [15].

The high-spin regime of ^{140}Nd is even more fragmented and explained by different two-neutron and two-proton excitations [16–18]. The 33(2)-ns $J^\pi = 10_1^+$ isomer decays via negative-parity states to the 0.6-ms $J^\pi = 7_1^-$ state. It is directly fed by $J^\pi = 11^-$ and $J^\pi = 10^-$ states [18]. A second $J^\pi = 10^+$ state was identified at 4155 keV, fed by positive-parity states [16]. Furthermore, ^{140}Nd exhibits a six-quasiparticle $J^\pi = 20^+$ isomer with a half-life of $T_{1/2} = 1.23(7)\,\mu$s at 7430 keV [19].

Similar to the $J^\pi = 10^+$ isomers along $N = 80$, $J^\pi = 19/2^-$ isomers are a common feature of nuclei along $N = 81$ [4,20,21]. A compilation of several partial level schemes above the $J^\pi = 19/2^-$ isomers is shown in Fig. 1(b).

The level scheme of ^{133}Te is known up to 6.2 MeV with tentative spin assignments up to $J^\pi = (31/2^-)$ [24,25]. A $J^\pi = (19/2^-)$ state at 1.610 MeV is found to be isomeric with an adopted half-life of $T_{1/2} = 100(5)$ ns [26]. In ^{135}Xe the high-spin regime is investigated up to 4.07 MeV, however, no spin and parities are known beyond the $J^\pi = 19/2^-$ state which is identified as an isomer with a half-life of $T_{1/2} = 9.0(9)$ ns [20].

Pioneering studies of ^{137}Ba mainly focused on low- and medium-spin states. Data were obtained utilizing β decay [27,28], neutron-induced reactions [29], and Coulomb excitation [30]. The spins, parities, and half-lives of the ground state and the $J^\pi = 11/2^-$ isomer at 661.659(3) keV with a half-life of 2.552(1) min are well established. First results on medium-spin states of ^{137}Ba were obtained by Kerek *et al.*

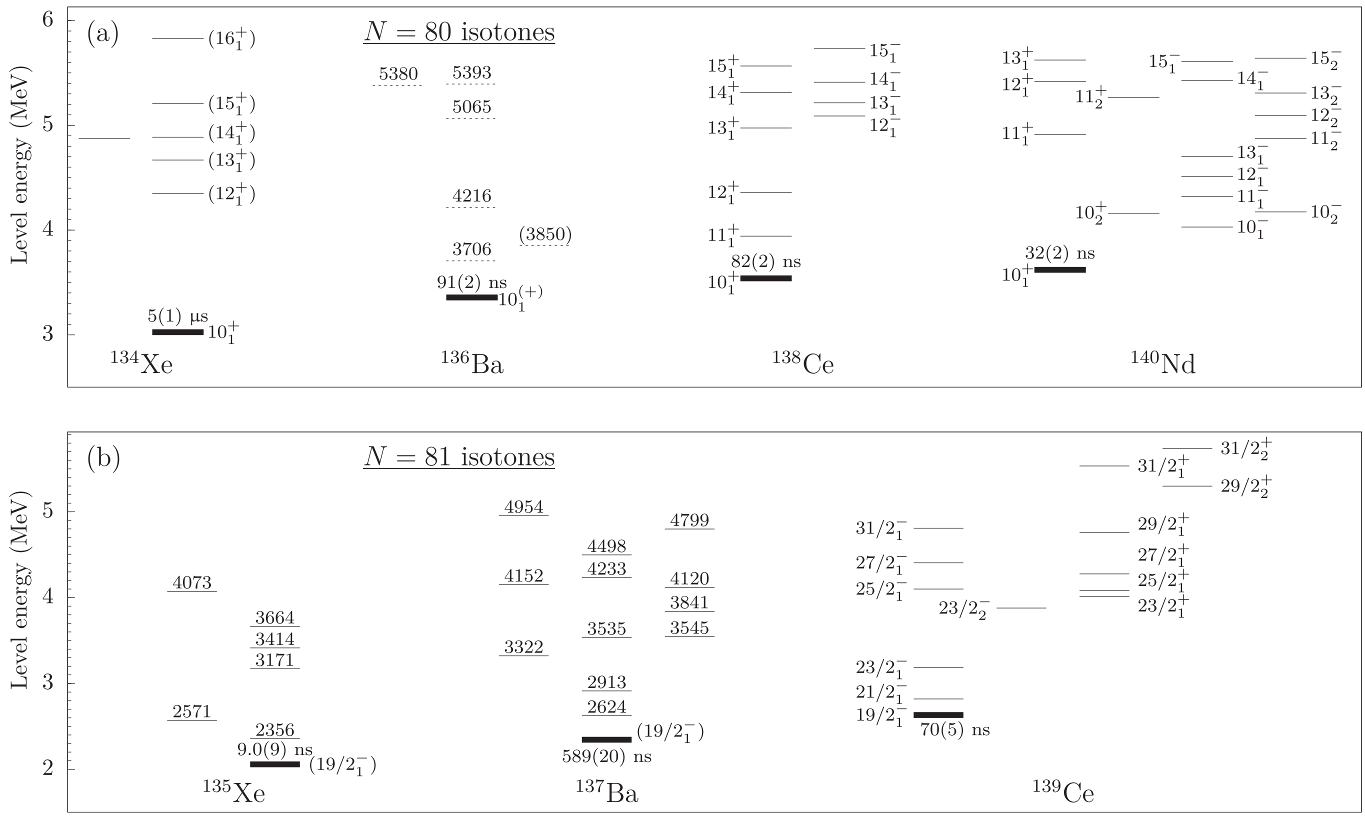

FIG. 1. Comparison of high-spin states above (a) the $J^\pi = 10_1^+$ isomers along $N = 80$ and (b) above the $J^\pi = 19/2_1^-$ isomers along $N = 81$. There is a significant lack of information on spin assignments in ^{136}Ba and ^{137}Ba. Data taken from Refs. [3,9,15,16,18,20–23].

in 1973 [21], via an α-induced reaction on a ^{136}Xe-enriched gas target. An isomeric state at $E_x = 2350$ keV with possible spin assignments $J^\pi = (15/2, 17/2, 19/2)$ and a half-life of $T_{1/2} = 590(100)$ ns was observed. This state was found to decay via a 120-1568-keV γ-ray cascade, finally populating the long-lived $J^\pi = 11/2_1^-$ isomer. The authors of the present work studied ^{137}Ba as a multinucleon-transfer and fusion-evaporation product using the Advanced Gamma-ray Tracking Array (AGATA) + PRISMA setup at LNL Legnaro, the GAMMASPHERE array at Lawrence Berkeley National Laboratory and the HORUS array at Cologne [20]. The level scheme was extended up to approximately 5 MeV excitation energy. Spin and parity assignments of high-spin states were not subjects of the work [20].

In ^{139}Ce the yrast negative-parity band based on the $J^\pi = 19/2^-$ isomer is well established up to an excitation energy of approximately 8 MeV [31,32]. A band on top of a $J^\pi = 19/2^-$ isomer was initially proposed to be of negative parity [31,32]. Recently, this structure was revised to be a positive-parity cascade built on top of a $J^\pi = 23/2^+$ bandhead decaying into the $J^\pi = 19/2^-$ isomer [23].

Adding two more protons, a plethora of high-spin bands were discovered in ^{141}Nd [33,34]. In an earlier experiment [4], delayed time distributions indicated a possible $J = 19/2^-$ isomeric state with $T_{1/2} = 26(5)$ ns at an energy of $2886 + x$ keV. However, this isomer was not confirmed by subsequent studies [33,34]. Moreover, no evidence of a positive-parity band connected to the $J^\pi = 19/2^-$ isomer was found to date. Thus, the typical features of $J^\pi = 19/2^-$ isomers and the associated feeding high-spin structures along $N = 81$ could be first discontinued in ^{141}Nd.

Along the $N = 80$ and $N = 81$ isotones, spin and parity assignments are missing inter alia for ^{136}Ba and ^{137}Ba. Available information is limited to in part tentative excitation energies. The aim of the present work is to complement these earlier studies with spin and parity assignments of the high-spin states. The systematics along the $N = 80$ chain suggest that the yrast $E2\ 12^+ \rightarrow 10^+$ cascades are first interrupted in ^{136}Ba accompanied by a change in nuclear structure. This motivates a refined investigation of the high-spin features above the isomeric $J^\pi = 10^+$ state in ^{136}Ba and above the isomeric $J^\pi = 19/2^-$ state in ^{137}Ba.

In this paper new results on ^{136}Ba and ^{137}Ba are presented. ^{136}Ba was populated in a ^{136}Xe + ^{238}U multinucleon-transfer (MNT) experiment employing the AGATA γ-ray spectrometer [35] in combination with the magnetic mass spectrometer PRISMA [36–38]. Moreover, ^{136}Ba is investigated in two ^{9}Be + ^{130}Te and one ^{11}B + ^{130}Te fusion-evaporation experiment employing two different configurations of the High-efficiency Observatory for γ-Ray Unique Spectroscopy (HORUS) [39] at the Institute of Nuclear Physics, University of Cologne. ^{137}Ba was populated in the ^{11}B + ^{130}Te fusion-evaporation experiment. The HORUS experiments provide detailed information on $\gamma\gamma$ coincidences and angular correlations.

This paper is organized as follows: the experimental setup and data analysis of the experiments are described in Sec. II, followed by the experimental results in Sec. III. A comparison with large-scale shell-model calculations is presented in Sec. IV before the paper is completed with a summary and conclusions.

II. EXPERIMENTAL PROCEDURE

A. ^{136}Xe + ^{238}U multinucleon transfer

In this experiment, ^{136}Ba was populated in a ^{136}Xe + ^{238}U multinucleon-transfer experiment at the Laboratori Nazionali di Legnaro, Italy. The 6.84 MeV/nucleon ^{136}Xe beam, accelerated by the PIAVE+ALPI accelerator complex, impinged onto a 1- and a 2-mg/cm^2 ^{238}U target. An isotopic identification of the nuclei of interest was provided by the magnetic spectrometer PRISMA placed at the reaction's grazing angle of $\theta_{\mathrm{lab}} = 50^\circ$. γ rays from excited states in both beam- and targetlike nuclei were detected with the AGATA γ-ray spectrometer [35] in the demonstrator configuration [40] placed 23.5 cm from the target position. The array consisted of 15 large-volume electronically segmented high-purity Ge (HPGe) detectors in five triple cryostats [41]. An event registered by the PRISMA focal-plane detector in coincidence with an AGATA event was taken as a trigger for the data acquisition. In this way the origin of the γ rays is distinguished, background from beta decay is reduced, and a major fraction of isomeric γ-ray transitions is suppressed.

Pulse-shape analysis of the digitized detector signals was applied to determine the individual interaction points within the HPGe shell [42], enabling the Orsay forward-tracking algorithm [43] to reconstruct the individual emitted γ-ray energies, determine the first interaction point of the γ ray in the germanium, and, thus, the emission angle. Together with the kinematic information from PRISMA, a precise Doppler correction was performed. Further details on the analysis can be found in Ref. [44].

B. Part I: ^{9}Be + ^{130}Te fusion-evaporation reaction

In this experiment excited states in ^{136}Ba were populated in a ^{9}Be + ^{130}Te fusion-evaporation reaction. The FN Tandem accelerator of the Institute of Nuclear Physics, University of Cologne, provided a 40-MeV ^{9}Be beam. In this and two additional experiments, introduced in Secs. II B–II D, the target consisted of 99.3% enriched ^{130}Te with a thickness of 1.8 mg/cm^2, evaporated onto a 120-mg/cm^2-thick Bi backing plus a 132-mg/cm^2-thick Cu layer for heat dissipation. In the three experiments, all reaction products were stopped inside the Bi backing. γ rays from excited reaction products were measured with a γ-ray array equipped with 11 high-purity germanium (HPGe) detectors, placed in rings at 45° (six detectors) and 143° (five detectors) with respect to the beam axis. In total, 9×10^7 $\gamma\gamma$-coincidence events were collected.

C. Part II: ^{9}Be + ^{130}Te fusion-evaporation reaction

Another ^{9}Be + ^{130}Te fusion-evaporation reaction was performed at 43 MeV beam energy. The HORUS array comprised 14 HPGe detectors, six of them equipped with BGO Compton-suppression shields. The detectors were positioned on the eight corners and six faces of a cube. To reduce background radiation from x rays, each detector was shielded by 2-mm-thick sheets of lead and copper. Note that the relative efficiency of the first experiment (Sec. II B) exceeds the relative efficiency of the second experiment by a factor of more than 16 at a γ-ray energy of 100 keV. However, the total $\gamma\gamma$ statistic is more than one order of magnitude higher than in the first experiment.

D. ^{11}B + ^{130}Te fusion-evaporation reaction

In the third experiment, ^{136}Ba and ^{137}Ba were populated via a ^{11}B + ^{130}Te fusion-evaporation reaction. Several fusion-evaporation codes predict a relative cross section of <1% for the evaporation channels of interest. The HORUS array was arranged similarly to the second ^{136}Ba experiment (Sec. II C). However, no additional shielding in front of the detectors was mounted. In total, 1.5×10^{10} $\gamma\gamma$-coincidence events were recorded. Additional information about the experimental setup and the results of the $\gamma\gamma$ analysis of this experiment can be found in Ref. [20].

In all three fusion-evaporation experiments, γ-ray events were processed triggerless and recorded utilizing the synchronized 80-MHz XIA$^{\mathrm{TM}}$Digital Gamma Finder (DGF) data-acquisition system. The data were analyzed offline using the codes SOCO-V2 [45] and TV [46].

The HORUS spectrometer arranged in the cube configuration allows us to investigate multipole-mixing ratios of transitions between excited states with the $\gamma\gamma$ angular-correlation code CORLEONE [47,48] based on the phase convention by Krane, Steffen, and Wheeler [49,50]. Different hypotheses of involved spins J_1, J_2, J_3 and multipole-mixing ratios δ_1, δ_2 of two coincident γ rays in a cascade $J_1 \xrightarrow{\delta_1} J_2 \xrightarrow{\delta_2} J_3$ are evaluated by χ^2 fits of the correlation function $W(\Theta_1, \Theta_2, \Phi) = W(J_1, \delta_1, J_2, \delta_2, J_3)$ to experimental intensities in eight different correlation groups, each associated with detector pairs at angles $\Theta_{1,2}$ with respect to the beam axis and a relative angle Φ between the planes spanned by the detectors and the beam axis. Note that the correlation intensities also depend on the orientation parameter σ: the fusion-evaporation reaction orients the spin of the initial level J_1 with respect to the beam axis. The orientation is described by a Gaussian distribution of the magnetic substates with mean value $\langle m \rangle = 0$ and variance σ^2. The width of the alignment distribution was found to be constant at $\sigma = 2.1$. More details on the angular-correlation analysis with CORLEONE are given in Refs. [51,52]

III. EXPERIMENTAL RESULTS

A. ^{136}Ba

The level scheme of ^{136}Ba deduced in the four experiments is presented in Fig. 2(a). New parity assignments of states above the $J^\pi = 10^+$ isomer are based on the parity assignments of the isomeric 3357-keV state in ^{136}Ba given in Refs. [3,14]. The $J^\pi = 10^+$ assignment with the tentative positive parity is strongly supported by systematics, shell-model calculations, and measured DCO ratios [3,14].

The Doppler-corrected AGATA singles γ-ray spectrum of ^{136}Ba in the ^{136}Xe + ^{238}U experiment is shown in Fig. 3(a). The mass spectrum along the Ba isotopes identified with

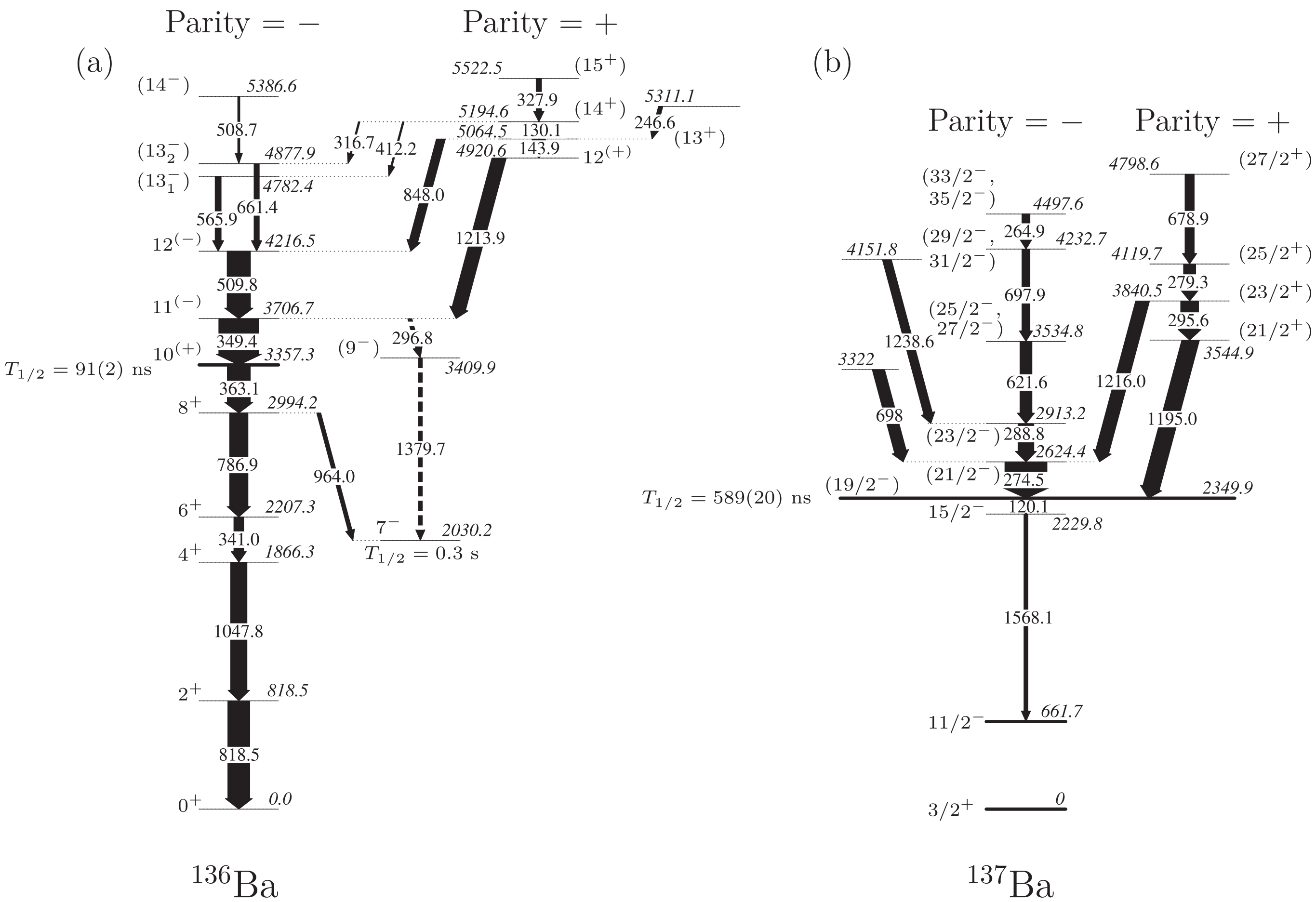

FIG. 2. (a) Level scheme assigned to ^{136}Ba in the present work. Transitions and excitation energies are given in keV. γ-ray intensities above the $J^{\pi} = 10^{+}$ isomer are deduced from the ^{9}Be + ^{130}Te experiment and normalized to the 349-keV transition. (b) Level scheme assigned to ^{137}Ba and normalized to the 275-keV transition. Transitions and excitation energies are taken from the previous work, using the same ^{11}B + ^{130}Te experiment, presented in Ref. [20]. Tentative assignments are given in brackets and dashed lines. In both isotopes new spin/parity assignments are based on the spin/parity assignments of the isomeric 3357.3-keV state in ^{136}Ba given in Ref. [14] and on the spin/parity assignments of the isomeric 2349.9-keV state in ^{137}Ba given in Refs. [20,21]. See text for details.

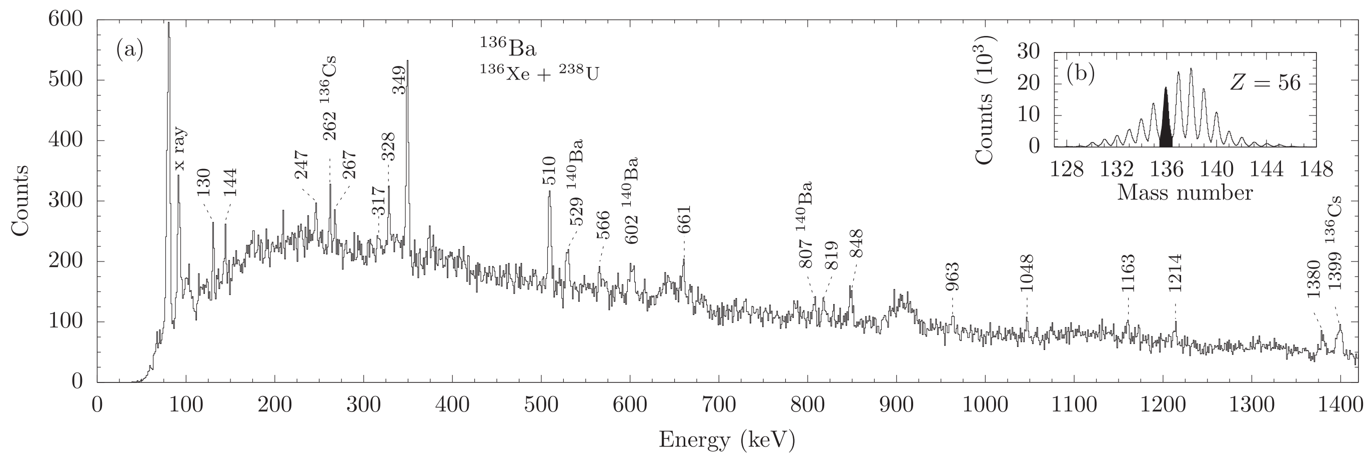

FIG. 3. (a) Doppler-corrected γ-ray spectrum gated on ^{136}Ba identified in PRISMA in the ^{136}Xe + ^{238}U experiment. γ-ray energies are given in keV. (b) Mass spectrum of Ba isotopes identified with PRISMA. The applied mass gate on ^{136}Ba is marked black. A gate on the prompt time peak between AGATA and PRISMA is applied to reduce random background.

TABLE I. Energies, spin assignments, and relative in-beam intensities for γ-ray transitions in ^{136}Ba above the $J^\pi = 10_1^+$ isomer at $E_x = 3357.3$ keV. Fitted energies and relative intensities normalized to the 349.4-keV transition are taken from two experiments: $I_\gamma^{^{11}\mathrm{B}}$ from ^{11}B + ^{130}Te and $I_\gamma^{^{9}\mathrm{Be}}$ from ^{9}Be + ^{130}Te.

E_γ (keV)	E_i (keV)	E_f (keV)	I_i^π	I_f^π	$I_\gamma^{^{11}\mathrm{B}}$	$I_\gamma^{^{9}\mathrm{Be}}$
130.1	5194.6	5064.5	(14^+)	(13^+)	20(2)	18(2)
143.9	5064.5	4920.6	(13^+)	$12^{(+)}$	29(2)	23(2)
296.8	3706.7	3409.9	$11^{(-)}$	(9^-)	–	weak
316.7	5194.6	4877.9	(14^+)	(13_2^-)	9(2)	weak
246.6	5311.1	5064.5	–	(13^+)	12(3)	10(1)
327.9	5522.5	5194.6	(15^+)	(14^+)	12(3)	13(2)
349.4	3706.7	3357.3	$11^{(-)}$	$10^{(+)}$	≡100	≡100
412.2	5194.6	4782.4	(14^+)	(13_1^-)	10(2)	weak
508.7	5386.6	4877.9	(14^-)	(13_2^-)	weak	weak
509.8	4216.5	3706.7	$12^{(-)}$	$11^{(-)}$	62(9)	63(7)
565.9	4782.4	4216.5	(13_1^-)	$12^{(-)}$	25(3)	15(1)
661.4	4877.9	4216.5	(13_2^-)	$12^{(-)}$	20(2)	13(1)
848.0	5064.5	4216.5	(13^+)	$12^{(-)}$	30(3)	27(3)
1213.9	4920.6	3706.7	$12^{(+)}$	$11^{(-)}$	42(4)	35(3)
1379.7	3409.9	2030.2	(9^-)	7^-	–	weak

PRISMA and the applied gate on ^{136}Ba is shown in the inset Fig. 3(b). Transitions at γ-ray energies of 529, 602, and 807 keV are contaminants from the $+4n$ channel ^{140}Ba. Moderately weak lines at 262 and 1399 keV can be associated to known transitions in the isobar ^{136}Cs. Due to the restriction to prompt events in the time-difference spectrum between PRISMA and AGATA, i.e., $\Delta t_{\mathrm{PRISMA\text{-}AGATA}} \approx 16$ ns, transitions between states below the $E_x = 3357$ keV, $J^\pi = 10^+$ isomer are found to be suppressed in the spectrum. The largest peaks in the spectrum are located at 349 and 510 keV. In previous works both transitions were placed on top of the 3357-keV isomer to form a cascade deexciting the 4217-keV state [3,14]. Further peaks at 130, 144, 247, 328, 848, and 1214 keV are consistent with those found by Valiente-Dobón *et al.* [3]. However, the placement of 130- and 247-keV transitions was unknown in the level scheme of the previous work due to similar relative peak intensities.

Measured intensities of coincident γ rays from the HORUS experiments are summarized in the right-hand side of Table I. All intensities are efficiency corrected and normalized to the intensity of the 349-keV transition. Intensities are extracted from the ^{9}Be + ^{130}Te experiment ($I_\gamma^{^{9}\mathrm{Be}}$) as well as from the ^{11}B + ^{130}Te experiment ($I_\gamma^{^{11}\mathrm{B}}$). The independently measured intensities show a consistent assignment of states and transitions. The uncertainties in the transition energies are ±0.5 keV. Spin/parity assignments are supported by angular-correlation measurements and shell-model calculations. Various HORUS background-subtracted prompt $\gamma\gamma$-coincidence spectra from the first ^{9}Be + ^{130}Te experiment (see Sec. II B) with gates on transitions above the $J^\pi = 10^+$ isomer are shown in Figs. 4(a)–4(d). Contaminant transitions in the spectrum gated on the 328-keV transition [Fig. 4(c)] stem from $35/2^- \to 33/2^-$ transition in ^{135}Ba [53]. Coincident transitions deexciting the isomeric $E_x = 3357$-keV state are suppressed in intensity, due to the prompt $\gamma\gamma$-coincidence time gate of 175 ns.

Figure 4(a) presents the γ-ray spectrum with a gate on the 349-keV transition. Coincidences are labeled with filled arrowheads. The spectrum exhibits anticipated coincidences at 144, 328, 510, 848, and 1214 keV. Unassigned peaks at 130, 247, 566, and 661 keV, observed in the AGATA experiment, are coincident to the 349-keV transition. In the previous work [3], the 144- and 1214-keV γ rays are arranged to form a state at $E_x = 3850$ keV. A gate on the 848-keV transition is shown in Fig. 4(b). The absence of the 144-1214-keV cascade requires the 848-keV transition to be placed parallel to this cascade. The intensity of the 1214-keV peak in the $\gamma\gamma$-coincidence spectrum gated on 349 keV exceeds the one of the 144-keV line. Moreover, the 144-1214-keV cascade corresponds to the sum energy of the 848-510-keV cascade. Therefore, in accordance with the measured intensity relations of the 1214- and 144-keV transitions, the 144-keV transition has to be placed on top of the 1214-keV transition, resulting in a new state at 4921 keV excitation energy.

Coincidences with the 848-keV and 1214-keV transitions as well as intensity balances require a placement of the 130, 247, and 328-keV transitions above the 5065-keV state. Since the 130-keV transition is mutually coincident with the 328-keV transition [cf. Fig. 4(c)], both transitions form a 328-130-keV cascade on top of the $E_x = 5065$-keV state. The ordering of the 328- and 130-keV transitions agrees with the intensity balance measured in the $\gamma\gamma$ projections gated on the 144-, 349-, 848-, and 1214-keV transitions. Additionally, Fig. 4(d) shows that the 247-keV transition is not coincident with the 328-130-keV cascade. Consequently, the 247-keV transition is placed parallel to the 328-130-keV cascade to establish a state at $E_x = 5311$ keV.

Moreover, Fig. 4(a) shows two additional coincidences at 566 and 661 keV, however, both transitions are neither coincident with the transitions at 848 and 328 keV, nor with the 247-keV transition [cf. Figs. 4(a)–4(d)]. Due to insufficient statistics we use the higher $\gamma\gamma$ statistics from the second ^{9}Be + ^{130}Te experiment (see Sec. II C) to place the 566- and 661-keV transitions in the level scheme. We remind the reader that although the total $\gamma\gamma$ statistics of this experiment is higher, the efficiency at small energies is limited due to the use of absorbers.

Figures 4(e)–4(g) show double-gated $\gamma\gamma\gamma$-coincidence and sums of double-gated $\gamma\gamma\gamma$-coincidence spectra. Both the 566- and 661-keV transitions emerge in the $\gamma\gamma\gamma$ projection gated on 510 and 349 keV, as displayed in Fig. 4(e). Hence, the transitions have to feed the 4217-keV state. Since the 566- and 661-keV transitions are not in mutual coincidence [cf. Figs. 4(f)–4(g)] both have to be placed parallel, directly feeding the $E_x = 4217$-keV state.

Furthermore, the spectrum gated on the 510-349-keV cascade [cf. Fig. 4(e)] reveals weak lines at 317 and 412 keV. The 317-keV transition corresponds to the energy difference between the new established states at 4878 and 5195 keV, while the 412-keV transition corresponds to the transition between the new established states at 4782 and 5195 keV. As expected, the 412-keV transition is only observed in coincidence with the 566-keV transition [cf. Fig. 4(f)] and

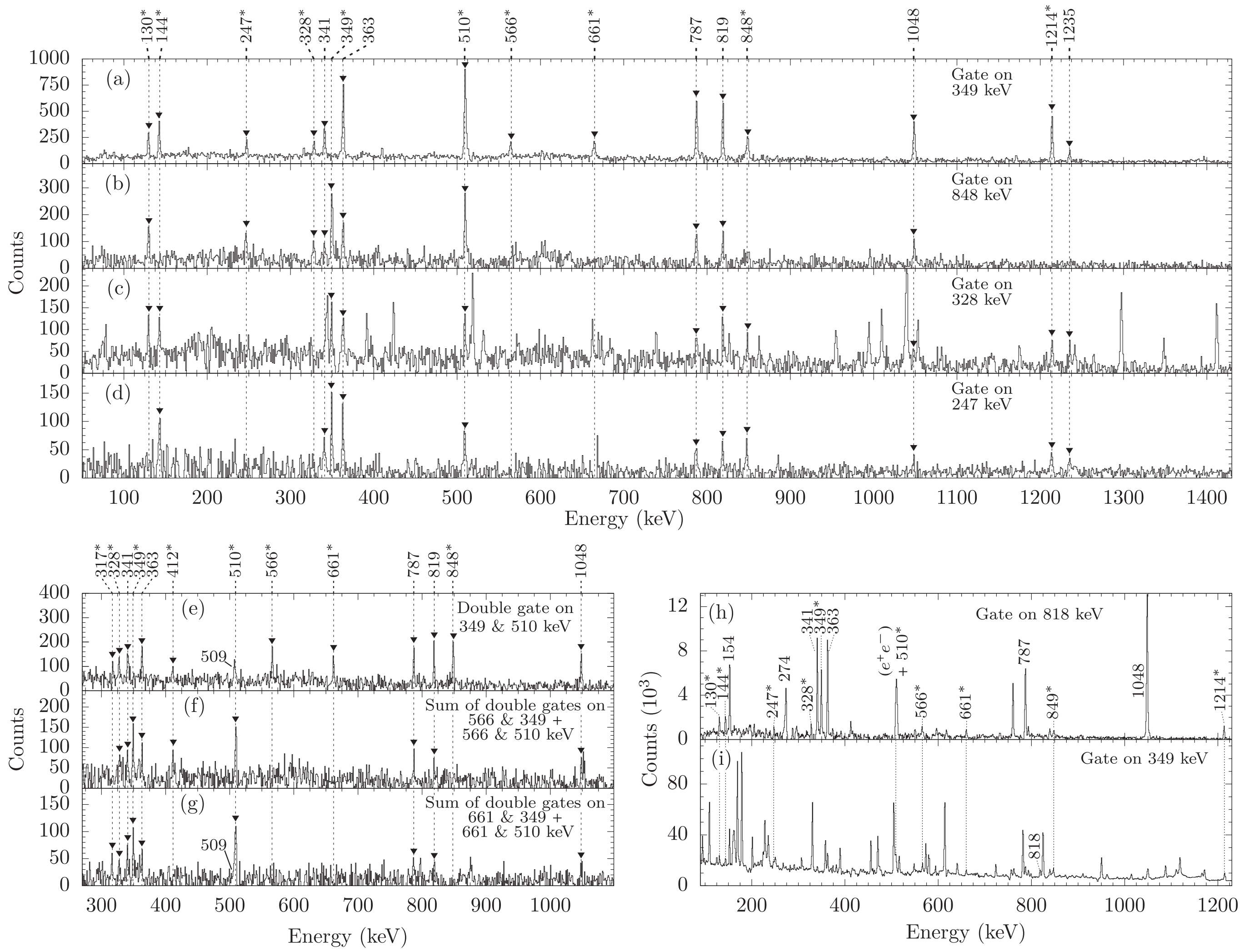

FIG. 4. Prompt $\gamma\gamma$ double-coincidence spectra from the first ^{9}Be + ^{130}Te experiment (see Sec. II B) with gates on (a) 349, (b) 848, (c) 328, and (d) 247 keV. Transitions above the $J^{\pi} = 10^{+}$ isomer are marked with asterisks. Coincidences are labeled by filled arrowheads. Contaminant transitions in the spectrum gated on the 328 keV stem from transitions in ^{135}Ba. $\gamma\gamma\gamma$ triple-coincidence spectra from the second ^{9}Be + ^{130}Te experiment (see Sec. II C) with (e) a double gate on 349 and 510 keV, a sum of double-gated triples coincidence spectra gated on (f) 566 and 510 and 566 and 349 keV, and a similar sum spectra gated on (g) 661 and 510 and 661 and 349 keV. Prompt $\gamma\gamma$ double-coincidence spectra with a gate on (h) 818 and (i) 349 keV from the ^{11}B + ^{130}Te experiment (see Sec. II D). The gate on 349 keV is contaminated with transitions from ^{137}La.

the 317-keV transition is in coincidence with the 661-keV transition [cf. Fig. 4(g)].

A further 509-keV transition is in coincidence with the 510-349-keV cascade, as shown in Fig. 4(e). The centroid of this peak is clearly separated by 0.9 keV from the 510-keV peak position in Fig. 4(f). Since the full width at half maximum (FWHM) of the coincident 510-keV transition gated on 566-keV is broader than the similar peak gated on 661 keV, the 509-keV transition is identified as another transition above the 4878-keV state.

An intense 1380-keV transition is observed in the AGATA spectrum in Fig. 3. In accordance with previous studies performed with the AGATA dataset [9,20], a transition from a contaminant can be excluded. In the HORUS experiment this transition is observed to be coincidence with transitions stemming from the $5^{-} \rightarrow 2^{+}$ decay in ^{134}Ba and in coincidence with a 297-keV transition. Assuming a 1380-keV transition above the $J^{\pi} = 7^{-}$ isomer at $E_x = 2030$ keV, the energy difference between the 3707-keV state and a proposed $E_x = 3410$ keV state corresponds to 297 keV. Accordingly, the 297-1380-keV cascade is tentatively placed above the $J^{\pi} = 7^{-}$ isomer, connecting the $E_x = 3707$-keV state with the isomer. This assignment is further supported by the recent observation of a similar 415-1099-keV cascade on top of the $J^{\pi} = 7^{-}$ isomer in the isotone ^{134}Xe [9].

^{136}Ba was also populated in the ^{11}B + ^{130}Te fusion-evaporation experiment with a significantly lower relative cross section (see Sec. II D). Figures 4(h) and 4(i) show exemplary prompt $\gamma\gamma$-coincidence spectra with gates on the 818- and 349-keV transitions. Besides dominant coincident transitions originating from the 348-keV ($33/2^{+} \rightarrow 31/2^{-}$) decay in ^{137}La [54], also transitions from ^{136}Ba, including

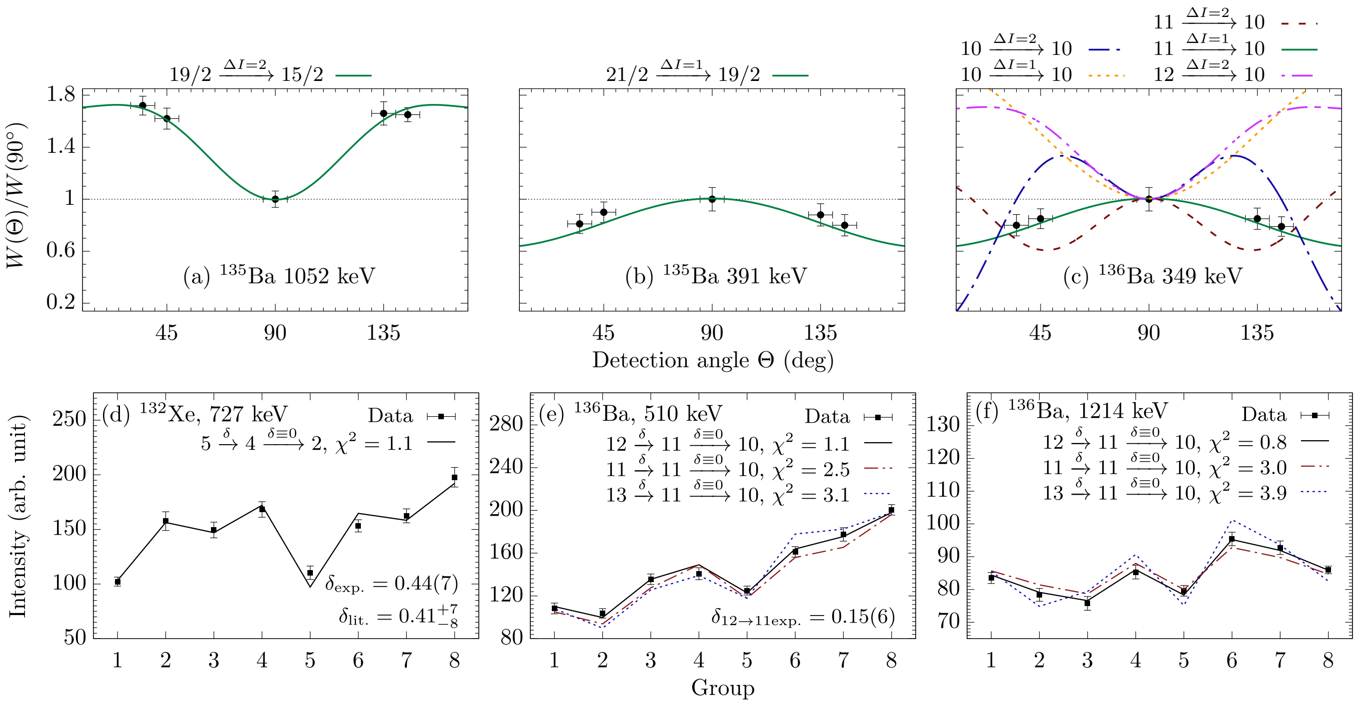

FIG. 5. Benchmark angular distribution of (a) the 1052-keV ($19/2^- \rightarrow 15/2^-$) γ-ray transition and (b) the 391-keV ($21/2^- \rightarrow 19/2^-$) γ-ray transition, both in ^{135}Ba. Experimental values (data points) are compared to pure dipole and quadrupole hypotheses (solid lines). (c) Angular distribution of the 349-keV transition, feeding the $J^\pi = 10^+$ isomer in ^{136}Ba. Several pure dipole and quadrupole hypotheses (lines) are plotted. (d) Benchmark $\gamma\gamma$ angular correlations for the $5_1^+ \rightarrow 4_1^+ \rightarrow 2_1^+$ (727-773-keV) cascade in ^{132}Xe. Experimental values (data points) are compared to calculated angular-correlation functions $W(\Theta_1, \Theta_2, \Phi)$ (lines) for eight correlation groups using the code CORLEONE. Investigation for (e) the 510-349-keV cascade and (f) the 1214-349-keV cascade in ^{136}Ba. Several spin hypotheses are plotted.

the new established transitions, are observed well above the background. Intensities ($I_\gamma^{^{11}\mathrm{B}}$), normalized to the intensity of the 349-keV transition, are listed in Table I. The observed coincidences in the ^{11}B + ^{130}Te experiment are consistent with the aforementioned results and strongly support the new results on ^{136}Ba.

The detectors in the HORUS setup of the ^{9}Be + ^{130}Te experiment (see Sec. II C) were arranged in a cube configuration, yielding five rings at relative angles of 35° (ring 1), 45° (ring 2), 90° (ring 3), 135° (ring 4), and 145° (ring 5) with respect to the beam axis. Figure 5(a) shows the distribution of the measured singles γ-ray intensity of the well-known 1052-keV transition ($19/2^- \xrightarrow{E2} 15/2^-$) in ^{135}Ba in the different rings, normalized to the intensity of ring 3. Moreover, Fig. 5(b) shows a similar distribution for the 391-keV transition ($21/2^- \xrightarrow{E1} 19/2^-$) in ^{135}Ba. Both distributions are compared with theoretical pure dipole- and quadrupole-transition hypotheses as described by Yamazaki *et al.* [55]. Both angular distributions are symmetric around 90°. The intensity of the quadrupole 1052-keV transition ($\Delta I = 2$) in Fig. 5(a) is maximum along the beam axis, whereas the one of the dipole 391-keV transition ($\Delta I = 1$) in Fig. 5(b) is maximum perpendicular to the beam axis, demonstrating spin alignment with respect to the beam axis.

The characteristic investigation of dipole and quadrupole radiation signatures in the HORUS experiment is used to determine the multipolarity of the 349-keV transition in ^{136}Ba. In Fig. 5(c) the singles γ-ray intensity distribution of the 349-keV transition is compared to different theoretical pure dipole and quadrupole distributions for spins $J = 10, 11, 12$ of the $E_x = 3707$-keV state. The 12 $\xrightarrow{\Delta I=2}$ 10 and 10 $\xrightarrow{\Delta I=1}$ 10 hypotheses can be clearly rejected. Since the 349-keV γ ray has a Weisskopf half-life estimate of $T_{1/2} = 0.17$ ms for an $E3$ transition, an $E3$ character is disregarded. Possible 10 $\xrightarrow{\Delta I=2}$ 10 and 11 $\xrightarrow{\Delta I=2}$ 10 hypotheses show large discrepancies between theoretical and experimental values. Moreover, a mixed dipole-quadrupole transition with initial spin of $J^\pi = 10^+$ does not provide a better agreement. Hence, the four above-mentioned hypotheses can be rejected. A pure dipole decay and an initial spin of $J = 11$ for the $E_x = 3707$-keV state yields the best agreement with the experimental intensity distribution.

Based on the assigned spin of the $E_x = 3707$-keV state, further spin hypotheses are tested for the $E_x = 4217$-keV and the newly established $E_x = 4921$-keV states applying the procedure of $\gamma\gamma$ angular correlation measurements discussed in Sec. II. Angular-distribution functions $W(\Theta_1, \Theta_2, \Phi)$ of two coincident γ-ray transitions are fitted to experimental γ-ray intensity distributions obtained by gates on depopulating transitions in the $\gamma\gamma$-coincidence matrices of eight angular-correlation groups. Figure 5(d) shows a benchmark angular-correlation fit of the 727-keV decay, gated on the 773-keV $E2$ transition in ^{132}Xe. The fit of a $5^+ \xrightarrow{\delta} 4^+ \xrightarrow{E2} 2^+$ hypothesis yields a good agreement with the experimental distribution. Moreover, the obtained $E2/M1$ multipole-mixing ratio of

$\delta_{\text{exp.}} = 0.44(7)$ agrees well with the evaluated value of $\delta = 0.41^{+7}_{-8}$ [56].

Similarly, keeping the spin of the 3357- and the 3707-keV state in ^{136}Ba fixed, spins of $J = 11$, 12, and 13 were tested for the $E_x = 4217$-keV state. One multipole-mixing ratio δ in the $J_1 \xrightarrow{\delta_1} J_2 \xrightarrow{\delta_2} J_3$ cascade is fixed while the other is varied in order to avoid an overdeterminacy of the fit. For a parity-changing $E1$ transition, a multipole-mixing ratio in the order of $\delta \approx 0$ is expected. Scenarios of $11 \xrightarrow{\delta_1=0} 11 \xrightarrow{\delta_2} 10$ and $12 \xrightarrow{\delta_1=0} 11 \xrightarrow{\delta_2} 10$ for the 510-349-keV cascade yield χ^2 values of 10 and 14. Obviously, a parity-changing 510-keV $E1$ transition can be rejected. Moreover, a $13 \xrightarrow{\delta_1=0} 11 \xrightarrow{\delta_2} 10$ assumption does not fit the experimental data, which excludes an $E2$ transition with 510 keV. Vice versa, keeping $\delta_2 = 0$ fixed, a much better agreement is obtained. Figure 5(e) visualizes the angular-correlation distribution for the 510-349 keV cascade in ^{136}Ba with respect to the different groups. The $12 \xrightarrow{\delta_1} 11 \xrightarrow{\delta_2=0} 10$ hypothesis with $\delta_1 = -0.15(6)$ ($\chi^2 = 1.1$) gives the best agreement with the experimental $W(\Theta_1, \Theta_2, \Phi)$ distribution in all correlation groups. Thus, a spin of $J = 12$ is assigned to the 4217-keV state. Apart from that, similar fits assuming a larger fixed δ_2 value for the 349-keV transition yield significantly worse χ^2 values of the $12 \xrightarrow{\delta_1} 11 \xrightarrow{\delta_2} 10$ hypothesis (i.e., $\delta_2 \equiv \pm 0.05$; $\chi^2 > 2.6$ and $\delta_2 \equiv \pm 0.1$; $\chi^2 > 3.3$). Hence, on the basis of a pure-dipole character for the 349-keV γ-ray as shown in Fig. 5(c) and the overall agreement with the shell-model calculations presented in Sec. IV A, a parity changing $E1$ transition is proposed leading to a negative parity assignment of the 3707-keV state.

Employing the same method, the spin of the newly established excited state at $E_x = 4921$ keV is determined, as shown in Fig. 5(f). Spins of $J = 11$, 12, and 13 are tested. Assuming $\delta_2 = 0$, the 1214-349-keV cascade is best reproduced by a $12 \xrightarrow{\delta_1} 11 \xrightarrow{\delta_2} 10$ sequence with $\delta_1 = -0.01(12)$. Vice versa, keeping $\delta_1 = 0$ fixed, δ_2 is determined to be in agreement with zero. The obtained χ^2 values of both fits are similar, showing the mutual consistency of both hypotheses. Consequently, similar to the negative-parity $E_x = 4217$-keV state, the $E_x = 4920$-keV state has a spin of $J = 12$. The pure dipole character of the 1214-keV transition suggests a $E1$ character of this transition, indicating that the $E_x = 4920$-keV state has different spin than the $E_x = 3707$-keV state and is therefore most probably of positive parity. Moreover, the independently measured 1214-349-keV cascade supports a pure-dipole $E1$ 349-keV transition.

The $\gamma\gamma$ angular-correlation analysis is further exploited to verify the validity of the 297-1380-keV cascade on top of the $J^\pi = 7^-$ isomer. The spin of the initial $J = 11$ state and that of the final $J = 7$ state are fixed. A spin assumption of $J = 9$ for the $E_x = 3410$-keV state yields a χ^2 value of 1.8, compared to χ^2 values of 2.2 and 2.3 for $J = 10$ and $J = 8$ hypotheses. Since an $E3$ or $M2$ transition in this cascade would corroborate another isomer, a spin assignment of $J = 9$ for the $E_x = 3410$-keV state is necessary to keep a prompt decay character. Consequently, the angular-correlation measurement supports the 297-1380-keV cascade in ^{136}Ba.

B. ^{137}Ba

In a previous work by this group [20], the level scheme of ^{137}Ba above the $J^\pi = 19/2^-$ isomer was extended to the structure presented in Fig. 2(b), using the $\gamma\gamma$ coincidences from the ^{11}B + ^{130}Te experiment introduced in Sec. II D. This paper focuses on the angular-distribution and angular-correlation analysis of this data set. Note that the new determined spins and parity of the high-spin states is based on the tentative $J^\pi = 19/2^-$ assignment of the isomeric 2350-keV state in ^{137}Ba given in Refs. [20,21]. However, the assignment is strongly supported by systematics and shell-model calculations.

Due to the low cross section of the $p3n$ evaporation channel, the basis of the data analysis are double-γ HPGe coincidences to reduce the complexity of the γ-ray spectra of the different rings of the HORUS setup. The fusion-evaporation reaction orients the spin of the initial level with respect to the beam axis. However, according to the very long half-life of the $J^\pi = 19/2^-$ state, the 120-1568-keV cascade is no longer aligned with respect to the beam axis; it decays instead isotropic. Thus, a γ-ray gate on 1568 keV does affect the alignment with respect to the beam axis for coincident transitions above the isomer.

To verify that the spins above the isomer are still aligned with respect to the beam axis, a benchmark angular γ-ray distribution of the well-known 1172-keV ($23/2^- \xrightarrow{E2} 19/2^-$ [54]) transition in ^{137}La is shown in Fig. 6(a). The intensities in the different rings are extracted from the corresponding γ-ray spectra, gated on the 782-keV ($15/2^- \rightarrow 11/2^-$) transition, located below the $J^\pi = 19/2^-$ [$T_{1/2} = 360(40)$ ns [57]] isomer. A good agreement between measured and theoretical intensity distribution of a pure quadropole transition is demonstrated.

In ^{137}Ba the $J^\pi = 19/2^-$ [$T_{1/2} = 0.589(20)$ μs [20]] isomer decays via a 120-1568-keV cascade. Applying a 1568-keV gate to all rings, comparisons between measured and theoretical angular distributions for the 275- and 1195-keV transitions in ^{137}Ba are shown in Figs. 6(b) and 6(c). In both cases, the highest intensity was measured in the detectors perpendicular to the beam axis, which is opposite to the distribution of the benchmark quadrupole transition presented in Fig. 6(a). Therefore, both experimentally determined intensity distributions are incompatible with a quadrupole $23/2 \xrightarrow{\Delta I=2} 19/2$ transition. Also an $E3$ transition can be clearly rejected for both γ rays, since the Weisskopf half-life estimate is several orders of magnitude larger compared to a competitive quadrupole transition. Moreover, pure as well as mixed quadrupole/dipole $19/2 \xrightarrow{\Delta I=1,2} 19/2$ transitions do not fit the experimental data. Overall, a $J = 21/2$ hypothesis for both initial states match the experimental values best.

Spins of the 2913- and 3841-keV states are determined using the $\gamma\gamma$-coincidence angular-correlation technique. The number of groups has to be reduced in order to perform

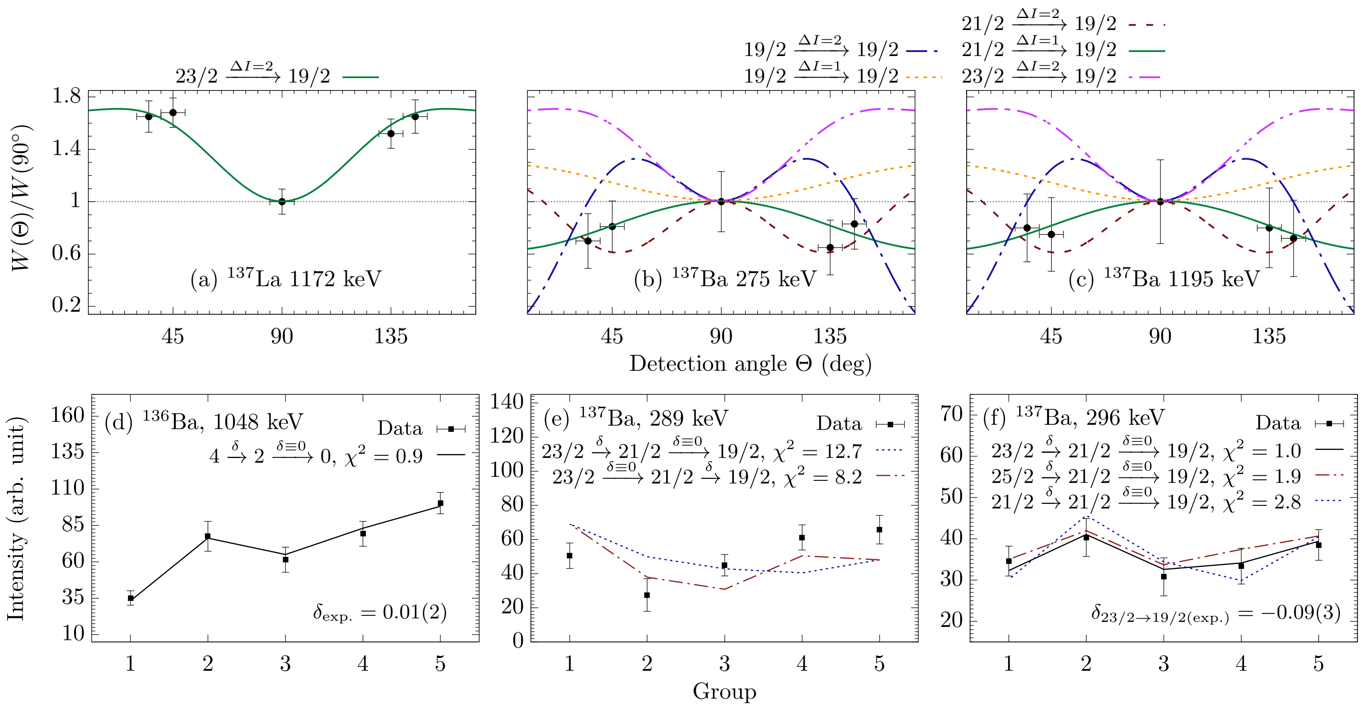

FIG. 6. Angular distributions of transitions in ^{137}La and ^{137}Ba. Experimental distribution is obtained in the γ-ray spectra, gated on disoriented transitions below the isomers. (a) Benchmark angular distribution of the well-known 1172-keV ($23/2^- \rightarrow 19/2^-$) γ-ray transition in ^{137}La. The pure quadrupole hypothesis is well reproduced with this approach. Angular distribution of (b) 275- and (c) 1195-keV transition, decaying into the $19/2^-$ isomer in ^{137}Ba. Intensities are extracted from $\gamma\gamma$ coincident spectra with a gate on the $15/2^- \rightarrow 11/2^-$ transition. Several pure dipole and quadrupole hypotheses (lines) are plotted. (d) Benchmark $\gamma\gamma$ angular correlations for the $4_1^+ \rightarrow 2_1^+ \rightarrow 0_1^+$ (1048-818-keV) cascade in ^{136}Ba. Investigation for (e) the 289-275-keV cascade and (f) the 296-1195-keV cascade in ^{137}Ba. Several spin hypotheses are plotted.

angular-correlation measurements in the elusive Ba channels. To ensure the quality of the angular-correlation analysis, a benchmark fit of the well-established $4^+ \rightarrow 2^+ \rightarrow 0^+$ cascade in ^{136}Ba is presented in Fig. 6(d). The $E2$ character of the 1048-keV transition is well reproduced.

The singles γ-ray angular-distribution measurement suggested a spin of $J = 21/2$ for both the 2624- and 3545-keV state [cf. Fig. 6(b) and 6(c)]. Consequently, the spin values of the 2913- and 3841-keV states are limited to $J = 21/2$, 23/2, and 25/2. Figure 6(e) shows the experimental angular-correlation distribution of the 289-keV transition in the different groups, gated on the 275-keV transition. Assuming a vanishing multipole-mixing ration ($\delta_1 = 0$) of the 289-keV transition and a variable δ_2 value of the 275-keV transition, fits of the three aforementioned hypotheses results in χ^2 values larger than 4. Furthermore, fixing the 275-keV transition to a dipole character ($\delta_2 = 0$) and varying the δ_1 value of the 289-keV transition, χ^2 values larger than 6 were obtained. Since the 275- and 289-keV transitions are incompatible with a multipole-mixing ratio of zero, a parity-changing $E1$ character of the 275- or 289-keV transition can be ruled out. Likewise, a parity-conserving $E2$ character with a spin change from $J = 25/2$ to $J = 21/2$ for the 289-keV transition is not compatible with the experimental distribution. Figure 6(e) shows two examples for fits with corresponding χ^2 values of 12.7 and 8.2. Since the 289-275-keV cascade built on the $J^\pi = 19/2^-$ state has no parity-changing character, we propose negative-parity states $J^\pi = 21/2^-$ at $E_x =$ 2624-keV and $J^\pi = 23/2^-$ at $E_x = 2913$-keV.

Figure 6(f) shows the experimentally deduced angular-correlation intensity distribution for the coincident γ rays at 1195 and 296 keV, compared to calculated values for different scenarios of the spin and parity of the 3841-keV state. Fixing the spin value of the 3545-keV state to $J = 21/2$, hypotheses with pure dipole character ($21/2 \xrightarrow{\delta_1=0} 21/2$ or $23/2 \xrightarrow{\delta_1=0} 21/2$) as well as a pure quadrupole character ($25/2 \xrightarrow{\delta_1=0} 21/2$) yield a limited agreement with the data. Instead, a good match is obtained by assuming a dominant dipole component ($\delta_2 = 0$) for the $21/2 \rightarrow 19/2$ 1195-keV transition and a nonzero δ_1 value for the 296-keV transition. A hypothesis of $J = 23/2$ for the $E_x = 3841$ keV state yields the best result. The nonvanishing multipole-mixing ratio $\delta_1 = -0.09(3)$ clearly indicates that the 296-keV transition is parity conserving. Assuming a nonzero fixed δ_2 value of the 1195-keV transition and a variable δ_1 value of the 296-keV transition, the χ^2 value of the $23/2 \xrightarrow{\delta_1} 21/2 \xrightarrow{\delta_2} 19/2$ hypothesis get larger (i.e., $\delta_2 = \pm 0.05$; $\chi^2 > 2.2$ and $\delta_2 = \pm 0.1$; $\chi^2 > 2.9$). Based on the results of the shell-model calculations presented in Sec. IV B, this observation supports a pure-dipole $E1$ 1195-keV transition which is in line with a change from negative to positive parity.

IV. SHELL MODEL

The extended level schemes of ^{136}Ba and ^{137}Ba are compared with the results of shell-model theory. All shell-model calculations were carried out in an untruncated *gdsh* valence space outside doubly magic ^{100}Sn, employing the shell-model code NUSHELLX@MSU [58], the massive-parallelization code KSHELL [59], and the ANTOINE shell-model code [60].

The first calculation is conducted with the effective interaction GCN50:82 [61,62]. The interaction is derived from a realistic G matrix based on the Bonn-C potential [63]. Empirical monopole corrections to the original G matrix are introduced by fitting different combinations of two-body matrix elements to sets of experimental excitation energies from even-even and even-odd semimagic nuclei.

The second calculation is conducted in the framework of the realistic shell model [64,65], denoted as realistic SM. Single-particle energies and two-body effective interaction are determined from the established CD-Bonn free nucleon-nucleon potential [63] using the $V_{\text{low-}k}$ approach with a cutoff momentum of $\Lambda = 2.6\ \text{fm}^{-1}$, plus the Coulomb force for protons. The effective shell-model Hamiltonian is derived iteratively by means of the many-body perturbation theory in the $\hat{Q}$-box folded diagram expansion, including all diagrams up to third order in the interaction. More details can be found in Ref. [66].

A third calculation is performed utilizing the framework of the pair-truncated shell model, denoted as PQM130 (Pairing+QQ+Multipole for mass region 130). The approach leverages a pairing-plus-quadrupole interaction that consists of spherical single-particle energies, a monopole pairing, a quadrupole pairing, and a quadrupole-quadrupole interaction. The Hamiltonian in each neutron and proton space is diagonalized separately and afterwards the total Hamiltonian is diagonalized in the truncated space. More details on the calculation are given in Refs. [67,68].

Another calculation is carried out with the jj55pn Hamiltonian (referred to as the SN100PN interaction) [69]. The Hamiltonian consists of four terms covering the neutron-neutron, neutron-proton, proton-proton, and Coulomb repulsion between the protons individually. A renormalized G matrix derived from the CD-Bonn interaction [63] was employed to construct the realistic two-body residual interaction. The proton and neutron single-particle energies are based upon the energy levels in ^{133}Sb and ^{131}Sn.

A. ^{136}Ba

As a first benchmark for the validity of the shell-model results in the high-spin regime, reduced transition probabilities $B(E2; 10_1^+ \rightarrow 8_1^+)$ are calculated with the GCN50:82, Realistic SM, and SN100PN interactions. Effective charges are chosen as $e_\pi = 1.82$ and $e_\nu = 0.82$ in the GCN50:82 and SN100PN interaction, while an effective microscopic $E2$ operator, derived consistently with the effective Hamiltonian, is employed in realistic SM. The effective charge values are equal to the charges used in a previous study of ^{136}Ba [3].

The calculated $B(E2; 10_1^+ \rightarrow 8_1^+)$ values of 0.81 $e^2\,\text{fm}^4$ (GCN50:82), 0.44 $e^2\,\text{fm}^4$ (SN100PN), and 0.22 $e^2\,\text{fm}^4$ (realistic SM) are in reasonable agreement with the previously reported experimental values of $0.97(2)\,e^2\,\text{fm}^4$ [3] and $0.96(10)\,e^2\,\text{fm}^4$ [14]. The agreement between the calculated and experimental $B(E2; 10_1^+ \rightarrow 8_1^+)$ values has improved considerably compared to the shell-model calculations conducted in Ref. [3].

Calculated level energies of four shell-model calculations are compared to the experimental levels of ^{136}Ba, as shown in Fig. 7 [(c) GCN50:82; (d) PQM130; (e) realistic SM; and (f) SN100PN]. Since states above the $J^\pi = 10^+$ isomer are the subject of this discussion, only these states are displayed. However, also the excitation energies of the yrast states $J^\pi = 2^+,\ 4^+,\ 6^+$, and 8^+ at excitation energies of $E_x = 819,\ 1867,\ 2207$, and 2994 keV are well reproduced. The different shell-model calculations locate the corresponding states at energies of $E_x = 842,\ 1873,\ 2195,\ 3036$ (GCN50:80), $E_x = 1041,\ 1959,\ 2297,\ 3209$ (realistic SM), $E_x = 814,\ 1638,\ 2230,\ 3109$ (PQM130), and $E_x = 893,\ 1896,\ 2083,\ 2959$ keV (SN100PN).

The calculations predict the $J^\pi = 10_1^+$ state with the $\nu h_{11/2}^{-2}$ configuration at excitation energies of 3332 (GCN), 3354 (realistic SM), 3164 (PQM130), and 3126 keV (SN100PN), which are in good agreement with the experimentally determined energy of 3357 keV. In particular, the GCN50:82 interaction provides an excellent agreement with the well-known yrast states $J^\pi \leqq 10^+$. Larger discrepancies between the calculations emerge in the high-spin regime; e.g., the predictions for the first excited $J^\pi = 12^+$ state differs by 0.5 MeV.

The angular-correlation and angular-distribution measurements in Sec. III A indicated a $J^\pi = 11$ assignment for the 3707-keV state and a pure-dipole character for the 349-keV transition. It is noteworthy that all interactions do not predict a yrast positive-parity state with spin $J > 10$ until approximately 1 MeV above the $J^\pi = 10^+$ state. However, all four interactions yield excited $J^\pi = 10_2^+,\ 10_1^-$, and 11_1^- states only a few hundred keV above the isomer. Moreover, $J^\pi = 11^+$ states are coherently predicted at higher energies than the $J^\pi = 11^-$ states. Accordingly, a parity-changing $E1$ transition is proposed and the state at $E_x = 3707$ keV is identified as the $J^\pi = 11^-$ state, based on these theoretical findings. Assuming a proceeding negative-parity character of this band, the states at $E_x = 4782$ and $E_x = 4878$ keV, decaying parallel into the $J^\pi = 12^-$ 4217-keV state, can most likely be interpreted as the first and second excited $J^\pi = 13^-$ states.

In the calculations the energy difference between the $J^\pi = 12_1^+$ and $J^\pi = 10_1^+$ state amount to 1555 (GCN50:82), 1551 (realistic SM), 1543 (PQM130), and 1442 keV (SN100PN). The calculated values are in good agreement with the experimentally observed energy difference of 1562 keV between the $J^\pi = 10_1^+$ and the $E_x = 4920$-keV state. In the aforementioned discussion of Fig. 5(f) a pure-dipole character of the 1214-keV transition was confirmed, which suggests a parity change. Combining this experimental result with the shell-model results, the $E_x = 4920$-keV state is clearly assigned to $J^\pi = 12^+$.

On top of the $E_x = 4921$-keV state, a low-energy 328-130-144-keV cascade is observed. The calculated transition

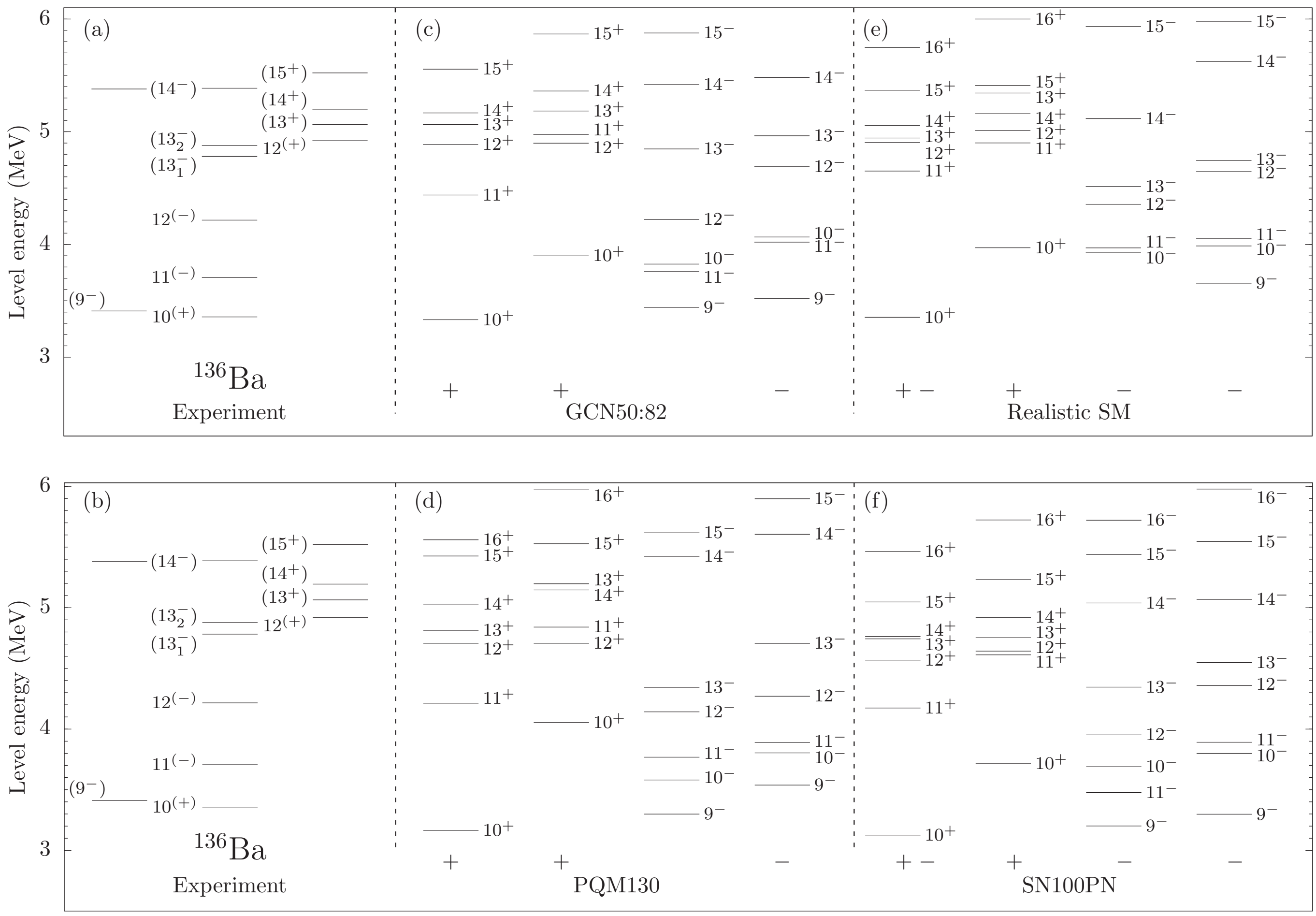

FIG. 7. Comparison of experimental energy spectra with the results of shell-model calculations for ^{136}Ba. Only states above the $J^\pi = 10^+$ state are displayed. For clarity, the states are separated into columns for positive- and negative-parity states, as well as for yrast and yrare states. (a),(b) Experimental energy spectra, shell-model results obtained with (c) GCN50:82, (d) PQM130, (e) realistic SM and, (f) SN100PN interactions.

energies in the $15^+ \rightarrow 14^+ \rightarrow 13^+ \rightarrow 12^+$ cascade are 388-103-177 (GCN), 314-111-39 (realistic SM), 397-215-106 (PQM130), and 233-111-135 keV (SN100PN), respectively. According to the good agreement between calculated and experimental energy differences, the 328-130-144-keV cascade can most likely be attributed to the $15^+ \rightarrow 14^+ \rightarrow 13^+ \rightarrow 12^+$ sequence. Shell-model calculations suggest a dominant $M1$ character for this band; i.e., GCN50:82 predicts multipole-mixing ratios of $\delta_{15\rightarrow14} = -0.05$, $\delta_{14\rightarrow13} = -0.01$, and $\delta_{13\rightarrow12} = -0.02$ which are very similar to the values calculated with SN100PN. In the calculations $J^\pi = 9^-$ states are predicted slightly above the $J^\pi = 10^+$ isomer. In accordance with the angular-correlation measurement, a tentative spin assignment of $J^\pi = (9^-)$ for the $E_x = 3410$-keV state is made.

The shell-model results provide insight into the structure of the levels built on top of the isomeric $J^\pi = 10^+_1$ state. The nuclear structure of ^{136}Ba and the $-2p$ isotone ^{134}Xe have similar characteristics. Figure 8 shows a detailed decomposition of several states into their proton and neutron configurations in (a)–(f) ^{136}Ba and (g)–(l) ^{134}Xe computed with GCN50:82 (filled blue boxes) and SN100PN (empty red boxes). The decomposition of the total angular momentum of states in ^{134}Xe and ^{136}Ba are presented in Figs. 9(a)–9(l) indicating which nucleon pairs are broken to obtain the total angular momentum of the calculated states.

Although more fragmented in ^{136}Ba, the configurations resemble the ones in ^{134}Xe. In the different positive- and negative-parity states, protons are easily redistributed from $g_{7/2}$ to $d_{5/2}$, i.e., these orbitals are energetically close together.

The configurations of the $J^\pi = 8^+_1$ state in ^{134}Xe and ^{136}Ba are predicted to be highly fragmented in both calculations, as displayed in Figs. 8(a) and 8(g). In ^{134}Xe, the four valence protons mainly occupy the $\pi(g^4_{7/2})$ and the $\pi(g^3_{7/2}d^1_{5/2})$ configuration. The total angular momentum of the $J^\pi = 8^+$ state is mainly generated from these configurations in the proton space, as visible in Fig. 9(g). Excitations into the proton $h_{11/2}$ orbital can be neglected (<2%). Using GCN50:82, the neutron configurations $\nu h^{-2}_{11/2}$, $\nu(h^{-1}_{11/2}s^{-1}_{1/2})$, and $\nu d^{-2}_{3/2}$ account for 20%, 10%, and 16% of the overall configuration in the $J^\pi = 8^+_1$ state in ^{136}Ba, respectively. In the realistic-SM calculation main configurations are couplings of the $\pi(g^5_{7/2}d^1_{5/2})$ proton configuration to (17%) $\nu d^{-2}_{3/2}$ and (15%) $\nu h^{-2}_{11/2}$, which is in good agreement with the results of the GCN50:82 and

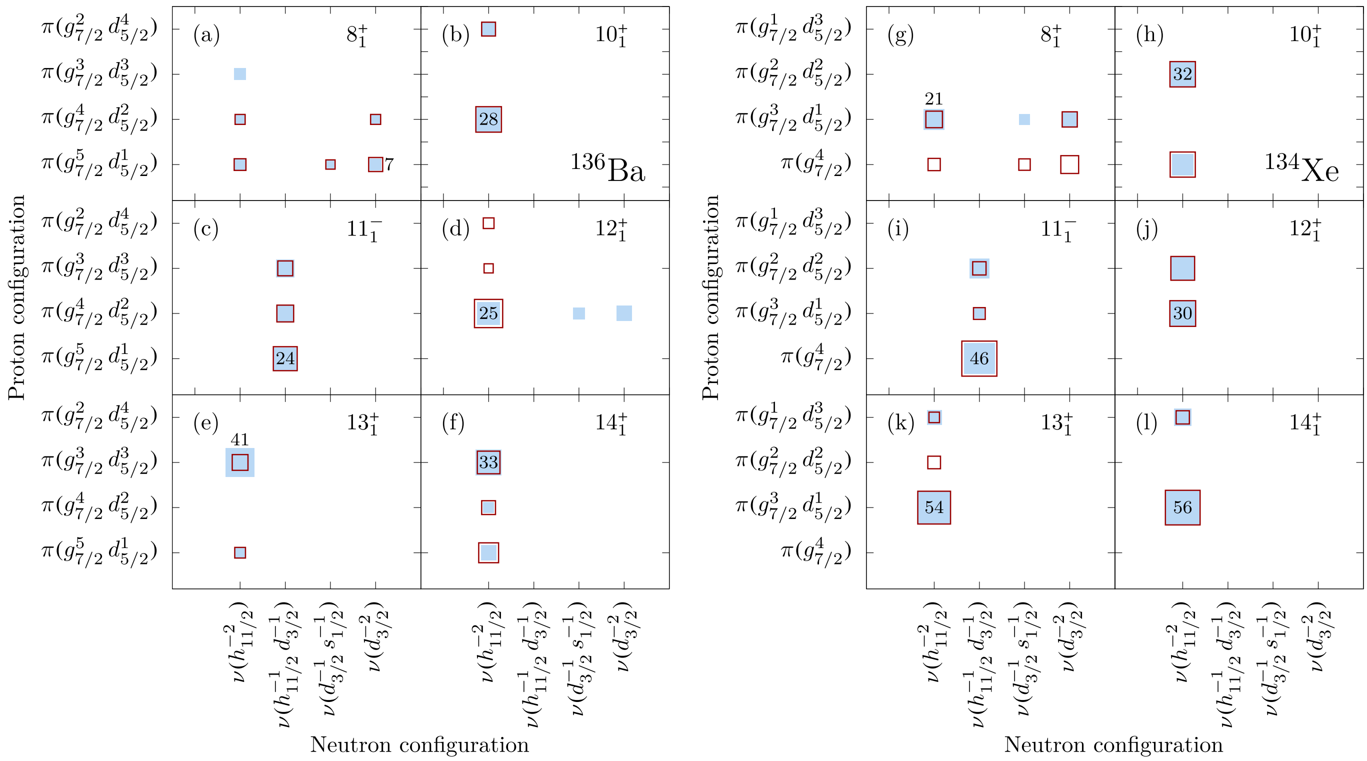

FIG. 8. Decomposition of the total wave function configuration into its proton and neutron components for several positive- and negative-parity states in (a)–(f) ^{136}Ba and (g)–(l) ^{134}Xe, employing the GCN50:82 (filled blue boxes) and the SN100PN interaction (empty red boxes). Strongest components in the GCN50:82 interaction are labeled with corresponding percentages. The other configurations of both calculations are drawn with areas proportional to their percentages.

SN100PN calculations. Similarly to ^{134}Xe, the $J^\pi = 8^+$ state in ^{136}Ba is dominated by proton spins of (45%) $I_\pi = 8$ and (37%) $I_\pi = 6$, as displayed in Fig. 9(a).

The wave function of the isomeric $J^\pi = 10_1^+$ state in ^{136}Ba is dominated by the neutron $\nu(h_{11/2}^{-2})$ configuration with spins of 56% $\nu_{10^+} \otimes \pi_{0^+}$ and 30% $\nu_{10^+} \otimes \pi_{2^+}$. A major $\nu(h_{11/2}^{-2})$ configuration for the $J^\pi = 10_1^+$ state is also in accordance with the SN100PN and realistic SM calculations. Significant deviations between the calculations arise for the $J^\pi = 12_1^+$ state in ^{136}Ba. The decomposition matrix of the $J^\pi = 12_1^+$ bandhead of the positive-parity band computed by the GCN50:82 interaction, displayed in Fig. 8(d), shows an additional occupation of the neutron $d_{3/2}$ and $s_{1/2}$ orbital, which reduces the occupation of the $\nu(h_{11/2}^{-2})$ configuration.

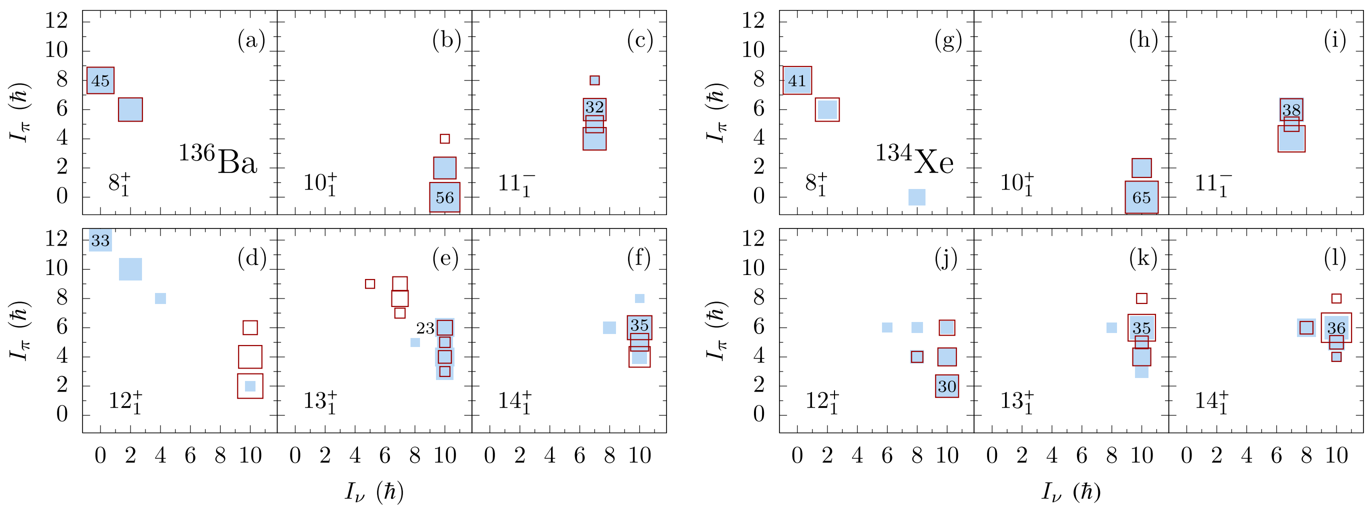

FIG. 9. Decomposition of the total angular momentum of selected states of (a)–(f) ^{136}Ba and (g)–(l) ^{134}Xe, using the GCN50:82 interaction (filled blue boxes) and the SN100PN interaction (empty red boxes) into their proton and neutron spins.

A declining impact of the $\nu(h_{11/2}^{-2})$ configuration of the $J^\pi = 12_1^+$ state in ^{136}Ba is also predicted by the realistic SM where $\pi(g_{7/2}^5 h_{11/2}^1) \otimes \nu(d_{3/2}^{-1} h_{11/2}^{-1})$ is computed as the main configuration with a probability of 51%. However, the SN100PN interaction does not predict a change of neutron occupation between the $J^\pi = 10_1^+$ and $J^\pi = 12_1^+$ states. Such discrepancies between both calculations are not observed for states in ^{134}Xe.

The differences in the predicted structure of the $J^\pi = 12^+$ state is mirrored in the spin composition, as visible in Fig. 9(d). While the SN100PN interaction predicts a dominant neutron spin of (91%) $I_\nu = 10^+$, the GCN50:82 predicts this fully aligned neutron-spin configuration to be insignificant (7%). Instead, major contributions stem from $\pi_{12^+} \otimes \nu_{0^+}$ and $\pi_{10^+} \otimes \nu_{2^+}$. The proton spin is generated dominantly by the $\pi(g_{7/2}^4 d_{5/2}^2)$ configuration with a maximum spin contribution of $I_\pi = 12$. The proton $h_{11/2}$ orbital does not contribute considerably (<2%) to the configuration of the $J^\pi = 12^+$ state using GCN50:82.

Going to higher spins along the positive-parity band, a strong $\nu(h_{11/2}^{-2})$ contribution returns to prevail for $J^\pi \geqslant 13_1^+$ states in the GCN50:82 calculation. Configurations including the neutron $d_{3/2}$ orbital become negligibly small in the GCN50:82 and SN100PN interactions. In contrast, the leading neutron configuration of the negative-parity states with $J^\pi > 10_1^-$ is $\nu(h_{11/2}^{-1} d_{3/2}^{-1})$. The neutron $\nu(h_{11/2}^{-2})$ configuration nearly vanishes in the decomposition of the negative-parity states.

The role of the different proton and neutron orbitals is further scrutinized by investigating the evolution of average occupation numbers of neutrons in the *gdsh* model space for several high-spin states in $N = 80$ isotones, as listed in Table II. In all even-mass isotones from ^{134}Xe to ^{138}Ce, the average occupation of the neutron $h_{11/2}$ orbital for the $J^\pi = 10^+$ states is $N_\nu \approx 10$, indicating a two-neutron $\nu h_{11/2}^{-2}$ configuration. However, in the GCN50:82 and realistic SM interactions, the $\nu d_{3/2}$ orbital is gaining significance for the $J^\pi = 11_1^-$ and 12_1^+ states from ^{136}Ba onwards. Furthermore, both states have only one neutron hole in the $\nu h_{11/2}$ orbital ($N_\nu \approx 11$). For completeness, the corresponding average occupation of the neutron $d_{3/2}$, $s_{1/2}$, and $h_{11/2}$ orbitals in the realistic SM calculation have values of 3.12, 1.99, 11.01 for the $J^\pi = 11_1^-$ state and 3.23, 1.87, 11.00 for the $J^\pi = 12_1^+$ state, respectively. Accordingly, proton configurations are vital to generate the spin, which is consistent with the results presented in Figs. 8(c) and 8(d). Hence, the configuration of the $J^\pi = 12_1^+$ state in ^{136}Ba, calculated by GCN50:82 and realistic SM, mirrors the configuration of the $J^\pi = 11_1^-$ state rather than that of the $J^\pi = 10_1^+$ state, which supports a decay of the $J^\pi = 12_1^+$ state into the $J^\pi = 11_1^-$ state.

The dominating proton configuration of the yrast $J^\pi = 8^+$ state causes the isomeric character of the two-neutron hole $J^\pi = 10_1^+$ state [3]. In a similar way, the unobserved $12^+ \rightarrow 10^+$ transition can be understood microscopically. ^{136}Ba is the lowest-mass isotone along the $N = 80$ chain in which an angular momentum of $J = 12$ can be generated exclusively from protons in the $g_{7/2}$ and $d_{5/2}$ orbitals [i.e., $\pi(g_{7/2}^4 d_{5/2}^2)$]. The dominating proton configuration of the $J^\pi = 12^+$ state, as calculated by the GCN50:82 interaction and the realistic-SM interaction, hinders a decay into the two-neutron hole $J^\pi = 10^+$ state. Calculated reduced transition probabilities $B(E2; 12^+ \rightarrow 10^+)$ underpin the reliability of the GCN50:82 and realistic-SM interaction. Corresponding values are compatible in ^{134}Xe (215 $e^2\,\mathrm{fm}^4$ with GCN50:82 and 222 $e^2\,\mathrm{fm}^4$ with SN100PN), while they differ significantly in ^{136}Ba: The larger proton component in the $J^\pi = 12^+$ state causes a lower $B(E2; 12^+ \rightarrow 10^+)$ value of 62 $e^2\,\mathrm{fm}^4$ in the GCN50:82 and of 3 $e^2\,\mathrm{fm}^4$ in the realistic-SM calculation, compared to $B(E2; 12^+ \rightarrow 10^+) = 375\,e^2\,\mathrm{fm}^4$ using SN100PN. The low $B(E2; 12^+ \rightarrow 10^+)$ values in the GCN50:82 and realistic-SM calculations is in agreement with the experimentally unobservability of this transition.

TABLE II. Average neutron occupation numbers in each single-particle orbit of the *gdsh* model space for observed high-spin states in ^{134}Xe, ^{136}Ba, and ^{138}Ce using the GCN50:82 and SN100PN interaction.

Isotope	J^π	$g_{7/2}$	$d_{5/2}$	$d_{3/2}$	$s_{1/2}$	$h_{11/2}$
				GCN50:81		
^{134}Xe	10_1^+	8.00	6.00	4.00	2.00	10.00
	11_1^-	7.97	5.97	3.06	1.99	11.00
	12_1^+	8.00	6.00	4.00	2.00	10.00
^{136}Ba	10_1^+	7.99	5.99	4.00	2.00	10.03
	11_1^-	7.96	5.96	3.09	1.99	11.00
	12_1^+	7.87	5.86	3.57	1.79	10.91
^{138}Ce	10_1^+	7.98	5.98	3.99	2.00	10.05
	11_1^-	7.94	5.95	3.11	1.99	11.00
	12_1^+	7.94	5.96	3.16	1.94	11.00
				SN100PN		
^{134}Xe	10_1^+	8.00	6.00	4.00	2.00	10.00
	11_1^-	7.98	5.96	3.07	1.99	11.00
	12_1^+	8.00	6.00	4.00	2.00	10.00
^{136}Ba	10_1^+	8.00	6.00	4.00	2.00	10.00
	11_1^-	7.97	5.95	3.11	1.98	11.00
	12_1^+	8.00	5.99	3.99	2.00	10.03
^{138}Ce	10_1^+	7.99	5.99	4.00	2.00	10.02
	11_1^-	7.95	5.93	3.13	1.99	11.00
	12_1^+	7.96	5.94	3.21	1.89	11.00

Interestingly, adding two protons to ^{136}Ba, the occupation number of $N_\nu \approx 11$ for the neutron $h_{11/2}$ orbital in Table II indicates that the SN100PN interaction predicts an emerging proton component for the $J^\pi = 12^+$ state in ^{138}Ce.

B. ^{137}Ba

Calculated level energies for states above the $J = 19/2^-$ isomer in ^{137}Ba [(c) GCN50:82; (d) PQM130; (e) realistic SM and (f) SN100PN], are compared to experimental level energies in Fig. 10. The pivotal $J = 11/2^-$ neutron-hole isomer at $E_x = 662$ keV is predicted at excitation energies of 534 (GCN50:82), 643 (realistic SM), 692 (PQM130), and 478 keV (SN100PN). The shell-model calculations compute the 120-1567-keV cascade to have γ-ray energies of 285-1396 (GCN50:82), 412-1491 (PQM130), and 231-1396 keV

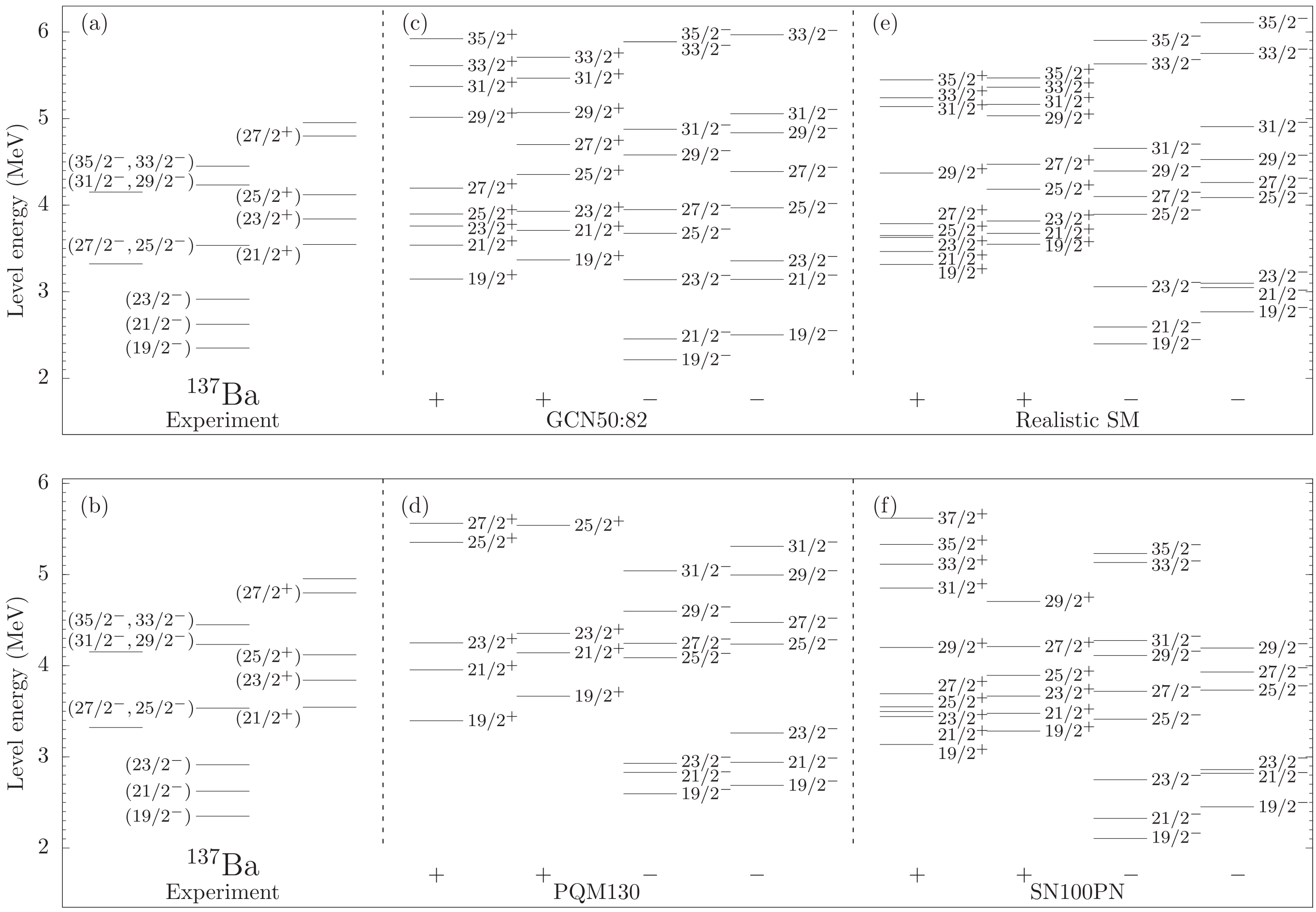

FIG. 10. Comparison of experimental energy spectra with the results of shell-model calculations for ^{137}Ba. Only states above the $J^\pi = 19/2^-$ state are displayed. For clarity, the states are separated into columns for positive- and negative-parity states, as well as for yrast and yrare excited states. (a),(b) Experimental energy spectra, shell-model results obtained with (c) GCN50:82, (d) PQM130, (e) realistic SM, and (f) SN100PN interactions.

(SN100PN). Going to higher spins, the energy differences in the four calculations between states of same spin and parity amount for up to 1 MeV.

In the calculated excitation pattern, the $J^\pi = 21/2^-_1$ states emerge at 240 (GCN50:82), 195 (realistic SM), 234 (PQM130), and 220 keV (SN100PN) above the $J^\pi = 19/2^-_1$ states. Moreover, $J^\pi = 23/2^-_1$ states are predicted 684 (GCN50:82), 465 (realistic SM), 100 (PQM130), and 425 keV (SN100PN) higher in excitation energy with respect to the $J^\pi = 21/2^-_1$ state. In accordance with the results of $\gamma\gamma$ angular-correlation measurements [see Figs. 6(b) and 6(e)], which confirmed mixed $M1/E2$ 289- and 275-keV transitions and therefore a parity-conserving 289-275-keV cascade, the $E_x = 2624$- and $E_x = 2913$-keV states are identified as the first excited $J^\pi = 21/2^-$ and $23/2^-$ states, respectively.

Going to higher spins along the negative-parity band, in particular GCN50:82 tend to group pairs of yrast spins ($J^\pi = 25/2^-$, $27/2^-$) and ($J^\pi = 29/2^-$, $31/2^-$). Both groups are separated by a larger energy gap compared to the energy gaps between both states within the group. This observation associates the $E_x = 3611$-keV state with $J^\pi = (25/2^-, 27/2^-)$ and the $E_x = 4233$-keV state with $J^\pi = (29/2^-, 31/2^-)$.

Similar to the $E_x = 2624$-keV state, also the spin of the $E_x = 3545$-keV state is measured to be of spin $J = 21/2$ [see Fig. 6(c)]. Positive-parity states of similar spin ($J \geqslant 19/2^+_1$) are calculated to appear at higher excitation energy than the $J^\pi = 19/2^-_1$ state. The energy difference between the $J^\pi = 19/2^-_1$ and $21/2^+_1$ states is predicted to be 1323 (GCN50:82), 1067 (realistic SM), 1360 (PQM130), and 1337 keV (SN100PN). In accordance with the experimental results obtained in the angular-correlation and angular-distribution investigations [see Figs. 6(c) and 6(f)], the state at $E_x = 3545$ keV is interpreted as the first excited $J^\pi = 21/2^+$ state and, thus, as the bandhead of the positive-parity band.

Moreover, assuming a $J = 23/2$ assignment for the 3841-keV state, the multipole-mixing ratio of the 296-keV transition is measured as $\delta = -0.09(3)$ which suggests that the 3841-keV state has the same parity as the 3545-keV state [see Fig. 6(f)]. Excited $J = 23/2^+_1$ states are calculated 152 to 453 keV above the $J = 21/2^+_1$ states. Consequently, a spin of $J^\pi = 23/2^+$ for the $E_x = 3841$-keV state is in agreement with shell-model calculations.

Due to the large density of predicted states above 4 MeV, no unambiguous assignment for the $E_x = 4120$- and 4799-keV states is possible. Since both states do not exhibit decay

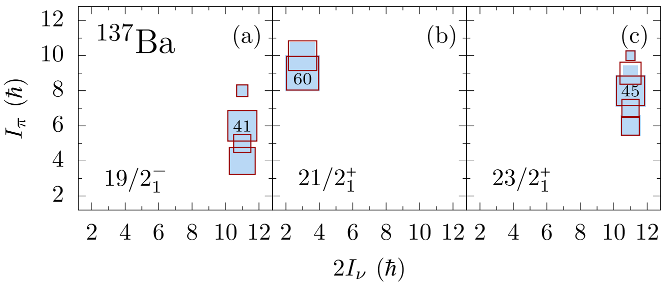

FIG. 11. Decomposition of the total angular momentum of selected states of ^{137}Ba, using the GCN50:82 interaction (filled blue boxes) and the SN100PN interaction (empty red boxes) into their proton and neutron spins $I_\pi \otimes I_\nu$.

branches into the $J^\pi = 19/2^-$ or $21/2^-$ state, they have most likely spins $J > 23/2$. By a similar argument the 3322- and 4152-keV states are interpreted to have a spin of $J > 21/2$. Otherwise, they would directly decay to the $J^\pi = 19/2^-$ state.

The theoretical wave functions of ^{137}Ba are not as fragmented as in ^{136}Ba. The decomposition of the total angular momentum $I = I_\pi \otimes I_\nu$ into its proton and neutron components for the $J^\pi = 19/2_1^-$, $21/2_1^+$, and $23/2_1^+$ states in ^{137}Ba predicted by the GCN50:82 and SN100PN is presented in Fig. 11. Table III shows the calculated average neutron occupation numbers of each orbital in the *gdsh* model space. For GCN50:82, the $J^\pi = 19/2_1^-$ isomer consists mainly (29%) of the $\nu h_{11/2}^{-1} \otimes \pi(g_{7/2}^5 d_{5/2}^1)$, 21% of the $\nu h_{11/2}^{-1} \otimes \pi(g_{7/2}^3 d_{5/2}^3)$, and 13% of the $\nu h_{11/2}^{-1} \otimes \pi(g_{7/2}^4 d_{5/2}^2)$ configuration. The dominating neutron-hole $\nu h_{11/2}^{-1}$ configuration is also visible in the average occupation numbers with an occupation of $N_\nu \approx 11$ in the neutron $h_{11/2}$ orbital. Also the SN100PN and the realistic-SM calculation predict a strong neutron-hole $\nu h_{11/2}^{-1}$ configuration for the $J^\pi = 19/2_1^-$ state. Couplings of this configuration to proton configurations with spins of 4^+ (33%), 5^+ (16%), and 6^+ (41%) contribute to the $J^\pi = 19/2_1^-$ state. Also for the $J^\pi = 21/2^-$, $J^\pi = 23/2^-$, and higher-lying negative-parity states the neutron $\nu h_{11/2}^{-1}$ configuration dominates.

The positive-parity bands in ^{136}Ba and ^{137}Ba have mirroring structures. In each nucleus, positive-parity bands are connected via a high-energy (≈1.2 MeV) transition to the negative-parity band. Like the $J^\pi = 12^+$ bandhead in ^{136}Ba, the $J^\pi = 21/2^+$ bandhead in ^{137}Ba shows a smaller degree of $\nu d_{3/2}$ occupation than for the $J^\pi = 19/2^-$ state. The $\nu h_{11/2}$ orbital becomes fully occupied, as calculated by GCN50:82, realistic SM, and SN100PN (see Table III). GCN50:82 predicts a mixture of (67%) $\nu d_{3/2}^{-1} \otimes \pi(g_{7/2}^5 d_{5/2}^1)$ and (11%) $\nu d_{3/2}^{-1} \otimes \pi(g_{7/2}^3 d_{5/2}^3)$ with dominating proton-spin components of $I_\pi = 9^+$ and 10^+ coupled to neutron spin $I_\nu = 3/2^+$ in the $J^\pi = 21/2^+$ state in ^{137}Ba. All three interactions predict a similar structure for the $J^\pi = 21/2^+$ state. From the second excited state in this band onwards ($J^\pi \geqslant 23/2_1^+$), the valence neutron hole is mainly occupying the $\nu h_{11/2}$ orbital. As a consequence a dominating neutron spin of $I_\nu = 11/2^-$ returns to prevail, as shown in Fig. 11(c). According to the distinct similarities of the configurations, the $J^\pi = 21/2^+$ bandhead in ^{137}Ba can be interpreted as the configuration of the $J^\pi = 12^+$ state in ^{136}Ba coupled to a $\nu h_{11/2}$ neutron hole. Interestingly, in ^{137}Ba SN100PN is able to describe the predominant proton character of the $J^\pi = 21/2^+$ state, which is the $J^\pi = 12^+$ state analogon in the even-even core ^{136}Ba, to which a single neutron is coupled, but it is unable to describe the proton structure of the $J^\pi = 12^+$ state in ^{136}Ba.

TABLE III. Average neutron occupation numbers in each single-particle orbit of the *gdsh* model space in ^{137}Ba, calculated using the GCN50:82 and SN100PN interaction.

J^π	$g_{7/2}$	$d_{5/2}$	$d_{3/2}$	$s_{1/2}$	$h_{11/2}$
		GCN50:82			
$19/2_1^-$	8.00	6.00	4.00	2.00	11.00
$21/2_1^+$	7.98	5.98	3.07	1.98	11.99
$23/2_1^+$	8.00	6.00	4.00	2.00	11.00
		SN100PN			
$19/2_1^-$	8.00	6.00	4.00	2.00	11.00
$21/2_1^+$	7.99	5.98	3.08	1.96	12.00
$23/2_1^+$	8.00	6.00	4.00	2.00	11.00

V. CONCLUSIONS

In summary, four experiments employing two ^{9}Be + ^{130}Te and one ^{11}B + ^{130}Te fusion-evaporation reactions as well as the ^{136}Xe + ^{238}U multinucleon-transfer reaction were used to investigate high-spin states above the $J^\pi = 10^+$ isomer in ^{136}Ba and above the $J^\pi = 19/2^-$ isomer in ^{137}Ba. The level scheme of ^{136}Ba was revised, incorporating nine new states and transitions. Proper spin and multipolarity assignments were determined by γ-ray angular distribution measurements and $\gamma\gamma$ coincidence relations. The $E_x = 4920$-keV state is identified as the $J^\pi = 12^+$ state. The high-spin regime of ^{136}Ba differs significantly from the lower mass isotones.

While the high-spin regimes of both ^{132}Te and ^{134}Xe exhibit high-energy $12^+ \rightarrow 10^+$ yrast transitions, no such transition is observed in ^{136}Ba. Instead the $J^\pi = 10^+$ isomer is fed by a $J^\pi = 11^-$ state. This disruption in the nuclear structure along the $N = 80$ isotones is explained by a dominant proton configuration of the $J^\pi = 12^+$ state in ^{136}Ba. While the $J^\pi = 10^+$ isomer consists mainly of neutron configurations, a pure proton configuration for the $J^\pi = 12^+$ state and the interrupting $J^\pi = 11^-$ state is energetically favorable compared to the continuation via a $\nu h_{11/2}$ configuration. The configuration of the $J^\pi = 12^+$ state mirrors the structure of the $J^\pi = 8^+$ state below the isomer. ^{136}Ba is the first isotone along $N = 80$ for which a combined proton alignment in the $g_{7/2}$ and $d_{5/2}$ orbitals can form a spin of $J = 12$. Corresponding shell-model calculations yield ambiguous results. Only the SN100PN interaction predicts a predominant neutron character of the $J^\pi = 12^+$ state, while GCN50:82 and realistic SM exhibit the emerging proton configuration. In previous publications, it was found that the proton-neutron part of the SN100PN interaction falls short to reproduce several nuclear-structure features in the mass region. SN100PN could not reproduce backbending in the high-spin regime of ^{131}Xe [70] and the decay features of isomeric states in ^{135}Xe and ^{137}Ba [20]. Similar conclusions on the monopole part were also discussed in Ref. [71]. In the present study, it is worthy of attention that only interactions with improved and corrected monopole parts, i.e., GCN50:82 and realistic SM, reproduce the nonobservation of the $12^+ \rightarrow 10^+$ transition by the different structure of these two levels.

In ^{137}Ba spins above the $J^\pi = 19/2^-$ isomer at $E_x = 2350$ keV were measured for the first time. The $E_x = 3545$-keV state is proposed to be the bandhead of the positive-parity band, which is explained as the coupling of the aforementioned $J^\pi = 12^+$ state of the even-even core ^{136}Ba and a neutron. The identification of the high-spin structures complete the systematics for $N = 80$ and $N = 81$ isotones in the vicinity of the $N = 82$ shell closure. In future, measurements of lifetimes and g factors that serve as sensitive probes for nucleon alignment should be performed to independently confirm the proposed proton character of the positive-parity bandheads in ^{136}Ba and ^{137}Ba.

ACKNOWLEDGMENTS

We thank the IKP FN Tandem accelerator team for the support during the experiment. Furthermore, we express our thanks to Dr. E. Teruya and Dr. N. Yoshinaga from Saitama University, Japan, for providing the results of their shell-model calculation with the PQM130 interaction. The research leading to these results has received funding from the German BMBF under Contracts No. 05P15PKFN9 TP1 and No. 05P18PKFN9 TP1, from the European Union Seventh Framework Programme FP7/2007-2013 under Grant Agreement No. 262010 - ENSAR, from the Spanish Ministerio de Ciencia e Innovación under Contract No. FPA2011-29854-C04, from the Spanish Ministerio de Economía y Competitividad under Contract No. FPA2014-57196-C5, and from the UK Science and Technology Facilities Council (STFC). L.K. and A.V. thank the Bonn-Cologne Graduate School of Physics and Astronomy (BCGS) for financial support. One of the authors (A. Gadea) has been supported by the Generalitat Valenciana, Spain, under Grant No. PROMETEOII/2014/019, and EU under the FEDER program.

[1] B. Fogelberg, K. Heyde, and J. Sau, Energy levels and transition probabilities in ^{130}Sn, Nucl. Phys. A **352**, 157 (1981).

[2] J. Genevey, J. A. Pinston, C. Foin, M. Rejmund, R. F. Casten, H. Faust, and S. Oberstedt, Conversion electron measurements of isomeric transitions in ^{130,132}Te and ^{134}Xe, Phys. Rev. C **63**, 054315 (2001).

[3] J. J. Valiente-Dobón, P. H. Regan, C. Wheldon, C. Y. Wu, N. Yoshinaga, K. Higashiyama, J. F. Smith, D. Cline, R. S. Chakrawarthy, R. Chapman, M. Cromaz, P. Fallon, S. J. Freeman, A. Görgen, W. Gelletly, A. Hayes, H. Hua, S. D. Langdown, I. Y. Lee, X. Liang *et al.*, ^{136}Ba studied via deep-inelastic collisions: Identification of the $(\nu h_{11/2})^{-2}_{10^+}$ isomer, Phys. Rev. C **69**, 024316 (2004).

[4] J. Ludziejewski, J. Bialkowski, Z. Haratym, L.-E. de Geer, A. Kerek, and J. Kozyczkowski, The life-time measurements of some high-spin states in the ^{138,139}Ce and ^{141,142}Nd nuclei, Phys. Scr. **14**, 133 (1976).

[5] J. C. Merdinger, F. A. Beck, E. Bozek, T. Byrski, C. Gehringer, Y. Schutz, and J. P. Vivien, Magnetic moments of the $I^\pi = 10^+$ isomers in Ce and Nd $N = 80$ isotones, Nucl. Phys. A **346**, 281 (1980).

[6] M. Lach, J. Styczen, R. Julin, M. Piiparinen, H. Beuscher, P. Kleinheinz, and J. Blomqvist, The 10^+ states of $\nu h^{-2}_{11/2}$ and $\pi h^2_{11/2}$ character in the $N = 80$ isotones ^{144}Gd and ^{142}Sm, Z. Phys. A **319**, 235 (1984).

[7] H. A. Roth, S. E. Arnell, D. Foltescu, Ö. Skeppstedt, J. Blomqvist, G. de Angelis, D. Bazzacco, and S. Lunardi, Yrast level structure of the neutron-deficient $N = 80$ isotones ^{146}Dy, ^{147}Ho and ^{148}Er up to high-spin values, Eur. Phys. J. A **10**, 275 (2001).

[8] S. Biswas, R. Palit, A. Navin, M. Rejmund, A. Bisoi, M. S. Sarkar, S. Sarkar, S. Bhattacharyya, D. C. Biswas, M. Caamaño, M. P. Carpenter, D. Choudhury, E. Clément, L. S. Danu, O. Delaune, F. Farget, G. de France, S. S. Hota, B. Jacquot, A. Lemasson *et al.*, Structure of $^{132}_{52}$Te$_{80}$: The two-particle and two-hole spectrum of $^{132}_{50}$Sn$_{82}$, Phys. Rev. C **93**, 034324 (2016).

[9] A. Vogt, B. Birkenbach, P. Reiter, A. Blazhev, M. Siciliano, J. J. Valiente-Dobón, C. Wheldon, D. Bazzacco, M. Bowry, A. Bracco, B. Bruyneel, R. S. Chakrawarthy, R. Chapman, D. Cline, L. Corradi, F. C. L. Crespi, M. Cromaz, G. de Angelis, J. Eberth, P. Fallon *et al.*, High-spin structure of ^{134}Xe, Phys. Rev. C **93**, 054325 (2016).

[10] P. J. Rothschild, A. M. Baxter, S. M. Burnett, M. P. Fewell, G. J. Gyapong, and R. H. Spear, Quadrupole moment of the first excited state of ^{136}Ba, Phys. Rev. C **34**, 732 (1986).

[11] M. Ohshima, S. Hayashibe, N. Kawamura, Y. Itoh, M. Fujioka, and T. Ishimatsu, Magnetic moment of the 2140.2 kev 5^- state in ^{136}Ba, Hyperfine Interact. **7**, 103 (1979).

[12] W. Gelletly, J. A. Moragues, M. A. J. Mariscotti, and W. R. Kane, ^{135}Ba(n,γ) reaction and level structure of ^{136}Ba, Phys. Rev. **181**, 1682 (1969).

[13] E. Dragulescu, G. Semenescu, and I. Iftimia, Nuclear structure studies of nuclei near $N = 80$, J. Phys. **53**, 447 (1999).

[14] T. Shizuma, Z. G. Gan, K. Ogawa, H. Nakada, M. Oshima, Y. Toh, T. Hayakawa, Y. Hatsukawa, M. Sugawara, Y. Utsuno, and Z. Liu, A new isomer in ^{136}Ba populated by deep inelastic collisions, Eur. Phys. J. A **20**, 207 (2004).

[15] T. Bhattacharjee, S. Chanda, S. Bhattacharyya, S. K. Basu, R. K. Bhowmik, J. J. Das, U. Datta Pramanik, S. S. Ghugre, N. Madhavan, A. Mukherjee, G. Mukherjee, S. Muralithar, and R. P. Singh, Band structures in near spherical ^{138}Ce, Nucl. Phys. A **825**, 16 (2009).

[16] C. M. Petrache, M. Fantuzi, G. LoBianco, D. Mengoni, A. Neusser-Neffgen, H. Hübel, A. Al-Khatib, P. Bringel, A. Bürger, N. Nenoff, G. Schönwasser, A. K. Singh, I. Ragnarsson, G. B. Hagemann, B. Herskind, D. R. Jensen, G. Sletten, P. Fallon, A. Görgen, P. Bednarczyk *et al.*, Evolution from spherical single-particle structure to stable triaxiality at high spins in ^{140}Nd, Phys. Rev. C **72**, 064318 (2005).

[17] E. Gülmez, H. Li, and J. A. Cizewski, Level structure of ^{140}Nd, Phys. Rev. C **36**, 2371 (1987).

[18] C. M. Petrache, R. A. Bark, S. T. H. Murray, M. Fantuzi, E. A. Lawrie, S. Lang, J. J. Lawrie, S. M. Maliage, D. Mengoni, S. M. Mullins, S. S. Ntshangase, D. Petrache, T. M. Ramashidzha, and I. Ragnarsson, Six-quasiparticle isomer in ^{140}Nd, Phys. Rev. C **74**, 034304 (2006).

[19] M. Ferraton, R. Bourgain, C. M. Petrache, D. Verney, F. Ibrahim, N. de Séréville, S. Franchoo, M. Lebois, C. Phan Viet, L. Sagui, I. Stefan, J. F. Clavelin, and M. Vilmay, Lifetime measurement of the six-quasiparticle isomer in ^{140}Nd and evidence for an isomer above the $19/2^+$ state in ^{139}Nd, Eur. Phys. J. A **35**, 167 (2008).

[20] A. Vogt, B. Birkenbach, P. Reiter, A. Blazhev, M. Siciliano, K. Hadyńska-Klęk, J. J. Valiente-Dobón, C. Wheldon, E. Teruya, N. Yoshinaga, K. Arnswald, D. Bazzacco, M. Bowry, A. Bracco, B. Bruyneel, R. S. Chakrawarthy, R. Chapman, D. Cline, L. Corradi, F. C. L Crespi et al., Isomers and high-spin structures in the $N = 81$ isotones ^{135}Xe and ^{137}Ba, Phys. Rev. C **95**, 024316 (2017).

[21] A. Kerek and J. Kownacki, The level structure of the $N = 81$ and 82 nucleides ^{137,138}Ba as investigated in ^{136}Xe(α, xn) reactions, Nucl. Phys. A **206**, 245 (1973).

[22] Evaluated Nuclear Structure Data File (ENSDF), http://www.nndc.bnl.gov/ensdf

[23] S. Kaim, C. M. Petrache, A. Gargano, N. Itaco, T. Zerrouki, R. Leguillon, A. Astier, I. Deloncle, T. Konstantinopoulos, J. M. Régis, D. Wilmsen, B. Melon, A. Nannini, C. Ducoin, D. Guinet, and T. Bhattacharjee, High-spin spectroscopy of ^{139}Ce, Phys. Rev. C **91**, 024318 (2015).

[24] P. Bhattacharyya, P. J. Daly, C. T. Zhang, Z. W. Grabowski, S. K. Saha, B. Fornal, R. Broda, W. Urban, I. Ahmad, D. Seweryniak, I. Wiedenhöver, M. P. Carpenter, R. V. F. Janssens, T. L. Khoo, T. Lauritsen, C. J. Lister, P. Reiter, and J. Blomqvist, Yrast excitations in $n = 81$ nuclei ^{132}Sb and ^{133}Te from ^{248}Cm fission, Phys. Rev. C **64**, 054312 (2001).

[25] J. K. Hwang, A. V. Ramayya, J. H. Hamilton, C. J. Beyer, J. O. Rasmussen, Y. X. Luo, S. C. Wu, T. N. Ginter, C. M. Folden, P. Fallon, P. M. Zielinski, K. E. Gregorich, A. O. Macchiavelli, M. Stoyer, S. J. Asztalos, A. Covello, and A. Gargano, Particle-hole excited states in ^{133}Te, Phys. Rev. C **65**, 034319 (2002).

[26] Yu. Khazov, A. Rodionov, and F. G. Kondev, Nuclear data sheets for $A = 133$, Nucl. Data Sheets **112**, 855 (2011).

[27] B. K. Wagner, P. E. Garrett, Minfang Yeh, and S. W. Yates, On the first excited state of ^{137}Ba, J. Radioanal. Nucl. Chem. **219**, 217 (1997).

[28] I. Bikit, I. Aničin, J. Slivka, M. Krmar, J. Puzović, and Lj. Čonkić, Population of the 283 keV level of ^{137}Ba by the β decay of ^{137}Cs, Phys. Rev. C **54**, 3270 (1996).

[29] V. A. Bondarenko, I. L. Kuvaga, P. T. Prokofjev, A. M. Sukhovoj, V. A. Khitrov, Yu. P. Popov, S. Brant, and V. Paar, Levels of ^{137}Ba studied with neutron-induced reactions, Nucl. Phys. A **582**, 1 (1995).

[30] E. Dragulescu, M. Ivascu, R. Mihu, D. Popescu, G. Semenescu, A. Velenik, and V. Paar, Coulomb excitation of levels in ^{135}Ba and ^{137}Ba, J. Phys. G **10**, 1099 (1984).

[31] S. Chanda, T. Bhattacharjee, S. Bhattacharyya, A. Mukherjee, S. K. Basu, I. Ragnarsson, R. K. Bhowmik, S. Muralithar, R. P. Singh, S. S. Ghugre, and U. D. Pramanik, Seven-quasiparticle bands in ^{139}Ce, Phys. Rev. C **79**, 054332 (2009).

[32] D. Bucurescu, G. Căta-Danil, I. Căta-Danil, M. Ivaşcu, N. Mărginean, R. Mărginean, L. C. Mihăilescu, C. Rusu, and G. Suliman, Gamma-ray spectroscopy of the nucleus ^{139}Ce, Eur. Phys. J. A **27**, 301 (2006).

[33] S. Bhowal, C. Lahiri, R. Raut, P. Singh, M. K. Raju, A. Goswami, A. K. Singh, S. Bhattacharya, T. Bhattacharjee, G. Mukherjee et al., Energy levels in ^{141}Nd from fusion evaporation study, J. Phys. G. **38**, 035105 (2011).

[34] T. Zerrouki, C. M. Petrache, R. Leguillon, K. Hauschild, A. Korichi, A. Lopez Martens, S. Frauendorf, I. Ragnarsson, H. Hübel, A. Neußer-Neffgen, A. Al-Khatib, P. Bringel, A. Bürger, N. Nenoff, G. Schönwaßer, A. K. Singh, D. Curien, G. B. Hagemann, B. Herskind, G. Sletten, P. Fallon, A. Görgen, and P. Bednarczyk, Shape evolution and magnetic rotation in ^{141}Nd, Eur. Phys. J. A **51**, 50 (2015).

[35] S. Akkoyun et al., AGATA – Advanced GAmma Tracking Array, Nucl. Instrum. Methods Phys. Res., Sect. A **668**, 26 (2012).

[36] A. M. Stefanini, L. Corradi, G. Maron, A. Pisent, M. Trotta, A. M. Vinodkumar, S. Beghini, G. Montagnoli, F. Scarlassara, G. F. Segato, A. De Rosa, G. Inglima, D. Pierroutsakou, M. Romoli, M. Sandoli, G. Pollarolo, and A. Latina, The heavy-ion magnetic spectrometer PRISMA, Nucl. Phys. A **701**, 217 (2002).

[37] L. Corradi, S. Szilner, G. Pollarolo, D. Montanari, E. Fioretto, A. M. Stefanini, J. J. Valiente-Dobón, E. Farnea, C. Michelagnoli, G. Montagnoli, F. Scarlassara, C. A. Ur, T. Mijatović, D. Jelavić Malenica, N. Soić, and F. Haas, Multinucleon transfer reactions: Present status and perspectives, Nucl. Instrum. Methods Phys. Res., Sect. B **317**, 743 (2013).

[38] S. Szilner, C. A. Ur, L. Corradi, N. Marginean, G. Pollarolo, A. M. Stefanini, S. Beghini, B. R. Behera, E. Fioretto, A. Gadea, B. Guiot, A. Latina, P. Mason, G. Montagnoli, F. Scarlassara, M. Trotta, G. de Angelis, F. Della Vedova, E. Farnea, F. Haas et al., Multinucleon transfer reactions in closed-shell nuclei, Phys. Rev. C **76**, 024604 (2007).

[39] L. Netterdon, V. Derya, J. Endres, C. Fransen, A. Hennig, J. Mayer, C. Müller-Gatermann, A. Sauerwein, P. Scholz, M. Spieker, and A. Zilges, The γ-ray spectrometer HORUS and its applications for nuclear astrophysics, Nucl. Instrum. Methods Phys. Res., Sect. A **754**, 94 (2014).

[40] A. Gadea, E. Farnea, J. J. Valiente-Dobón, B. Million, D. Mengoni, D. Bazzacco, F. Recchia, A. Dewald, Th. Pissulla, W. Rother, G. de Angelis et al., Conceptual design and infrastructure for the installation of the first AGATA sub-array at LNL, Nucl. Instrum. Methods Phys. Res., Sect. A **654**, 88 (2011).

[41] A. Wiens, H. Hess, B. Birkenbach, B. Bruyneel, J. Eberth, D. Lersch, G. Pascovici, P. Reiter, and H.-G. Thomas, The AGATA triple cluster detector, Nucl. Instrum. Methods Phys. Res., Sect. A **618**, 223 (2010).

[42] B. Bruyneel, B. Birkenbach, and P. Reiter, Pulse shape analysis and position determination in segmented HPGe detectors: The AGATA detector library, Eur. Phys. J. A **52**, 70 (2016).

[43] A. Lopez-Martens, K. Hauschild, A. Korichi, J. Roccaz, and J.-P. Thibaud, γ-ray tracking algorithms: a comparison, Nucl. Instrum. Methods Phys. Res., Sect. A **533**, 454 (2004).

[44] A. Vogt, B. Birkenbach, P. Reiter, L. Corradi, T. Mijatović, D. Montanari, S. Szilner, D. Bazzacco, M. Bowry, A. Bracco, B. Bruyneel, F. C. L. Crespi, G. de Angelis, P. Désesquelles, J. Eberth, E. Farnea, E. Fioretto, A. Gadea, K. Geibel, A.

Gengelbach *et al.*, Light and heavy transfer products in ^{136}Xe + ^{238}U multinucleon transfer reactions, Phys. Rev. C **92**, 024619 (2015).
[45] N. Saed-Samii, Lifetime measurements using the FATIMA array in combination with EXOGAM@ILL, Diplomarbeit, Universität zu Köln (unpublished).
[46] J. Theuerkauf, Die Analyse von zwei- und mehrdimensionalen $\gamma\gamma$-Koinzidenzspektren an Beispielen aus Hochspinexperimenten in der Massengegend um ^{146}Gd, Ph.D. thesis, Universität zu Köln, 1994.
[47] I. Wiedenhöver, computer code CORLEONE, 1997.
[48] I. Wiedenhöver, O. Vogel, H. Klein, A. Dewald, P. von Brentano, J. Gableske, R. Krücken, N. Nicolay, A. Gelberg, P. Petkov, A. Gizon, J. Gizon, D. Bazzaco, C. Rossi Alvarez, G. de Angelis, S. Lunardi, P. Pavan, D. R. Napoli, S. Frauendorf, F. Dönau, R. V. F. Janssens, and M. P. Carpenter, Detailed angular correlation analysis with 4π spectrometers: Spin determinations and multipolarity mixing measurements in ^{128}Ba, Phys. Rev. C **58**, 721 (1998).
[49] K. S. Krane and R. M. Steffen, Determination of the $E2/M1$ Multipole Mixing Ratios of the Gamma Transitions in ^{110}Cd, Phys. Rev. C **2**, 724 (1970).
[50] K. S. Krane, R. M. Steffen, and R. M. Wheeler, Directional correlations of gamma radiations emitted from nuclear states oriented by nuclear reactions or cryogenic methods, At. Data Nucl. Data Tables **11**, 351 (1973).
[51] A. Linnemann, Das HORUS-Würfelspektrometer und Multiphononanregungen in ^{106}Cd, Ph.D. thesis, Universität zu Köln, 2006.
[52] L. Bettermann, C. Fransen, S. Heinze, J. Jolie, A. Linnemann, D. Mücher, W. Rother, T. Ahn, A. Costin, N. Pietralla, and Y. Luo, Candidates for the one-phonon mixed-symmetry state in ^{130}Xe, Phys. Rev. C **79**, 034315 (2009).
[53] S. Kumar, A. K. Jain, Alpana Goel, S. S. Malik, R. Palit, H. C. Jain, I. Mazumdar, P. K. Joshi, Z. Naik, A. Dhal, T. Trivedi, I. Mehrotra, S. Appannababu, L. Chaturvedi, V. Kumar, R. Kumar, D. Negi, R. P. Singh, S. Muralithar, R. K. Bhowmik, and S. C. Pancholi, Band structure and shape coexistence in $^{135}_{56}$Ba$_{79}$, Phys. Rev. C **81**, 067304 (2010).
[54] S. Chanda, T. Bhattacharjee, S. Bhattacharyya, S. K. Basu, R. K. Bhowmik, S. Muralithar, R.P. Singh, B. Mukherjee, N. S. Pattabiraman, S. S. Ghugre, and M. B. Chatterjee, High spin spectroscopy of ^{137}La, Nucl Phys. A **775**, 153 (2006).
[55] T. Yamazaki, Tables of coefficients for angular distribution of gamma rays from aligned nuclei, Nucl. Data, Sect. A **3**, 1 (1967).
[56] Y. Khazov, A. A. Roionpv, S. Sakharov, and B. Singh, Nuclear data sheets for $A = 132$, Nucl. Data Sheets **104**, 497 (2005).
[57] M. Kortelahti, A. Pakkanen, M. Piiparinen, T. Komppa, and R. Komu, Medium-spin levels and a 360 ns $I^\pi = 19/2^-$ isomer in the $N = 80$ nucleus ^{137}La, Nucl. Phys. A **376**, 1 (1982).
[58] B. A. Brown and W. D. M. Rae, The Shell-Model Code NuShellX@MSU, Nucl. Data Sheets **120**, 115 (2014).
[59] N. Shimizu, Nuclear shell-model code for massive parallel computation, "KSHELL", arXiv:1310.5431.
[60] E. Caurier, G. Martínez-Pinedo, F. Nowacki, A. Poves, and A. P. Zuker, The shell model as a unified view of nuclear structure, Rev. Mod. Phys. **77**, 427 (2005).
[61] E. Caurier, F. Nowacki, A. Poves, and K. Sieja, Collectivity in the light xenon isotopes: A shell model study, Phys. Rev. C **82**, 064304 (2010).
[62] E. Caurier, F. Nowacki, and A. Poves, Shell Model description of the $\beta\beta$ decay of ^{136}Xe, Phys. Lett. B **711**, 62 (2012).
[63] R. Machleidt, F. Sammarruca, and Y. Song, Nonlocal nature of the nuclear force and its impact on nuclear structure, Phys. Rev. C **53**, R1483 (1996).
[64] L. Coraggio, A. Covello, A. Gargano, N. Itaco, and T. T. S. Kuo, Effective shell-model hamiltonians from realistic nucleon-nucleon potentials within a perturbative approach, Ann. Phys. **327**, 2125 (2012).
[65] L. Coraggio, A. Covello, A. Gargano, N. Itaco, and T. T. S. Kuo, Shell-model calculations and realistic effective interactions, Prog. Part. Nucl. Phys. **62**, 135 (2009).
[66] L. Coraggio, L. De Angelis, T. Fukui, A. Gargano, and N. Itaco, Calculation of gamow-teller and two-neutrino double-β decay properties for ^{130}Te and ^{136}Xe with a realistic nucleon-nucleon potential, Phys. Rev. C **95**, 064324 (2017).
[67] E. Teruya, N. Yoshinaga, K. Higashiyama, and A. Odahara, Shell-model calculations of nuclei around mass 130, Phys. Rev. C **92**, 034320 (2015).
[68] K. Higashiyama and N. Yoshinaga, Pair-truncated shell-model analysis of nuclei around mass 130, Phys. Rev. C **83**, 034321 (2011).
[69] B. A. Brown, N. J. Stone, J. R. Stone, I. S. Towner, and M. Hjorth-Jensen, Magnetic moments of the 2_1^+ states around ^{132}Sn, Phys. Rev. C **71**, 044317 (2005).
[70] L. Kaya, A. Vogt, P. Reiter, M. Siciliano, B. Birkenbach, A. Blazhev, L. Coraggio, E. Teruya, N. Yoshinaga, K. Higashiyama, K. Arnswald, D. Bazzacco, A. Bracco, B. Bruyneel, L. Corradi, F. C. L. Crespi, G. de Angelis, J. Eberth, E. Farnea, E. Fioretto *et al.*, High-spin structure in the transitional nucleus ^{131}Xe: Competitive neutron and proton alignment in the vicinity of the $N = 82$ shell closure, Phys. Rev. C **98**, 014309 (2018).
[71] Y. Utsuno, T. Otsuka, N. Shimizu, M. Honma, T. Mizusaki, Y. Tsunoda, and T. Abe, Recent shell-model results for exotic nuclei, EPJ Web Conf. **66**, 02106 (2014).

Publication IV: Isomer spectroscopy in ^{133}Ba and high-spin structure of ^{134}Ba

Isomer spectroscopy in ^{133}Ba and high-spin structure of ^{134}Ba

L. Kaya,[1,*] A. Vogt,[1] P. Reiter,[1] M. Siciliano,[2,3,4] N. Shimizu,[5] Y. Utsuno,[5,6] H.-K. Wang,[7] A. Gargano,[8] L. Coraggio,[8] N. Itaco,[8,9] K. Arnswald,[1] D. Bazzacco,[10] B. Birkenbach,[1] A. Blazhev,[1] A. Bracco,[11] B. Bruyneel,[4] L. Corradi,[3] F. C. L. Crespi,[11] G. de Angelis,[3] M. Droste,[1] J. Eberth,[1] A. Esmaylzadeh,[1] E. Farnea,[10,†] E. Fioretto,[3] C. Fransen,[1] A. Gadea,[12] A. Giaz,[11] A. Görgen,[13,4] A. Gottardo,[3] K. Hadyńska-Klęk,[3] H. Hess,[1] R. Hirsch,[1] P. R. John,[14] J. Jolie,[1] A. Jungclaus,[15] V. Karayonchev,[1] L. Kornwebel,[1] W. Korten,[4] S. Leoni,[11] L. Lewandowski,[1] S. Lunardi,[2,10] R. Menegazzo,[10] D. Mengoni,[2,10] C. Michelagnoli,[16] T. Mijatović,[17] G. Montagnoli,[2,10] D. Montanari,[2,10] C. Müller-Gatermann,[1] D. Napoli,[3] Zs. Podolyák,[18] G. Pollarolo,[19] F. Recchia,[2,10] J.-M. Régis,[1] N. Saed-Samii,[1] E. Şahin,[13] F. Scarlassara,[2,10] K. Schomacker,[1] M. Seidlitz,[1] B. Siebeck,[1] P.-A. Söderström,[20] A. M. Stefanini,[3] O. Stezowski,[21] S. Szilner,[17] B. Szpak,[22] E. Teruya,[23] C. Ur,[10] J. J. Valiente-Dobón,[3] K. Wolf,[1] K. Yanase,[23] N. Yoshinaga,[23] and K. O. Zell[1]

[1]*Institut für Kernphysik, Universität zu Köln, D-50937 Köln, Germany*
[2]*Dipartimento di Fisica e Astronomia, Università di Padova, I-35131 Padova, Italy*
[3]*Istituto Nazionale di Fisica Nucleare, Laboratori Nazionali di Legnaro, I-35020 Legnaro, Italy*
[4]*Institut de Recherche sur les lois Fondamentales de l'Univers – IRFU, CEA/DSM, Université de Paris-Saclay, F-91191 Gif-sur-Yvette Cedex, France*
[5]*Center for Nuclear Study, The University of Tokyo, Hongo, Bunkyo-ku, Tokyo 113-0033, Japan*
[6]*Advanced Science Research Center, Japan Atomic Energy Agency, Tokai, Ibaraki 319-1195, Japan*
[7]*College of Physics and Telecommunication Engineering, Zhoukou Normal University, Henan 466000, People's Republic of China*
[8]*Istituto Nazionale di Fisica Nucleare, Sezione di Napoli, I-80126 Napoli, Italy*
[9]*Dipartimento di Matematica e Fisica, Università degli Studi della Campania "Luigi Vanvitelli," I-8110 Caserta, Italy*
[10]*Istituto Nazionale di Fisica Nucleare, Sezione di Padova, I-35131 Padova, Italy*
[11]*Dipartimento di Fisica, Università di Milano and INFN Sezione di Milano, I-20133 Milano, Italy*
[12]*Instituto de Física Corpuscular, CSIC-Universidad de Valencia, E-46071 Valencia, Spain*
[13]*Department of Physics, University of Oslo, P. O. Box 1048 Blindern, N-0316 Oslo, Norway*
[14]*Institut für Kernphysik, Technische Universität Darmstadt, D-64289 Darmstadt, Germany*
[15]*Instituto de Estructura de la Materia, CSIC, Madrid, E-28006 Madrid, Spain*
[16]*Institut Laue-Langevin (ILL), 38042 Grenoble Cedex 9, France*
[17]*Ruđer Bošković Institute, HR-10 002 Zagreb, Croatia*
[18]*Department of Physics, University of Surrey, Guildford, Surrey GU2 7XH, United Kingdom*
[19]*Dipartimento di Fisica Teorica dell'Università di Torino and INFN, I-10125 Torino, Italy*
[20]*Extreme Light Infrastructure-Nuclear Physics (ELI-NP), 077125 Bucharest-Magurele, Romania*
[21]*Université de Lyon, Université Lyon-1, CNRS/IN2P3, UMR5822, IPNL, F-69622 Villeurbanne Cedex, France*
[22]*Henryk Niewodniczański Institute of Nuclear Physics PAN, PL-31342 Kraków, Poland*
[23]*Department of Physics, Saitama University, Saitama City 338-8570, Japan*

(Received 24 May 2019; published 14 August 2019)

The transitional nuclei ^{134}Ba and ^{133}Ba are investigated after multinucleon transfer employing the high-resolution Advanced GAmma Tracking Array coupled to the magnetic spectrometer PRISMA at the Laboratori Nazionali di Legnaro, Italy, and after fusion-evaporation reaction at the FN tandem accelerator of the University of Cologne, Germany. The $J^\pi = 19/2^+$ state at 1942 keV in ^{133}Ba is identified as an isomer with a half-life of 66.6(20) ns corresponding to a $B(E1)$ value of $7.7(4) \times 10^{-6}\, e^2\,\mathrm{fm}^2$ for the $J^\pi = 19/2^+$ to $J^\pi = 19/2^-$ transition. The level scheme of ^{134}Ba above the $J^\pi = 10^+$ isomer is extended to approximately 6 MeV. A pronounced backbending is observed at $\hbar\omega = 0.38$ MeV along the positive-parity yrast band. The results are compared to the high-spin systematics of the $Z = 56$ isotopes. Large-scale shell-model calculations employing the GCN50:82, SN100PN, SNV, PQM130, Realistic SM, and EPQQM interactions reproduce the experimental findings and elucidate the structure of the high-spin states. The shell-model calculations employing the GCN50:82 and PQM130 interactions reproduce alignment properties and provide detailed insight into the microscopic origin of this phenomenon in transitional ^{134}Ba.

DOI: 10.1103/PhysRevC.100.024323

*Corresponding author: levent.kaya@ikp.uni-koeln.de
†Deceased.

I. INTRODUCTION

Excitations in nuclei around mass $A \approx 130$ arise from the complex interplay of single-particle and collective degrees of freedom. Quasiparticle excitations play a key role for the presence of yrast-trap isomers. Several shell-model interactions are available for the description of neutron-rich $A \approx 130$ nuclei such as GCN50:82 [1,2], SN100PN [3], SNV [4], PQM130 [5,6], and Realistic SM [7,8] including the configuration space for proton and neutrons $0g_{7/2}$, $1d_{5/2}$, $1d_{3/2}$, $s_{1/2}$, and $0h_{11/2}$ orbitals. Calculated transition probabilities between states formed from these orbitals, especially of hindered transitions, are of particular interest for tests of all components of effective interactions, such as proton-proton, neutron-neutron, and proton-neutron correlations. However, the description of transition probabilities in this valence space is limited in the sense that $E1$ transitions cannot be evaluated since only the $h_{11/2}$ orbital acts as an intruder-parity orbital. Recent interactions have been driven by studies of excitations across the $N = 82$ neutron shell incorporating the two neutron orbits $\nu 1f_{7/2}$ and $\nu 2p_{3/2}$. For example, the recently developed extended pairing plus quadrupole-quadrupole force with monopole corrections model (EPQQM) interaction provides an extended cross-shell description of the $Z \geqslant 50$, $N \leqslant 82$ region [9].

A. Isomers along $N = 77$ isotones

Along the $N = 77$ chain from ^{127}Sn to ^{137}Nd, $J^\pi = 19/2^+$ isomers are observed in almost all isotones beside ^{129}Te and they were extensively studied in the past. Starting from semimagic ^{127}Sn, Pinston *et al.* [10] identified a $J^\pi = 19/2^+$ isomer with a half-life of 4.5(3) μs, decaying via a low-energy 17-keV $E2$ transition toward the $J^\pi = 15/2^+$ state. Furthermore, a higher-lying $J^\pi = 23/2^+$ isomer was reported in ^{127}Sn (0.9(3) μs [11]). The seniority $\nu = 3$ multiplet is completed by the observation of a $J^\pi = (27/2^-)$ isomer with a half-life of 0.25(3) μs [11]. So far, only in ^{129}Te below ^{137}Nd the $J^\pi = 19/2^+$ state remained unobserved. A $J^\pi = 23/2^+$ isomers ($T_{1/2} = 33(3)$ ns [12]) is known in ^{129}Te. Adding four protons, the level scheme of ^{131}Xe was recently extended to approximately 5 MeV [13]. The first $J^\pi = 19/2^+$ state at 1805 keV, decaying via a 189.2-keV γ ray into the $J^\pi = 19/2^-$ state, has been identified as an isomer with an adopted half-life of 14(3) ns [14].

The data on low-spin states in ^{133}Ba originate from earlier work employing β decay [15], (d, p) [16], and (n, γ) reactions [17]. The $J^\pi = 11/2^-$ neutron-hole isomer at 288 keV with a half-life of 38.93(10) h has been known to be the bandhead of the negative-parity yrast band since the 1940s [18]. First results on states above the $J^\pi = 11/2^-$ isomer were reported by Gizon *et al.* [19] employing a ^{12}C + ^{124}Sn reaction. Excited states were observed up to 2.5-MeV excitation energy, among them a delayed γ-ray cascade with energies of 83, 681, and 889 keV deexciting an isomeric state at 1942 keV. In accordance with the level scheme of ^{131}Xe, ^{135}Ce, and ^{137}Nd a spin of $J^\pi = 19/2^+$ was assigned to this state. However, a precise half-life of the 1942-keV state was not evaluated; the half-life was constrained to be between 2 and 5 ns. Later, the level scheme was significantly extended by Juutinen *et al.* [20], using ^{13}C-induced reactions and the NORDBALL γ-ray array. In total, nine collective bands up to 7 MeV were observed. Moreover, it was concluded that the half-life of the 1942-keV state has to be much longer than the reported value in Ref. [19]. According to intensity correlations and a comparison with the $T_{1/2} = 52(6)$ ns $J^\pi = 5^-$ isomer in ^{134}Ba [21], a half-life of 40–50 ns was suggested by the authors of Ref. [20].

Above ^{133}Ba, approaching the $Z = 64$ subshell closure, isomeric $J^\pi = 19/2^+$ states are established in ^{135}Ce at $E_x =$ 2125 keV ($T_{1/2} = 8.2(4)$ ns [22]) and in ^{137}Nd at $E_x =$ 2223.4 keV (1–4 ns [23]). All known $J^\pi = 19/2^+$ isomers from ^{131}Xe to ^{137}Nd decay through strong $E1$ transitions.

B. High-spin structures of $Z = 56$ isotopes and $N = 78$ isotones

The combined contribution of neutron holes in the $N =$ 82 core and proton particles in the high-$h_{11/2}$ orbital gives rise to a plethora of high-spin structures with multi-quasi-particle character. Backbending and upbending phenomena in the positive-parity yrast bands of even-even Ba isotopes with mass $A \leqslant 132$ were systematically investigated in the past. Experimental data show the presence of two aligned S bands [24] very close in energy. While one band can be assigned to quasineutron alignment, the other can be assigned to proton alignment [25–32]. The description of such collective phenomena within the shell model is quite demanding. Therefore, the majority of theoretical investigations of such systems were performed within collective models like the interacting boson model [33–35], mean-field methods [36,37], or the cranked shell model [38,39]. However, Ba isotopes have come within reach of untruncated shell-model calculations and, thus, are benchmarks for the predictive power of shell-model calculations [40–42], more specifically, the interplay between single-particle and collective excitations is subject of individual orbitals and interactions.

Similarly to the $J^\pi = 19/2^+$ isomers along the $N = 77$ chain, $J^\pi = 10^+$ states are characteristic isomers in $N = 78$ isotones. These isomers are interpreted as fully aligned $\nu h_{11/2}^{-2}$ configurations. The energy difference between $J^\pi = 10^+$ and the $J^\pi = 8^+$ states ranges from 18.5 keV in ^{130}Te to 378 keV in ^{142}Gd. The smooth evolution of the half-life with respect to the proton number is interrupted by a remarkable long half-life of $T_{1/2} = 8.39(11)$ ms [43] for the $J^\pi = 10^+$ isomer in ^{132}Xe, whereby the $J^\pi = 8_1^+$ state has not been observed to date [44]. Adding two protons, the half-life of the $J^\pi = 10^+$ state in ^{134}Ba was reported to be 2.63(14) μs [45]. In fact, the measured negative magnetic moment of this state ($\mu =$ $-2.0(1)$ μ_N [45,46]) strongly supports a $\nu h_{11/2}^{-2}$ configuration. The isomeric $J^\pi = 5^-$ state in ^{134}Ba at $E_x = 1986$ keV is subject of this publication. A previous half-life value was measured to be 52(6) ns following a ^{4}He + ^{133}Cs reaction by Ref. [21] and its longevity was attributed to a mixture of $\nu(s_{1/2}h_{11/2})$ and $\nu(d_{3/2}h_{11/2})$ configurations.

The low-spin structure of ^{134}Ba was studied in detail employing β decay [47], Coulomb excitation [48], and $(n, n'\gamma)$ reactions [49]. In contrast, information on the high-spin structure above the $J^\pi = 10^+$ ($T_{1/2} = 2.63(14)$ μs [45]) isomer is tentative. The only evaluated data on high-spin states [50] refers to a preliminary level scheme from a JYFL (Accelerator Laboratory of the University of Jyväskyl) annual report by Lönnroth *et al.* [51] in 1990. In that study, two parallel cascades on top of the $J^\pi = 10^+$ isomer were identified using a ^{13}C + ^{124}Sn reaction inside the NORDBALL γ-ray spectrometer. Besides that result, two high-spin level schemes from works utilizing ^{14}C + ^{124}Sn and ^{9}Be + ^{130}Te reactions [52,53], respectively, differ significantly from each other as well as from evaluated data [50,51].

The scarce and contradictory experimental data in ^{133}Ba and ^{134}Ba together with recent theoretical advances motivate a refined investigation of high-spin features in both nuclei. In this article, we report and discuss new results on the high-spin regime of ^{133}Ba and ^{134}Ba. Excited states were populated in two complementary experiments using different reaction mechanisms. ^{134}Ba was populated in a ^{136}Xe + ^{208}Pb multinucleon-transfer experiment employing the high-resolution position-sensitive Advanced GAmma Tracking Array (AGATA) [54] in combination with the magnetic mass spectrometer PRISMA [55–57]. Furthermore, both ^{133}Ba and ^{134}Ba were investigated with a ^{13}C + ^{124}Sn fusion-evaporation experiment at the Institute of Nuclear Physics, University of Cologne. This paper is organized as follows: The experimental setup and data analysis of the two experiments are described in Sec. II, followed by the experimental results in Sec. III. A detailed comparison with shell-model calculations and systematics is presented in Sec. IV before the paper closes with a summary and conclusions in Sec. V.

II. EXPERIMENTAL PROCEDURE

A. ^{13}C + ^{124}Sn fusion-evaporation reaction

^{133}Ba and ^{134}Ba were populated simultaneously in a ^{13}C + ^{124}Sn fusion-evaporation reaction. The FN tandem accelerator of the Institute of Nuclear Physics, University of Cologne, delivered a 55-MeV ^{13}C beam impinging onto an enriched ^{124}Sn target with a thickness of 1.8 mg/cm^2 evaporated onto a 120-mg/cm^2-thick Bi backing plus a thick Cu layer for heat dissipation. The beam energy was optimized to populate mainly ^{133}Ba and ^{134}Ba via the (^{13}C, $4n$) and (^{13}C, $3n$) reaction channels, respectively. Both recoils and beam particles were stopped in the backing of the target. About 10^8 $\gamma\gamma$ coincidences were recorded. γ Rays were detected with a mixed γ-ray detector array employing eight high-purity germanium (hereafter called HPGe) and 12 cerium-doped lanthanum-bromide (hereafter called LaBr$_3$) detectors, mounted in the frame of the High efficiency Observatory for γ-Ray Unique Spectroscopy (HORUS) array [58]. Six of the LaBr$_3$ detectors were surrounded by bismuth-germanate (BGO) veto detectors to suppress the Compton background [59]. Coincident events were processed and recorded utilizing the synchronized 80-MHz XIA Digital Gamma Finder (DGF) data-acquisition system and stored to disk. The data were sorted offline using the SOCO-V2 [60] code and analyzed utilizing the ROOT [61] and TV [62] software packages.

Multipole-mixing ratios of transitions between excited states were investigated with the $\gamma\gamma$ angular-correlation code CORLEONE [63,64] based on the phase convention by Krane, Steffen, and Wheeler [65,66]. Different hypotheses of involved spins J_1, J_2, J_3 and multipole-mixing ratios δ_1, δ_2 of two coincident γ rays in a cascade $J_1 \xrightarrow{\delta_1} J_2 \xrightarrow{\delta_2} J_3$ were evaluated by χ^2 fits of the correlation function $W(\Theta_1, \Theta_2, \Phi) = W(J_1, \delta_1, J_2, \delta_2, J_3)$ to experimental intensities in six different correlation groups, each associated with detector pairs at angles $\Theta_{1,2}$ with respect to the beam axis and a relative angle Φ between the planes spanned by the detectors and the beam axis. More details on the angular-correlation analysis with CORLEONE are given in Refs. [67,68]

B. ^{136}Xe + ^{208}Pb multinucleon transfer

In a second experiment, ^{134}Ba was populated in a ^{136}Xe + ^{208}Pb multinucleon-transfer experiment at the Laboratori Nazionali di Legnaro, Italy. In this experiment, a 6.84-MeV/nucleon ^{136}Xe beam, accelerated by the PIAVE+ ALPI accelerator complex, impinged onto a 1-mg/cm^2 ^{208}Pb target. AGATA [54], in a first demonstrator configuration [69], was placed at a distance of 18.8 cm from the target position to measure γ rays from excited states. The array consisted of nine large-volume electronically segmented HPGe detectors in three triple cryostats [70]. An isotopic identification of the nuclei of interest was provided by the magnetic spectrometer PRISMA placed at the reaction's grazing angle of $\theta_{\mathrm{lab}} = 42^\circ$. An event registered by the PRISMA focal-plane detector in coincidence with an AGATA event was taken as a trigger for the data acquisition. In this way, the origin of the γ rays is distinguished, background from β decay is reduced, and a major fraction of isomeric γ-ray transitions is suppressed.

Pulse-shape analysis of the digitized detector signals was applied to determine the individual interaction points within the HPGe detectors [71], enabling the Orsay forward-tracking algorithm [72] to reconstruct the individual emitted γ-ray energies and determine the first interaction point of the γ ray in the germanium and, thus, the emission angle. Together with the kinematic information from PRISMA, a precise Doppler correction was performed. Further details on the analysis can be found in Refs. [73,74].

III. EXPERIMENTAL RESULTS

A. ^{133}Ba

A partial level scheme of ^{133}Ba, including transitions of interest to this paper, is presented in Fig. 1(a). The determined half-lives of several isomeric states in ^{133}Ba and ^{134}Ba are summarized in Table I.

The 2366-keV ($J^\pi = 23/2^+$) state decays directly into the $J^\pi = 19/2^+$ isomer in ^{133}Ba. Figure 2(a) shows a E_γ-time matrix gated on the 424-keV ($23/2^+ \rightarrow 19/2^+$) transition. Coincidences between all eight HPGe detectors of the HORUS array were employed. The timestamps of the 424-keV transition were defined as reference time, and the maximum range for the correlation windows was chosen as 1.5 µs. Background contributions were subtracted by means of a similar matrix, gated on an area close to the 424-keV peak. Figure 2(b) presents the one-dimensional γ-ray spectrum time and energy gated on prompt events relative to

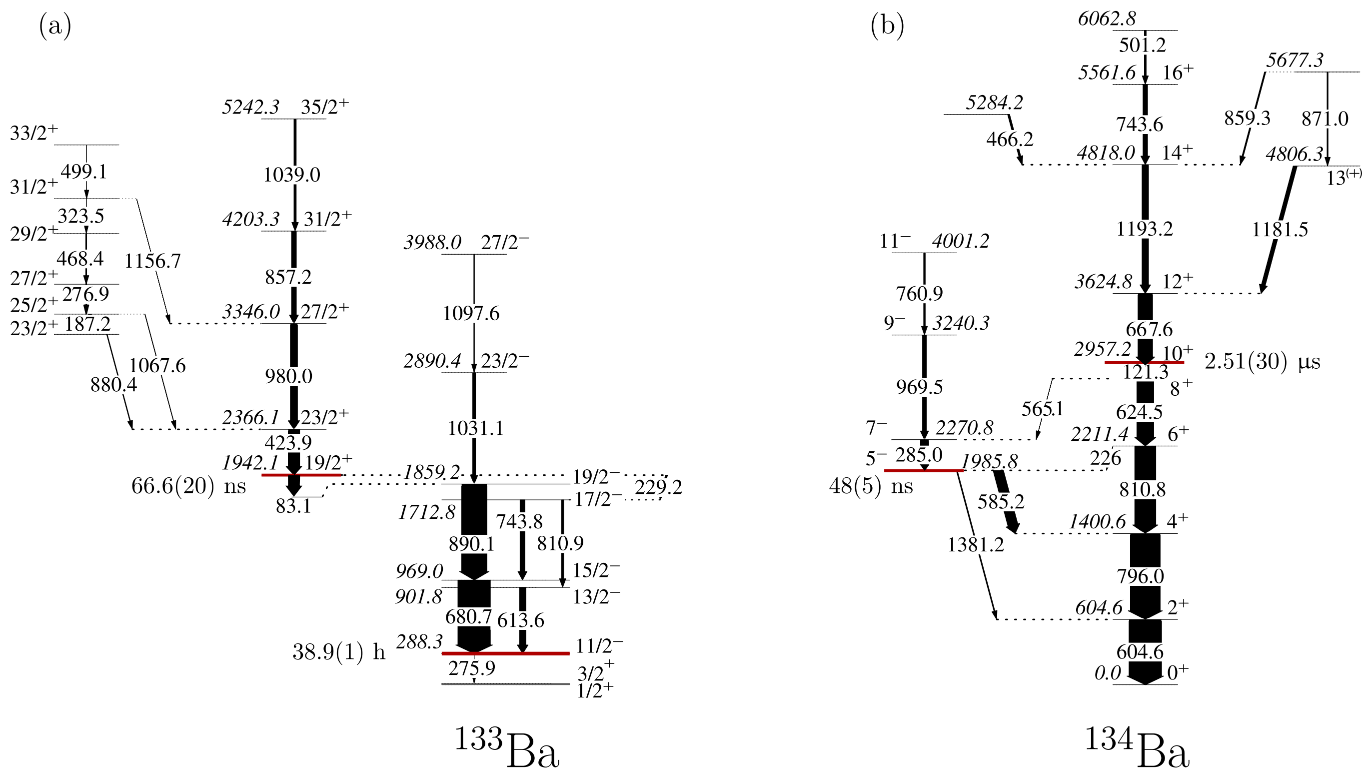

FIG. 1. (a) Partial level scheme of ^{133}Ba including transitions feeding or deexciting the 1942-keV state which is subject of this paper. Transitions and excitation energies are given in keV. Intensities, energies, and spins are adopted from Ref. [20]. For the $J^\pi = 19/2^+$ and $J^\pi = 11/2^-$ [50] states, the corresponding $T_{1/2}$ values are given in the figure. (b) Level scheme assigned to ^{134}Ba with the newly observed γ rays above the $T_{1/2} = 2.51(30)$ μs ($J^\pi = 10^+$) and $T_{1/2} = 48(5)$ ns ($J^\pi = 5^-$) isomers. Intensities are extracted from the HORUS data and normalized to the intensity of the 605-keV transition. The given half-lives of the $J^\pi = 19/2^+$ state in ^{133}Ba and of the $J^\pi = 5^-$ and 10^+ states in ^{134}Ba were newly determined.

the 424-keV transition as illustrated by the two-dimensional gate in Fig. 2(a). As expected, the feeding pattern of the 2366-keV state emerges in the spectrum up to the $J^\pi = 35/2^+$ state with strong transitions at 857, 980, and 1039 keV and less intensive transitions at 324, 468, 277, and 1068 keV. In addition, transitions below the isomer at 83, 229, 614, 681, 744, 810, and 890 keV are present, since the prompt area has a finite width.

For negative time differences, only random coincidences, e.g., e^-e^+ annihilation, are visible. Delayed transitions were obtained by gating on the positive time differences with respect to the 424-keV transition. Such a gate is visualized in the E_γ-time matrix shown in Fig. 2(c). The corresponding

TABLE I. Measured half-lives of selected isomers observed in the ^{13}C + ^{124}Sn experiment. The different columns indicate the nucleus, excitation energy, spin and parity of the isomeric state, the deduced weighted mean half-life, and previous results reported in the literature.

Isotope	E_x (keV)	J_i^π	$T_{1/2}$	
			Present work	Literature
^{133}Ba	1942	$19/2^+$	66.6(20) ns	2–5 ns [19]
^{134}Ba	2957	10^+	2.51(30) μs	2.63(14) μs [45]
^{134}Ba	1986	5^-	48(5) ns	52(6) ns [21]

one-dimensional projection onto the energy axis is displayed in Fig. 2(d). The observation of members of γ-ray cascades deexciting the $J^\pi = 19/2^+$ state and the absence of the 1068-, 980- and, 857-keV feeding transitions confirm the presence of an isomer at $E_x = 1942$ keV in this nucleus. The half-life of the 1942-keV state has to be considerably longer than the proposed $T_{1/2} = 2$–5 ns [19], taking into account the measured time resolution of $\Delta t_{\mathrm{FWHM}} \approx 36$ ns.

In order to investigate the half-life of the $J^\pi = 19/2^+$ isomer, $\gamma\gamma$ matrices with various delayed coincidence time windows in the range between 3 (37.5 ns) and 20 ticks (250 ns) are generated. Coincidences between all eight HPGe detectors are taken into account. Subsequently, the intensities of the 681- and 890-keV γ-ray transitions (below the isomer) are determined in the $\gamma\gamma$ projection gated on the 424-keV transition (above the isomer). The direct decay of the $E_x =$ 1942-keV state at $E_\gamma = 83$ keV is partially contaminated by x rays of the ^{209}Bi backing which have very similar energies. Consequently, since the Weisskopf half-life estimates for $E_\gamma = 890$ and 681 keV is in the order of picoseconds and, therefore, considerably shorter than the half-life of the state of interest, an indirect gate is applied. The intensities N_t of the 681- and 890-keV γ-ray transitions, as a function of delayed coincidence time-window length, are fitted to Eq. (1):

$$N_t = N_0\left(1 - Ae^{-\frac{\ln(2)}{T_{1/2}}\Delta t}\right), \tag{1}$$

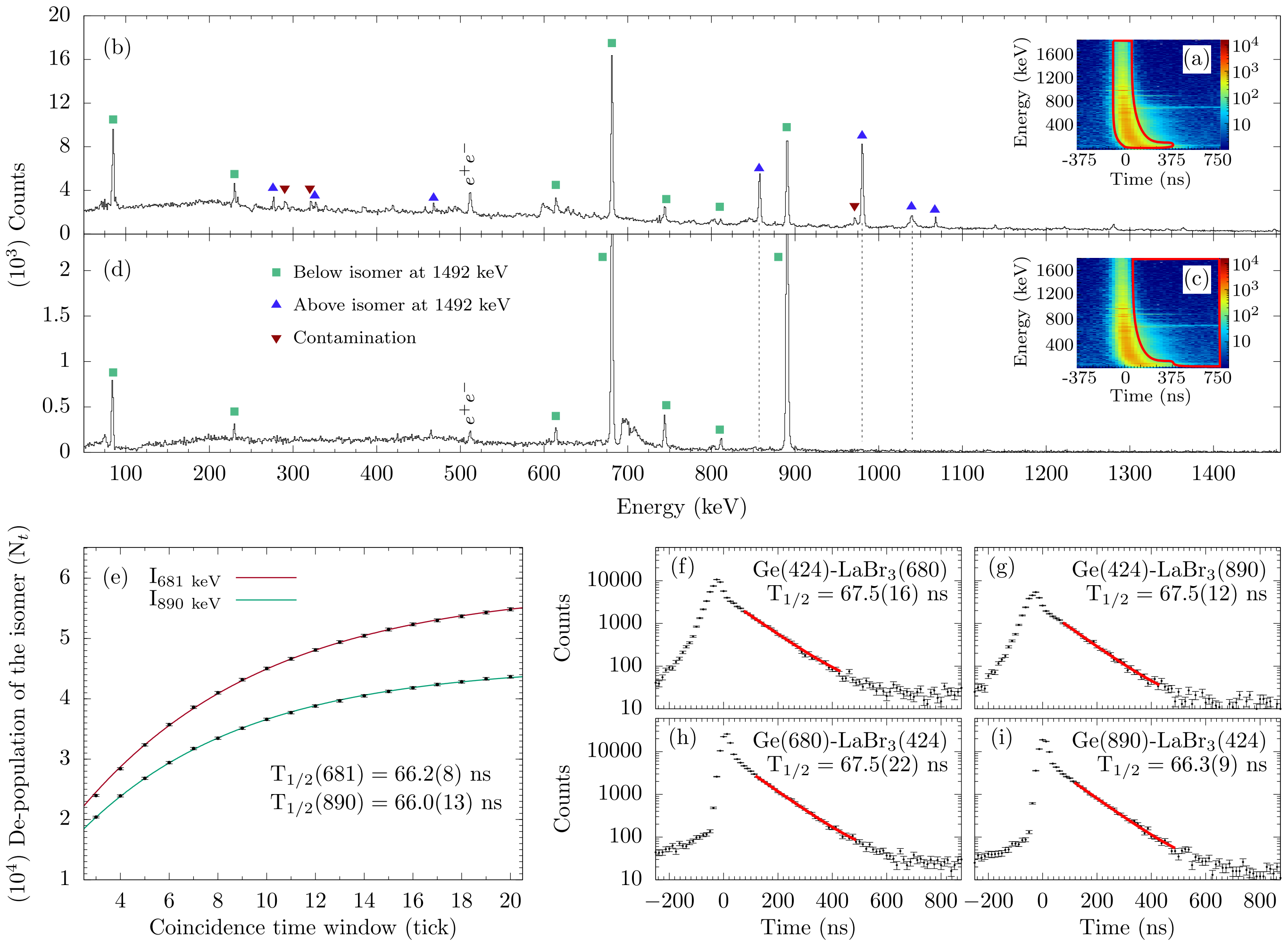

FIG. 2. [(a) and (c)] Two-dimensional E_γ-time matrices showing the time distribution of coincident γ-ray transitions relative to the 424-keV transition. The applied two-dimensional gates are surrounded by thick solid red lines. (b) Prompt and (d) delayed one-dimensional γ-ray spectra with respect to the 424-keV transition. (e) Plot of the fitted intensities of the 681- and 890-keV γ-ray transitions in the $\gamma\gamma$ projection gated on the 424-keV transitions as a function of coincidence time windows. The solid lines correspond to the fitted time distribution [see Eq. (1)]. One data acquisition time unit (tick) corresponds to 12.5 ns. [(f)–(i)] Gated E_γ-E_γ-time distributions and final lifetime fits for gating combinations between $LaBr_3$ and HPGe detectors. Half-lives are determined by exponential fits of the delayed component. The fit is drawn with a red solid line. The given half-lives include only the statistical uncertainties of the fits. For the total error see text.

where N_0, A, and the half-life $T_{1/2}$ are treated as free fitting parameters. Recently, this approach was successfully applied to isomers in the ns regime in ^{127}Xe [75]. Figure 2(e) presents the intensities of the 681- and 890-keV γ-ray transitions, gated on the 424-keV transition, with respect to the different coincidence time windows. The determined half-lives of $T_{1/2}(681\text{ keV}) = 66.2(8)$ ns and $T_{1/2}(890\text{ keV}) = 66.0(13)$ ns are in good agreement.

The combination of the excellent high-energy resolution of the HPGe detectors and the fast-timing capability of the $LaBr_3$ detectors is used to determine the half-life of the $E_x = 1942$-keV state independently from the aforementioned approach. A three-dimensional E_γ-E_γ-time cube is exploited, comprising energies of two γ rays respectively detected by a HPGe and a $LaBr_3$ detector and the corresponding timestamp difference between both events. Applying a narrow HPGe gate on the 424-, 680-, or 890-keV transitions, coincident γ-ray peaks are well separated from other lines in the $LaBr_3$ spectrum allowing clear gate conditions. Figures 2(f)–2(i) show several spectra of time differences between HPGe and $LaBr_3$ events. In the time spectra shown in Figs. 2(f) and 2(g), the feeding 424-keV γ ray is detected by HPGe detectors and the decaying 680- and 890-keV transitions are detected by $LaBr_3$ detectors. In contrast, in Figs. 2(h) and 2(i) the 424-keV feeding transition is detected by $LaBr_3$ detectors, while the decaying 680- and 890-keV transitions are detected by HPGe detectors. Using the $LaBr_3$ detectors as start detectors, the prompt curve is sharper, as illustrated by comparing Figs. 2(f) and 2(g) with Figs. 2(h) and 2(i). The short-lived component in the prompt peak is mainly caused by Compton background. Half-lives are extracted by fitting a function of the form $N(t) = a\exp[t\ln(2)/T_{1/2})] + b$ to the tail of the time distributions. The parameter b is determined from the background and kept constant. Exponential fits of the long-lived slope component yield half-life values of 67.5(16), 67.5(12), 67.5(22), and 66.3(9) ns, visualized with a red solid line in Figs. 2(f)–2(i).

TABLE II. Energies, spin assignments, and relative in-beam intensities for new γ-ray transitions in ^{134}Ba above the $J^\pi = 10^+$ isomer at $E_x = 2957$ keV. Fitted energies and relative intensities normalized to the 668-keV transition are taken from two experiments: I_γ^1 from the HORUS ^{13}C + ^{124}Sn reaction and I_γ^2 from the AGATA ^{136}Xe + ^{208}Pb experiment.

E_γ (keV)	E_i (keV)	E_f (keV)	I_i^π	I_f^π	I_γ^1	I_γ^2
466.2	5284.2	4818.0	–	14^+	16(3)	23(3)
501.2	6062.8	5561.6	–	16^+	14(2)	–
667.6	3624.8	2957.2	12^+	10^+	≡ 100	≡ 100
743.6	5561.6	4818.0	16^+	14^+	30(4)	20(2)
859.3	5677.3	4818.0	–	14^+	Weak	–
871.0	5677.3	4806.2	–	$13^{(+)}$	Weak	–
1181.5	4806.3	3624.8	$13^{(+)}$	12^+	38(4)	–
1193.2	4818.0	3624.8	14^+	12^+	50(5)	62(9)

Moreover, the independently determined values from Fig. 2(e) are in good agreement, showing the complementarity between both approaches. Systematic errors from background contributions at the borders of the fit interval as well as uncertainties in the determination of the background parameter are conservatively taken into account. The weighted mean half-life value over the six independent values results in $T_{1/2} = 66.6 \pm 0.5$ (stat.) $\pm$ 1.9 (syst.) ns for the 1942-keV state in ^{133}Ba. This corresponds to a $B(E1; 19/2^+ \rightarrow 19/2^-)$ value of $7.7(4) \times 10^{-6}$ e^2 fm^2 using relative γ-ray intensities of 100(12)% and 9(1)% for the 83- and 229-keV transitions, respectively.

B. ^{134}Ba

The extended level scheme of ^{134}Ba achieved in the present work is displayed in Fig. 1(b). Measured intensities of coincident γ rays above the $J^\pi = 10^+$ isomer in ^{134}Ba obtained from the HORUS and AGATA experiments are summarized in Table II. Intensities are from the HORUS ^{13}C + ^{124}Sn reaction (I_γ^1) as well as from the AGATA ^{136}Xe + ^{208}Pb experiment (I_γ^2). The independently measured intensities show a consistent assignment of states and transitions. The uncertainties in the transition energies are ±0.5 keV. Spin-parity assignments are supported by angular-correlation measurements, shell-model calculations, and systematics.

The beam-like Doppler-corrected singles γ-ray spectra of ^{134}Ba from the ^{136}Xe + ^{208}Pb AGATA experiment is shown in Fig. 3(a). The corresponding Ba mass distributions is depicted in the inset Fig. 3(b). Random background is significantly suppressed by gating on the prompt peak in the time-difference distribution between AGATA and PRISMA. The full width at half-maximum (FWHM) of the prompt coincidence peak is about 16 ns for identified beamlike particles. Due to the presence of two long-lived $J^\pi = 10_1^+$ and $J^\pi = 5_1^-$ isomers in the level scheme of ^{134}Ba, transitions of the yrast $10^+ \rightarrow 8^+ \rightarrow 6^+ \rightarrow 4^+ \rightarrow 2^+ \rightarrow 0^+$ cascade and the $5^- \rightarrow 4^+$ transition are suppressed in the spectrum. None of the known low-spin excited yrare states below 3 MeV [49] were populated. As reported in Ref. [51], we identify the 285-, 761-, and 970-keV γ rays to be transitions of the negative-parity band of ^{134}Ba. The measured relative intensities of the three γ rays support the known ordering of the γ rays within the negative-parity band. New peaks well above the background level are observed at energies of 171, 178, 466, 668, 744, and 1193 keV. As the negative-parity band is completely identified, it is most likely that the new transitions are members of cascades feeding the $J^\pi = 10^+$ isomer. The existence of 681–914–800-keV and 1131–547-keV cascades feeding the $J^\pi = 10^+$ isomer suggested by Lönnroth *et al.* [51] could not be confirmed. Transitions at energies of 171 and 178 keV could not be assigned using the HORUS data, as discussed below.

^{134}Ba was also populated in the ^{13}C + ^{124}Sn fusion-evaporation reaction. Figure 4(a) shows a background-subtracted E_γ-time matrix, gated on the delayed $2^+ \rightarrow 0^+$ 605-keV transition. Transitions feeding the $J^\pi = 10^+$ isomer are visible at negative time differences in this matrix representation. Time distributions following an exponential decay curve are visible at energies of 668 and 1193 keV. The

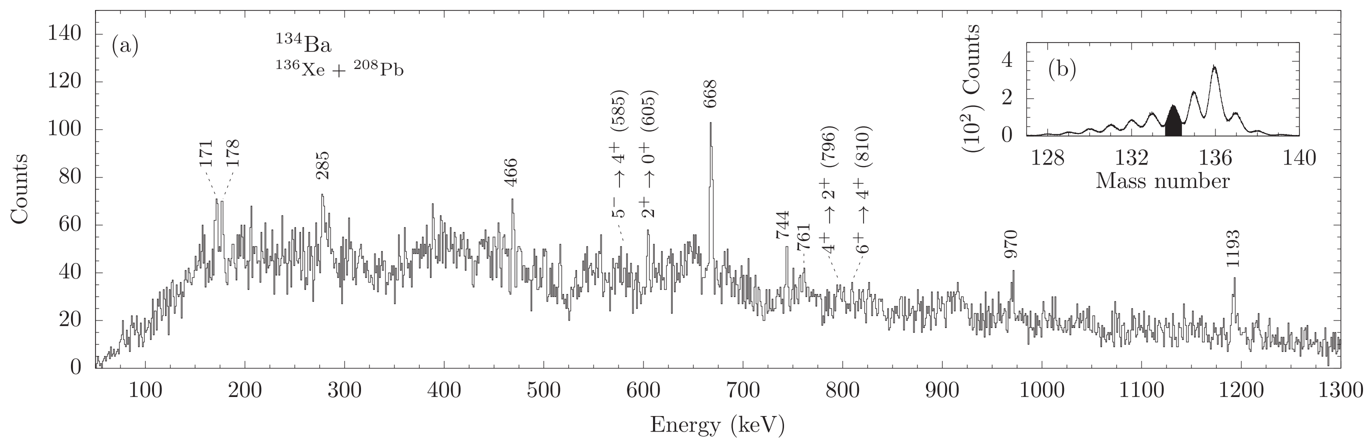

FIG. 3. (a) Doppler-corrected γ-ray spectrum gated on ^{134}Ba identified with PRISMA in the ^{136}Xe + ^{208}Pb experiment. Random background is reduced with a gate on the prompt peak in the spectrum of time differences between AGATA and PRISMA. Inset (b) represents the mass spectrum of the Ba isotopes obtained with PRISMA. The applied mass gate on ^{134}Ba is marked black.

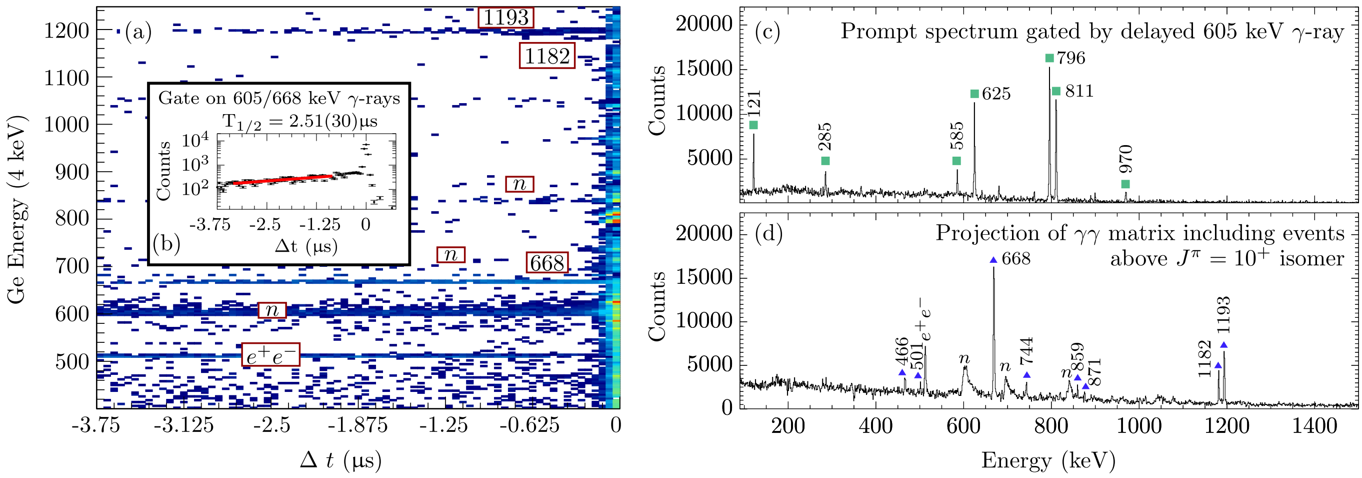

FIG. 4. Results of the HORUS experiment showing (a) E_γ-time matrix with respect to the $2^+ \rightarrow 0^+$ 605-keV transition. (b) Time difference spectrum between the 668- and 605-keV transitions, extracted from the E_γ-time matrix. (c) One-dimensional HORUS γ-ray spectrum gated on the 605-keV transition. Transitions below the $J^\pi = 10^+$ isomer are predominantly visible. (d) Projection of a HORUS $\gamma\gamma$ matrix sorted by gating on negative timestamp differences relative to the timestamp of the delayed ground-state band of ^{134}Ba with 605-, 796-, 810-, 625- or 121-keV transitions. Only transitions above the $J^\pi = 10^+$ isomer are visible. Ge($n, n\gamma$) edges are marked with n. See text for details.

isomer half-life is deduced from the analysis of timestamp differences between the 668- and 605-keV transitions, obtained by projecting the time distribution of the 668-keV transition onto the x axis in Fig. 4(a). The time spectrum and an exponential fit is shown in the inset in Fig. 4(b). The determined half-life of $T_{1/2} = 2.51(30)$ μs is in excellent agreement with the evaluated half-life value for the $J^\pi = 10^+$ state by Bell *et al.* [45]. Consequently, in accordance with the observation in the AGATA experiment shown in Fig. 3(a), the 668-keV transition is unambiguously assigned to a state above the $J^\pi = 10^+$ isomer in ^{134}Ba.

Transitions below the long-lived $J^\pi = 10^+$ isomer were identified by a time- and energy-gated one-dimensional γ-ray spectrum exhibiting coincidences within the prompt time peak relative to the delayed 605-keV transition. The corresponding spectrum is shown in Fig. 4(c). The positive-parity $E2$ ground-state band is visible up to the $10^+ \rightarrow 8^+$ 121-keV decay. To assign the new transitions to the known level scheme of ^{134}Ba, events were further sorted into a three-dimensional $\gamma\gamma\gamma$-cube, whereby one γ ray corresponds to a transition in the $E2$ ground-state band up to the $J^\pi = 10^+$ isomer (605, 796, 810, 625, or 121 keV). Thereafter, events were further processed into a prompt two-dimensional $\gamma\gamma$ matrix including double coincidences (within 100 ns) which meet the condition of negative timestamp differences in the range between -3.75 μs and -0.3 μs from the reference timestamps of the delayed 605-, 796-, 810-, 625-, or 121-keV transitions. The requirement ensure that the $\gamma\gamma$ matrix exhibits only transitions above the $J^\pi = 10^+$ isomer. Figure 4(d) shows the γ-ray projection of this matrix. The spectrum is dominated by transitions at 466, 668, 744, 1182, and 1193 keV. The intensity balance in both the AGATA [Fig. 3(a)] and HORUS [Fig. 4(d)] experiments require the newly observed 668-keV transition to be placed directly above the $J^\pi = 10^+$ isomer, deexciting a new state at 3625-keV excitation energy. Various $\gamma\gamma$-coincidence spectra from this matrix are shown in Figs. 5(a)–5(d). Figure 5(a) presents the γ-ray spectrum with a gate on 668 keV. The spectrum exhibits anticipated coincidence peaks at 466, 501, 744, 859, 871, 1182, and 1193 keV. The 668-keV transition is in mutual coincidence with the 1193-, 744-, and 501-keV transitions [Figs. 5(b) and 5(c)]. Thus, all three γ rays form a cascade on top of the 3625-keV state. By gating on the 668-keV transition, the intensity balance requires that the 1193-keV transition is placed on top of the 668-keV transition. Moreover, the ordering of the 744-, and the 501-keV transitions above the newly established $E_x = 4818$ keV state agrees with the intensity balance of the $\gamma\gamma$ projections gated on the 668- and 1193-keV transitions. Other peaks at 466, 859, 871, and 1182 keV are observed to be in coincident with the 668-keV transition [Fig. 5(a)]. Moreover, the 871- and 1182-keV lines are in mutual coincidence depopulating two states at $E_x = 5677$ and 4806 keV. The absence of the 871–1182-keV cascade and the occurrence of the 859-keV peak in Fig. 5(b) requires the 859-keV transition to be placed parallel to this cascade. Additionally, the 871–1182-keV cascade corresponds to the sum energy of the 1193–859-keV cascade, supporting the assignment. A 466-keV transition is in coincidence with the 1193–668-keV cascade [Figs. 5(a) and 5(b)] but not with the 744-keV transition. Consequently, the 466-keV γ ray is placed on top of the 4818-keV state.

Going to the negative-parity band, Fig. 5(d) shows a γ-ray spectrum for ^{134}Ba obtained by gating on the $5^- \rightarrow 4^+$ 585-keV transition. The spectrum demonstrates that the 761–970–285-keV cascade is placed on top of the $J^\pi = 5^-$ isomer. The inset Fig. 5(d) visualizes the time spectrum between the 761–970–285-keV and the 585–796–605-keV cascades. An exponential fit yields a half-life of 48(5) ns, which is in good agreement with the previous value of 52(6) ns [21].

Spin assignments can be tested in the HORUS experiment with the procedure discussed in Sec. II A. Figure 6(a) shows a benchmark angular-correlation fit of the experimentally deduced relative intensity distribution (data points) with a theoretical angular-correlation function (line) of the $4^+ \rightarrow 2^+$

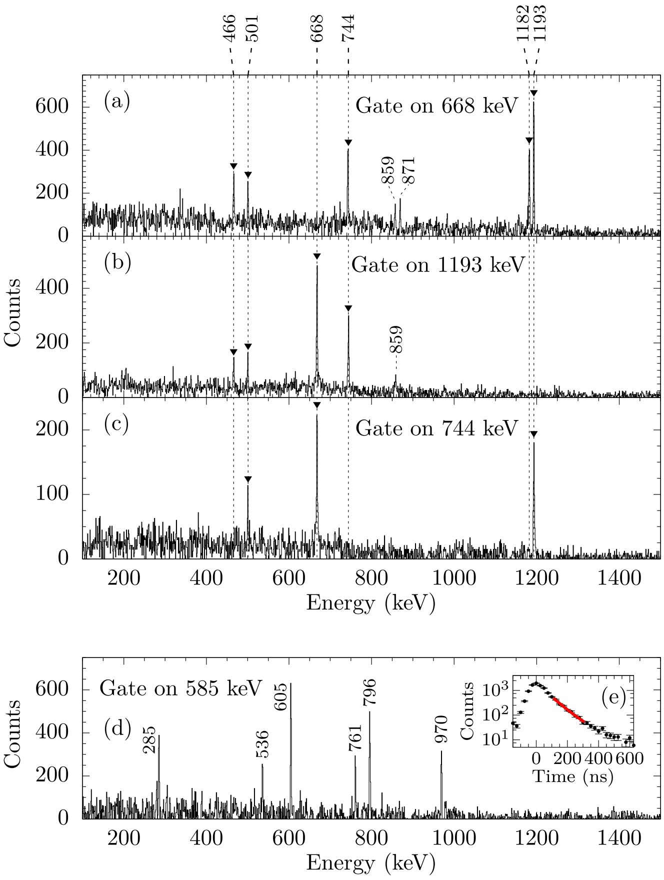

FIG. 5. γ-Ray spectra above the $J^{\pi} = 10^+$ isomer, gated on (a) 668, (b) 1193, and (c) 744 keV. (d) $\gamma\gamma$-coincidence spectra with a gate on the $5^- \rightarrow 4^+$ 585-keV transition. (e) Time spectrum between the 761–970–285-keV (prompt) and 585–796–605-keV (delayed) cascades with an exponential decay-curve fit (red solid line). The fitted half-life is 48(5) ns.

796-keV decay in ^{134}Ba, gated on the 605-keV transition. Fixing the multipole-mixing ratio of the 605-keV transition to quadrupole character ($\delta_1 = 0$) and varying the δ_2 value yields a χ^2 minimum of 1.1. The obtained multipole-mixing ratio of $\delta_2 = 0.02(3)$ is in agreement with the expected quadrupole character.

Based on the known $J^{\pi} = 10^+$ spin of the 2957-keV state, the spins of the newly established 3625- and 4818-keV states in ^{134}Ba are evaluated. Scenarios of $J_1 = \{10, 11, 12\} \rightarrow \delta_1 J_2 = 10 \xrightarrow{\delta}{}_2 =$ fixed$J_3 = 10$ and $J_1 = \{11, 12, 13\} \xrightarrow{\delta_1} J_2 = 11 \xrightarrow{\delta_2=\text{fixed}} J_3 = 10$ were tested for the 1193–668-keV cascade. Fits with several fixed multipole-mixing ratios of the 668-keV transitions ($\delta_2 = 0,\ \pm 0.05,\ \pm 0.1,\ \pm 0.15, \ldots$) yields χ^2 values of larger then 2.3. In contrast, the $J_1 = 14 \xrightarrow{\delta_1} J_2 = 12 \xrightarrow{\delta_2=0} J_3 = 10$ hypothesis with fitted $\delta_1 = -0.01(3)$ value for the 1193-keV transition yields the best χ^2 value of 1.3, as shown in Fig. 6(b). Apart from that, similar fits assuming a nonzero δ_2 value for the 668-keV transition yield significantly worse χ^2 values. Hence, the best agreement is obtained for a pure-quadrupole $J_1 = 14 \rightarrow J_2 = 12 \rightarrow J_3 = 10$ cascade. Since a $M2$ multipolarity in this cascade would cause long-lived states and other isomers, a positive parity is assigned to the 3625- and 4818-keV states. Employing the same method, the spin of the newly established excited state at 5562 keV is determined. The 744–1193-keV cascade is best reproduced assuming a spin of $J = 16$ for the 5562-keV state ($\chi^2 = 1.4$). In accordance with the fitted $\delta_1 = 0.01(2)$ value, a positive parity is assigned for the 5562-keV state. In contrast, the 1182-keV transition yields a dipole character with multipole-mixing ratio of $\delta_1 = -0.06(4)$. Consequently, the spin-parity of the 4806-keV state is interpreted as $J = 13^{(+)}$.

The bandhead of the negative-parity band at $E_x = 1986$ keV and the first excited state above the bandhead at $E_x = 2271$ keV were identified as $J^{\pi} = 5^-$ and $J^{\pi} = 7^-$ states by Lönnroth *et al.* [51]. However, spin-parity assignments of states on top of the bandbead with excitation energies of 3240 and 4001 keV were tentative in the previous work. Similarly to the aforementioned discussion, Fig. 6(c) shows the experimentally deduced angular-correlation intensity distribution for the coincident γ rays at 285 and 970 keV, compared to calculated values for different scenarios with spin values of $J = 7$, 8, and 9 for the 3240-keV state. A hypothesis of $J = 9$ for the 3240-keV state yields the best result. The vanishing multipole-mixing ratio of $\delta_1 = 0.00(2)$ indicates a negative parity of the 3240-keV state. Going to higher states in the band, angular-correlation fits with spin assignments of $J = 9$ and 10 for the 4001-keV state yield only limited agreement with the data. Instead, a good match is obtained by assuming

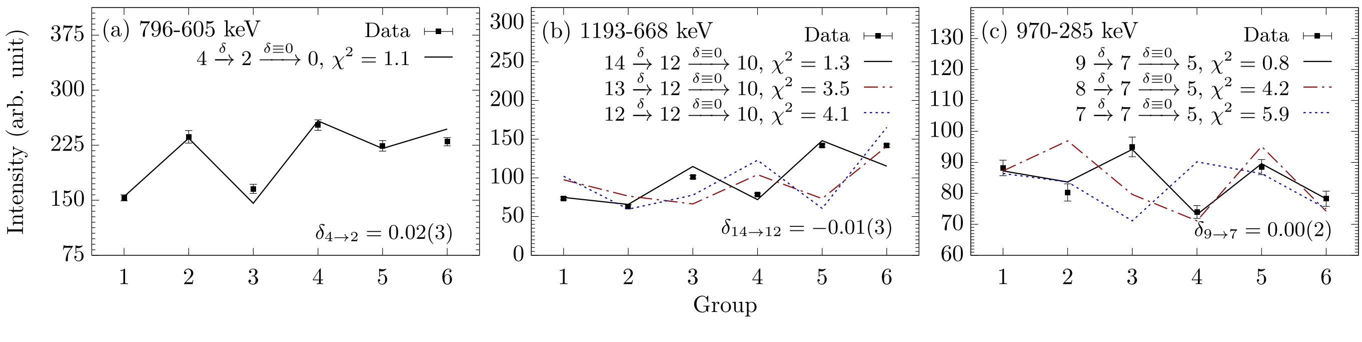

FIG. 6. (a) Benchmark $\gamma\gamma$ angular correlations for the $4^+ \rightarrow 2^+ \rightarrow 0^+$ (796–605-keV) cascade in ^{134}Ba. Experimental values (data points) are compared to calculated angular-correlation functions $W(\Theta_1, \Theta_2, \Phi)$ (lines) for six correlation groups using the code CORLEONE [63,64]. Investigation for (b) the newly established 668-1193-keV cascade and (c) the 285–970-keV cascade in ^{134}Ba.

a $J = 11$ state with dominant quadrupole ($E2$) character [$\delta_1 = 0.02(3)$]. The results are given in Fig. 1(b).

IV. SHELL-MODEL CALCULATIONS AND DISCUSSION

The obtained lifetime of the $19/2^+$ state in ^{133}Ba and the extended high-spin level schemes of ^{134}Ba are discussed and compared with the results of shell-model calculations and systematics. Five shell-model calculations were carried out in an untruncated $50 \leqslant Z, N \leqslant 82$ *gdsh* valence space. The single-particle space is generated by the valence nucleons occupying the $0g_{7/2}$, $1d_{5/2}$, $1d_{3/2}$, $2s_{1/2}$, and $0h_{11/2}$ orbitals, outside doubly magic ^{100}Sn. In a further calculation using the EPQQM interaction, the *gdsh* valence space is extended by the $1f_{7/2}$ neutron orbit above the $N = 82$ shell closure to calculate the $E1$ transition strength value of the $19/2^+ \rightarrow 19/2^-$ transition in ^{133}Ba. Shell-model calculations were carried out employing the shell-model code NuShellX@Msu [76], the massive-parallelization code KSHELL [77], and the ANTOINE shell-model code [78].

The first calculation is conducted with the effective interaction GCN50:82 [1,2]. The interaction is derived from a realistic G matrix based on the Bonn-C potential [79]. Empirical monopole corrections to the original G matrix are introduced by fitting different combinations of two-body matrix elements to sets of experimental excitation energies from even-even and even-odd semimagic nuclei.

The second calculation is carried out with the jj55pn Hamiltonian (referred to as the SN100PN interaction) [3]. The Hamiltonian consists of four terms describing the neutron-neutron, neutron-proton, proton-proton, and Coulomb repulsion between the protons individually. A renormalized G matrix derived from the CD-Bonn interaction [79] was employed to construct the realistic two-body residual interaction. The proton and neutron single-particle energies are based on the energy levels in ^{133}Sb and ^{131}Sn.

Another calculation is conducted with the SNV interaction [4]. The interaction combines the proton-proton N82GYM interaction [80] with the semiempirical SNBG3 neutron-neutron interaction [81] and the monopole-based universal (V_{MU}) interaction for the proton-neutron part [82,83]. Both the SNBG3 and N82GYM interactions are G-matrix-based interactions. The SNBG3 interaction is obtained by combining the next-to-next-to-next-to-leading order interaction with a χ^2 fit of levels including 3_1^- states along ($N < 82$) Sn isotopes. Strengths of the central and the tensor force from the orginal V_{MU} interaction are multiplied by 0.84 and 1.3, respectively, to fit the experimental data of one-proton separation energies in Sb isotopes [84]. Very recently, the interaction successfully described the g factor of the $J^\pi = 23/2^+$ state in ^{135}La [4].

A fourth calculation is performed utilizing the framework of the pair-truncated shell model, denoted as PQM130 (pairing+QQ+ multipole for mass region 130). The approach leverages a pairing-plus-quadrupole interaction that consists of spherical single-particle energies, a monopole-pairing, a quadrupole-pairing, and a quadrupole-quadrupole interaction. The Hamiltonian in each neutron and proton space is diagonalized separately and afterward the total Hamiltonian is diagonalized in the truncated space. More details on the calculation are given in Refs. [5,6].

A fifth calculation is performed in the framework of the realistic shell model [7,8], denoted as Realistic SM. Single-particle energies and two-body effective interaction are determined from the established CD-Bonn free nucleon-nucleon potential [79] using the $V_{\mathrm{low}\text{-}k}$ approach with a cutoff momentum of $\Lambda = 2.6$ fm^{-1}, plus the Coulomb force for protons. The effective shell-model Hamiltonian is derived iteratively by means of the many-body perturbation theory in the $\hat{Q}$-box folded diagram expansion, including all diagrams up to third order in the interaction. More details can be found in Ref. [85].

The last calculation is conducted in the framework of the extended pairing plus quadrupole-quadrupole force with monopole corrections model (EPQQM) [86–89]. Single-particle energies (SPEs) were adopted from the experimental excited states of ^{133}Sb (proton SPEs) and ^{131}Sn (neutron SPEs). The *gdsh* valence space is enlarged by the $\nu 1f_{7/2}$ neutron orbit above the $N = 82$ shell closure. Calculations within this large valence space allow us to describe $E1$ transitions. The interaction was recently successfully applied to neutron-rich nuclei around ^{132}Sn [9,90–93].

A. ^{134}Ba

A comparison of the experimentally obtained energy spectrum of ^{134}Ba with the results of the shell-model calculations is presented in Fig. 7. Moreover, yrare $J^\pi = 2_2^+$, 4_2^+, and 8_2^+ states from the literature are compared as further benchmarks for the validity of the shell-model calculations. All calculations reproduce the hitherto known members of the positive-parity ground-state band up to the $J^\pi = 10^+$ isomer quite well. In particular, the excitation energy of the $J^\pi = 10^+$ isomer is predicted at 2.953 (GCN50:82), 2.517 (SN100PN), 2.911 (SNV), 2.915 (PQM130), and 3.010 MeV (Realistic SM) which are in good agreement with the experimentally determined 2.957 MeV. The small 121-keV energy gap between the $J^\pi = 8^+$ and the 10^+ states is reasonably reproduced by the calculated energy gaps of 10 and 60 keV in the GCN50:82 and PQM130 interactions, respectively. However, the order of $J^\pi = 10^+$ and 8^+ states is interchanged in the SN100PN, SNV, and Realistic SM calculations.

In Sec. III B a $16^+ \rightarrow 14^+ \rightarrow 12^+ \rightarrow 10^+$ cascade with γ-ray energies of 744, 1193, and 668 keV was newly established. This assignment is supported by calculated transition energies of 672, 1327, and 609 keV (GCN50:82), 674, 1016, and 765 keV (SNV), 744, 1215, and 675 keV (PQM130), and 893, 997, and 732 keV (Realistic SM) for this cascade. Although the excitation spectrum calculated by SN100PN is more compressed, the relative position of the $J^\pi = 16^+$, 14^+, 12^+, and 10^+ states are in good agreement with the experimental excitation spectrum.

The 5677-keV state decays partially via a one-step decay into the $J^\pi = 14^+$ state and via a two-step cascade through the $J^\pi = 13^{(+)}$ state into the $J^\pi = 12^+$ state. Consequently, this state is interpreted to have a spin of $J = 14$ or 15. The yrast $J^\pi = 15^+$ state is predicted at 376 (GCN50:82), 352 (SNV), 478 (SN100PN), and 514 keV (PQM130) above the $J^\pi = 14_1^+$ state, which contradicts the observed 859-keV

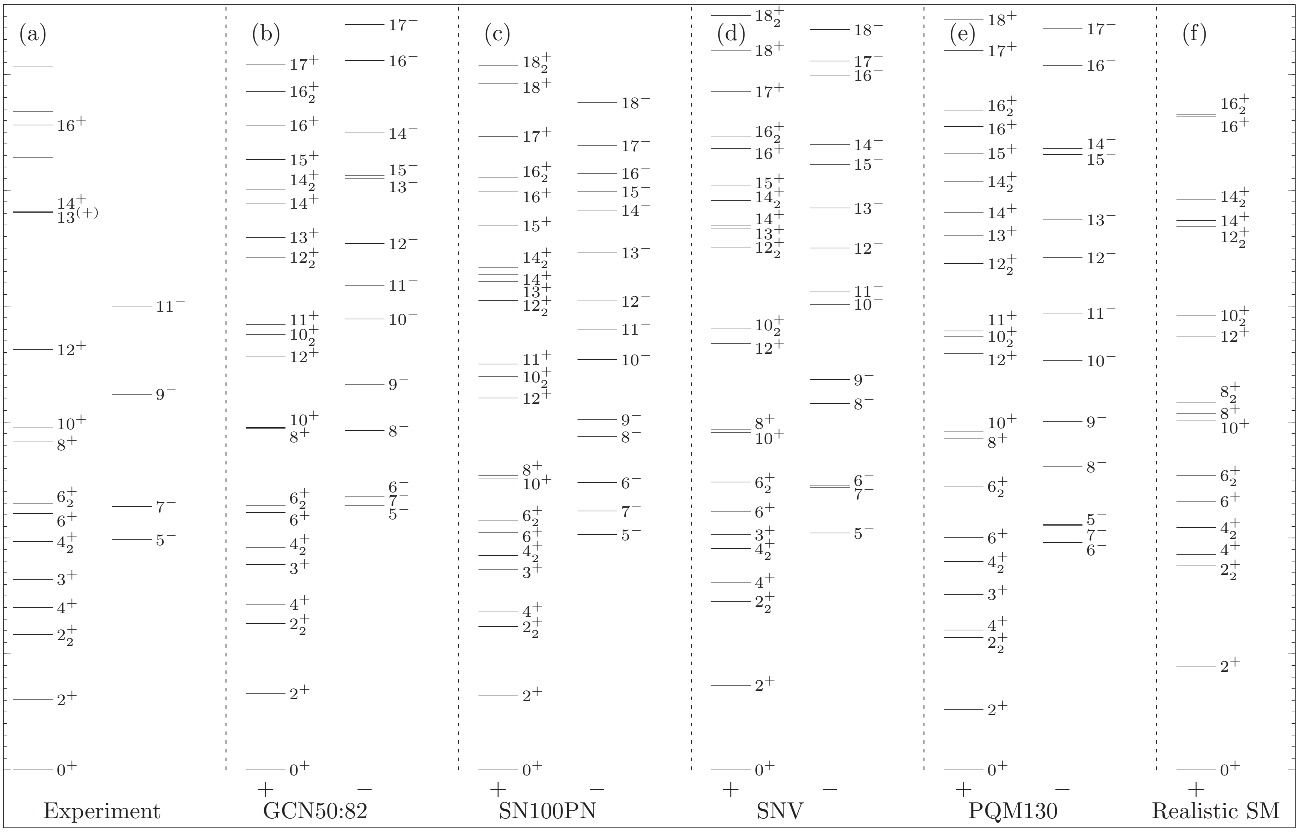

FIG. 7. Comparison of experimental energy spectra with the results of shell-model calculations for ^{134}Ba. (a) Experimental energy spectrum. The results obtained with the different interactions are separated in different columns: (b) GCN50:82, (c) SN100PN, (d) SNV, (e) PQM130, and (f) Realistic SM. For clarity, the states are separated into columns for the negative- and the positive-parity states.

energy difference between the $E_x = 5677$ keV and the $J^\pi = 14^+$ state. Similarly, a possible $J^\pi = 14^+_2$ state is predicted slightly above the $J^\pi = 14^+_1$ state. Consequently, a positive parity for the state at $E_x = 5677$ keV is unlikely. A better agreement of a $J^\pi = 14^+_2$ or 15^+_1 assignment is achieved for the 5284-keV state which is only 466 keV above the $J^\pi = 14^+_1$ state. However, no conclusive assignment can be made, since the calculated level density of states is too high.

Going to the negative-parity band, the calculations tend to slightly overpredict the excitation energy of the $J^\pi = 5^-$ bandhead. GCN50:82 predict the state at 2278 keV, SN100PN at 2030 keV, SNV at 2043 keV, and PQM130 at 2118 keV compared to the experimental 1986-keV excitation energy. A good agreement is obtained for the position of the calculated $J^\pi = 7^-$ state which deviates only 84 (GCN50:82), 37 (SN100PN), 163 (SNV), and 161 keV (PQM) from the experimental excitation energy. On the other hand, $J^\pi = 5^-$, 6^-, and 7^- states are permuted in the PQM130 calculation. All shell-model calculations consistently support a large energy gap of 972 (GCN50:82), 788 (SN100PN), 933 (SNV), and 895 keV (PQM130) between the $J^\pi = 9^-$ and $J^\pi = 7^-$ states, which agrees well with the observed 970 keV. The $J^\pi = 11^-$ state is calculated to be 763–935 keV higher in excitation energy with respect to the $J^\pi = 9^-$ state, supporting an $J^\pi = 11^-$ assignment for the $E_x = 4001$-keV state.

Moreover, the shell-model results provide insight into the structure of the isomeric states and the new established levels in ^{134}Ba. States below the $J^\pi = 10^+$ isomer are dominated by proton spin contributions. For example, the total spin of the $J^\pi = 8^+$ state is attributed to 26% $\nu_{2^+} \otimes \pi_{6^+}$ and 20% $\nu_{0^+} \otimes \pi_{8^+}$ with a leading configuration of $\nu(d^{-2}_{3/2}h^{-2}_{11/2}) \otimes \pi(g^4_{7/2}d^2_{5/2})$, using GCN50:82. On the other hand, a predominant neutron character takes over from the $J^\pi = 10^+$ state onward. The $J^\pi = 10^+$ isomer is calculated to be of $(\nu h^{-2}_{11/2})$ character with a spin configuration of 39% $\nu_{10^+} \otimes \pi_{0^+}$ and 32% $\nu_{10^+} \otimes \pi_{2^+}$. Likewise, the yrast states $J^\pi = 12^+$, 14^+, and 16^+ consist of a neutron ν_{10^+} configuration coupled to even-spin proton configurations. According to the GCN50:82 calculation, the leading configurations of the $J^\pi = 5^-$ isomer are (3%) $\nu(d^{-1}_{3/2}h^{-1}_{11/2})$ and (10%) $\nu(s^{-1}_{1/2}h^{-1}_{11/2})$. The calculation describes the negative-parity states above the $J^\pi = 5^-$ isomer with a neutron angular momentum of $7\hbar$ coupled to the proton quadrupole excited states (0^+, 2^+, 4^+).

Figures 8(a) and 8(b) show the evolution of several states in the positive- and negative-parity yrast band along the $N = 78$ isotones ranging from ^{130}Te to ^{142}Gd. The newly established states of ^{134}Ba are marked with thicker lines. The $16^+ \to 14^+ \to 12^+ \to 10^+$ cascade in ^{134}Ba fits the systematics [Fig. 8(a)]. Moreover, the reevaluated negative-parity band is in good agreement with the systematics [Fig. 8(b)]. Similarly to the $N = 78$ chain, Fig. 8(c) presents the evolution of positive-parity excited states along the Ba isotopes. The mid-shell Ba nuclei exhibit excitation spectra which are rotational in character, while a gradual change to a vibrational character

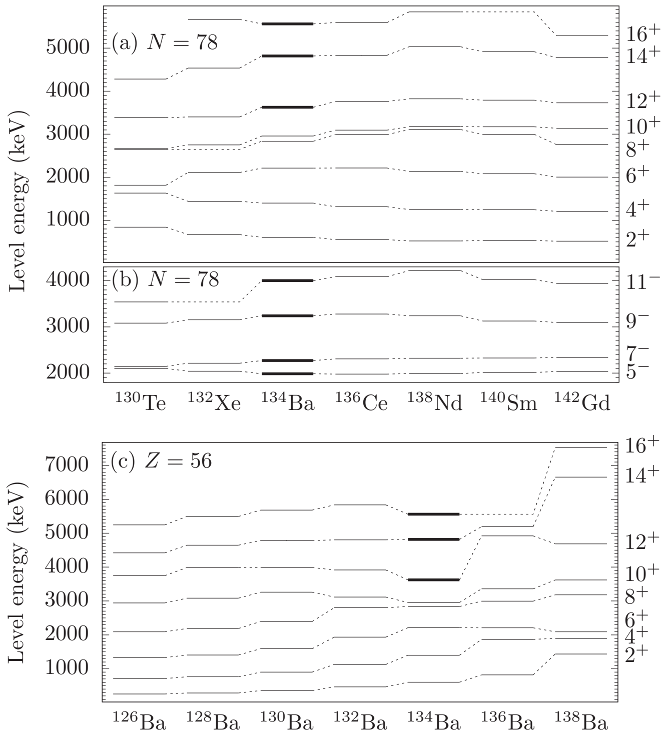

FIG. 8. Evolution of excited states along the even-mass $N = 78$ isotones for (a) the positive-parity yrast states and (b) for the negative-parity yrast states. (c) Evolution of positive-parity yrast states along the $Z = 56$ even-mass Ba isotopes. Newly discovered states in ^{134}Ba are marked with thick lines. Data taken from Refs. [50, 94–96].

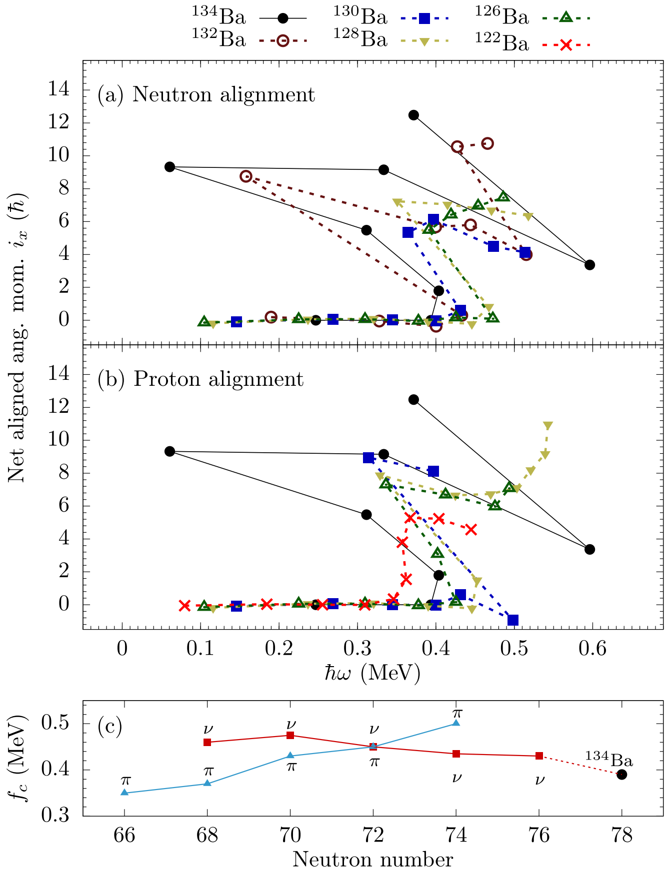

FIG. 9. Evolution of net aligned angular momenta $i_x(\hbar)$ along the even-mass Ba chain as a function of rotational frequency $\hbar\omega$. Isotopes along the Ba chain exhibit two S bands with (a) neutron-hole ($\nu h_{11/2}^{-2}$) and (b) proton ($\pi h_{11/2}^{2}$) configurations. (c) Summary of observed crossing frequencies between ground-state band and S bands based on proton (π) and neutron (ν) configurations for Ba isotops. The frequencies have been determined from net aligned angular momenta plots. Data extracted from Refs. [50,96].

is observed when approaching the $N = 82$ shell closure. ^{134}Ba lies in between, demonstrating the transitional character of this nucleus.

Backbending and upbending phenomena in the positive-parity yrast bands of even-even Ba isotopes were systematically investigated in the past. A comparison of the net aligned angular momentum $i_x(\omega)$ of the positive-parity band in ^{134}Ba with the corresponding bands in lower even-mass neighbors $^{132-126}$Ba and ^{122}Ba is displayed in Figs. 9(a) and 9(b). The ground-state cascade below the crossing serve as reference and is fitted according to Harris *et al.* [97] via $I_{x,\text{coll.}} = a\omega + c\omega^3$. The determined parameter is incorporated into the net aligned angular momentum for a given spin $J^{i,f}$ of the state: $i_x = I_x - I_{x,\text{coll.}}$, where $I_x = (I_x^i + I_x^f)/2$ with $I^{i,f} = \sqrt{J^{i,f}(J^{i,f}+1)}$. Starting from the midshell ^{122}Ba, proton and neutron-hole align in a continuous way along the yrast line. Blocking arguments are used to assign the first alignment to a proton crossing [25]. In ^{124}Ba the yrast sequence above the $J^\pi = 10^+$ state splits into two streched $E2$ cascades with two distinct alignments. According to blocking arguments and by comparing crossing frequencies in neighboring nuclei ^{125}Ba and ^{125}Cs, the alignment in ^{124}Ba with the lower critical frequency was assigned to a pair of $h_{11/2}$ protons, while the alignment with the higher critical frequency is generated by a $h_{11/2}$ neutron-hole pair [26].

The band structure in ^{126}Ba has similar character like the one in ^{124}Ba. Calculated routhians indicate a higher crossing frequency for neutron-hole pairs than for proton pairs in ^{126}Ba [27]. Since the two S bands in ^{128}Ba are degenerated, no unambiguous assignment is possible [28,29]. A change in the nuclear structure is observed in ^{130}Ba where four $J = 10^+$ states are observed within a small energy range of 343 keV. Two $J = 10^+$ states are the bandheads of the S bands. Cranking calculations suggest that the proton alignment occurs after neutron-hole alignment [30]. A negative g factor of the $J^\pi = 10^+$ state unambiguously assigned a neutron-hole $\nu h_{11/2}^{-2}$ configuration to the S band in ^{132}Ba [31]. This assignment was confirmed by calculations within the framework of pair-truncated shell-model approach [32]. So far, no evidence for proton alignment was reported in literature for ^{132}Ba.

While the net aligned angular momentum plot for the S band originating from neutron-hole alignment is shown in Fig. 9(a), the similar plot for proton alignment is displayed in Fig. 9(b). Overall, the alignment pattern of ^{132}Ba shows a considerable similarity with respect to ^{134}Ba [cf. Fig. 9(a)]. The crossing frequency at which the alignment occurs is mass dependent in both cases. Figure 9(c) shows a summary of

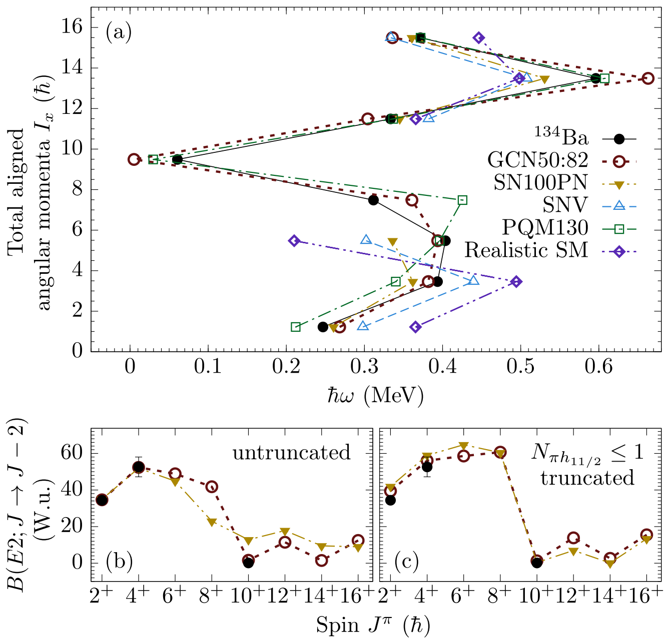

FIG. 10. (a) Comparison between experimental and calculated total aligned angular momenta I_x as a function of the rotational frequency $\hbar\omega$, employing GCN50:82, SN100PN, SNV, PQM130, and Realstic SM calculations for ^{134}Ba. Only a partial comparison with SN100PN and SNV is displayed since both interactions predict the $J^\pi = 8^+_1$ state above the $J^\pi = 10^+_1$ state. [(b) and (c)] Calculated reduced quadrupole transition strengths for yrast $B(E2)$ values employing the GCN50:82 and SN100PN interactions. Experimental values are visualized as black filled dots, taken from Refs. [45,48]. (b) The first calculations use the complete *gdsh* valence space; (c) the second prohibit more than one proton in the $\pi h_{11/2}$ orbital.

experimentally determined crossing frequencies between S bands and the ground-state bands for proton and neutron-hole alignment as a function of neutron number along Ba isotopes. Since the proton alignment increases and the neutron alignment decreases with mass number, the new determined crossing frequency in ^{134}Ba matches the systematics of neutron-hole alignment. Consequently, in accordance with the similarity with the neutron-hole alignment in ^{132}Ba [cf. Fig. 9(a)], it is reasonable to assign the band crossing in ^{134}Ba to neutron-hole $\nu h_{11/2}^{-2}$ alignment.

To further inspect the above-mentioned alignment properties in ^{134}Ba, the results of the shell-model calculations are reparametrized into the total aligned angular momenta I_x as a function of the rotational frequency $\hbar\omega$. Figure 10(a) compares the extracted theoretical and experimental total aligned angular momenta for all five calculations. Calculated I_x values for the $J^\pi = 8^+_1$ and 10^+_1 states of the SNV, SN100PN, and Realistic SM interactions are not considered, since all three interactions have a reversed ordering of both states. The critical frequency at which alignment occurs is slightly underestimated by the SN100PN interaction, while the SNV and Realistic SM interactions overpredict the alignment frequency slightly. Overall, GCN50:82 yields the best agreement with the experimental critical frequency. Both GCN50:82 and PQM130 interactions tend to slightly underpredict the minimal rotational frequency at the position of the $J^\pi = 10^+$ state. The experimentally observed second alignment at the $J^\pi = 16^+$ state is predicted correctly by all calculations. In fact, all five theoretical calculations provide a fair agreement of the experimental backbending pattern in ^{134}Ba.

It is well known, that reduced transition strength values $B(E2; J^\pi \to J^\pi - 2)$ are reduced in the vicinity of the backbending region [98]. Consequently, calculated $B(E2)$ values serve as test for the predictive power of shell-model calculations for nucleon alignment. In Fig. 10(b), calculated $B(E2)$ values along the positive-parity yrast band are compared to available experimental data in ^{134}Ba [45,48]. The SN100PN and the GCN50:82 interactions are employed using effective charges of $e_\pi = 1.75e$ and $e_\nu = 0.75e$. They are optimized to reproduce the $B(E2; 2^+ \to 0^+)$ and $B(E2; 4^+ \to 2^+)$ values. Both interactions are capable to predict the continuous drop of transition strength from the $J^\pi = 4^+$ state to the isomeric $J^\pi = 10^+$ state. Going to higher spins, low $B(E2)$ values prevail beyond the $J^\pi = 10^+$ state for both interactions.

The role of the $\pi h_{11/2}$ and $\nu h_{11/2}$ orbitals are scrutinized by a separate calculation by prohibiting more than one proton in the $\pi h_{11/2}$ orbital. Using this truncation, proton alignment components are prevented in the calculations. Results of calculated $B(E2)$ values are presented in Fig. 10(c). Obviously, the overall result is very similar to the untruncated calculation; the good agreement with respect to the experimental values remain unaltered. Moreover, the truncated results of both interactions resembles each other. The decreasing trend of the $B(E2)$ values at spin $6\hbar$ and $8\hbar$ is interrupted by this truncation. The increase of the $B(E2)$ values at spin $6\hbar$ and $8\hbar$ indicate that proton components are crucial to describe both states. On the other hand, $B(E2)$ values between states above the $J^\pi = 10^+$ isomer are unaffected by the truncation, underpinning the assumption that these states are predominantly of neutron character with negligible proton $h_{11/2}$ configuration admixture. This observation is in accordance with the negative measured g factor of the $J^\pi = 10^+$ state by Bell *et al.* [45]. It is concluded that proton components play a critical role at the beginning of the alignment process at the $J^\pi = 6^+$ state and subsequently two-neutron $h_{11/2}$ alignment becomes pivotal above the $J^\pi = 10^+$ state.

B. ^{133}Ba

The level structure of the even-odd isotope ^{133}Ba is more complex in comparison to the even-even partner ^{134}Ba. Since $B(E1)$ transition strength values cannot be evaluated in the $0g_{7/2}1d_{5/2}1d_{3/2}2s_{1/2}0h_{11/2}$ valence space, a microscopic discussion of the isomeric property of the $J^\pi = 19/2^+$ state is presented in the following by the GCN50:82, SN100PN, and SNV calculations. Subsequently, results from a truncated calculation including the neutron $\nu 1f_{7/2}$ orbital are discussed using EPQQM. An untruncated calculation in the $gdsh + \nu(1f_{7/2}2p_{3/2})$ valence space is not feasible since the m-scheme dimension would exceed the nowadays computational limits of approximately 10^{11}.

The calculated excitation energy of each positive-negative parity state as a function of the angular momentum J were

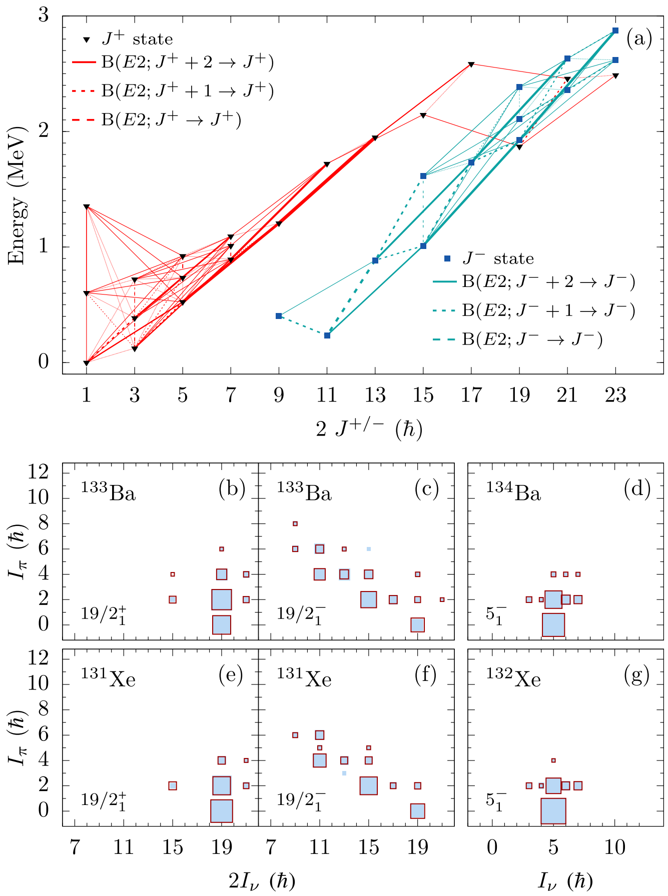

FIG. 11. (a) $E2$ map: Calculated excitation energy against spin of positive- and negative-parity states of ^{133}Ba obtained by the SNV calculation. The widths indicate the $E2$ transition probabilities. Decomposition of the total angular momentum $I_\pi \otimes I_\nu$ in their proton and neutron components for $J^\pi = 19/2^+_1$ and $J^\pi = 19/2^-_1$ states in [(b) and (c)] ^{133}Ba and [(e) and (f)] ^{131}Xe, employing the GCN50:82 (filled blue boxes) and the SN100PN interaction (empty red boxes). $J^\pi = 19/2^+_1$ states arise from couplings of a $h^{-1}_{11/2}$ neutron-hole to the $J^\pi = 5^-$ states in (d) ^{134}Ba and (g) ^{132}Xe.

computed utilizing the SNV interaction. A so-called $E2$ map [76] of the results is shown in Fig. 11(a). States are connected with lines. The linewidths are proportional to the $B(E2)$ strength between the states. The adopted effective charges are 1.6e and 0.8e for protons and neutrons, respectively. The SNV interaction predicts the $J^\pi = 19/2^+$ state at 1870 keV, which is in good agreement with the experimental value of 1942 keV. Other positive-parity states with spins $15/2\hbar$ and $17/2\hbar$ are predicted at excitation energies of 2145 and 2585 keV, which is significantly higher than the excitation energy of the $J^\pi = 19/2^+$ state. Consequently, the $J^\pi = 19/2^+$ state cannot decay into another positive-parity state and becomes a spin-gap isomer.

A similar isomeric $J^\pi = 19/2^+$ state with a half-life of 14(3) ns was observed in the $-2p$ isotone ^{131}Xe [14]. Figures 11(b) and 11(c) and Figs. 11(e) and 11(f) show the decomposition of the total angular momentum $I_\pi \otimes I_\nu$ in proton and neutron components for $J^\pi = 19/2^+_1$ and $19/2^-_1$ states in ^{133}Ba and ^{131}Xe, employing the GCN50:82 (filled blue boxes) and the SN100PN interactions (empty red boxes). No significant deviations between both calculations are visible. Differences have been observed very recently in ^{136}Ba [96]. The experimental energy gaps between both states are 189 keV in ^{131}Xe and 83 keV in ^{133}Ba. Theoretical values are higher with 362 and 188 keV in ^{131}Xe (GCN50:82 and SN100PN) and 249 and 164 keV in ^{133}Ba. Both interactions predict the $J^\pi = 19/2^+$ state to have predominant $\nu_{19/2^+} \otimes \pi_{0^+}$ spin configuration. Neutron $\nu(h^{-2}_{11/2}s^{-1}_{1/2}d^{-2}_{3/2})$ components account for 29 and 31% (GCN50:82 and SN100PN) in ^{131}Xe and 22 and 24% in ^{133}Ba. Significant proton couplings to this neutron configuration are 7/16% $\pi(g^4_{7/2})$ and 9/8% $\pi(g^2_{7/2}d^2_{5/2})$ in ^{131}Xe and 9/12% $\pi(g^4_{7/2}d^2_{5/2})$ in ^{133}Ba.

The $J^\pi = 19/2^-$ states in ^{131}Xe and ^{133}Ba have a fragmented pattern of proton and neutron components as visible in Figs. 11(c) and 11(f). The spin mainly arises from couplings of $\nu_{19/2^-} \otimes \pi_{0^+}$, $\nu_{15/2^-} \otimes \pi_{2^+}$, and $\nu_{11/2^-} \otimes \pi_{4^+}$. The dominant configuration is attributed to 9/7% $\nu(h^{-3}_{11/2}d^{-2}_{3/2}) \otimes \pi(g^2_{7/2}d^2_{5/2})$ in ^{131}Xe and 7/9% $\nu(h^{-3}_{11/2}d^{-2}_{3/2}) \otimes \pi(g^4_{7/2}d^2_{5/2})$ in ^{133}Ba. The isomeric character can be traced back to the stretched neutron spin $\nu_{19/2^+}$ of the $J^\pi = 19/2^+$ state, which hinders a decay into the $\nu_{11/2^-}$ components of the $J^\pi = 19/2^-$ state in both nuclei. Overall, the $J^\pi = 19/2^+$ and $19/2^-$ states have very similar structures in both nuclei. Consequently, the additional proton pair of ^{133}Ba is mainly paired with respect to ^{131}Xe.

Two refined calculations using the EPQQM interaction are employed: (i) an untruncated calculation without cross-shell excitations comprising the *gdsh* valence space and (ii) a truncated calculation prohibiting proton excitations into the $1d_{3/2}$, $2s_{1/2}$, and $0h_{11/2}$ orbitals but allowing cross-shell excitations into the neutron $1f_{7/2}$ orbital. The upper part of Table III shows the untruncated calculated occupation numbers of protons and neutrons for the $J^\pi = 19/2^+$ and $19/2^-$ states in ^{133}Ba. The EPQQM results confirm the leading configurations of $\nu(h^{-2}_{11/2}s^{-1}_{1/2})$ ($N_{\nu h_{11/2}} = 9.97$, $N_{\nu s_{1/2}} = 1.35$) for initial $J^\pi = 19/2^+$ state and of $\nu(h^{-3}_{11/2})$ ($N_{\nu h_{11/2}} = 9.02$) for final $J^\pi = 19/2^-$ state consistently with the other calculations

TABLE III. Average occupation numbers for protons (π) and neutrons (ν) in each single-particle orbit of the *gdsh* model space for $J^\pi = 19/2^+$ and $19/2^-$ states in ^{133}Ba employing the EPQQM interaction.

J^π	π/ν	$0g_{7/2}$	$1d_{5/2}$	$1d_{3/2}$	$2s_{1/2}$	$0h_{11/2}$	$1f_{7/2}$
		Untruncated calculation without cross-shell					
$19/2^+_1$	π	3.59	2.17	0.16	0.06	0.03	–
$19/2^+_1$	ν	7.73	5.57	2.37	1.35	9.97	–
$19/2^-_1$	π	3.83	1.67	0.28	0.17	0.05	–
$19/2^-_1$	ν	7.81	5.74	2.88	1.55	9.02	–
		Truncated calculation with cross-shell					
$19/2^+_1$	π	3.91	2.09	–	–	–	–
$19/2^+_1$	ν	7.67	5.48	2.51	1.35	9.77	0.22
$19/2^-_1$	π	3.95	2.05	–	–	–	–
$19/2^-_1$	ν	7.81	5.73	2.94	1.52	8.81	0.20

TABLE IV. Average neutron occupation numbers in each single-particle orbit of the *gdsh* model space in ^{133}Ba and ^{134}Ba, calculated using the GCN50:82 and SNV interactions.

Isotope	J^π	$0g_{7/2}$	$1d_{5/2}$	$1d_{3/2}$	$2s_{1/2}$	$0h_{11/2}$
				GCN50:82		
^{133}Ba	$19/2_1^+$	7.76	5.73	2.28	1.39	9.84
^{134}Ba	5_1^-	7.78	5.73	2.46	1.35	10.69
				SNV		
^{133}Ba	$19/2_1^+$	7.87	5.53	2.23	1.35	9.92
^{134}Ba	5_1^-	7.88	5.56	2.33	1.37	10.87

(cf. Table IV in discussion below). The $J^\pi = 19/2^+$ state is calculated to have 1.94 MeV excitation energy which is in excellent agreement with the experimental value.

In addition, the valence space is enlarged by the neutron $1f_{7/2}$ orbital. In order to make the dimension of the configuration space tractable, proton excitations into the $1d_{3/2}$, $2s_{1/2}$, and $0h_{11/2}$ orbitals are forbidden, which is reasonable since the corresponding occupation is neglected small and EPQQM predicts a high degree of $g_{7/2}$ and $d_{5/2}$ occupation for protons at both states (see Table III). Applying this truncation, the excitation energy of the $J^\pi = 19/2_1^+$ state is slightly shifted to 1.75 MeV. The impact of the truncation and the inclusion of the $1f_{7/2}$ orbital on the calculated average occupation numbers is visualized in the lower part of Table III.

The occupation of the $1f_{7/2}$ orbital amounts to approximately 0.2. The pure two ($N_{\nu h_{11/2}} = 9.97$) and three ($N_{\nu h_{11/2}} = 9.02$) neutron-hole configuration from the untruncated calculation of initial and final states is rearranged in favor of the $\nu 1f_{7/2}$ occupation (cf. $N_{\nu h_{11/2}} = 9.77$ for inital and $N_{\nu h_{11/2}} = 8.81$ for final states). The $E1$ transition operator between both states is driven by the share of $1f_{7/2}$ cross-shell configurations. Thus, it has a perturbative but decisive role for a detailed description of the overall configuration of these states. The theoretical $B(E1; 19/2_1^+ \rightarrow 19/2_1^-)$ transition strength is computed to be $5 \times 10^{-4}\ e^2\,\mathrm{fm}^2$. Effective charges of $e_\pi = 1.7$ and $e_\nu = 0.7$ were employed. The theoretical $B(E1)$ value overpredicts the experimental value of $7.7(4) \times 10^{-6}\ e^2\,\mathrm{fm}^2$ by almost two orders of magnitude.

In Refs. [10,19,23] it was suggested that the $J^\pi = 19/2^+$ states in odd-mass nuclei along $N = 77$ arise from couplings of a neutron-hole to the $J^\pi = 5^-$ state in even-mass $N = 78$ nuclei. As mentioned above in Sec. IV A, the leading configuration of the $J^\pi = 5^-$ state in ^{134}Ba is $\nu(s_{1/2}^{-1}h_{11/2}^{-1})$ generating fully stretched $\nu_{5^-} \otimes \pi_{0^+}$ and $\nu_{5^-} \otimes \pi_{2^+}$ spin contributions. [see Fig. 11(d)]. The same applies for ^{132}Xe as shown in Fig. 11(g). In accordance with the Pauli principle, an additional $h_{11/2}$ neutron-hole couples with a spin of $9/2\hbar$ to this configuration. Consequently, the spin decompositions of both states are very similar but those of the $J^\pi = 19/2^+$ state is shifted by a neutron spin of $9/2\hbar$ with respect to the $J^\pi = 5^-$ state in both nuclei. The leading $\nu(h_{11/2}^{-2}s_{1/2}^{-1})$ configuration of the $J^\pi = 19/2^+$ state in ^{133}Ba and the connection to the $J^\pi = 5^-$ isomer in ^{134}Ba are scrutinized by investigating the evolution of calculated average occupation numbers of neutrons in the *gdsh* model space for $J^\pi = 19/2^+$ and 5^- isomers in ^{133}Ba and ^{134}Ba, respectively, as listed in Table IV. The average occupation of the neutron $h_{11/2}$ orbital for the $J^\pi = 5^-$ state in ^{134}Ba is $N_\nu \approx 10.78$ indicating a one-neutron $\nu h_{11/2}^{-1}$ configuration. A partial occupation of the $\nu s_{1/2}$ orbital ($N_\nu \approx 1.36$) supports a predominant $\nu h_{11/2}^{-1}s_{1/2}^{-1}$ configuration. Compared to this, a decrease to $N_\nu \approx 9.88$ for the $\nu h_{11/2}$ orbital of the $J^\pi = 19/2^+$ state is observed, while the occupation of the remaining orbitals stays constant. These observations and the aforementioned disscusion of spin contributions corroborates that the $J^\pi = 19/2^+$ state arises predominatly from a coupling of a neutron-hole and the $J^\pi = 5^-$ state in ^{134}Ba, as suggested in Refs. [10,19,23].

V. CONCLUSIONS

In summary, two experiments employing the ^{136}Xe + ^{208}Pb multinucleon-transfer reaction and the ^{13}C + ^{124}Sn fusion-evaporation reaction were used to measure half-lives of high-spin isomers in ^{133,134}Ba and to establish new high-spin states in ^{134}Ba. The level scheme of ^{134}Ba was extended to approximately 6 MeV. A pronounced backbending along the positive-parity yrast band was identified at around $\hbar\omega = 0.38$ MeV. Comparisons with crossing frequencies along the even-Ba chain indicated that the backbending can be traced back to neutron alignment. In general, the new experimental results such as the backbending phenomena are reproduced by the GCN50:82 and PQM130 interactions; however, SNV, SN100PN, and Realistic SM predict the $J^\pi = 8^+$ state slightly above the $J^\pi = 10^+$ isomer. A detailed inspection using truncated calculations for ^{134}Ba reveals that the alignment of yrast states above the $J^\pi = 10^+$ isomer is clearly of neutron character. Beside previous investigations in few other nuclei, like ^{132}Ba [41], ^{132,134,136}Ce [42], and ^{131}Xe [13], these results demonstrate convincingly the applicability of modern shell-model interactions in order to describe the interplay between single-particle and collective excitation in this transitional region which arises from the specific $h_{11/2}$ intruder orbital. Backbending and alignment properties are traced back to the wave function and their decomposition into specific single particle contributions.

The previously evaluated half-life of 2–5 ns for the 1942-keV state in ^{133}Ba was revised to $T_{1/2} = 66.6(20)$ ns. The new half-life of this isomeric state completes the systematics of $J^\pi = 19/2^+$ isomers for the $N = 77$ isotones. Large-scale shell-model calculations using the SNV, GCN50:82, and SN100PN have been performed to explain the level structure of ^{133}Ba and the underlying configuration of the measured $J^\pi = 19/2^+$ isomer. The calculations point out that the isomer can be interpreted as predominant $^{134}\mathrm{Ba}(5_1^-) \otimes \nu(0h_{11/2}^{-1})$ configuration. A truncated calculation using EPQQM in an enlarged valence space yield a $B(E1; 19/2_1^+ \rightarrow 19/2_1^-)$ value which is two orders of magnitude too high compared to the experimental value. In the future, untruncated calculations in the full *gdsh* valence space incorporating cross-shell configuration $\nu 1f_{1/2}$ and $\nu 2p_{3/2}$ are of highest interest to provide a more complete description of the $50 \leqslant Z, N \leqslant 82$ nuclei.

ACKNOWLEDGMENTS

We thank the IKP FN tandem accelerator team for the support during the experiment. The research leading to these results has received funding from the German BMBF under Contracts No. 05P15PKFN9 TP1 and No. 05P18PKFN9 TP1, from the European Union Seventh Framework Programme FP7/2007-2013 under Grant No. 262010-ENSAR, from the Spanish Ministerio de Ciencia e Innovación under Contract No. FPA2011-29854-C04, from the Spanish Ministerio de Economía y Competitividad under Contract No. FPA2014-57196-C5, and from the U.K. Science and Technology Facilities Council (STFC). One of the authors (A. Gadea) has been supported by the Generalitat Valenciana, Spain, under Grant No. PROMETEOII/2014/019 and EU under the FEDER program.

[1] E. Caurier, F. Nowacki, A. Poves, and K. Sieja, Collectivity in the light xenon isotopes: A shell model study, Phys. Rev. C **82**, 064304 (2010).

[2] E. Caurier, F. Nowacki, and A. Poves, Shell Model description of the $\beta\beta$ decay of ^{136}Xe, Phys. Lett. B **711**, 62 (2012).

[3] B. A. Brown, N. J. Stone, J. R. Stone, I. S. Towner, and M. Hjorth-Jensen, Magnetic moments of the 2_1^+ states around ^{132}Sn, Phys. Rev. C **71**, 044317 (2005).

[4] Md. S. R. Laskar, S. Saha, R. Palit, S. N. Mishra, N. Shimizu, Y. Utsuno, E. Ideguchi, Z. Naik, F. S. Babra, S. Biswas, S. Kumar, S. K. Mohanta, C. S. Palshetkar, P. Singh, and P. C. Srivastava, g-factor measurement of the 2738 kev isomer in ^{135}La, Phys. Rev. C **99**, 014308 (2019).

[5] E. Teruya, N. Yoshinaga, K. Higashiyama, and A. Odahara, Shell-model calculations of nuclei around mass 130, Phys. Rev. C **92**, 034320 (2015).

[6] K. Higashiyama and N. Yoshinaga, Pair-truncated shell-model analysis of nuclei around mass 130, Phys. Rev. C **83**, 034321 (2011).

[7] L. Coraggio, A. Covello, A. Gargano, N. Itaco, and T. T. S. Kuo, Effective shell-model hamiltonians from realistic nucleon-nucleon potentials within a perturbative approach, Ann. Phys. **327**, 2125 (2012).

[8] L. Coraggio, A. Covello, A. Gargano, N. Itaco, and T. T. S. Kuo, Shell-model calculations and realistic effective interactions, Prog. Part. Nucl. Phys. **62**, 135 (2009).

[9] H.-K. Wang, S. K. Ghorui, K. Kaneko, Y. Sun, and Z. H. Li, Large-scale shell-model study for excitations across the neutron $N = 82$ shell gap in $^{131-133}$Sb, Phys. Rev. C **96**, 054313 (2017).

[10] J. A. Pinston, C. Foin, J. Genevey, R. Béraud, E. Chabanat, H. Faust, S. Oberstedt, and B. Weiss, Microsecond isomers in ^{125,127,129}Sn, Phys. Rev. C **61**, 024312 (2000).

[11] R. L. Lozeva, G. S. Simpson, H. Grawe, G. Neyens, L. A. Atanasova, D. L. Balabanski, D. Bazzacco, F. Becker, P. Bednarczyk, G. Benzoni, N. Blasi, A. Blazhev, A. Bracco, C. Brandau, L. Cáceres, F. Camera, S. K. Chamoli, F. C. L. Crespi, J.-M. Daugas, P. Detistov, M. De Rydt, P. Doornenbal, C. Fahlander, E. Farnea, G. Georgiev, J. Gerl, K. A. Gladnishki, M. Górska, J. Grębosz, M. Hass, R. Hoischen, G. Ilie, M. Ionescu-Bujor, A. Iordachescu, J. Jolie, A. Jungclaus, M. Kmiecik, I. Kojouharov, N. Kurz, S. P. Lakshmi, G. Lo Bianco, S. Mallion, A. Maj, D. Montanari, O. Perru, M. Pfützner, S. Pietri, J. A. Pinston, Zs. Podolyák, W. Prokopowicz, D. Rudolph, G. Rusev, T. R. Saitoh, A. Saltarelli, H. Schaffner, R. Schwengner, S. Tashenov, K. Turzó, J. J. Valiente-Dobón, N. Vermeulen, J. Walker, E. Werner-Malento, O. Wieland, and H.-J. Wollersheim, New sub-μs isomers in ^{125,127,129}Sn and isomer systematics of $^{124-130}$Sn, Phys. Rev. C **77**, 064313 (2008).

[12] C. T. Zhang, P. Bhattacharyya, P. J. Daly, Z. W. Grabowski, R. H. Mayer, M. Sferrazza, R. Broda, B. Fornal, W. Krolas, T. Pawlat, D. Bazzacco, S. Lunardi, C. Rossi Alvarez, and G. de Angelis, Yrast excitations in $A = 126 - 131$Te nuclei from deep inelastic ^{130}Te + ^{64}Ni reactions, Nucl. Phys. A **628**, 386 (1998).

[13] L. Kaya, A. Vogt, P. Reiter, M. Siciliano, B. Birkenbach, A. Blazhev, L. Coraggio, E. Teruya, N. Yoshinaga, K. Higashiyama, K. Arnswald, D. Bazzacco, A. Bracco, B. Bruyneel, L. Corradi, F. C. L. Crespi, G. de Angelis, J. Eberth, E. Farnea, E. Fioretto, C. Fransen, B. Fu, A. Gadea, A. Gargano, A. Giaz, A. Görgen, A. Gottardo, K. Hadyńska-Klęk, H. Hess, R. Hetzenegger, R. Hirsch, N. Itaco, P. R. John, J. Jolie, A. Jungclaus, W. Korten, S. Leoni, L. Lewandowski, S. Lunardi, R. Menegazzo, D. Mengoni, C. Michelagnoli, T. Mijatović, G. Montagnoli, D. Montanari, C. Müller-Gatermann, D. Napoli, Zs. Podolyák, G. Pollarolo, A. Pullia, M. Queiser, F. Recchia, D. Rosiak, N. Saed-Samii, E. Şahin, F. Scarlassara, D. Schneiders, M. Seidlitz, B. Siebeck, J. F. Smith, P.-A. Söderström, A. M. Stefanini, T. Steinbach, O. Stezowski, S. Szilner, B. Szpak, C. Ur, J. J. Valiente-Dobón, K. Wolf, and K. O. Zell, High-spin structure in the transitional nucleus ^{131}Xe: Competitive neutron and proton alignment in the vicinity of the $N = 82$ shell closure, Phys. Rev. C **98**, 014309 (2018).

[14] A. Kerek, A. Luukko, M. Grecescu, and J. Sztarkier, Two- and three-quasiparticle states in ^{132}Xe and ^{131}Xe, Nucl. Phys. A **172**, 603 (1971).

[15] E. A. Henry and R. A. Meyer, Decay of 3.912-h ^{133}La to ^{133}Ba and level structure of the $N = 77$ nuclei, Phys. Rev. C **13**, 2501 (1976).

[16] D. von Ehrenstein, G. C. Morrison, J. A. Nolen, and N. Williams, Study of the (d, p) reaction on the even-A barium isotopes 130-138, Phys. Rev. C **1**, 2066 (1970).

[17] A. Y. Dauenhauer and K. S. Krane, Neutron capture cross sections of ^{130,132,134,136,138}Ba, Phys. Rev. C **85**, 064301 (2012).

[18] J. M. Cork and Gail P. Smith, Radioactive isotopes of barium from cesium, Phys. Rev. **60**, 480 (1941).

[19] J. Gizon, A. Gizon, and D.J. Horen, Band structure in ^{131,132,133}Ba observed by (^{12}C, xn) reactions, Nucl. Phys. A **252**, 509 (1975).

[20] S. Juutinen, P. Šimeček, P. Ahonen, M. Carpenter, C. Fahlander, J. Gascon, R. Julin, A. Lampinen, T. Lönnroth, J. Nyberg, A. Pakkanen, M. Piiparinen, K. Schiffer, G. Sletten, S. Törmänen, and A. Virtanen, Shape coexistence in the transitional ^{133}Ba nucleus, Phys. Rev. C **51**, 1699 (1995).

[21] T. Morek, H. Beuscher, B. Bochev, D. R. Haenni, R. M. Lieder, T. Kutsarova, M. Muller-Veggian, and A. Neskakis, Isomeric states in ^{134}Ba, Z. Phys. A **298**, 267 (1980).

[22] A. Zemel, C. Broude, E. Dafni, A. Gelberg, M. B. Goldberg, J. Gerber, G. J. Kumbartzki, and K. H. Speidel, Magnetic moment of the $19/2^+$ isomer in ^{135}Ce, Z. Phys. A **304**, 269 (1982).

[23] J. Gizon, A. Gizon, M. R. Maier, R. M. Diamond, and F. S. Stephens, Deformed states of neutron-deficient cerium and neodymium nuclei, Nucl. Phys. A **222**, 557 (1974).
[24] R. O. Sayer, J. S. Smith, and W. T. Milner, Rotational and quasirotational bands in even-even nuclei, At. Data Nucl. Data Tables **15**, 85 (1975).
[25] R. Wyss, A. Granderath, R. Bengtsson, P. von Brentano, A. Dewald, A. Gelberg, A. Gizon, J. Gizon, S. Harissopulos, A. Johnson, W. Lieberz, W. Nazarewicz, J. Nyberg, and K. Schiffer, Interplay between proton and neutron S-bands in the Xe-Ba-Ce-region, Nucl. Phys. A **505**, 337 (1989).
[26] J. P. Martin, V. Barci, H. El-Samman, A. Gizon, J. Gizon, W. Klamra, B. M. Nyak'o, F. A. Beck, Th. Byrski, and J. C. Merdinger, Collective band structures and particle alignments in ^{124}Ba, ^{125}Ba and ^{125}Ce, Nucl. Phys. A **489**, 169 (1988).
[27] D. Ward, V. P. Janzen, H. R. Andrews, D. C. Radford, G. C. Ball, D. Horn, J. C. Waddington, J. K. Johansson, F. Banville, J. Gascon, S. Monaro, N. Nadon, S. Pilotte, D. Prevost, P. Taras, and R. Wyss, Gamma-ray spectroscopy of ^{126}Ba, Nucl. Phys. A **529**, 315 (1991).
[28] K. Schiffer, A. Dewald, A. Gelberg, R. Reinhardt, K. O. Zell, S. Xiangfu, and P. von Brentano, Band crossings in ^{128}Ba, Nucl. Phys. A **458**, 337 (1986).
[29] H. Wolters, K. Schiffer, A. Gelberg, A. Dewald, J. Eberth, R. Reinhardt, K. O. Zell, P. V. Brentano, D. Alber, and H. Grawe, High spin states in ^{128}Ba, Z. Phys. A **328**, 15 (1987).
[30] S. Xiangfu, D. Bazzacco, W. Gast, A. Gelberg, U. Kaup, A. Dewald, K. O. Zell, and P. von Brentano, Band crossing in ^{130}Ba, Phys. Rev. C **28**, 1167 (1983).
[31] S. Harissopulos, A. Gelberg, A. Dewald, M. Hass, L. Weissman, and C. Broude, Measurement of the magnetic moment of the 10^+ isomer in ^{132}Ba, Phys. Rev. C **52**, 1796 (1995).
[32] K. Higashiyama, N. Yoshinaga, and K. Tanabe, Pair-truncated shell-model approach to backbending and low-lying states in ^{132}Ba, Phys. Rev. C **67**, 044305 (2003).
[33] N. Yoshida, A. Arima, and T. Otsuka, Description of high-spin states in the interacting boson model, Phys. Lett. B **114**, 86 (1982).
[34] R. F. Casten and P. von Brentano, An extensive region of $O(6)$-like nuclei near $A = 130$, Phys. Lett. B **152**, 22 (1985).
[35] K. Nomura, T. Nikšić, and D. Vretenar, Shape-phase transitions in odd-mass γ-soft nuclei with mass $A \approx 130$, Phys. Rev. C **96**, 014304 (2017).
[36] A. Granderath, P. F. Mantica, R. Bengtsson, R. Wyss, P. von Brentano, A. Gelberg, and F. Seiffert, Shapes and rotational structures of neutron $h_{11/2}$ configurations in the Xe-Ba-Ce region, Nucl. Phys. A **597**, 427 (1996).
[37] L. M. Robledo, R. R. Rodríguez-Guzmán, and P. Sarriguren, Evolution of nuclear shapes in medium mass isotopes from a microscopic perspective, Phys. Rev. C **78**, 034314 (2008).
[38] C.-B. Moon, C. S. Lee, T. Komatsubara, Y. Sasaki, and K. Furuno, Structure of the negative parity bands in ^{125}Xe, Phys. Rev. C **76**, 067301 (2007).
[39] Y. Huang, Z. G. Xiao, S. J. Zhu, C. Qi, Q. Xu, W. J. Cheng, H. J. Li, L. M. Lyu, R. S. Wang, W. H. Yan, H. Yi, Y. Zhang, Q. M. Chen, C. Y. He, S. P. Hu, C. B. Li, H. W. Li, P. W. Luo, X. G. Wu, Y. H. Wu, Y. Zheng, and J. Zhong, High-spin structures in the ^{129}Xe nucleus, Phys. Rev. C **93**, 064315 (2016).
[40] K. Higashiyama, N. Yoshinaga, and K. Tanabe, Shell model study of backbending phenomena in Xe isotopes, Phys. Rev. C **65**, 054317 (2002).
[41] Y. Lei and Z. Y. Xu, $(h_{11/2})^2$ alignments in neutron-rich ^{132}Ba with negative-parity pairs, Phys. Rev. C **92**, 014317 (2015).
[42] T. Takahashi, N. Yoshinaga, and K. Higashiyama, Backbending phenomena in ^{132,134,136}Ce with a pair-truncated shell model, Phys. Rev. C **71**, 014305 (2005).
[43] H. F. Brinckmann, C. Heiser, and W. D. Fromm, Ein Hochangeregter isomerer Kernzustand in ^{132}Xe, Nucl. Phys. A **96**, 318 (1967).
[44] Yu. Khazov, A. A. Rodionov, S. Sakharov, and B. Singh, Nuclear Data Sheets for $A = 132$, Nucl. Data Sheets **104**, 497 (2005).
[45] C. Bell, P. Raghavan, Y. Niv, D. E. Murnick, and P. Pappas, Lifetime and g-factor of the 10^+ isomeric state ^{134}Ba, Bull. Am. Phys. Soc. **27**, DF10 (1982).
[46] N. J. Stone, Table of nuclear magnetic dipole and electric quadrupole moments, At. Data Nucl. Data Tables **90**, 75 (2005).
[47] J. Burde, S. Eshhar, A. Ginzburg, and A. Molchadzki, Absolute transition probabilities in ^{134}Ba, Nucl. Phys. A **250**, 141 (1975).
[48] A. M. Kleinfeld, A. Bockisch, and K.P. Lieb, Reorientation effect and multiple coulomb excitation measurements of ^{134}Ba, Nucl. Phys. A **283**, 526 (1977).
[49] B. Fazekas, T. Belgya, G. Molnar, A. Veres, R. A. Gatenby, S. W. Yates, and T. Otsuka, Level scheme and mixed-symmetry states of ^{134}Ba from in-beam $(n, n'\gamma)$ measurements, Nuc. Phys. A **548**, 249 (1992).
[50] Evaluated Nuclear Structure Data File (ENSDF), http://www.nndc.bnl.gov/ensdf.
[51] T. Lönnroth, S. Tormanen, C. Fahlander, P. Granholm, R. Julin, S. Juutinen, P. Manngard, J. Nyberg, A. Pakkanen, K. Schiffer, G. Sletten, and A. Virtanen, Coexistence of shapes in transitional ^{132,133,134}Ba, JYFL Ann. Rept. 1989-1990 (1990), p. 99.
[52] W. T. Cluff, The High-Spin Structure of ^{134,135}Ba and ^{120}Te, Ph.D. thesis, Florida State University (2008).
[53] X. Che, S. Zhu, M. Li, Y. Yu, Y. Chen, H. Ding, L. Zhu, X. Wu, G. Li, Y. Liu *et al.*, Level structure with high excitation states in ^{134}Ba, High Energy Phys. Nucl. Phys. **31**, 621 (2007).
[54] S. Akkoyun *et al.*, AGATA—Advanced GAmma Tracking Array, Nucl. Instrum. Methods A **668**, 26 (2012).
[55] A. M. Stefanini, L. Corradi, G. Maron, A. Pisent, M. Trotta, A. M. Vinodkumar, S. Beghini, G. Montagnoli, F. Scarlassara, G. F. Segato, A. De Rosa, G. Inglima, D. Pierroutsakou, M. Romoli, M. Sandoli, G. Pollarolo, and A. Latina, The heavy-ion magnetic spectrometer PRISMA, Nucl. Phys. A **701**, 217 (2002).
[56] L. Corradi, S. Szilner, G. Pollarolo, D. Montanari, E. Fioretto, A. M. Stefanini, J. J. Valiente-Dobón, E. Farnea, C. Michelagnoli, G. Montagnoli, F. Scarlassara, C. A. Ur, T. Mijatović, D. Jelavić Malenica, N. Soić, and F. Haas, Multinucleon transfer reactions: Present status and perspectives, Nucl. Instrum. Methods B **317**, 743 (2013).
[57] S. Szilner, C. A. Ur, L. Corradi, N. Marginean, G. Pollarolo, A. M. Stefanini, S. Beghini, B. R. Behera, E. Fioretto, A. Gadea, B. Guiot, A. Latina, P. Mason, G. Montagnoli, F. Scarlassara, M. Trotta, G. de Angelis, F. Della Vedova, E. Farnea, F. Haas, S. Lenzi, S. Lunardi, R. Marginean, R. Menegazzo, D. R. Napoli, M. Nespolo, I. V. Pokrovsky, F. Recchia, M. Romoli, M.-D. Salsac, N. Soić, and J. J. Valiente-Dobón, Multinucleon transfer reactions in closed-shell nuclei, Phys. Rev. C **76**, 024604 (2007).

[58] L. Netterdon, V. Derya, J. Endres, C. Fransen, A. Hennig, J. Mayer, C. Müller-Gatermann, A. Sauerwein, P. Scholz, M. Spieker, and A. Zilges, The γ-ray spectrometer HORUS and its applications for nuclear astrophysics, Nucl. Instrum. Methods A **754**, 94 (2014).

[59] J.-M. Régis, M. Dannhoff, J. Jolie, C. Müller-Gatermann, and N. Saed-Samii, On the time response of background obtained in γ-ray spectroscopy experiments using $LaBr_3$(Ce) detectors with different shielding, Nucl. Instr. Methods A **811**, 42 (2016).

[60] N. Saed-Samii, Diplomarbeit, Universität zu Köln (2013) (unpublished).

[61] R. Brun and F. Rademakers, Root-an object oriented data analysis framework, Nucl. Instrum. Methods A **389**, 81 (1997).

[62] J. Theuerkauf, Die Analyse von zwei- und mehrdimensionalen $\gamma\gamma$-Koinzidenzspektren an Beispielen aus Hochspinexperimenten in der Massengegend um ^{146}Gd, Ph.D. thesis, Universität zu Köln (1994).

[63] I. Wiedenhöver, Computer code CORLEONE (1997) (unpublished).

[64] I. Wiedenhöver, O. Vogel, H. Klein, A. Dewald, P. von Brentano, J. Gableske, R. Krücken, N. Nicolay, A. Gelberg, P. Petkov, A. Gizon, J. Gizon, D. Bazzacco, C. Rossi Alvarez, G. de Angelis, S. Lunardi, P. Pavan, D. R. Napoli, S. Frauendorf, F. Dönau, R. V. F. Janssens, and M. P. Carpenter, Detailed angular correlation analysis with 4π spectrometers: Spin determinations and multipolarity mixing measurements in ^{128}Ba, Phys. Rev. C **58**, 721 (1998).

[65] K. S. Krane and R. M. Steffen, Determination of the $E2/M1$ multipole mixing ratios of the gamma transitions in ^{110}Cd, Phys. Rev. C **2**, 724 (1970).

[66] K. S. Krane, R. M. Steffen, and R. M. Wheeler, Directional correlations of gamma radiations emitted from nuclear states oriented by nuclear reactions or cryogenic methods, At. Data Nucl. Data Tables **11**, 351 (1973).

[67] A. Linnemann, Das HORUS-Würfelspektrometer und Multiphononanregungen in ^{106}Cd, Ph.D. thesis, Universität zu Köln (2006).

[68] L. Bettermann, C. Fransen, S. Heinze, J. Jolie, A. Linnemann, D. Mücher, W. Rother, T. Ahn, A. Costin, N. Pietralla, and Y. Luo, Candidates for the one-phonon mixed-symmetry state in ^{130}Xe, Phys. Rev. C **79**, 034315 (2009).

[69] A. Gadea, E. Farnea, J. J. Valiente-Dobón, B. Million, D. Mengoni, D. Bazzacco, F. Recchia, A. Dewald, Th. Pissulla, W. Rother, G. de Angelis *et al.*, Conceptual design and infrastructure for the installation of the first AGATA sub-array at LNL, Nucl. Instrum. Methods A **654**, 88 (2011).

[70] A. Wiens, H. Hess, B. Birkenbach, B. Bruyneel, J. Eberth, D. Lersch, G. Pascovici, P. Reiter, and H.-G. Thomas, The AGATA triple cluster detector, Nucl. Instrum. Methods A **618**, 223 (2010).

[71] B. Bruyneel, B. Birkenbach, and P. Reiter, Pulse shape analysis and position determination in segmented HPGe detectors: The AGATA detector library, Eur. Phys. J. A **52**, 70 (2016).

[72] A. Lopez-Martens, K. Hauschild, A. Korichi, J. Roccaz, and J-P. Thibaud, γ-ray tracking algorithms: A comparison, Nucl. Instrum. Methods A **533**, 454 (2004).

[73] R. S. Kempley *et al.*, Cross Coincidences in the ^{136}Xe + ^{208}Pb deep-inelastic reaction, Acta. Phys. Pol. B **42**, 717 (2011).

[74] M. Siciliano *et al.*, Neutron-rich nuclei in the vicinity of ^{208}Pb, LNL Annual Report 2014 **241**, 63 (2015).

[75] S. Chakraborty, H. P. Sharma, S. S. Tiwary, C. Majumder, P. Banerjee, S. Ganguly, S. Rai, Pragati, Swati Modi, P. Arumugam, Mayank, S. Kumar, R. Palit, A. Kumar, S. S. Bhattacharjee, R. P. Singh, and S. Muralithar, Rotational band on a three-quasineutron isomer in ^{127}Xe, Phys. Rev. C **97**, 054311 (2018).

[76] B. A. Brown and W. D. M. Rae, The shell-model code NuShellX@MSU, Nucl. Data Sheets **120**, 115 (2014).

[77] N. Shimizu, Nuclear shell-model code for massive parallel computation, KSHELL (2013), arXiv:1310.5431 [nucl-ph].

[78] E. Caurier, G. Martínez-Pinedo, F. Nowacki, A. Poves, and A. P. Zuker, The shell model as a unified view of nuclear structure, Rev. Mod. Phys. **77**, 427 (2005).

[79] R. Machleidt, F. Sammarruca, and Y. Song, Nonlocal nature of the nuclear force and its impact on nuclear structure, Phys. Rev. C **53**, R1483 (1996).

[80] M. Honma, T. Otsuka, T. Mizusaki, and M. Hjorth-Jensen, Shell-model fits for Sn isotopes, RIKEN Accel. Progr. Rep. **49**, 77 (2015).

[81] M. Honma, T. Otsuka, T. Mizusaki, and M. Hjorth-Jensen, Shell-model fits for Sn isotopes, RIKEN Accel. Prog. Rep. **45**, 35 (2012).

[82] Y. Utsuno, T. Otsuka, B. A. Brown, M. Honma, T. Mizusaki, and N. Shimizu, Shape transitions in exotic Si and S isotopes and tensor-force-driven jahn-teller effect, Phys. Rev. C **86**, 051301(R) (2012).

[83] T. Otsuka, T. Suzuki, M. Honma, Y. Utsuno, N. Tsunoda, K. Tsukiyama, and M. Hjorth-Jensen, Novel Features of Nuclear Forces and Shell Evolution in Exotic Nuclei, Phys. Rev. Lett. **104**, 012501 (2010).

[84] Y. Utsuno, T. Otsuka, N. Shimizu, M. Honma, T. Mizusaki, Y. Tsunoda, and T. Abe, Recent shell-model results for exotic nuclei, EPJ Web Conf. **66**, 02106 (2014).

[85] L. Coraggio, L. De Angelis, T. Fukui, A. Gargano, and N. Itaco, Calculation of Gamow-Teller and two-neutrino double-β decay properties for ^{130}Te and ^{136}Xe with a realistic nucleon-nucleon potential, Phys. Rev. C **95**, 064324 (2017).

[86] M. Hasegawa, K. Kaneko, and S. Tazaki, Improvement of the extended p+qq interaction by modifying the monopole field, Nucl. Phys. A **688**, 765 (2001).

[87] K. Kaneko, M. Hasegawa, and T. Mizusaki, Quadrupole and octupole softness in the $N = Z$ nucleus ^{64}Ge, Phys. Rev. C **66**, 051306(R) (2002).

[88] K. Kaneko, Y. Sun, M. Hasegawa, and T. Mizusaki, Shell model study of single-particle and collective structure in neutron-rich Cr isotopes, Phys. Rev. C **78**, 064312 (2008).

[89] K. Kaneko, Y. Sun, T. Mizusaki, and M. Hasegawa, Shell-model study for neutron-rich *sd*-shell nuclei, Phys. Rev. C **83**, 014320 (2011).

[90] H.-K. Wang, Y. Sun, H. Jin, K. Kaneko, and S. Tazaki, Structure analysis for hole-nuclei close to ^{132}Sn by a large-scale shell-model calculation, Phys. Rev. C **88**, 054310 (2013).

[91] H.-K. Wang, K. Kaneko, and Y. Sun, Quenching of the neutron $N = 82$ shell gap near ^{120}Sr with monopole-driving core excitations, Phys. Rev. C **91**, 021303(R) (2015).

[92] H.-K. Wang, K. Kaneko, Y. Sun, Y. Q. He, S.-F. Li, and J. Li, Monopole effects, isomeric states, and cross-shell excitations in the $A = 129$ hole nuclei near ^{132}Sn, Phys. Rev. C **95**, 011304(R) (2017).

[93] H.-K. Wang, K. Kaneko, and Y. Sun, Isomerism and persistence of the $N = 82$ shell closure in the neutron-rich ^{132}Sn region, Phys. Rev. C **89**, 064311 (2014).

[94] A. Astier, M.-G. Porquet, Ts. Venkova, D. Verney, Ch. Theisen, G. Duchêne, F. Azaiez, G. Barreau, D. Curien, I. Deloncle, O. Dorvaux, B. J. P. Gall, M. Houry, R. Lucas, N. Redon, M. Rousseau, and O. Stézowski, High-spin structures of five N = 82 isotopes: $^{136}_{54}$Xe, $^{137}_{55}$Cs, $^{138}_{56}$Ba, $^{139}_{57}$La, and $^{140}_{58}$Ce, Phys. Rev. C **85**, 064316 (2012).

[95] A. Vogt, M. Siciliano, B. Birkenbach, P. Reiter, K. Hadyńska-Klęk, C. Wheldon, J. J. Valiente-Dobón, E. Teruya, N. Yoshinaga, K. Arnswald, D. Bazzacco, A. Blazhev, A. Bracco, B. Bruyneel, R. S. Chakrawarthy, R. Chapman, D. Cline, L. Corradi, F. C. L. Crespi, M. Cromaz, G. de Angelis, J. Eberth, P. Fallon, E. Farnea, E. Fioretto, C. Fransen, S. J. Freeman, B. Fu, A. Gadea, W. Gelletly, A. Giaz, A. Görgen, A. Gottardo, A. B. Hayes, H. Hess, R. Hetzenegger, R. Hirsch, H. Hua, P. R. John, J. Jolie, A. Jungclaus, V. Karayonchev, L. Kaya, W. Korten, I. Y. Lee, S. Leoni, X. Liang, S. Lunardi, A. O. Macchiavelli, R. Menegazzo, D. Mengoni, C. Michelagnoli, T. Mijatović, G. Montagnoli, D. Montanari, C. Müller-Gatermann, D. Napoli, C. J. Pearson, Zs. Podolyák, G. Pollarolo, A. Pullia, M. Queiser, F. Recchia, P. H. Regan, J.-M. Régis, N. Saed-Samii, E. Şahin, F. Scarlassara, M. Seidlitz, B. Siebeck, G. Sletten, J. F. Smith, P.-A. Söderström, A. M. Stefanini, O. Stezowski, S. Szilner, B. Szpak, R. Teng, C. Ur, D. D. Warner, K. Wolf, C. Y. Wu, and K. O. Zell, High-spin structures in ^{132}Xe and ^{133}Xe and evidence for isomers along the $N = 79$ isotones, Phys. Rev. C **96**, 024321 (2017).

[96] L. Kaya, A. Vogt, P. Reiter, C. Müller-Gatermann, A. Gargano, L. Coraggio, N. Itaco, A. Blazhev, K. Arnswald, D. Bazzacco, B. Birkenbach, A. Bracco, B. Bruyneel, L. Corradi, F. C. L. Crespi, G. de Angelis, M. Droste, J. Eberth, E. Farnea, E. Fioretto, C. Fransen, A. Gadea, A. Giaz, A. Görgen, A. Gottardo, K. Hadyńska-Klęk, H. Hess, R. Hetzenegger, R. Hirsch, P. R. John, J. Jolie, A. Jungclaus, W. Korten, S. Leoni, L. Lewandowski, S. Lunardi, R. Menegazzo, D. Mengoni, C. Michelagnoli, T. Mijatović, G. Montagnoli, D. Montanari, D. Napoli, Zs. Podolyák, G. Pollarolo, F. Recchia, D. Rosiak, N. Saed-Samii, E. Şahin, M. Siciliano, F. Scarlassara, M. Seidlitz, P.-A. Söderström, A. M. Stefanini, O. Stezowski, S. Szilner, B. Szpak, C. Ur, J. J. Valiente-Dobón, M. Weinert, K. Wolf, and K. O. Zell, Identification of high-spin proton configurations in ^{136}Ba and ^{137}Ba, Phys. Rev. C **99**, 014301 (2019).

[97] Samuel M. Harris, Higher order corrections to the cranking model, Phys. Rev. **138**, B509 (1965).

[98] A. Dewald, Transition probabilities in transitional nuclei in the $A = 130$ region, Prog. Part. Nucl. Phys. **28**, 409 (1992).

Addendum: $19/2^+$ isomer in the $N = 77$ isotone ^{137}Nd

Similar to the $J^\pi = 23/2^+$ isomers along the $N = 79$ chain, isomeric $J^\pi = 19/2^+$ states appear along the $N = 77$ chain. As discussed in Sec. 1.1.1 of this thesis (see Figure 3(b)), precise half-lives were evaluated in ^{127}Sn [32], ^{131}Xe [33], and ^{135}Ce [34]. Only estimates of the corresponding half-lives in the lower ns regime were reported for ^{133}Ba [36] and ^{137}Nd [35]. The investigation of the $J^\pi = 19/2^+$ isomer in ^{133}Ba is subject of the publication "*Isomer spectroscopy in* ^{133}*Ba and high-spin structure of* ^{134}*Ba*", presented in this thesis. Considering the results of this publication, the last remaining $J^\pi = 19/2^+$ state with insufficiently known half-life information is the 2222-keV state in ^{137}Nd. The high-spin structure above the $J^\pi = 11/2^-$ isomer in ^{137}Nd was thoroughly investigated by several heavy-ion experiments [2]. Only a single study aimed at the investigation of high-spin isomers. Gizon *et al.* [35] determined a half-life range of 1 to 4 ns for the 2222-keV state in ^{137}Nd utilizing a pulsed ^{16}O + ^{124}Te experiment. This state was assigned with spin/parity of $J^\pi = 19/2^+$, based on the fact that an alternative parity-conserving $M1$ transition exhibits an unusually large hindrance factor.

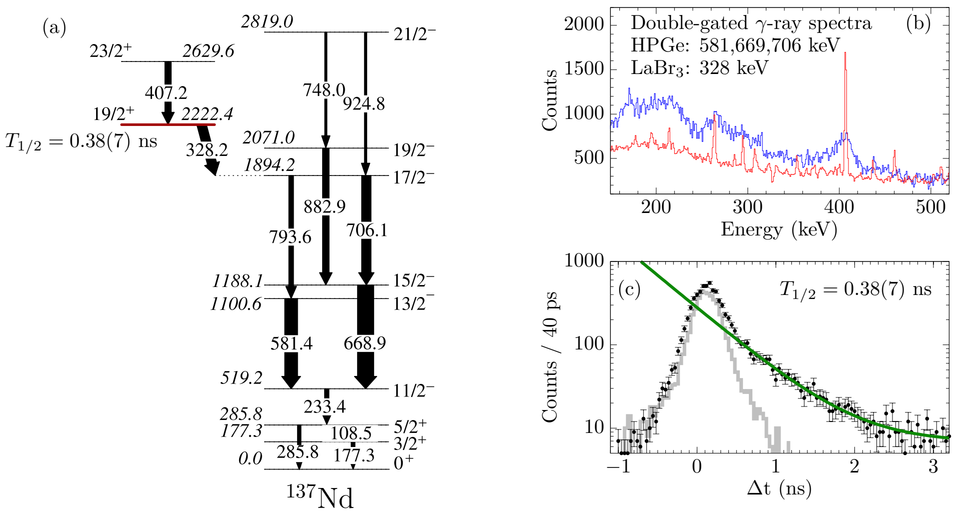

Figure 11: (a) Partial levelscheme of ^{137}Nd. Energies and spins are adopted from Ref. [35]. (b) $LaBr_3$ (blue) and HPGe (red) γ-ray spectra with applied double HPGe-$LaBr_3$ gates. (c) Time-difference spectrum between 407 and 328-keV transitions. The thick green line indicates the exponential fit used to extract the half-life of the $J^\pi = 19/2^+$ state. The grey step function shows a prompt time spectrum.

A possible onset of $J^\pi = 19/2^+$ isomerism along the $N = 77$ chain was subject of a ^{16}O+^{125}Te fusion-evaporation experiment utilizing the electronic fast-timing technique at the IKP Cologne in order to measure lower nano-, and picosecond-scale half-lives in ^{137}Nd. Gamma rays were detected using eleven HPGe detectors, mounted in two rings at 45° and 142.3° with respect to the beam axis. In addition, seven $LaBr_3$ detectors were placed around the target chamber perpendicular to the beam axis. Three time-to-amplitude (TAC) converters were used to measure the time difference between γ rays, detected in two $LaBr_3$ detectors in HPGe-gated triple-coincidence spectra.

To increase the statistics in the analysis of the 2222-keV state, a sum spectrum of three doubly-gated spectra with a constant $LaBr_3$ gate on the 328-keV transition and different HPGe gates on the 581, 669, and 706-keV transitions is analysed. In order to ensure clear conditions for the second $LaBr_3$ gate, the final doubly-gated $LaBr_3$ and HPGe spectra are shown in Fig. 11(b). The 407-keV peak in the $LaBr_3$ spectrum is not contaminated by other transitions. By setting a third gate in the summed $LaBr_3$ spectrum, delayed and anti-delayed TAC spectra are obtained. Figure 11(c) shows the sum of anti-delayed and inverted delayed TAC time-difference spectrum. The half-life of the $J^{\pi} = 19/2^{+}$ state at 2222 keV in ^{137}Nd is longer than the width of the prompt peak. Therefore, a slope appears on the delayed side of the prompt peak. In addition, a time-difference spectrum between the 706-, and 669-keV transitions is plotted by a grey step function, demonstrating that the residual background of the prompt peak is negligible in the region of the slope. The thick green line indicates the exponential fit of the data points. A fit results in a preliminary half-life of 0.38(7) ns, taking into account systematic errors. The value is slightly lower than the obtained value of 1-4 ns from Ref. [35]. However, the new value shows a smooth onset of decreasing half-lives of $J^{\pi} = 19/2^{+}$ states while filling of the proton number along the $N = 77$ chain.

Manuscript I:
Excited states in doubly-odd ^{130}I

Manuscript: Excited states in doubly-odd ^{130}I

L. Kaya,[1,a] A. Vogt,[1] P. Reiter,[1] M. Siciliano,[2,3,4] C. Müller-Gatermann,[1] H.-K. Wang,[5] A. Gargano,[6] G. De Gregorio,[6] K. Arnswald,[1] D. Bazzacco,[7] B. Birkenbach,[1] A. Blazhev,[1] A. Bracco,[8] B. Bruyneel,[4] L. Coraggio,[6] L. Corradi,[3] F. C. L. Crespi,[8] G. de Angelis,[3] M. Droste,[1] J. Eberth,[1] E. Farnea,[7,b] E. Fioretto,[3] C. Fransen,[1] A. Gadea,[9] A. Giaz,[8] A. Görgen,[10,4] A. Gottardo,[3] K. Hadyńska-Klęk,[3] H. Hess,[1] R. Hirsch,[1] N. Itaco,[6,11] P. R. John,[12] J. Jolie,[1] A. Jungclaus,[13] W. Korten,[4] S. Leoni,[8] L. Lewandowski,[1] S. Lunardi,[2,7] R. Menegazzo,[7] D. Mengoni,[2,7] C. Michelagnoli,[14] T. Mijatović,[15] G. Montagnoli,[2,7] D. Montanari,[2,7] D. Napoli,[3] Zs. Podolyák,[16] G. Pollarolo,[17] F. Recchia,[2,7] N. Saed-Samii,[1] E. Şahin,[10] F. Scarlassara,[2,7] M. Seidlitz,[1] P.-A. Söderström,[18] A. M. Stefanini,[3] O. Stezowski,[19] S. Szilner,[15] B. Szpak,[20] C. Ur,[7] J. J. Valiente-Dobón,[3] and K. O. Zell[1]

[1] *Institut für Kernphysik, Universität zu Köln, D-50937 Köln, Germany*
[2] *Dipartimento di Fisica e Astronomia, Università di Padova, I-35131 Padova, Italy*
[3] *Istituto Nazionale di Fisica Nucleare, Laboratori Nazionali di Legnaro, I-35020 Legnaro, Italy*
[4] *Institut de Recherche sur les lois Fondamentales de l'Univers – IRFU, CEA/DSM, Université de Paris-Saclay, F-91191 Gif-sur-Yvette Cedex, France*
[5] *College of Physics and Telecommunication Engineering, Zhoukou Normal University, Henan 466000, People's Republic of China*
[6] *Istituto Nazionale di Fisica Nucleare, Sezione di Napoli, I-80126 Napoli, Italy*
[7] *Istituto Nazionale di Fisica Nucleare, Sezione di Padova, I-35131 Padova, Italy*
[8] *Dipartimento di Fisica, Università di Milano and INFN Sezione di Milano, I-20133 Milano, Italy*
[9] *Instituto de Física Corpuscular, CSIC-Universidad de Valencia, E-46071 Valencia, Spain*
[10] *Department of Physics, University of Oslo, P. O. Box 1048 Blindern, N-0316 Oslo, Norway*
[11] *Dipartimento di Matematica e Fisica, Università degli Studi della Campania "Luigi Vanvitelli", viale A. Lincoln 5, I-8110 Caserta, Italy*
[12] *Institut für Kernphysik, Technische Universität Darmstadt, D-64289 Darmstadt, Germany*
[13] *Instituto de Estructura de la Materia, CSIC, Madrid, E-28006 Madrid, Spain*
[14] *Institut Laue-Langevin (ILL), 38042 Grenoble Cedex 9, France*
[15] *Ruder Bošković Institute, HR-10 002 Zagreb, Croatia*
[16] *Department of Physics, University of Surrey, Guildford, Surrey GU2 7XH, United Kingdom*
[17] *Dipartimento di Fisica Teorica dell'Università di Torino and INFN, I-10125 Torino, Italy*
[18] *Extreme Light Infrastructure-Nuclear Physics (ELI-NP), 077125 Bucharest-Magurele, Romania*
[19] *Université de Lyon, Université Lyon-1, CNRS/IN2P3, UMR5822, IPNL, F-69622 Villeurbanne Cedex, France*
[20] *Henryk Niewodniczański Institute of Nuclear Physics PAN, PL-31342 Kraków, Poland*

The transitional nucleus ^{130}I is investigated after multinucleon transfer (MNT) in the ^{136}Xe+^{238}U and ^{136}Xe+^{208}Pb reactions employing the high-resolution Advanced GAmma Tracking Array (AGATA) coupled to the magnetic spectrometer PRISMA at the Laboratori Nazionali di Legnaro, Italy and in the fusion-evaporation reaction ^{124}Sn(^{9}Be,$p2n$)^{130}I as an elusive reaction product employing a γ-ray array in combination with a silicon detector to gate on evaporated protons at the University of Cologne, Germany. The previously unknown high-spin level scheme of ^{130}I is established up to 2.8 MeV. Members of the $\pi g_{7/2} \otimes \nu h_{11/2}$ and $\pi h_{11/2} \otimes \nu h_{11/2}$ configurations are interpreted in terms of systematics and a comparison with results of large-scale shell-model calculations.

I. INTRODUCTION

Shell-model studies of the nuclear structure above doubly-magic nucleus ^{132}Sn are mainly focused on even-even systems. Nuclei with odd proton and neutron numbers represent a challenging topic for experimentalists and theorists. However, such studies furnish important information on pairing energies and direct information on the proton-neutron interaction. This is essential for spherical shell-model theory and can be obtained from odd-odd nuclei by studying multiplets arising from correlations between valence particles. Due to the strong residual pairing force between the unpaired nucleons, odd-odd nuclei show an intricate nuclear structure. These complex systems give rise to a strong mixing of single-particle and collective excitations. Therefore, doubly-odd I isotopes near the $N = 82$ neutron closed shell provide an interesting benchmark for the predictive power of modern effective shell-model interactions.

Figure 1 presents a partial nuclei chart of the $N \leq 82$, $Z \geq 50$ region. The nuclei are color coded with the maximum excitation energy of states previously reported from γ-ray spectroscopy experiments. Obviously, precise and extensive experimental information is available for most of the nuclei between Te and Ba isotopes. However, the

[a] Corresponding author: levent.kaya@ikp.uni-koeln.de
[b] Deceased.

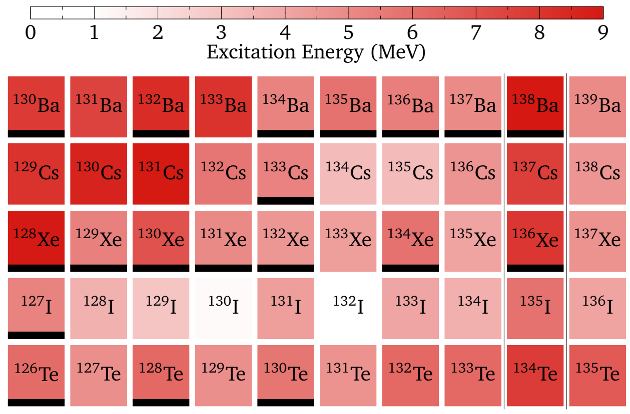

Figure 1. Part of the nuclei chart showing the transitional Te-I-Xe-Cs-Ba region. The colour code indicates the maximum excitation energy measured in high-spin γ-ray spectroscopy experiments. Black horizontal lines mark stable isotopes. Data compiled from Ref. [1].

systematics of iodine isotopes lacks some detailed knowledge. The high-spin level structure of doubly-odd I isotopes is associated with two-quasiparticle (2-QP) configurations. In face of the neutron-rich structure, bands build on couplings of the unpaired neutron in the $h_{11/2}$ orbital with the unpaired proton occupying one of the $0g_{7/2}$, $1d_{5/2}$, $1d_{3/2}$, $2s_{1/2}$, and $0h_{11/2}$ orbitals are of special interest. In fact, collective bands build on the $J^\pi = 8^-$ state with $\pi g_{7/2}/d_{5/2} \otimes \nu h_{11/2}$ configurations were systematically reported in a series of doubly-odd I isotopes [1–6]. The band undergoes a transition from a collective structure in midshell iodine isotopes [6] to a sequence of single-particle states in ^{134}I [7]. Similarly, a gradual change of the rotational-like $\pi h_{11/2} \otimes \nu h_{11/2}$ 2-QP band based on the $J^\pi = 10^+$ state to a vibration-like structure was observed along the doubly-odd I chain towards the $N = 82$ shell closure [1–6]. No complementary information were obtained for the neutron-rich nuclei ^{130}I and ^{132}I, where results on excited states are limited to direct reactions with light ions and β-decay studies.

The spin and parity assignment of the $J^\pi = 5^+$ ground state in ^{130}I with a half-life of $T_{1/2} = 12.6$ h is known since the 1950s [8]. Prior to this work, excited states in ^{130}I were studied solely via proton-induced ^{130}Te$(p, n\gamma)$ [9, 10] and neutron-induced ^{129}I(n, γ) [10] reactions by means of γ-ray spectroscopy. The first study [9] obtained a level scheme with excited states up to approx. 1 MeV excitation energy and spin values not higher than 6 $\hbar$. A $J^\pi = 6^-$ isomer at 85 keV with a half-life of 229(14) ns and a negative g factor was found to directly decay into the ground state [9]. Based on that work, a very comprehensive spectroscopic study was performed by Sakharov *et al.* [10] utilizing gamma and conversion electron spectroscopy at ILL in Grenoble with a setup combining the bent crystal spectrometer GAMS [11] and the electron spectrometer BILL [12] in conjunction with an HPGe array, at LNPI in Gatchina with the magnetic spectrometer BETSI [13] in combination with an HPGe and Si(Li) array, and finally at the Q3D spectrometer [14] using the Munich tandem accelerator. As a result of the different experiments, the previously known level scheme was extended by 43 excited states with precise measured excitation energies and unique spin assignments. A comparison between the observed excitation patterns of ^{130}I from (n, γ) and (d, p) reactions revealed several two-quasiparticle multiplets originating from different proton-neutron (p-n) configurations. A nanosecond $J^\pi = 8^-$ isomer ($T_{1/2} = 315(15)$ ns) was found to be a member of the $\pi g_{7/2} \otimes \nu h_{11/2}$ configuration. Moreover, the $J^\pi = 6^-$ states split into two distinct p-n multiplets. The yrast $J^\pi = 6^-$ isomer is decaying via a 69.5-keV γ-ray towards the ground state with a half-life of 133(7) ns, identified as another member of the $\pi g_{7/2} \otimes \nu h_{11/2}$ multiplet. In contrast, the previously known second excited $J^\pi = 6^-$ isomer at 85 keV was confirmed with a remeasured half-life of 254(4) ns and associated with the $\pi d_{5/2} \otimes \nu h_{11/2}$ multiplet.

In this article, excited states in ^{130}I were populated in three different experiments. Multinucleon-transfer reactions have proven to be an efficient way for the population of intermediate to high-spin states of $A = 130$ nuclei. The combination of the high-resolution position-sensitive Advanced GAmma Tracking Array (AGATA) [15] and the PRISMA magnetic mass spectrometer [16–18] at the Laboratori Nazionali di Legnaro (LNL, Italy) was employed to study transitions in ^{130}I after ^{136}Xe + ^{238}U and ^{136}Xe + ^{208}Pb multinucleon transfer. Furthermore, ^{130}I was populated in a ^{124}Sn(^{9}Be, $p2n$)^{130}I fusion-evaporation reaction at the Institute of Nuclear Physics, University of Cologne. A γ-ray array was coupled to a silicon detector for the detection of evaporated protons.

This paper is organized as follows: the experimental setup, data analysis and the experimental results of the three experiments are presented in Sec. II. A comparison with results from modern shell-model calculations is presented in Sec. III before the paper closes with a summary and an outlook in Sec. IV.

II. EXPERIMENTAL PROCEDURE, DATA ANALYSIS AND RESULTS

A. ^{136}Xe + ^{238}U multinucleon transfer

States in ^{130}I were excited in a ^{136}Xe + ^{238}U multinucleon-transfer experiment at the Laboratori Nazionali di Legnaro (LNL), Italy. The PIAVE+ALPI accelerator provided a ^{136}Xe beam with an energy of 7.35 MeV/nucleon and a beam current of 2 pnA to bombard two different ^{238}U targets with thicknesses of 1 and 2 mg/cm^2. The ^{238}U targets are supported by 0.8-mg/cm^2 thick Nb foils facing the beam. AGATA was employed in its full demonstrator configuration with 15 HPGe detectors in five triple cryostats placed in the nom-

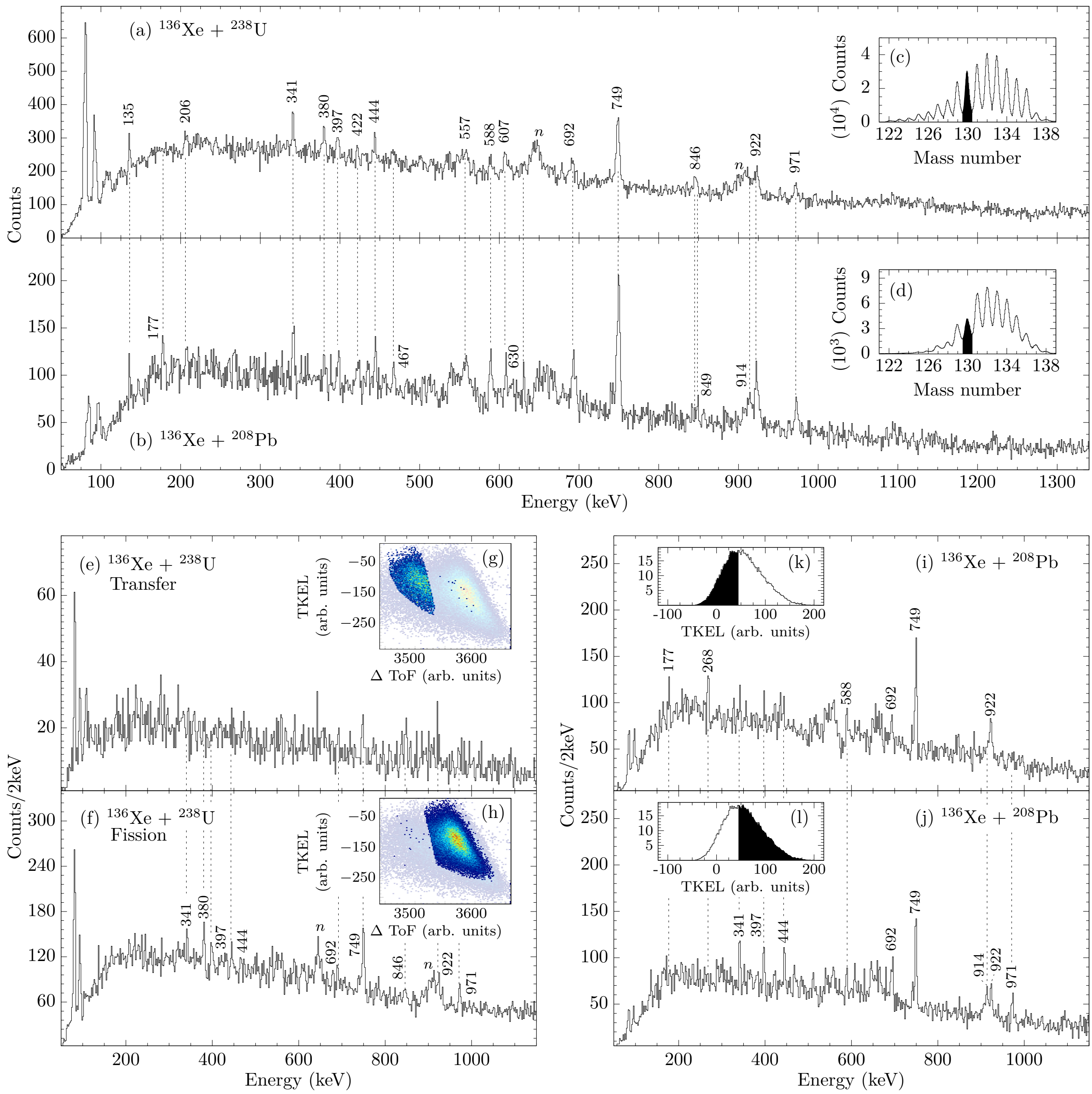

Figure 2. Doppler-corrected γ-ray spectra gated on ^{130}I identified with PRISMA in the (a) ^{136}Xe + ^{238}U and (b) ^{136}Xe + ^{208}Pb experiments. Both insets (c) and (d) represent the mass spectra of the I isotopes obtained with PRISMA. The applied mass gates on ^{130}I are marked black. γ-ray spectrum of ^{130}I with a gate on (e) transfer-, and (f) fission-like events from the ^{136}Xe + ^{238}U experiment. Matrix of the time difference ΔToF between PRISMA and DANTE with respect to the total kinetic energy loss of ^{130}I, visualizing the applied two dimensional gates on (g) transfer-, and (h) fission-like events. γ-ray spectrum of ^{130}I with gates on (i) low TKEL and (j) high TKEL values, respectively. The applied gates on the TKEL distributions are shown in the insets (k) and (l).

inal position, 23.5 cm away from the target. Information on the data analysis of this experiment is comprised in Ref. [19]. The light projectile-like reaction fragments of interest were identified by the magnetic spectrometer PRISMA [16–18] placed at the reaction's grazing angle $\theta_{\mathrm{lab}} = 50^\circ$. Pulse-shape analysis of the digitized detector signals was applied to determine the individual interaction points within the HPGe shell [20], allowing the

Orsay forward-tracking algorithm [21] to reconstruct the individual γ-ray energies, determine the first interaction point of the γ ray in the germanium and, thus, the emission angle. Together with the kinematic information from PRISMA, a precise Doppler correction was performed on an event-by-event basis. In order to retrieve a kinematic coincidence between different reaction products, the microchannel plate detector DANTE (Detector Array for Multinucleon Transfer Ejectiles) [22] was placed at the grazing angle for the target-like reaction products. The Doppler-corrected singles γ-ray spectrum of ^{130}I is shown in Fig. 2(a), while the corresponding mass spectrum along I isotopes is depicted in the inset Fig. 2(c). Random background is significantly suppressed by gating on the prompt time-difference peak with full width at half maximum (FWHM) of approx. 16 ns between AGATA and PRISMA. Contaminant γ-ray transitions from the adjacent $\pm1p$ and $\pm1n$ channels can be ruled out. Due to the presence of the long-lived $J^\pi = 6^-_{1,2}$ and $J^\pi = 8^-$ states in the level scheme of ^{130}I [10], decays from these states are not observed in the spectrum. The largest peak is located at 749 keV. Further peaks at 135, 206, 341, 380, 397, 422, 444, 557, 558, 607, 692, 846, 922, and 972 keV are visible in the spectrum. Since none of the decays from known low-spin excited states below 1 MeV excitation energy [9, 10] are observed in the γ-ray spectrum, it is most probably to assume that these transitions are attributed to cascades feeding the high-spin band-head. However, the accumulated statistic in the ^{136}Xe + ^{238}U experiment is insufficient to assign the new transitions in a level scheme of excited states via a $\gamma\gamma$ analysis.

Two production pathways were used to populate nuclei in this experiment; namely fission and MNT reactions. MNT reactions are a gateway to populate a large abundance of states from low to high spins and excitation energies, while fission reactions favor to select highly excited states [17]. The measured time-of-flight differences (ΔToF) of coincident reaction products between PRISMA and the DANTE MCP enables the discrimination of both production pathways. The different ΔToF values in fission and MNT modes can be traced back to the different kinetic energies of fission and transfer products. Recently, is was demonstrated that a similar analysis procedure provides additional information for the assignment of new transitions within the level scheme of ^{134}Xe [19, 23]. Figs. 2(g) and (h) present a matrix of ΔToF plotted against the total kinetic energy-loss (TKEL) value of the reaction, reconstructed from the measured momentum vector of the beam-like recoils inside PRISMA and the energy information provided by the DANTE MCP [24]. The calculated TKEL values for the fission fragments are only qualitative since this quantity is actually based on a binary-partner reaction system. Nonetheless, transfer-like and fission-like fragments are separated as two distinct domains in the matrix. A gate on MNT events, i.e. restricting the ToF domain and gating on TKEL values representing deep-inelastic reactions, yields preferably cold ^{130}I reaction products. The corresponding γ-ray spectrum is shown in Fig. 2(e). Otherwise, a gate on fission fragments predominantly selects highly excited ^{130}I nuclei (c.f. Fig. 2(f)). The statistics in the fission channel exceeds the number of counts in the MNT channel by a factor of seven. In both production mechanisms, the 749-keV transition is dominating the γ-ray spectra. Transitions at 341, 380, 397, 444, 692, 846, 922, and 971 keV are strongly represented in the fission part. This observation indicates that these transitions are most likely members of states located at higher excitation energies relative to the 749-keV transition. However, due to the limited statistic in the MNT channel, a more detailed analysis is not feasible.

Table I. Energies, spin assignments and relative in-beam intensities for γ-ray transitions in ^{130}I. Fitted energies and relative intensities normalized to the 748.8-keV transition are taken from two experiments: from the AGATA ^{136}Xe + ^{208}Pb (I^1_γ) and from the ^{9}Be + ^{124}Sn (I^2_γ) reactions. The uncertainties in the transition energies are ± 0.5 keV.

E_γ (keV)	E_i (keV)	E_f (keV)	I^1_γ	I^2_γ
135.2	$(2846.7 + x)$	$(2711.5 + x)$	14(4)	9(3)
177.4	—	—	14(3)	—
331.3	$(1740.2 + x)$	$(1406.1 + x)$	—	5(4)
340.5	$(1851.1 + x)$	$(1510.6 + x)$	25(4)	11(2)
380.3	—	—	15(3)	—
396.5	$(1907.1 + x)$	$(1510.6 + x)$	21(5)	13(2)
421.8	—	—	17(7)	—
443.8	$(2351.0 + x)$	$(1907.1 + x)$	24(5)	8(1)
466.9	—	—	12(4)	—
509.9	$(1915.1 + x)$	$(1406.1 + x)$	—	5(4)
587.8	$(1406.1 + x)$	$(818.3 + x)$	27(4)	23(3)
606.6	—	—	12(3)	—
630.0	—	—	14(3)	—
692.3	$(1510.6 + x)$	$(818.3 + x)$	54(6)	53(4)
748.8	$(818.3 + x)$	$(69.5 + x)$	≡ 100	≡ 100
845.6	—	—	13(4)	—
848.6	—	—	12(4)	—
914.0	—	—	10(4)	—
921.9	$(1740.2 + x)$	$(818.3 + x)$	36(5)	23(3)
971.3	$(2711.5 + x)$	$(1740.2 + x)$	16(4)	13(2)
1091.6	$(1909.9 + x)$	$(818.3 + x)$	—	5(4)

B. ^{136}Xe + ^{208}Pb multinucleon transfer

In a second multinucleon-transfer experiment states in ^{130}I were excited in a ^{136}Xe + ^{208}Pb reaction with a beam energy of 6.84 MeV per nucleon, delivered by the PIAVE+ALPI accelerator complex. The target had a thickness of 1-mg/cm^2. The Advanced GAmma Tracking Array (AGATA) [15] was employed in a first demon-

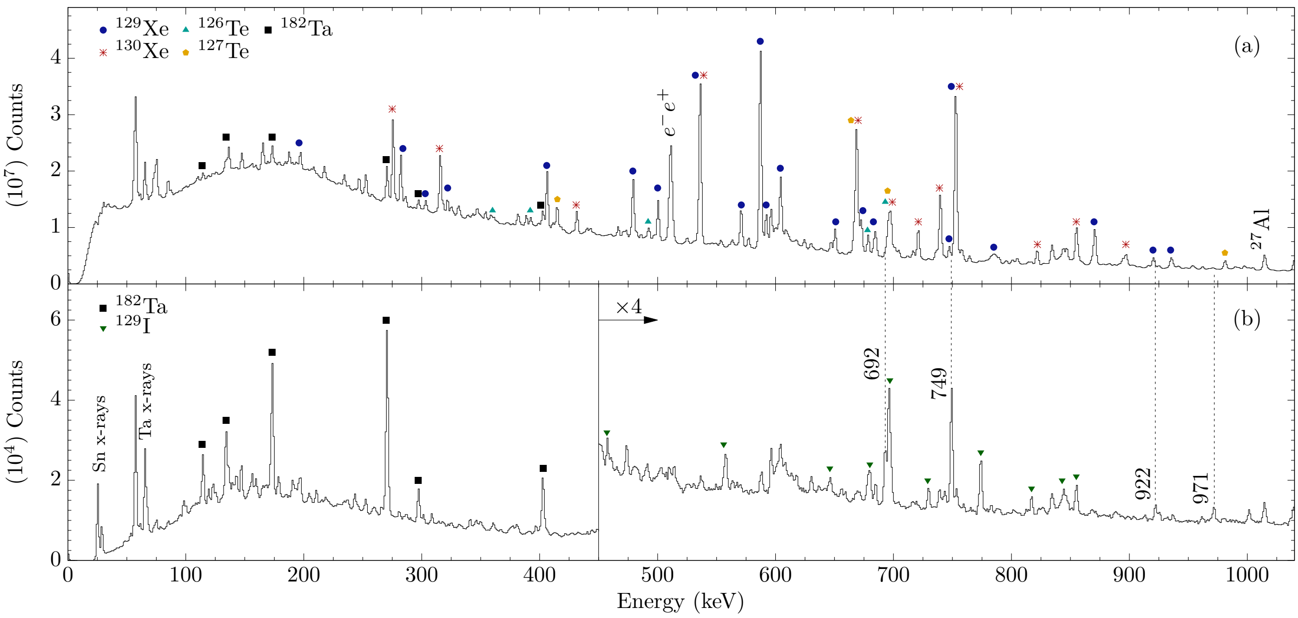

Figure 3. (a) Projection of the $\gamma\gamma$ matrix of the ^{9}Be + ^{124}Sn reaction. Strong peaks are stemming from the main reaction channels ^{129,130}Xe. (b) Gated $\gamma\gamma$ matrix with a gate on evaporated charged particles; Transitions from ^{129,130}I are prominently visible. Transitions from Te, Xe, I, and Ta isotopes are indicated with symbols and vertical dotted lines (^{130}I) in the spectrum.

strator configuration [22] with nine large-volume electronically segmented high-purity Ge (HPGe) detectors in three triple cryostats [25] placed with a distance of 18.8 cm from the target position. Besides the fact that PRISMA was placed at the reaction's grazing angle of $\theta_{\rm lab} = 50^{\circ}$, the experimental setup, data acquisition, and data analysis procedure are similar to the above-mentioned experiment in Sec. II A. Moreover, TKEL values are reconstructed similarly to the procedure in the ^{136}Xe + ^{238}U experiment, however, in this case, MNT is the predominant reaction pathway. Consequently, the TKEL is shared only between the two reaction products and the excitation energy of both reaction products is directly reflected in the TKEL distribution. Moreover, random background from fission is drastically reduced in this experiment. More details on the setup and data analysis are given in Refs. [26, 27]. The gated singles γ-ray spectrum and the corresponding gate on ^{130}I are depicted in Figs. 2(b) and (d), respectively. The spectrum supports the existence of the new lines in ^{130}I, identified in the ^{136}Xe + ^{238}U experiment. Transitions at γ-ray energies of 135, 206, 341, 397, 422, 444, 557, 588, 607, 692, 749, 846, 922, 971 keV are coherently observed in both MNT experiments. On the other hand, the 177, 467, 630, 849, 914-keV transitions are solely observed in the ^{136}Xe + ^{208}Pb experiment. Relative intensities I_{γ}^{1} from the ^{136}Xe + ^{208}Pb experiment are summarized in Tab. I. As expected from the ^{136}Xe + ^{238}U experiment, the 749-keV transition exhibits by far the largest intensity, which supports the assumption that it is placed on top of the band head.

The total excitation energy can be restricted by gating on the TKEL. A gate on small TKEL values can select reaction products which are less excited in energy and spin, while a gate on high TKEL values favors the population of higher-excited reaction products [17, 18]. Figures 2(i) and (j) show γ-ray spectra with gates on low and high TKEL values, respectively. Corresponding gates in the TKEL spectra are depicted in Figs. 2(k) and (l). The γ-ray spectrum gated on low TKEL values is dominated by the 749-keV transition which is in agreement with the observation of a relatively strong 749-keV transition in the transfer channel of the ^{136}Xe + ^{238}U experiment. Other transitions are located at 177, 268, 588, 692, and 922 keV. The peak content of the 749-keV transition exceeds the one of the second largest peak at 922 keV by a factor of approx. 5. This factor reduces to approx. 3.5 for the spectrum gated on high TKEL values. Moreover, other lines at 341, 397, 444, 914, and 971 keV emerge in the spectrum gated on high TKEL values, corroborating that these transitions are members of the high-spin structure, which supports the observation of the fission γ-ray spectrum in the ^{136}Xe + ^{238}U experiment.

C. ^{11}B + ^{124}Sn fusion evaporation

The construction of the level scheme of ^{130}I is finally based on the identification of the new transitions in the AGATA experiments and a complementary analysis of the ^{124}Sn(^{9}Be, $p2n$)^{130}I proton-gated $\gamma\gamma$ matrix. The extended and modified level scheme from this work is presented in Fig. 4. A 40-MeV ^{9}Be beam, delivered by the FN Tandem accelerator located at the Institute for Nuclear Physics, University of Cologne, impinged onto a 1.5-mg/cm^2 thick ^{124}Sn target which was evaporated onto a 1.9-mg/cm^2 ^{181}Ta backing. The thickness of the backing was chosen in such a way that all residual reaction products are stopped inside the backing and the amount of backscattered beam-particles is minimized. γ rays from excited states were measured employing two individual detector rings, equipped with six HPGe detectors at $\Theta_1 = 45°$ and five HPGe detectors at $\Theta_1 = 143°$ with respect to the beam axis. The relative cross section of approx. 1% for the population of ^{130}I is superimposed by the dominating ^{129,130}Xe neutron evaporation channels with several hundred millibarns. A detection of evaporated charged particles is imperative to enhance the peak-to-background ratio for the $p2n$ channel ^{130}I in the γ-ray spectrum. For this reason, evaporated charged particles were detected with an approx. 110-µm thick silicon detector mounted at backward angles with respect to the beam axis. Target and silicon detector were housed inside the Cologne plunger device [28]. The Si detector was shielded against backscattered beam particles by a 35-µm thick tantalum sheet. The thickness of the Ta sheet was deliberately chosen to stop backscattered beam particles and evaporated α particles inside the foil, while evaporated protons could reach the Si detector disk.

Coincident events were processed and recorded utilizing the synchronized 80-MHz XIA® Digital Gamma Finder (DGF) data-acquisition system and stored to disk. The data were analysed offline using the SOCO-V2 [29] and TV [30] codes. Events were sorted into (i) a general symmetrized two-dimensional matrix to study $\gamma\gamma$ coincidence relations, (ii) a three-dimensional cube for DSSSD-Ge-Ge coincidences, and (iii) a proton-γ-time cube. A total number of 1.5×10^{10} prompt $\gamma\gamma$ events and 3×10^6 proton-gated $\gamma\gamma$ events were recorded. The projection of the ungated $\gamma\gamma$ matrix is presented in Fig. 3(a). The major transitions originate from the main (^{9}Be, $xny\alpha$) reaction channels ^{129,130}Xe and ^{126,127}Te. Transitions from ^{182}Ta stem from the ^{181}Ta(^{9}Be,^{8}Be)^{182}Ta neutron-transfer reaction [31] in the tantalum foil in front of the Si detector and the tantalum backing of the target. Identified transitions from both AGATA MNT experiments (c.f. Sec. II A and II B) are not observed in the ungated projection. By setting a gate on Si energies above 100 keV, transitions assigned to the proton evaporation channels ^{129}I and ^{130}I are clearly visible in the projection of the proton-gated $\gamma\gamma$ matrix in Fig. 3(b). In addition, x-ray transitions of tin at 25.2 and 28.5 keV emerge in the gated projection. α particles from the decay of ^{8}Be could also reach the Si detector, explaining the strong peaks from ^{182}Ta. The analysis of the well-established ^{129}I level scheme shows transitions up to the $J^\pi = 23/2^+$ state at 2.6 MeV [32]. Moreover, candidates for transitions in ^{130}I at 692, 749, 922, and 971 keV are obviously visible well above the background in the proton-gated $\gamma\gamma$-projection.

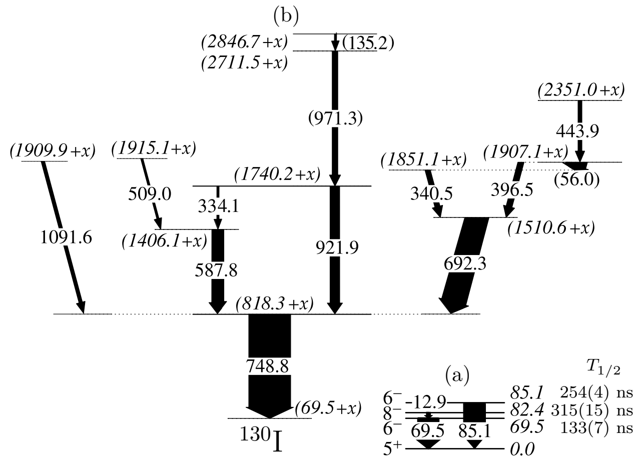

Figure 4. (a) Known low-spin level scheme of ^{130}I with the isomeric $J^\pi = 6^-_{1,2}$ and 8^- candidates for the high-spin band head [10] (see text for details). (b) High-spin level scheme of ^{130}I. The width of the arrows are proportional to the intensities above the (69.5 + x) state, extracted from the ^{9}Be + ^{124}Sn experiment and normalized to the 749-keV transition.

As mentioned in the introduction in Sec. I, the most promising candidate for the band head of the high-spin structure is the $J^\pi = 8^-$ isomer at 82.4 keV. However, also yrast and yrare $J^\pi = 6^-_{1,2}$ isomers are located at very similar energies. The arrangement of these states, as proposed by Ref. [10], is displayed in Fig. 4(a). Prompt-delayed coincidences between Si and HPGe detectors are exploited to connect the new transitions with the known level scheme of ^{130}I. Events in the Si detector are prompt with respect to the production of ^{130}I. Figure 5(a) presents the delayed γ-ray spectrum gated on prompt Si events with a gap of 225 ns. The spectrum at low energies is dominated by the x-ray transitions of Sn and Ta. The efficiency-corrected ratio between K_β and K_α x-ray transitions of Ta is measured to be 0.29(3) in the prompt proton-gated projection in Fig. 3(b), which is in accordance with the literature value of $K_\beta/K_\alpha = 0.26$ [33]. In the delayed γ-ray spectrum in Fig. 5(a), the intensity of the K_β x-ray transition is enhanced relative to the K_α transition; both transitions yield nearly the same amount of counts. This can be explained by the 69.5-keV γ-ray, deexciting the $J^\pi = 6^-_1$ isomer in ^{130}I, which is superimposed by the K_β x-ray transition of Ta. Moreover, the $6^-_2 \to 5^+$ 85.1-keV transition is not visible in the delayed spectrum. Consequently, it is assumed that the high-spin structure decays through the $J^\pi = 6^-_1$ state. However, a 12.9-keV $8^- \to 6^-_1$ transition can not be observed in this experiment due to the high internal conversion coefficient and the energy thresholds of the HPGe detectors.

Figure 5(b) shows the time difference spectrum between Si detector and the 69.5-keV γ-ray. In addition, a time-difference spectrum between Si detector and a nearby γ-ray domain is plotted by a grey step function. A distinct slope of the 69.5-keV γ-ray is visible well above the residual background. A first analysis of the decay curve of the 69.5-keV γ-ray indicates a considerably longer half-life than expected solely from the $J^{\pi} = 6_1^-$ state with $T_{1/2} = 133(7)$ ns. Thus, the delayed component of the $J^{\pi} = 8^-$ state has to be taken into account. However, a two-component fit can reproduce the experimental half-life values only within the two σ range. Most probably, the decay curve is influenced by the strong walk effect of the data acquisition at low γ-ray energies [34] and the nearby strong K_{β} x-ray transition of Ta. Consequently, the band head can not be uniquely assigned. Since no other long-lived states are known in ^{130}I, the extended and modified level scheme from this work, presented in Fig. 4(b), is based on a band head at an excitation energy of $69.5 + x$ keV, whereby x can by restricted to 0 or 12.9 keV. However, an assignment based on the $J^{\pi} = 8^-$ state should be preferred according to the measured time distribution in Fig. 4(b) and the systematics along the doubly-odd I chain (c.f. Sec. III A).

Various $\gamma\gamma$-coincidence spectra from the ^{9}Be + ^{124}Sn experiment are shown in Figs. 5(c)-(g). Intensities (I_{γ}^{2}) of the coincident γ rays from the fusion-evaporation experiment are summarized in the right-hand side of Tab. I. In accordance with the measured intensity relations from the ^{136}Xe + ^{208}Pb and ^{9}Be + ^{124}Sn experiments, the 749-keV transition has to be placed on top of the band-head at $69.5 + x$ keV, forming a new state at $818.3 + x$ keV. Figure 5(c) presents the γ-ray spectrum with a gate on the 749-keV transition. Coincidences are marked with labels. Peaks at 56, 135, 341, 397, 444, 509, 588, 692, 922, 971, and 1092 keV, observed in both AGATA experiments, are coincident to the 749-keV transition. The intensity of the 692-keV peak in the $\gamma\gamma$-coincidence spectrum exceeds those of the other lines, corroborating a new state at $1510.6 + x$ keV. The 341, 397, 444, and 749-keV transitions are also observed to be in coincidence with the 692-keV transition (c.f. Fig. 5(d)). The coincidence spectrum gated on the 397-keV transition is shown in Fig. 5(e). The spectrum exhibits anticipated coincidences at 444, 692, and 749 keV. The absence of the 341-keV transition in the spectrum requires the 397-keV transition to be placed parallel to this transition. Moreover, the 444-keV transition is in coincidence with both the 341-, and 397-keV transitions, requiring a new state at $1907 + x$ keV. The placement of the 341, 397, 444-keV transitions above the 692-keV transition is further supported by the presence of these transitions in the gated fission spectrum (cf. Fig. 2(f)) and in the spectrum gated on high TKEL values (cf. Fig. 2(j)). Moreover, all transitions, except of the 692-keV transition, are absent after gating on transfer-like events (cf. Fig. 2(e)) and low TKEL values (cf. Fig. 2(i)).

A gate on the 588-keV transition is shown in Fig. 5(f). Since the 334-, and 509-keV transitions are not mutually coincident, both transitions are arranged to feed the newly established state at $1406.1 + x$ keV. The spectrum gated on the 922-keV transition (cf. Fig. 5(g)) reveals clear coincidences with the 135-, 749-, and 971-keV transitions. The ordering of the 135- and 971-keV transitions is tentative since the intensities are equal within their uncertainties in both experiments (see Tab. I). However, a placement of the 135-keV transition at the head of this band is slightly favored. The ordering of the 922- and 971-keV transitions agrees with the intensity balance measured in the $\gamma\gamma$ projection gated on the 749-keV transition as well as with the AGATA measurement. In addition, the proposed 971-922-keV cascade is sup-

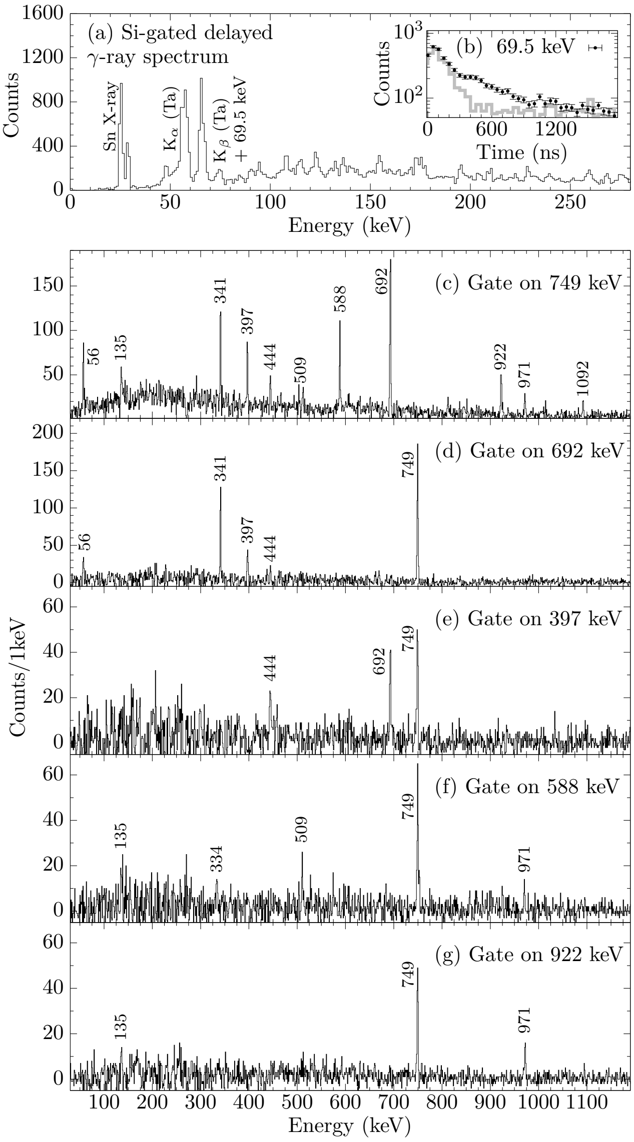

Figure 5. (a) Delayed γ-ray spectrum gated on prompt events in Si detector. (b) Time spectrum between events in the Si detector and the 69.5-keV γ-ray transition in the HPGe detectors. The grey step function shows a prompt time spectrum. Prompt ^{9}Be+^{124}Sn proton-gated $\gamma\gamma$-coincidence spectra with γ-ray gates on (c) 749, (d) 692, (e) 397, (f) 588, and (g) 922 keV. Coincidences are highlighted by energy labels.

ported by the absence of the 971-keV transition in the spectrum gated on low TKEL values (cf. Fig. 2(i)), while the 922-keV transition still remains in the spectrum. Moreover, the 922-keV γ-ray corresponds to the sum energy of the 334-588-keV cascade. Therefore, we assume that both decay pathways deexcite the new state at $1740.2 + x$ keV. The maximum excitation energy of $2846.7 + x$ keV in ^{130}I is consistent with the observed maximum excitation energy of 2.6 MeV in the ^{129}I channel, whose level scheme is well established from a study of the ^{7}Li + ^{124}Sn reaction [32]. The geometry of the HPGe array prohibits angular-distribution and angular-correlation measurements. Possible spin and parity assignments are discussed in Sec. III. A placement of unassigned γ-ray transitions observed in both AGATA experiments and listed in Tab. I within the level scheme is not feasible since these experiments did not yield reliable $\gamma\gamma$ coincidences.

III. DISCUSSION

A. Systematics along iodine isotopic chain

Negative-parity states based on the $J^\pi = 8^-$ isomer with a $\pi g_{7/2} \otimes \nu h_{11/2}$ 2-QP configuration were reported to be strongly populated in the doubly-odd $^{122-134}$I isotopes [1–4]. The configuration originates from the coupling of the $J^\pi = 11/2^-$ high-spin band-head of the odd-mass Xe isotopes with a $\nu h_{11/2}$ configuration and the $J^\pi = 7/2^+$ high-spin band-head of odd-mass iodine based on the $\pi g_{7/2}$ configuration [1]. Consequently, we propose that the $\pi g_{7/2} \otimes \nu h_{11/2}$ band is strongly populated via the ^{124}Sn(^{9}Be, $p2n$)^{130}I reaction. Figure 6(a) shows the evolution of negative-parity yrast-band states based on the $J^\pi = 8^-$ isomer along odd-odd $Z = 53$ isotopes. The level energies are normalized to the energy of the $J^\pi = 8^-$ isomer. A gradually increasing level spacing is observed towards the $N = 82$ shell closure. This trend was already interpreted as a decreasing collectivity from lighter to heavier iodine isotopes [3, 6]. The observation of many parallel decay branches feeding the state at $818 + x$ keV further emphasises the decreasing collectivity and the gradual change to a vibration-like structure of this band towards the $N = 82$ shell closure. The newly established state at $818+x$ keV in ^{130}I reasonably matches the evolution of excitation energies of the $J^\pi = 10^-$ states. A $J^\pi = 9^-$ assignment would disrupt the smooth evolution of $J^\pi = 9^-$ states since the energy gap between $J^\pi = 8^-$ and 9^- states in ^{128}I is only 411 keV. The unobserved yrast $J^\pi = 9^-$ state is most probably fed by the $J^\pi = 10^-$ state, however, according to the analysis of the ^{9}Be + ^{124}Sn experiment (Sec. II C), the branching can be estimated to be less than 8 % relative to the $10^- \rightarrow 8^-$ transition. This value is supported by a similar estimation in ^{134}I, whereby a value of 3.3 % was found for the same branching [2]. Moreover, $J^\pi = 11^-$, 12^-, and 13^- assignments for the $1511 + x$,

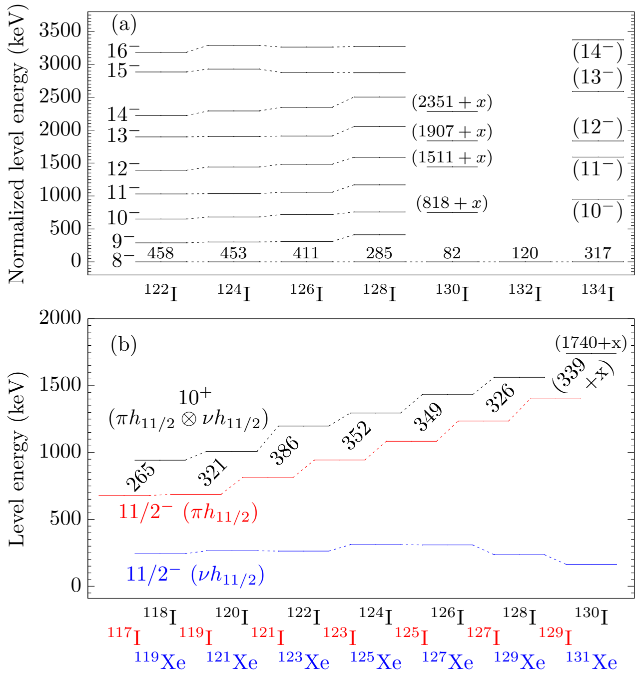

Figure 6. (a) Systematics of excited states in the $\pi g_{7/2} \otimes \nu h_{11/2}$ bands in even-mass $^{122-134}$I, normalized to the energy of the $J^\pi = 8^-$ state. The energy of the $J^\pi = 8^-$ state is given by text labels. (b) Systematics of $J^\pi = 10^+$ states with $\pi h_{11/2} \otimes \nu h_{11/2}$ configuration in even-mass $^{118-130}$I and $J^\pi = 11/2^-$ states with $\pi h_{11/2}$ and $\nu h_{11/2}$ configuration in odd-mass $^{117-129}$I and $^{119-131}$Xe, respectively. The energy difference between $J^\pi = 11/2^-$ and $J^\pi = 10^+$ states is highlighted with text labels. Data taken from Refs. [1–4, 32, 35, 36].

$1907 + x$, and $2351 + x$ states fit into the systematics of increasing excitation energies towards ^{134}I.

Similar to the $\pi g_{7/2} \otimes \nu h_{11/2}$ 2-QP bands, $\pi h_{11/2} \otimes \nu h_{11/2}$ 2-QP bands based on $J^\pi = 10^+$ states were coherently reported along the doubly-odd I chain [1–4, 37]. These bands are interpreted as couplings between $J^\pi = 11/2^-$ states with proton and neutron $h_{11/2}$ configurations in neighboring odd-mass I and Xe isotopes, respectively. Such a band was first identified in ^{116}I by Paul *et al.* [5]. In contrast to such lighter iodine systems in which a rotational-like structure is built on the $J^\pi = 10^+$ states, a vibrational-like structure dominates for ^{128}I [2, 3, 37]. Figure 6(b) shows the systematics of excitation energies for the $J^\pi = 10^+$ states with $\pi h_{11/2} \otimes \nu h_{11/2}$ configuration from ^{118}I to ^{130}I. Moreover, similar data on $J^\pi = 11/2^-$ states in neighbouring odd-A I and Xe isotopes are displayed. Obviously, the increasing trend of the $J^\pi = 10^+$ states can be traced back to the increasing energy of the $J^\pi = 11/2^-$ states in neighboring iodine isotopes, while the excitation energy of the $J^\pi = 11/2^-$ states in Xe isotopes remains nearly constant. As depicted in Fig. 6(b), the energy gap between the $J^\pi = 10^+$ and $11/2^-$ states varies only slightly within 121 keV from ^{118}I to ^{128}I. It is reasonable to assume that this energy gap remains constant in ^{130}I. The corresponding $J^\pi = 11/2^-$ state in ^{129}I is located at 1402 keV. Consequently, a $J^\pi = 10^+$ assignment for the $1740 + x$-keV state in ^{130}I is most appropriate, since the corresponding energy gap of $339+x$ keV matches the continuing systematics best.

B. Shell-model calculations

The extended high-spin level scheme of ^{130}I is compared to four shell-model calculations carried out in an untruncated $50 \leq Z, N \leq 82$ *gdsh* valence space. The single-particle space is generated by the valence nucleons occupying the $0g_{7/2}$, $1d_{5/2}$, $1d_{3/2}$, $2s_{1/2}$, and $0h_{11/2}$ orbitals, outside doubly-magic ^{100}Sn. The calculations were carried out employing the shell-model code NuShellX@Msu [38] and the massive-parallelization code KSHELL [39].

The first calculation is conducted with the effective interaction GCN50:82 [40, 41]. The interaction is derived from a realistic G matrix based on the CD-Bonn potential [42]. Empirical monopole corrections to the original G matrix were introduced by fitting different combinations of two-body matrix elements to sets of experimental excitation energies from even-even and even-odd semi-magic nuclei.

The second calculation is carried out with the jj55pn Hamiltonian (referred to as the SN100PN interaction) [43]. The Hamiltonian consists of four terms describing the neutron-neutron, neutron-proton, proton-proton, and Coulomb repulsion between the protons individually. A renormalized G matrix derived from the CD-Bonn interaction [42] was employed to construct the realistic two-body residual interaction. The proton and neutron single-particle energies are based on the energy levels in ^{133}Sb and ^{131}Sn.

Another calculation is performed in the framework of the realistic shell model [44, 45], denoted as Realistic SM. Single-particle energies and a two-body effective interaction are determined from the established CD-Bonn free nucleon-nucleon potential [42] using the $V_{\text{low-}k}$ approach with a cutoff momentum of $\Lambda = 2.6$ fm^{-1}, plus the Coulomb force for protons. The effective shell-model Hamiltonian is derived iteratively by means of the many-body perturbation theory in the $\hat{Q}$-box folded diagram expansion, including all diagrams up to third order in the interaction. More details can be found in Ref. [46].

The last calculation is conducted in the framework of the extended pairing plus quadrupole-quadrupole force model with monopole corrections (EPQQM) [47–50]. Single-particle energies (SPEs) were adopted from the experimental excited states of ^{133}Sb (proton SPEs) and ^{131}Sn (neutron SPEs).

Figure 7 compares the experimentally determined energies of levels in ^{130}I (Fig. 7(a) and (d)) with the results of the (b) GCN50:82, (c) SN100PN, (e) Realistic SM, and (f) EPQQM interactions. The angular momentum of the $J^\pi = 5^+$ ground state is not reproduced by any interaction. Instead, the first $J^\pi = 8^-$ state with a $\pi g_{7/2} \otimes \nu h_{11/2}$ configuration [10] is predicted as the ground state by the SN100PN, Realistic SM, and EPQQM interactions, while the GCN50:82 interaction computes the excitation energy of this state to 93 keV, which is in good agreement with the experimentally determined value of 82 keV. The excitation energies of the hitherto known first and second excited low-lying $J^\pi = 6^-$ states are fairly reproduced by all four calculations. As pointed out in Sec. III A, a $J^\pi = 10^-$ assignment for the state at $818 + x$ keV is preferred rather than a $J^\pi = 9^-$ assignment according to systematics. In the calculations, $J^\pi = 10^-$ states are coherently predicted at significantly higher energies than the $J^\pi = 9^-$ states. The different shell-model calculations locate the $J^\pi = 10^-$ state at energies of 930 (GCN50:82), 737 (SN100PN), 861 (Realistic SM), and 642 keV (EPQQM). Accordingly, a $J^\pi = 10^-$ assignment for this state is proposed, based on these theoretical findings. Assuming a proceeding negative-parity character of the 692-397-444-keV cascade, the states at $1511 + x$, $1907 + x$, and $2351 + x$ keV can be interpreted as $J^\pi = 11^-, 12^-$, and 13^- states, respectively. In the calculations, this sequence of γ-ray transitions is predicted as 589-267-558 (GCN50:82), 440-449-330 (SN100PN), 483-419-348 (Realistic SM), and 210-556-159 (EPQQM), where only the GCN50:82 interaction reaches a reasonable agreement. A positive-parity $J^\pi = 10^+$ assignment can most likely be attributed to the state at $1740 + x$ keV, which is in line with systematics (see Sec. III A). The calculations are in good accordance with predicted energies of 1844 (GCN50:82), 1530 (SN100PN), 1731 (Realistic SM), and 1769 keV (EPQQM), which further enforces this assignment.

Table II. The strongest components (≥ 5 %) of the wave function of yrast states in ^{130}I. Calculations were performed with the GCN50:82 interaction.

J^π	Configuration	Probability
8^-_1	$\pi g^3_{7/2} \otimes \nu h^{-1}_{11/2}$	14 %
	$\pi(g^1_{7/2} d^2_{5/2}) \otimes \nu h^{-1}_{11/2}$	6 %
10^-_1	$\pi g^3_{7/2} \otimes \nu(h^{-1}_{11/2} s^{-1}_{1/2} d^{-1}_{3/2})$	5 %
	$\pi g^3_{7/2} \otimes \nu h^{-1}_{11/2}$	14 %
11^-_1	$\pi(g^2_{7/2} d^1_{5/2}) \otimes \nu h^{-1}_{11/2}$	17 %
12^-_1	$\pi(g^2_{7/2} d^1_{5/2}) \otimes \nu h^{-1}_{11/2}$	39 %
13^-_1	$\pi(g^2_{7/2} d^1_{5/2}) \otimes \nu h^{-1}_{11/2}$	35 %
10^+_1	$\pi h^1_{11/2} g^2_{7/2} \otimes \nu h^{-1}_{11/2}$	27 %

The shell-model results provide a more detailed insight into the structure of states above the $J^\pi = 8^-$ isomer. Prior to this work, Coraggio *et al.* reported on a shell-model study of the doubly-odd ^{134}I isotope [7]. To our knowledge, these are the only realistic shell-model

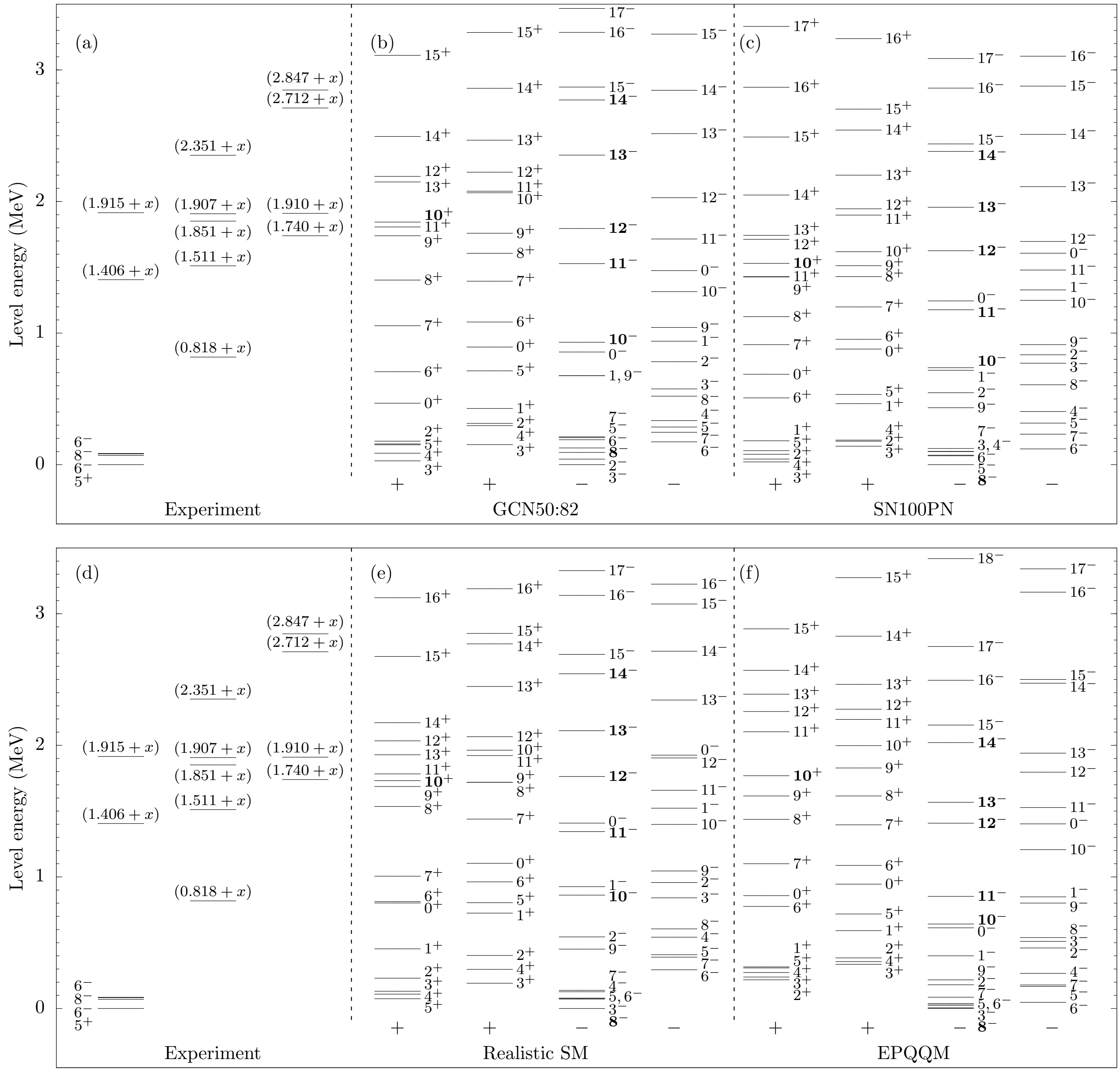

Figure 7. Comparison of experimental energy spectra of ^{130}I with the results of four shell-model calculations. (a) and (d) Experimental energy spectra are shown in the left panels. The results obtained with the different interactions are separated in different panels: (b) GCN50:82, (c) SN100PN, (e) Realistic SM, and (f) EPQQM. For clarity, the states are separated into columns for yrast and yrare states with negative and positive parity. Theoretical candidates for spin and parity assignments are highlighted with bold font.

calculations for iodine nuclei ($A < 135$) to date. The group used a realistic shell-model calculation to assign spins and parities and to interpret high-spin states of ^{134}I [2, 7]. The $J^\pi = 10^-$, 11^-, 12^-, and 14^- states in ^{134}I yield predominantly single-particle configurations with a neutron-hole $\nu h_{11/2}^{-1}$ configuration coupled to the three protons in $(g_{7/2})^3$ or $(g_{7/2})^2 d_{5/2}$ configurations.

A detailed decomposition of the $J^\pi = 10^+$, 8^-, 9^-, 10^-, 11^-, 12^- and 13^- states in ^{130}I into their proton and neutron configurations computed by the GCN50:82 interaction is presented in Tab. II. Obviously, the negative-parity states are build on the neutron-hole $\nu h_{11/2}^{-1}$ configuration coupled to the three protons distributed over the $g_{7/2}$ and $d_{5/2}$ orbitals. While the three protons are arranged in the $\pi g_{7/2}^3$ configuration for the $J^\pi = 8^-$ and 10^- states, the $\pi g_{7/2}^2 d_{5/2}^1$ configuration is pivotal for

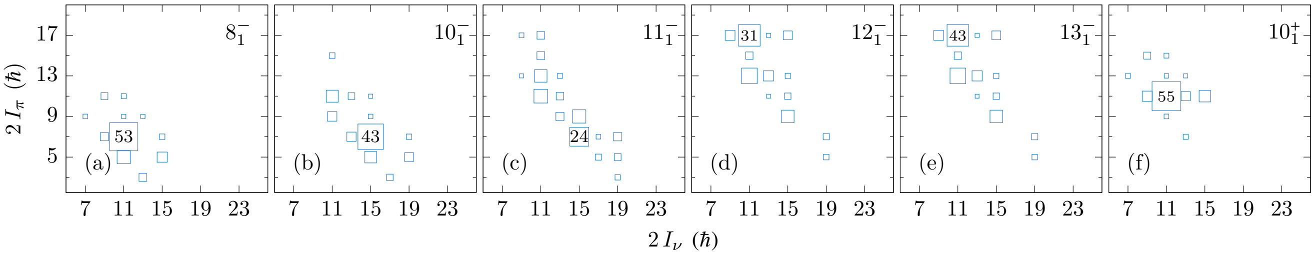

Figure 8. Decomposition of the total angular momentum $I = I_\pi \otimes I_\nu$ into its proton and neutron components for the (a) $J^\pi = 8_1^-$, (b) 10_1^-, (c) 11_1^-, (d) 12_2^-, (e) 13_1^-, and (f) 10_1^+ states in ^{130}I. Calculations were performed with the GCN50:82 interaction. The size of the boxes is proportional to the percentage of the particular configuration. Percentages above 1% are shown and strongest components are highlighted with corresponding percentages.

higher-lying states. Although more fragmented in ^{130}I, the leading configurations of the negative-parity states mirror those calculated for ^{134}I [7]. For the positive-parity $J^\pi = 10^+$ state in ^{130}I, one proton is predominantly occupying the $\pi h^1_{11/2}$ configuration, whereby the neutron hole is in the $\nu h^{-1}_{11/2}$ configuration.

The structure of the states is also scrutinized via a detailed decomposition of the total angular momentum $I = I_\pi \otimes I_\nu$ into its proton and neutron components visualized in Figs. 8(a)-(f), computed by the GCN50:82 interaction. The interaction predicts the $J^\pi = 8^-$ state to predominantly have $\pi\ 7/2^+ \otimes \nu\ 11/2^-$ spin configuration, whereby a proton pair in the $\pi g^3_{7/2}$ and $\pi(g^1_{7/2} d^2_{5/2})$ configurations is coupled to $I = 0$. A rearrangement of the neutron-spin configuration is observed for the $J^\pi = 10^-$ and 11^- states, where a proton spin of $\pi\ 7/2^+$ is mainly coupled to a neutron spin of $\nu\ 15/2^-$, originating from a fully-stretched $\nu(h^{-1}_{11/2} s^{-1}_{1/2} d^{-1}_{3/2})$ neutron configuration. Going to the $J^\pi = 12^-$ and 13^- states, the fully aligned $\pi\ 17/2^-$ spin of the proton $\pi(g^2_{7/2} d^1_{5/2})$ configuration is mainly coupled to $\nu\ 11/2^-$ neutron spin components. Finally, in the $J^\pi = 10^+$ state with the predominant $\pi(h^1_{11/2} g^2_{7/2}) \otimes \nu h^{-1}_{11/2}$ configuration, both protons in the $g_{7/2}$ orbital are mainly paired to spin zero.

IV. SUMMARY AND OUTLOOK

In summary, as a result of the combined analysis of three independent spectroscopic measurements, high-spin states in ^{130}I were established up to an excitation energy of $2847 + x$ keV, incorporating twelve new states. Prior to this work, only single-particle and low-spin states up to 1 MeV and spin $I \leq 8\hbar$ were reported for ^{130}I. For the new states, tentative spin-parity assignment were discussed which are backed by systematics along the $Z = 53$ chain. Most likely, the new high-spin structure is built on the $J^\pi = 8^-$ isomer with a $\pi g^3_{7/2} \otimes \nu h^{-1}_{11/2}$ configuration at 82.4 keV excitation energy. The new states close the gap along the doubly-odd I chain towards the recently investigated ^{134}I. The level structure above the $J^\pi = (10^-)$ state at $818 + x$ keV strongly mirrors the excitation pattern observed in ^{134}I which is dominated by strong single-particle excitations, emphasizing the transitional character of ^{130}I. Shell-model calculations with four interactions are in general in line with the experimental findings and affirm most of the assignments. A detailed inspection of the evolution of proton-, and neutron-spin and configuration decompositions of the new states corroborate that the negative-parity states are members of the $\pi g_{7/2}/d_{5/2} \otimes \nu h_{11/2}$ configuration.

Despite the new results on ^{130}I from this article, the high-spin structure along doubly-odd I isotopes towards ^{134}I is still pending information on ^{132}I (see Fig. 1). To date, information on excited states is limited to β-decay spectroscopy. Several up to now unknown lines appear in the gated γ-ray spectra of ^{132}I from our MNT experiments, presented in Secs. II A and II B. In future, dedicated MNT or fission reactions will allow for a more detailed analysis of ^{132}I.

ACKNOWLEDGMENTS

We thank the IKP FN Tandem accelerator team for the support during the experiment. The research leading to these results has received funding from the German BMBF under contract No. 05P15PKFN9 TP1 and 05P18PKFN9 TP1, from the European Union Seventh Framework Programme FP7/2007-2013 under Grant Agreement No. 262010 - ENSAR, from the Spanish Ministerio de Ciencia e Innovación under contract FPA2011-29854-C04, from the Spanish Ministerio de Economía y Competitividad under contract FPA2014-57196-C5, and from the U.K. Science and Technology Facilities Council (STFC). One of the authors (A. Gadea) has been supported by the Generalitat Valenciana, Spain, under the grant PROMETEOII/2014/019 and EU under the FEDER program.

[1] "Evaluated Nuclear Structure Data File (ENSDF) and XUNDL, (August 2019 Version) continuously updated data files (NNDC, Brookhaven NY)," http://www.nndc.bnl.gov/ensdf/.

[2] S. H. Liu, J. H. Hamilton, A. V. Ramayya, J. K. Hwang, A. V. Daniel, G. M. Ter-Akopian, Y. X. Luo, J. O. Rasmussen, S. J. Zhu, and W. C. Ma, "Identification of high spin states in ^{134}I from ^{252}Cf fission," Phys. Rev. C **79**, 067303 (2009).

[3] B. Ding, H. X. Wang, H. Jiang, Y. H. Zhang, X. H. Zhou, Y. M. Zhao, S. T. Wang, M. L. Liu, G. S. Li, Y. Zheng, N. T. Zhang, H. B. Zhou, Y. J. Ma, Y. Sasakiz, K. Yamada, H. Ohshima, S. Yokose, M. Ishizuka, T. Komatsubara, and K. Furuno, "High-spin level scheme of doubly odd ^{128}I," Phys. Rev. C **86**, 034302 (2012).

[4] Y. Zheng, L. H. Zhu, X. G. Wu, Z. C. Gao, C. Y. He, G. S. Li, L. L. Wang, Y. S. Chen, Y. Sun, X. Hao, Y. Liu, X. Q. Li, B. Pan, Y. J. Ma, Z. Y. Li, and H. B. Ding, "Abnormal signature inversion and multiple alignments in doubly odd ^{126}I," Phys. Rev. C **86**, 014320 (2012).

[5] E. S. Paul, D. B. Fossan, K. Hauschild, I. M. Hibbert, H. Schnare, J. M. Sears, I. Thorslund, R. Wadsworth, A. N. Wilson, and J. N. Wilson, "Evidence for the $\pi h_{11/2} \otimes \nu h_{11/2}$ configuration in doubly odd ^{116}I," J. Phys. G **21**, 995–999 (1995).

[6] E. S. Paul, H. R. Andrews, T. E. Drake, J. DeGraaf, V. P. Janzen, S. Pilotte, D. C. Radford, and D. Ward, "High-spin states in doubly odd ^{114}I," Phys. Rev. C **52**, 1691–1693 (1995).

[7] L. Coraggio, A. Covello, A. Gargano, and N. Itaco, "Shell-model interpretation of high-spin states in ^{134}I," Phys. Rev. C **80**, 061303 (2009).

[8] H. L. Garvin, T. M. Green, and E. Lipworth, "Nuclear spin of 12.6-hour iodine-130," Phys. Rev. Lett. **1**, 292–293 (1958).

[9] D. Bloch, *G-Factor-Messungen an Isomeren Zuständen in ^{126}I und ^{130}I, sowie Vorschläge für Niveauschemas dieser Kerne im Niederenergiebereich*, Ph.D. thesis, Fredrich-Alexander Univ., Erlangen-Nurnberg (1975).

[10] S. L. Sakharov, I. A. Kondurov, Yu. E. Loginov, V. V. Martynov, A. A. Rodionov, P. A. Sushkov, Yu. L. Khazov, A. I. Egorov, V. K. Isupov, H. G. Börner, F. Hoyler, S. Kerr, K. Schreckenbach, G. Hlawatsch, T. Von Egidy, and H. Lindner, "Low-lying ^{130}I excited states from the (n,γ) reaction," Nucl. Phys. A **494**, 36 – 74 (1989).

[11] E. G. Kessler, M. S. Dewey, R. D. Deslattes, A. Henins, H. G. Börner, M. Jentschel, and H. Lehmann, "The GAMS4 flat crystal facility," Nucl. Instrum. Meth. Phys. Res. A **457**, 187 – 202 (2001).

[12] W. Mampe, K. Schreckenbach, P. Jeuch, B. P. K. Maier, F. Braumandl, J. Larysz, and T. von Egidy, "The double focusing iron-core electron-spectrometer BILL for high resolution (n,e^-) measurements at the high flux reactor in grenoble," Nucl. Instrum. Meth. **154**, 127 – 149 (1978).

[13] K. S. Akhnazarov, B. A. Emelianov, D. M. Kaminker, Yu. L. Khazov, and S. L. Sakharov, "Supressing background and increasing luminosity of a β-spectrometer of internal target type for an investigation of the (n,e) reaction," Nucl. Instrum. Meth. **138**, 299 – 305 (1976).

[14] M. Löffler, H. J. Scheerer, and H. Vonach, "The ion optical properties of the munich Q3D-spectrograph investigated by means of a special experimental ray tracing method," Nucl. Instrum. Meth. **111**, 1 – 12 (1973).

[15] S. Akkoyun *et al.*, "AGATA – Advanced GAmma Tracking Array," Nucl. Instrum. Meth. Phys. Res. A **668**, 26 (2012).

[16] A. M. Stefanini, L. Corradi, G. Maron, A. Pisent, M. Trotta, A. M. Vinodkumar, S. Beghini, G. Montagnoli, F. Scarlassara, G. F. Segato, A. De Rosa, G. Inglima, D. Pierroutsakou, M. Romoli, M. Sandoli, G. Pollarolo, and A. Latina, "The heavy-ion magnetic spectrometer PRISMA," Nucl. Phys. A **701**, 217 – 221 (2002).

[17] S. Szilner, C. A. Ur, L. Corradi, N. Marginean, G. Pollarolo, A. M. Stefanini, S. Beghini, B. R. Behera, E. Fioretto, A. Gadea, B. Guiot, A. Latina, P. Mason, G. Montagnoli, F. Scarlassara, M. Trotta, G. de Angelis, F. Della Vedova, E. Farnea, F. Haas, S. Lenzi, S. Lunardi, R. Marginean, R. Menegazzo, D. R. Napoli, M. Nespolo, I. V. Pokrovsky, F. Recchia, M. Romoli, M.-D. Salsac, N. Soić, and J. J. Valiente-Dobón, "Multinucleon transfer reactions in closed-shell nuclei," Phys. Rev. C **76**, 024604 (2007).

[18] L. Corradi, S. Szilner, G. Pollarolo, D. Montanari, E. Fioretto, A.M. Stefanini, J. J. Valiente-Dobón, E. Farnea, C. Michelagnoli, G. Montagnoli, F. Scarlassara, C.A. Ur, T. Mijatović, D. J. Malenica, N. Soić, and F. Haas, "Multinucleon transfer reactions: Present status and perspectives," Nucl. Instrum. Meth. Phys. Res. B **317, Part B**, 743 – 751 (2013).

[19] A. Vogt, B. Birkenbach, P. Reiter, L. Corradi, T. Mijatović, D. Montanari, S. Szilner, D. Bazzacco, M. Bowry, A. Bracco, B. Bruyneel, F. C. L. Crespi, G. de Angelis, P. Désesquelles, J. Eberth, E. Farnea, E. Fioretto, A. Gadea, K. Geibel, A. Gengelbach, A. Giaz, A. Görgen, A. Gottardo, J. Grebosz, H. Hess, P. R. John, J. Jolie, D. S. Judson, A. Jungclaus, W. Korten, S. Leoni, S. Lunardi, R. Menegazzo, D. Mengoni, C. Michelagnoli, G. Montagnoli, D. Napoli, L. Pellegri, G. Pollarolo, A. Pullia, B. Quintana, F. Radeck, F. Recchia, D. Rosso, E. Şahin, M. D. Salsac, F. Scarlassara, P.-A. Söderström, A. M. Stefanini, T. Steinbach, O. Stezowski, B. Szpak, Ch. Theisen, C. Ur, J. J. Valiente-Dobón, V. Vandone, and A. Wiens, "Light and heavy transfer products in ^{136}Xe+^{238}U multinucleon transfer reactions," Phys. Rev. C **92**, 024619 (2015).

[20] B. Bruyneel, B. Birkenbach, and P. Reiter, "Pulse shape analysis and position determination in segmented HPGe detectors: The AGATA detector library," Eur. Phys. J. A **52**, 70 (2016).

[21] A. Lopez-Martens, K. Hauschild, A. Korichi, J. Roccaz, and J-P. Thibaud, "γ-ray tracking algorithms: a comparison," Nucl. Instrum. Meth. Phys. Res. A **533**, 454 – 466 (2004).

[22] A. Gadea, E. Farnea, J. J. Valiente-Dobón, B. Million, D. Mengoni, D. Bazzacco, F. Recchia, A. Dewald, Th. Pissulla, W. Rother, G. de Angelis, *et al.*, "Conceptual design and infrastructure for the installation of the first AGATA sub-array at LNL," Nucl. Instrum. Meth. Phys. Res. A **654**, 88 – 96 (2011).

[23] A. Vogt, B. Birkenbach, P. Reiter, A. Blazhev, M. Siciliano, J. J. Valiente-Dobón, C. Wheldon, D. Bazzacco, M. Bowry, A. Bracco, B. Bruyneel, R. S. Chakrawarthy,

R. Chapman, D. Cline, L. Corradi, F. C. L. Crespi, M. Cromaz, G. de Angelis, J. Eberth, P. Fallon, E. Farnea, E. Fioretto, S. J. Freeman, A. Gadea, K. Geibel, W. Gelletly, A. Gengelbach, A. Giaz, A. Görgen, A. Gottardo, A. B. Hayes, H. Hess, H. Hua, P. R. John, J. Jolie, A. Jungclaus, W. Korten, I. Y. Lee, S. Leoni, X. Liang, S. Lunardi, A. O. Macchiavelli, R. Menegazzo, D. Mengoni, C. Michelagnoli, T. Mijatović, G. Montagnoli, D. Montanari, D. Napoli, C. J. Pearson, L. Pellegri, Zs. Podolyák, G. Pollarolo, A. Pullia, F. Radeck, F. Recchia, P. H. Regan, E. Şahin, F. Scarlassara, G. Sletten, J. F. Smith, P.-A. Söderström, A. M. Stefanini, T. Steinbach, O. Stezowski, S. Szilner, B. Szpak, R. Teng, C. Ur, V. Vandone, D. Ward, D. D. Warner, A. Wiens, and C. Y. Wu, "High-spin structure of ^{134}Xe," Phys. Rev. C **93**, 054325 (2016).

[24] A. B. Brown, C. W. Snyder, W. A. Fowler, and C. C. Lauritsen, "Excited states of the mirror nuclei, ^{7}Li and ^{7}Be," Phys. Rev. **82**, 159–181 (1951).

[25] A. Wiens, H. Hess, B. Birkenbach, B. Bruyneel, J. Eberth, D. Lersch, G. Pascovici, P. Reiter, and H.-G. Thomas, "The AGATA triple cluster detector," Nucl. Instrum. Meth. Phys. Res. A **618**, 223 – 233 (2010).

[26] R. S. Kempley *et al.*, "Cross Coincidences in the ^{136}Xe + ^{208}Pb deep-inelastic reaction," Acta. Phys. Pol. B **42**, 717–720 (2011).

[27] M. Siciliano *et al.*, "Neutron-rich nuclei in the vicinity of ^{208}Pb," LNL Annual Report 2014 **241**, 63–64 (2015).

[28] A. Dewald, O. Möller, and P. Petkov, "Developing the recoil distance doppler-shift technique towards a versatile tool for lifetime measurements of excited nuclear states," Prog. Part. and Nucl. Phys. **67**, 786 – 839 (2012).

[29] N. Saed-Samii, *Lifetime measurements using the FATIMA array in combination with EXOGAM@ILL*, Diploma thesis, Universität zu Köln (2013), unpublished.

[30] J. Theuerkauf, Ph.D. thesis, Universität zu Köln (1994).

[31] G. S. Li, Y. D. Fang, A. Diaz-Torres, M. L. Liu, N. T. Zhang, X. H. Zhou, Y. H. Zhang, J. G. Wang, B. S. Gao, Y. H. Qiang, S. Guo, S. C. Wang, Z. Y. Zhang, J. F. Huang, K. L. Wang, Y. Zheng, and S. Mukherjee, "Isomer yield ratios in ^{184}Re from the ^{9}Be +^{181} Ta reaction," Phys. Rev. C **99**, 054617 (2019).

[32] D. Deleanu, D. L. Balabanski, Ts. Venkova, D. Bucurescu, N. Mărginean, E. Ganioğlu, Gh. C ăta Danil, L. Atanasova, I. C ăta Danil, P. Detistov, D. Filipescu, D. Ghiţă, T. Glodariu, M. Ivaşcu, R. Mărginean, C. Mihai, A. Negret, S. Pascu, T. Sava, L. Stroe, G. Suliman, and N. V. Zamfir, "Excited states in ^{129}I," Phys. Rev. C **87**, 014329 (2013).

[33] James H. Scofield, "Exchange corrections of K x-ray emission rates," Phys. Rev. A **9**, 1041–1049 (1974).

[34] M. Dewald, *γ-Spektroskopie und Lebensdaueranalyse isomerer Zustände in ^{100}Rh am Kölner Tandembeschleuniger*, Master thesis, Universität zu Köln (2014), unpublished.

[35] B. Ding, Y. H. Zhang, X. H. Zhou, G. X. Dong, F. R. Xu, M. L. Liu, G. S. Li, N. T. Zhang, H. X. Wang, H. B. Zhou, Y. J. Ma, Y. Sasakiz, K. Yamada, H. Ohshima, S. Yokose, M. Ishizuka, T. Komatsubara, and K. Furuno, "High-spin states in ^{127}I," Phys. Rev. C **85**, 044306 (2012).

[36] P. Singh, S. Nag, A. K. Singh, I. Ragnarsson, H. Hübel, A. Al-Khatib, P. Bringel, C. Engelhardt, A. Neußer-Neffgen, G. B. Hagemann, C. R. Hansen, B. Herskind, G. Sletten, A. Bracco, G. Benzoni, F. Camera, P. Fallon, R. M. Clark, M. P. Carpenter, R. V. F. Janssens, T. L. Khoo, T. Lauritsen, P. Chowdhury, and H. Amro, "Highly deformed high-spin band in ^{125}I," Phys. Rev. C **84**, 024316 (2011).

[37] C.-B. Moon, "Systematic features of the $\pi h_{11/2}\nu h_{11/2}$ bands in doubly-odd I," J. Korean Phys. Soc. **44**, 244–249 (2004).

[38] B. A. Brown and W. D. M. Rae, "The Shell-Model Code NuShellX@MSU," Nucl. Data Sheets **120**, 115 – 118 (2014).

[39] N. Shimizu, "Nuclear shell-model code for massive parallel computation, "KSHELL"," (2013), arXiv:1310.5431 [nucl-ph].

[40] E. Caurier, F. Nowacki, A. Poves, and K. Sieja, "Collectivity in the light xenon isotopes: A shell model study," Phys. Rev. C **82**, 064304 (2010).

[41] E. Caurier, F. Nowacki, and A. Poves, "Shell model description of the $\beta\beta$ decay of ^{136}Xe," Phys. Lett. B **711**, 62 – 64 (2012).

[42] R. Machleidt, F. Sammarruca, and Y. Song, "Nonlocal nature of the nuclear force and its impact on nuclear structure," Phys. Rev. C **53**, R1483–R1487 (1996).

[43] B. A. Brown, N. J. Stone, J. R. Stone, I. S. Towner, and M. Hjorth-Jensen, "Magnetic moments of the 2_1^+ states around ^{132}Sn," Phys. Rev. C **71**, 044317 (2005).

[44] L. Coraggio, A. Covello, A. Gargano, N. Itaco, and T. T. S. Kuo, "Effective shell-model hamiltonians from realistic nucleon-nucleon potentials within a perturbative approach," Annals of Physics **327**, 2125 – 2151 (2012).

[45] L. Coraggio, A. Covello, A. Gargano, N. Itaco, and T. T. S. Kuo, "Shell-model study of the $N = 82$ isotonic chain with a realistic effective Hamiltonian," Phys. Rev. C **80**, 044320 (2009).

[46] L. Coraggio, L. De Angelis, T. Fukui, A. Gargano, and N. Itaco, "Calculation of gamow-teller and two-neutrino double-β decay properties for ^{130}Te and ^{136}Xe with a realistic nucleon-nucleon potential," Phys. Rev. C **95**, 064324 (2017).

[47] M. Hasegawa, K. Kaneko, and S. Tazaki, "Improvement of the extended p+qq interaction by modifying the monopole field," Nucl. Phys. A **688**, 765 – 788 (2001).

[48] K. Kaneko, M. Hasegawa, and T. Mizusaki, "Quadrupole and octupole softness in the $N = Z$ nucleus ^{64}Ge," Phys. Rev. C **66**, 051306 (2002).

[49] K. Kaneko, Y. Sun, M. Hasegawa, and T. Mizusaki, "Shell model study of single-particle and collective structure in neutron-rich Cr isotopes," Phys. Rev. C **78**, 064312 (2008).

[50] K. Kaneko, Y. Sun, T. Mizusaki, and M. Hasegawa, "Shell-model study for neutron-rich sd-shell nuclei," Phys. Rev. C **83**, 014320 (2011).

Summary

High-spin structure in the transitional nucleus ^{131}Xe: Competitive neutron and proton alignment in the vicinity of the $N = 82$ shell closure

The nucleus ^{131}Xe lies in a transitional region between spherical Sn and well-deformed Ce nuclei. Moreover, the Xe chain shows rotational character in the lighter ($A \leq 130$) and shell-model character in the heavier ($A \geq 132$) isotopes. A new upbend along the ($\alpha = -1/2$) negative-parity yrast band at the position of the $J^{\pi} = 27/2^{-}$ state was observed very recently in ^{129}Xe [53]. The first publication "*High-spin structure in the transitional nucleus ^{131}Xe: Competitive neutron and proton alignment in the vicinity of the $N = 82$ shell closure*" presents results on alignment properties in ^{131}Xe obtained from the combined analysis of the AGATA ^{136}Xe+^{238}U, ^{136}Xe+^{208}Pb MNT experiments, and the HORUS ^{11}B+^{124}Sn fusion-evaporation experiment. The construction of the new level scheme is based on the identification of the new transitions in the AGATA+PRISMA experiments and a complementary analysis of the fusion-evaporation experiment at the HORUS γ-ray array. The new HORUS+DSSSD setup enables precise gates on the elusive ^{131}Xe channel [70]. As a main result of the three measurements, the level scheme of ^{131}Xe was extended up to an excitation energy of 5 MeV. A pronounced backbending along the negative-parity band on top of the one-quasiparticle $\nu h_{11/2}(\alpha = -1/2)$ band around $\hbar\omega = 0.4$ MeV was identified. Angular-correlation measurements were performed to determine the multipole character of the γ-ray transitions.

In past decades, the theoretical investigations of alignment properties were performed by means of collective approaches like interacting boson model [50, 106, 107], mean-field methods [49, 108], or the cranked-shell-model [53, 109]. In the present publication, the new experimental findings were faced with results of modern large-scale shell-model calculations considering the PQM130, SN100PN, GCN50:82, Realistic SM, and SN100-KTH interactions. It was demonstrated that the new experimental findings, including the pronounced alignments in ^{129,131}Xe, are well reproduced by the different shell-model interactions. Moreover, truncated calculations in $^{129-132}$Xe, prohibiting more than one proton in the $\pi h_{11/2}$ orbital, were compared with each other. The comparison between the different calculations revealed that the alignments in ^{129,131}Xe can be microscopically traced back to a pair of $h_{11/2}$ protons, closing a gap in the alignment systematics along the Xe chain. Particularly, calculated $B(E2)$ transition strengths in the negative-parity band are reduced for transitions between states were the alignment sets in. The outcomes of the work indicate that only interactions with improved and corrected monopole parts, i.e. GCN50:82, can describe the experiment findings like alignment and crossing frequency to its full extent.

Millisecond $23/2^+$ isomers in the $N = 79$ isotones ^{133}Xe and ^{135}Ba

The publication "*Millisecond* $23/2^+$ *isomers in the* $N = 79$ *isotones* ^{133}*Xe and* ^{135}*Ba*" contributes to the systematic investigation of $J^\pi = 23/2^+$ isomers along the $N = 79$ isotones [27, 30, 152]. In this work, the AGATA ^{136}Xe+^{208}Pb MNT experiment was combined with a pulsed-beam experiment utilizing a ^{9}Be+^{130}Te fusion-evaporation reaction at the HORUS spectrometer. Very recently, the 2107-keV state in ^{133}Xe was identified as a promising candidate for the $J^\pi = 23/2^+$ isomer [27]. Moreover, the analysis of the AGATA ^{136}Xe+^{208}Pb MNT experiment indicates an isomeric $J^\pi = 23/2^+$ counterpart at 2388-keV excitation energy in ^{135}Ba . Prior to this work, only the β-slider technique [153] allowed to investigate long-lived isomeric states in off-beam measurements at the FN tandem accelerator of the University of Cologne. The commissioning of the pulsing system, which was placed at the injection line of the FN tandem accelerator, was part of the preparation of the ^{9}Be+^{130}Te experiment. Exploiting γ-time correlations with respect to the beam pulse, half-lives of 8.64(13) ms in ^{133}Xe and 1.06(4) ms in ^{135}Ba were identified. The combined results of off-beam angular-correlation and internal-conversion coefficient measurements for the 231- and 254-keV transitions confirmed the spin/parity assignments of the 2107- and 2388-keV states in ^{133}Xe and ^{135}Ba, respectively. The small multipole-mixing ratios indicate a dominant $M2$ character of the 231- and 254-keV transitions. The experimental findings close a gap of $J^\pi = 23/2^+$ isomers along the $N = 79$ isotones. In addition, two experiments utilizing the pulsed-beam and electronic fast-timing technique were carried out to discover the anticipated $J^\pi = 23/2^+$ isomer in ^{137}Ce. As a main result, precise picosecond lifetimes for the $J^\pi = 21/2^-$ state at 2490 keV and the $J^\pi = 23/2^+$ state at 3225 keV were determined. However, no evidence for a long-lived $J^\pi = 23/2^+$ state in ^{137}Ce was observed.

Experimentally determined $B(M2)$ and $B(E3)$ transition strengths were compared to shell-model calculations employing the Realistic SM, GCN50:82, SN100PN, and SN100-KTH interactions. In particular, calculated $B(M2)$ values decently reproduce the measured transition strengths and predict correctly the systematic evolution from ^{129}Sn to ^{135}Ba. A detailed inspection of initial and final shell-model configurations indicate a dominant $\nu(h_{11/2}^{-2}d_{3/2}^{-1})$ configuration for the $J^\pi = 23/2^+$ states and a dominant $\nu(h_{11/2}^{-1}\pi g_{7/2}^{2})$ configuration for the $J^\pi = 19/2^-$ states. The isomeric character of the $J^\pi = 23/2^+$ states can be traced back to the change of the neutron configuration content and the required neutron spin transfer between initial and final states.

Identification of high-spin proton configurations in ^{136}Ba and ^{137}Ba

The level scheme of ^{136}Ba above the $J^\pi = 10^+$ isomer was recently significantly extended employing prompt-delayed correlations with the GAMMASPHERE array at Lawrence Berkeley National Laboratory following a MNT reaction [24]. However, spin assignments for the new states were not in the scope of that work. While the high-spin scheme of the lighter isotones ^{132}Te and ^{134}Xe are dominated by high-energy ($E_\gamma > 900$ keV) $12^+ \rightarrow 10^+$ transitions, no reasonable candidate for the $J^\pi = 12^+$ state in ^{136}Ba had been identified. As a result of the combined analysis of the AGATA ^{136}Xe+^{138}U MNT experiment and three fusion-evaporation experiments at the HORUS spectrometer, the publication "*Identification of high-spin proton configurations in* ^{136}*Ba and* ^{137}*Ba*" comprises revised and extended level schemes of ^{136}Ba and ^{137}Ba. In particular, the ordering of the 144-1214-keV cascade in ^{136}Ba was reversed and nine new states and transitions were incorporated into the level scheme. Moreover, exploiting γ-ray angular-distribution and $\gamma\gamma$ angular-correlation measurements, the 4920-keV state was identified as the $J^{\pi} = 12^{+}$ state, while the positive-parity yrast band between $J^{\pi} = 10^{+}$ and 12^{+} states was found to be interrupted by a $J^{\pi} = 11^{-}$ state in ^{136}Ba. Using the same technique, the 3545-keV state in ^{137}Ba was identified as the bandhead of the positive-parity band. The identification of the high-spin states refined the knowledge of high-spin structures in $N = 80$ and 81 isotones.

The experimental findings were compared to the results of untruncated large-scale shell-model calculations using the *gdsh* valence space for protons and neutrons. As a result of the GCN50:82 interaction, the $J^{\pi} = 10^{+}$ isomeric state was assigned to an almost pure $\nu h_{11/2}^{-2}$ neutron configuration, while the $J^{\pi} = 12^{+}$ state was identified as a fully aligned $\pi(g_{7/2}^{4} d_{5/2}^{2})$ proton spin configuration. Moreover, the $J^{\pi} = 11^{-}$ state was associated with a neutron character, corroborating the interruption of the positive-parity band. A continuation via a $\nu h_{11/2}^{-2}$ configuration is energetically favorable over a direct $12^{+} \rightarrow 10^{+}$ decay. Calculated $B(E2; 12^{+} \rightarrow 10^{+})$ values in ^{134}Xe and ^{136}Ba follow the observed decay pattern in both nuclei. However, SN100PN is not able to reproduce the nuclear-structure change of positive-parity states between $Z = 54$ and 56, most likely attributable to the deficient monopole part of the interaction. A comparison between calculated configurations of positive-parity states in ^{136}Ba and ^{137}Ba drive the interpretation of the $J^{\pi} = 21/2^{+}$ state in even-odd ^{137}Ba as the coupling of a valence neutron to the $J^{\pi} = 12^{+}$ state in even-even ^{136}Ba.

Isomer spectroscopy in ^{133}Ba and high-spin structure of ^{134}Ba

$J^{\pi} = 19/2^{+}$ isomers were systematically investigated along the $N = 77$ chain [32–36]. In the 1970s, the 1942-keV state in ^{133}Ba was identified as an isomer with a half-life in between 2 ns and 5 ns [36]. Later, Juutinen *et al.* [154] argued that the half-life of this state has to be much longer. Adding one neutron, the high-spin regime of ^{134}Ba was investigated several times in the past. However, the obtained results show significant differences from each other [2, 155–157]. The study presented in the publication "*Isomer spectroscopy in* ^{133}*Ba and high-spin structure of* ^{134}*Ba*" resolve the contradictory experimental findings in both nuclei. In this work, excited states in ^{133,134}Ba were populated in the AGATA ^{136}Xe+^{208}Pb MNT reaction and the ^{13}C+^{124}Sn fusion-evaporation experiment at the HORUS spectrometer, equipped with eight high-purity germanium and twelve cerium-doped lanthanum-bromide detectors, providing detailed $\gamma\gamma$ and $\gamma\gamma$-time correlations. The previously evaluated half-life of the 1942-keV state in ^{133}Ba was revised to $T_{1/2} = 66.6(20)$ ns. Likewise, the half-life of the 2222-keV ($J^{\pi} = 19/2^{+}$) state in ^{137}Nd was measured to be 0.38(7) ns, utilizing a ^{16}O+^{125}Te electronic fast-timing experiment. Both results close gaps of $J^{\pi} = 19/2^{+}$ isomers for $N = 77$ isotones. Moreover, the extended levelscheme of ^{134}Ba is based on the clear assignment of new transitions from the AGATA MNT experiment and complementary $\gamma\gamma$ information form the analysis of the fusion-evaporation experiment. A distinct backbending along the positive-parity yrast band was identified at $\hbar\omega \approx 0.38$ MeV. A systematic investigation of crossing frequencies along the even-Ba chain anticipate a neutron alignment at the position of the $J^\pi = 10^+$ state in ^{134}Ba.

Shell-model calculations with six different interactions were performed to elucidate the alignment structure of ^{134}Ba and the isomeric structure of the $J^\pi = 19/2^+$ state in ^{133}Ba. In general, backbending at the position of the $J^\pi = 10^+$ state is fairly reproduced for ^{134}Ba. Moreover, a second alignment at the $J^\pi = 16^+$ state is predicted correctly by all calculations. The trend of calculated $B(E2)$ values of transitions in the ground-state band is in agreement with the manifested neutron alignment in ^{134}Ba. Since $B(E1)$ values can not be evaluated in the $gdsh$ valence space, the $B(E1)$ transition strength of the $19/2^+ \to 19/2^-$ decay in ^{133}Ba was primarily investigated by means of a cross-shell calculation in an enlarged $gdsh + \nu f_{7/2}$ valence space by the EPQQM interaction. The discussion was completed by a theoretical $E2$ map, calculated with the novel SNV interaction.

Excited states in doubly-odd ^{130}I

The manuscript "*Excited states in doubly-odd ^{130}I*" presents first results on the high-spin structure of doubly-odd ^{130}I above the $J^\pi = 8^-$ isomeric band head. Prior to this work, excited states were solely investigated utilizing reactions with light particles like protons, deuterons and neutrons. Only the combination of ^{136}Xe+^{238}U, ^{136}Xe+^{208}Pb MNT experiments, and the ^{9}Be+^{124}Sn fusion-evaporation experiment provides sufficient information to establish the new level scheme of ^{130}I to approximately $2712 + x$ keV, incorporating eleven new states. Similar to the case of ^{131}Xe, a proton trigger was necessary to enhance the peak-to-background ratio of the elusive fusion-evaporation reaction product ^{130}I. Tentative spin-parity assignments, backed by systematics along the $Z = 53$ chain, were discussed. The level structure above the $J^\pi = (10^-)$ state at $818 + x$ keV resembles the excitation pattern observed in ^{134}I which is dominated by strong single-particle excitations, emphasizing the transitional character of ^{130}I.

Shell-model calculations with the GCN50:82, SN100PN, Realistic SM, and EPQQM interactions indicate that the sequence of the negative-parity states $J^\pi = 10^-...13^-$ are members of the proton-neutron $\pi g_{7/2}/d_{5/2} \otimes \nu h_{11/2}$ configuration. Moreover, spin and configuration decompositions of the newly observed states corroborate a $\pi h_{11/2} \otimes \nu h_{11/2}$ configuration for the $J^\pi = (10^+)$ band head of the positive-parity yrast band at $1740 + x$ keV in ^{130}I.

Outlook

Future work in the $50 \leq Z, N \leq 82$ region

Further studies in the $50 \leq Z, N \leq 82$ region are contemporary. Besides the still unobserved isomeric $J^\pi = 23/2^+$ state in ^{137}Ce, the systematics of the $N = 79$ isotonic is incomplete. Until now, no transitions from higher-lying states were observed which decay into the $J^\pi = 23/2^+$ isomers in ^{131}Te [30] and ^{135}Ba [139]. Moreover, there is a large disagreement between shell-model theory and experiment for the transition strength of the $23/2^+ \rightarrow 19/2^-$ decay in ^{131}Te [139]. In 2013 a recoil-decay tagging experiment at the JUROGAM+RITU+GREAT setup explored three transitions feeding the isomeric $J^\pi = (23/2^+)$ state at $E_x = 2616$ keV in ^{139}Nd [152]. A similar measurement would be of highest interest to elucidate the missing high-spin information in both nuclei.

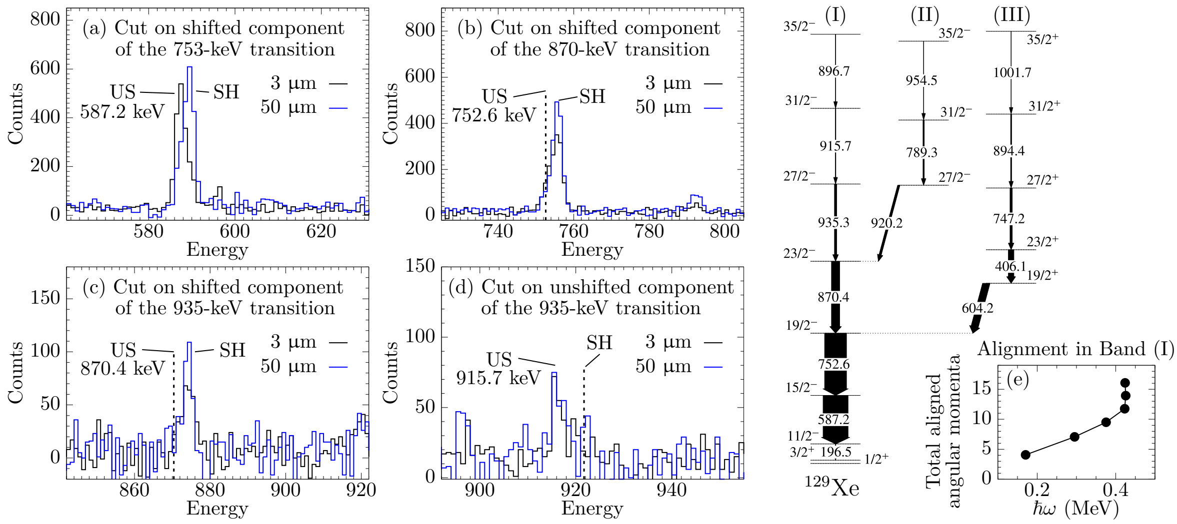

Figure 12: γ-ray spectra of the (a) 587, (b) 753, (c) 870, and (d) 916 keV transitions in ^{129}Xe. Spectra are generated from cuts on the (a)-(c) shifted components of the feeding transitions and from (d) the unshifted component of the 935 keV transition for target-to-stopper distances of (black) 3 μm and (blue) 50 μm. Doppler-shifted (SH) and unshifted (US) components are additionally labeled. (e) Total aligned angular momenta plot of band (I) of ^{129}Xe, plotted against the rotation frequency.

Just recently, an upbend along the $(\alpha = -1/2)$ negative-parity yrast band at the position of the $J^\pi = 27/2^-$ state was observed in ^{129}Xe [53]. In the alignment regions along yrast bands, a pronounced reduction of $B(E2)$ values is expected [59]. In the past, lifetime measurements were carried out by means of the recoil distance Doppler-shift method in the backbending regions of the yrast bands in ^{130,132,134}Ce [158]. Therefore, a future recoil distance Doppler-shift experiment can provide valuable information on lifetimes which are a sensitive probe for the nature of proton and neutron $0h_{11/2}$ alignment. First preliminary results on shifted and unshifted components of transitions in ^{129}Xe from a test measurement utilizing the ^{9}Be+^{124}Sn reaction at a beam energy of 40 MeV are presented in Fig. 12(a)-(d). γ rays were detected using 11 HPGe detectors, mounted in two rings at 45° and 142.3° with respect to the beam axis. Recoiling nuclei left the target with 0.7% of the speed of light. Data in this experiment were recorded at two different target-to-stopper distances; a very short distance of 3 μm and a larger distance of 50 μm. Each distance was measured for at least 18 hours. Spectra are generated from cuts on the shifted components of the (a) 753-, (b) 870-, and (c) 935-keV transitions. Regarding the $15/2^- \rightarrow 11/2^-$ transition, a pronounced unshifted component is visible for the target-to-stopper distance of 50-μm. On the other hand, for the target-to-stopper distance of 3 μm, the unshifted component dominates, clearly indicating a long lifetime of the $J^\pi = 15/2^-$ state. Due to the moderate recoil velocity, shifted and unshifted components are not clearly separated from each other, as visible in Fig. 12(a). For the (b) 980- and (c) 935-keV transitions mainly shifted components are observed for both target-to-stopper distances, indicating a rather short lifetime of the $J^\pi = 19/2^-$ and $23/2^-$ states compared to the $J^\pi = 15/2^-$ state. An indirect gate on the unshifted component of the 935-keV transition yields mainly unshifted components of the 916-keV transitions at both target-to-stopper distances (see Fig. 12(d)). This observation indicates either a short lifetime of the $J^\pi = 27/2^-$ state or a longe lifetime of the feeding $J^\pi = 31/2^-$ and $35/2^-$ states, which is in line with the anticipated long lifetime of both alignment states. The analysis is ongoing, however, statistics is very low for both states. Lifetime measurements in ^{125,127}Xe are also of highest interest, since no complimentary lifetime information are available for the corresponding backbending regions.

Another lifetime experiment which focused on ^{129}Xe aimed to close a gap in the systematics along the $Z = 54$ chain. While $J^\pi = 23/2^+$ isomers were studied in the neighboring isotopes ^{127}Xe ($T_{1/2} = 28(1)$ ns [20]) and ^{131}Xe ($T_{1/2} = 14(3)$ ns [33]), no complementary result is reported for the $J^\pi = 23/2^+$ state at 2426 keV in ^{129}Xe. According to systematics, it is expected that this state has a half-life of several nanoseconds, which is accessible in a ^{9}Be+^{124}Sn experiment, utilizing the electronic fast-timing technique. Shell-model calculations for ^{129}Xe, performed within the presented publication on ^{131}Xe, indicate a predominant $\nu(h^{-2}_{11/2}d^{-1}_{3/2})$ configuration for this state, which is in line with the isomeric $J^\pi = 23/2^+$ systematics.

Likewise, the identification of the not yet discovered yrast $J^\pi = 8^+$ and 6^+ states in ^{132}Xe can be addressed in upcoming beam times. The long half-life of the 8.39(11) ms [26] $J^\pi = 10^+$ isomer can be traced back to the structure of the $J^\pi = 8^+$ and 6^+ states. Shell-model calculations predict the $J^\pi = 8^+$ state either very close in energy to the $J^\pi = 10^+$ isomer or slightly above that state [27]. Therefore, a possible $10^+ \rightarrow 8^+$ transition can not be observed in a γ-ray fusion-evaporation or MNT experiment due to the very low transition energy and the usual energy thresholds of the HPGe detectors. Very recently, evidence for the $J^\pi = 6^+$ state was found at 2167 keV by Peters *et al.* [159], following a $(n, n'\gamma)$ measurement. The hitherto unknown $J^\pi = 8^+$ state might be populated via multiple Coulomb excitations. The observation would shed further light on the backbending mechanisms in ^{132}Xe as well as in ^{131}Xe. The fact that there are so many stable (eight) Te, (nine) Xe, and (seven) Ba isotopes opens the door for a comprehensive investigation via multistep Coulomb excitations.

New results on ^{130}I were reported in the manuscript "*Excited states in doubly-odd* ^{130}*I*". However, complementary information is missing for hard-to-reach ^{132}I, where excited states are limited to β-

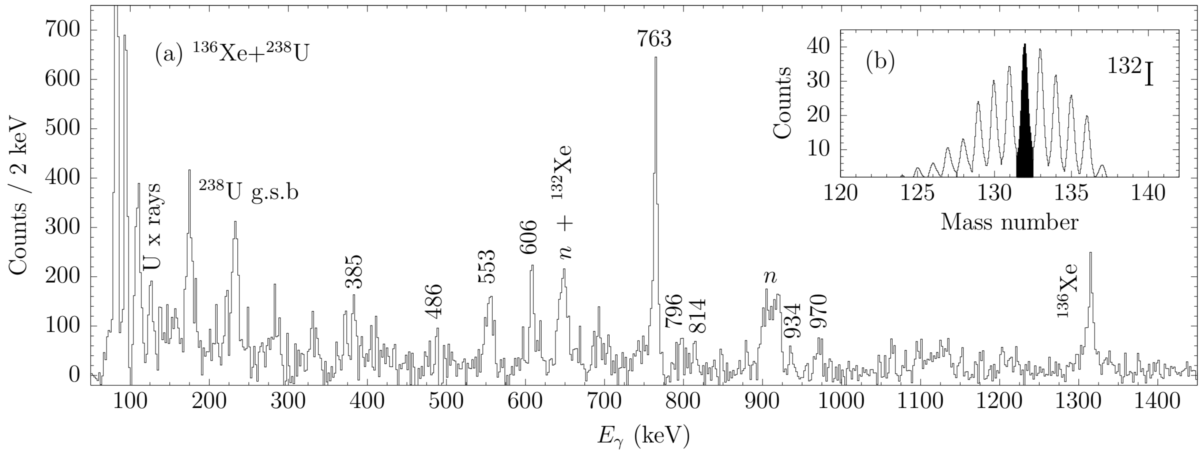

Figure 13: (a) AGATA γ-ray spectrum gated on mass and nuclear charge of ^{132}I identified with PRISMA. To get rid of the contaminant transitions from ^{132}Xe, the spectrum is adjusted by subtracting the normalized γ-ray spectrum of the isobar ^{132}Xe from the ^{132}I spectrum. (b) Mass spectrum of dedicated iodine isotopes with the applied gate.

decay spectroscopy of ^{132}Te [2, 160]. The nuclear structure of ^{132}I above 300 keV is still unknown. ^{132}I was also populated in the ^{238}U + ^{236}Xe AGATA MNT experiment in the one-proton and three-neutron stripping reaction and identified with PRISMA. The channel is the largest contribution to the iodine channel. The singles γ-ray spectrum of ^{132}I, corrected for contamination of the isobar ^{132}Xe, is shown in Fig. 13(a). The mass spectrum with the applied gate is shown in the inset Fig. 13(b). Contaminant transitions from ^{132}Xe stem from the intricate resolvability of the nuclear charge in the energy-loss spectra between $Z = 53$ and 54. Several candidates for new transitions in ^{132}I are found in the singles spectrum. Previously, none of the transitions were reported in the literature. A $\gamma\gamma$ analysis does not yield reliable results. In contrast to ^{130}I, ^{132}I can not be produced in standard fusion-evaporation reactions. Recently, the neighboring ^{131}I and ^{133}I were populated via MNT reactions employing ^{136}Xe beams onto Yb, Lu, W, and Os targets at Argonne National Laboratory using the GAMMASPHERE spectrometer. High-spin states up to 4.3 MeV were established in both isotopes [161]. In perspective, a similar MNT or complimentary fission experiment with a high efficiency γ-ray spectrometer provides data for a detailed spectroscopy of ^{132}I in order to close the gap along the iodine chain towards the $N = 82$ shell closure. Before publishing the above presented manuscript on ^{130}I elsewhere, new results on ^{132}I can be incorporated into the manuscript to get a deeper inside into the systematics.

Beside future experimental aspirations, theorists provide promising new developments and approaches for the $50 \leq Z, N \leq 82$ region. In recent past, it was several times concluded that the proton-neutron part of the SN100PN in not able to reproduce several nuclear-structure features in the mass region farther apart from the shell closures (see Refs. [69, 162, 163] and discussion in Sec. 1.2 of this thesis). Newly developed interactions like SNV and GCN50:82, where the proton-neutron part is replaced by monopole correction interactions, are capable to overcome the weaknesses of the SN100PN interaction [101]. New shell-model codes like the more advanced BIGSTICK code [164], which uses an efficient many-body truncation scheme, open the door for more demanding calculations towards lager m-scheme dimensions. An unified theoretical description of the region demands the consideration of additional single-particle orbitals across the $Z = 50$ or $N = 82$ shell closure. State-of-the-art calculations with the Monte-Carlo shell model are predestined to manage an extended model space which is not tractable for conventional SM calculations [4]. Recently, huge progress has been made in the development of many-body methods which goes beyond the shell-model approach. Ab-initio calculations with coupled-cluster method using the renormalization group (SRG)-transformed chiral $NN + 3N$ interactions were performed in heavy semimagic nuclei up to ^{132}Sn [165]. Ab-initio calculations are capable to treat nuclei properties in an unified formalism and may provide more insight into the underlying interactions between individual nucleons in this region of the nuclei chart.

Multinucleon transfer in the vicinity of ^{208}Pb

The region of the nuclei chart between the doubly-closed-shell nucleus ^{208}Pb and the well deformed actinides is rich in structural changes. Striking similarities in the underlying nuclear structure between the region around ^{208}Pb and ^{132}Sn were identified by mirrored proton-neutron multiplets of $\pi h_{9/2}\nu g_{9/2}$ in ^{210}Bi and $\pi g_{7/2}\nu f_{7/2}$ in ^{134}Sb [1]. The proximity of ^{208}Pb has become the object of numerous studies related to the discovery of very low-lying negative-parity collective states indicating the impotance of dynamical octupole deformation. Large electric octupole transition probabilities between low-lying $J^{\pi} = 3^{-}$ states and the $J^{\pi} = 0^{+}$ ground state were experimentally observed in ^{206}Pb [166], ^{208}Pb [167], and ^{210}Po [168].

Comprehensive experimental studies of single-closed nuclei together with microscopic shell-model calculations were performed along the $N = 126$ and $Z = 82$ chains [169, 170]. Severity tests of the proton-neutron part in $Z > 82$ nuclei far away from doubly-magic ^{208}Pb are still missing due to the lack of detailed knowledge of the level structure. Nonetheless, a couple of nuclei were investigated through empirical shell-model calculations [171]. Realistic shell-model studies in a restricted valence space were performed in ^{214}Po [172] and along Bi isotopes [173]. In the last few years, efforts were pursued by employing new interactions to describe nuclei around mass $A \approx 208$ within the enlarged shell-model space comprising the six single-particle orbitals between the magic numbers 82 and 126, namely, $0h_{9/2}$, $1f_{7/2}$, $0i_{3/2}$, $2p_{3/2}$, $1f_{5/2}$, and $2p_{1/2}$. Teruya *et al.* [174] presented a wide variety of calculated results for Pb, Bi, Po, At, Rn, and Fr isotopes in the neutron deficient region ($82 \leq Z$, $N \leq 126$). For this phenomenological effective two-body interaction, one set of the monopole pairing and quadrupole-quadrupole interactions including the multipole-pairing interactions is adopted. The interaction is very similar to the well-established pair-truncated shell-model PQM130 interaction in the $A = 130$ region, based on the similarities between the ^{208}Pb and ^{132}Sn regions [128]. Recently, the calculation was extended to nuclear structure features across the $N = 126$ neutron shell closure [175].

Apart from magnetic moments and transition strengths, a detailed knowledge of high-spin states is an experimental key observable. Figure 14 presents a partial nuclei chart of the region around doubly-magic ^{208}Pb, color coded with the maximum observed excitation energy of states within the yrast cascade. While the high-spin structure of nuclei north-west of ^{208}Pb ($N < 126$) is known in

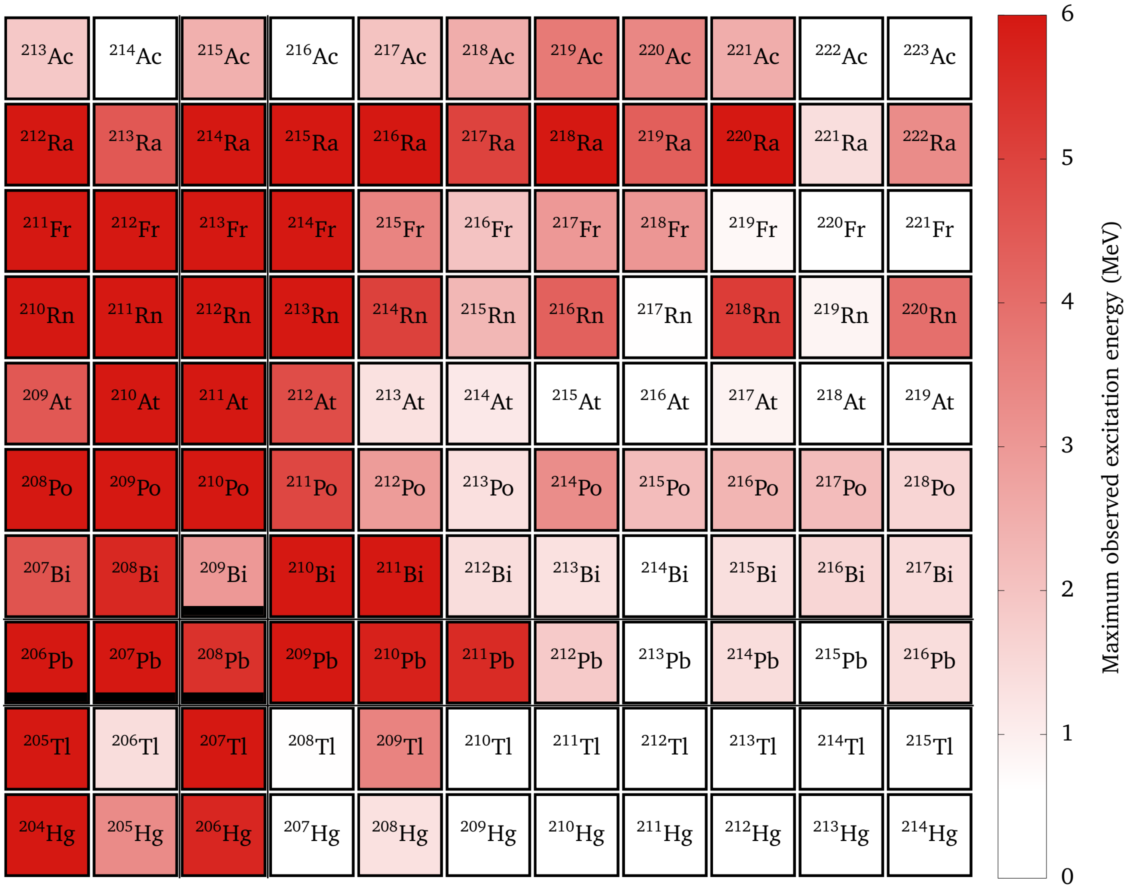

Figure 14: Partial nuclei chart around doubly-magic ^{208}Pb showing the maximum excitation energy of states in the yrast cascade observed in heavy-ion experiments. Data compiled from ENSDF/XUNDL data bases [2, 131].

detail, a significant lack of knowledge prevails for nuclei north-east of ^{208}Pb ($N > 126$). For example, the state with the highest known excitation energy is located in ^{210}Rn at approx. 12 MeV and has a spin value of 37 $\hbar$ following a ^{17}O+^{198}Pt reaction [176]. On the other hand, up to now, the region north-east of ^{208}Pb including neutron-rich Bi, Po, At, Rn, Fr, Ra, Ac, Th, Pa and U isotopes is hard to reach for in-beam spectroscopy. Since solely ^{206,207,208}Pb and ^{209}Bi are available as neutron-rich target materials for fusion-evaporation studies, the production of neutron-rich systems is very restricted. In the past, single nuclei like ^{215,216}Rn and ^{213,214}Po were populated in elusive fusion-evaporation reactions with very low cross sections of only few tens to hundreds μbarn [172, 177]. Multinucleon and deep-inelastic transfer reactions are the method of choice for the population of a wide range of nuclei in the $82 \leq Z$ region with sufficiently high cross sections for γ-ray spectroscopy. For example, multinucleon-transfer reactions were employed to populate high-spin bands of alternating parity states in ^{218,220,222}Rn and ^{222,224,226}Ra up to highest excitation energies and spins [178]. All isotopes were simultaneously populated following multinucleon transfer between a ^{136}Xe beam and a ^{232}Th target at 833 MeV at Lawrence Berkeley National Laboratory using the GAMMASPHERE spectrometer. Another deep-inelastic collision between a ^{208}Pb beam and a ^{238}U target was used to extend the level scheme of ^{206}Hg, ^{210}Pb, and ^{211}Bi to excitation energies above 5 MeV [179]. No complementary information was obtained for the neutron-rich nuclei like $^{212-217}$Bi, $^{215-218}$ Po, $^{213-219}$At, ^{217,219} Rn, and $^{219-221}$Fr. Results on excited states are mainly deduced from α-decay spectroscopy. In addition, no information about the level structure is available for the $Z < 82$ nuclei along the ($A \geq 208$) thallium and ($A \geq 207$) mercury chains.

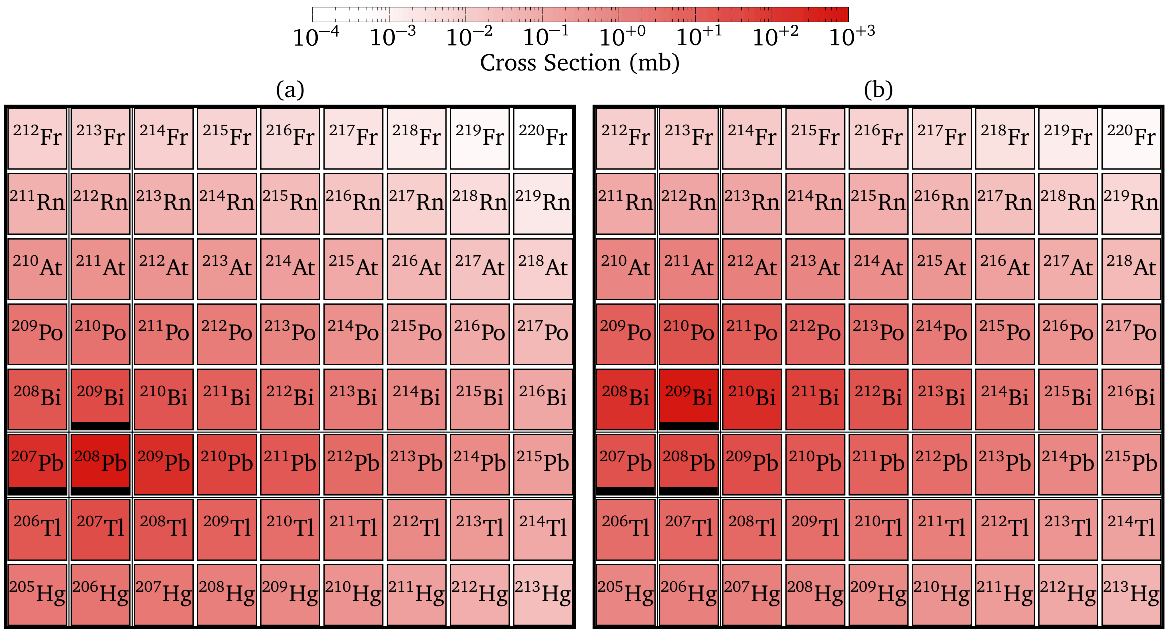

Figure 15: Calculated cross sections for (a) ^{136}Xe + ^{208}Pb and (b)^{136}Xe + ^{209}Bi MNT reacitions, both at beam energies of 1 GeV using the GRAZING-F code [180].

Figure 15 shows calculated cross sections for (a) ^{136}Xe + ^{208}Pb and (b)^{136}Xe + ^{209}Bi multinucleon-transfer reactions at beam energies of 1 GeV using the GRAZING-F code. The code uses a two step calculation; the initial GRAZING calculation [181] is followed by a second-stage calculation in which excited target-like nuclei are deexcited by fission and competing neutron evaporation. The calculations predict cross sections which are sufficiently large to perform γ-ray spectroscopy for nuclei of interest. In addition, recent calculations done by Zagrebaev and Greiner [182, 183] emphasized the possibility to produce heavy nuclei around ^{208}Pb by multinucleon transfer, utilizing multidimensional Langevin equations to describe the dynamics of heavy-ion low-energy dissipative collisions. The model describes not only multinucleon-transfer processes but also incorporates deep-inelastic collisions, quasifission, fusion-fission, and fusion reactions in a unified way. Theoretical predictions on cross sections are confirmed by several experimental results from the reaction studies performed at larger laboratories such as ANL, GANIL, and GSI. For example, the yields of over 200 projectile-like fragments and target-like fragments from the interaction of a ^{136}Xe beam at $E_{c.m.} = 450$ MeV on a thick target of ^{208}Pb were measured using offline γ-ray spectroscopy with GAMMASPHERE [74]. In that study, a transfer of up to six protons to the target was observed. Other studies employing ^{58,64}Ni beams at the SHIP filter at GSI [184] and a ^{136}Xe+^{198}Pt reaction at the VAMOS spectrometer at GANIL [185] obtained similar results.

During the 2010-2011 physics campaign at INFN Laboratori Nazionali di Legnaro (LNL), AGATA consisted of a maximum of five AGATA triple cluster detecors (15 HPGe crystals in total) [82, 83]. Subsequently, the array was successively expanded to the 1π configuration. Following the physics campaign at Grand Accélérateur National d'Ions Lourds (GANIL), AGATA will be hosted again at LNL. Meanwhile, a new detection system was installed at LNL, comprising of a Bragg chamber (hereafter the setup is called NOISE). In upcoming beam times, NOISE can be operated in coincidence with PRISMA to perform kinematic coincidence measurements [186]. A commissioning ^{197}Au $+^{130}$Te experiment yields first results on the final mass distribution of the heavy Au-like products and the effects of secondary processes like neutron evaporation and fission. [187]. In this study, Au-like products were detected with NOISE in kinematic coincidence with the lighter Te-like reaction products measured in the PRISMA spectrometer. Taking advantage of the higher γ-ray efficiency of the AGATA 1π configuration, the experimental setup of AGATA coupled to the PRISMA+NOISE system will provide an unique opportunity to investigate the nuclear structure of a large number of nuclei in the $82 \leq Z \leq 92$ region. The obstacle of high γ-ray background from excited fission fragments will be resolved by the detection of the surviving reaction products. Therefore, the NOISE array will be positioned on the grazing angle for the heavier target-like reaction product. By requiring the scattered particle in a narrow angle range, which corresponds to the grazing angle covered by PRISMA for the beam like particles, fission background is further reduced. Kinematic coincidences between the two reaction products will allow clean conditions for in-beam γ-ray spectroscopy with AGATA. Complementary information will be obtained for the neutron-rich nuclei like $^{207-214}$Hg, $^{208-215}$Ti, $^{212-216}$Pb, $^{212-217}$Bi, $^{215-218}$Po, $^{213-219}$At, ^{217,219}Rn, and $^{219-221}$Fr.

Bibliography

[1] L. Coraggio et al. "Similarity of nuclear structure in the ^{132}Sn and ^{208}Pb regions: Proton-neutron multiplets." *Phys. Rev. C* 80 (2009), p. 021305 (cit. on pp. 7, 136).

[2] Evaluated Nuclear Structure Data File (ENSDF). http://www.nndc.bnl.gov/ensdf (cit. on pp. 7–10, 13, 21, 67, 111, 131, 135, 137).

[3] Y. Khazov et al. "Nuclear Data Sheets for $A = 132$." *Nuclear Data Sheets* 104.3 (2005), pp. 497–790 (cit. on p. 7).

[4] T. Togashi et al. "Novel Shape Evolution in Sn Isotopes from Magic Numbers 50 to 82." *Phys. Rev. Lett.* 121 (2018), p. 062501 (cit. on pp. 7, 136).

[5] G. Lorusso et al. "β-Decay Half-Lives of 110 Neutron-Rich Nuclei across the $N = 82$ Shell Gap: Implications for the Mechanism and Universality of the Astrophysical r Process." *Phys. Rev. Lett.* 114 (2015), p. 192501 (cit. on p. 7).

[6] D. C. Radford et al. "Coulomb Excitation of Radioactive ^{132,134,136}Te Beams and the Low $B(E2)$ of ^{136}Te." *Phys. Rev. Lett.* 88 (2002), p. 222501 (cit. on p. 7).

[7] S. Mukhopadhyay et al. "Prompt γ spectroscopic studies of fragment nuclei in thermal neutron induced fission of ^{235}U." *Phys. Rev. C* 85 (2012), p. 064321 (cit. on p. 7).

[8] W. Urban et al. "Octupole correlations in neutron-rich, even-even barium isotopes." *Nucl. Phys. A* 613.1 (1997), pp. 107–131 (cit. on p. 7).

[9] J. G. Wang et al. "First identification of collective bands and octupole correlations in the neutron-rich ^{143}La nucleus." *Phys. Rev. C* 75 (2007), p. 064301 (cit. on pp. 7, 11).

[10] S. J. Zhu et al. "Octupole correlations in neutron-rich ^{143,145}Ba and a type of superdeformed band in ^{145}Ba." *Phys. Rev. C* 60 (1999), p. 051304 (cit. on p. 7).

[11] H. Wang et al. "First spectroscopic information from even-even nuclei in the region "southeast" of ^{132}Sn: Neutron-excitation dominance of the 2_1^+ state in ^{132}Cd." *Phys. Rev. C* 94 (2016), p. 051301 (cit. on p. 7).

[12] J. Taprogge et al. "$1p_{3/2}$ Proton-Hole State in ^{132}Sn and the Shell Structure Along $N = 82$." *Phys. Rev. Lett.* 112 (2014), p. 132501 (cit. on p. 7).

[13] K. L. Jones et al. "The magic nature of ^{132}Sn explored through the single-particle states of ^{133}Sn." *Nature* 465.7297 (2010), p. 454 (cit. on p. 7).

[14] P. Hoff et al. "Single-Neutron States in ^{133}Sn." *Phys. Rev. Lett.* 77 (1996), pp. 1020–1023 (cit. on p. 7).

[15] W. Urban et al. "Neutron single-particle energies in the ^{132}Sn region." *Eur. Phys. J. A* 5.3 (1999), pp. 239–241 (cit. on p. 7).

[16] B. A. Brown and W. D. M. Rae. "The Shell-Model Code NuShellX@MSU." *Nuclear Data Sheets* 120 (2014), pp. 115–118 (cit. on pp. 8, 16).

[17] B. A. Brown et al. "Magnetic moments of the 2_1^+ states around ^{132}Sn." *Phys. Rev. C* 71 (2005), p. 044317 (cit. on pp. 8, 17).

[18] B. Fogelberg et al. "Detailed Spectroscopy of the Doubly Closed Shell Nucleus ^{132}Sn : First Observation of Octupole Collectivity." *Phys. Rev. Lett.* 73 (1994), pp. 2413–2416 (cit. on p. 8).

[19] A. K. Jain et al. "Atlas of Nuclear Isomers." *Nuc. Data Sheets* 128 (2015), pp. 1–130 (cit. on pp. 9, 21).

[20] S. Chakraborty et al. "Rotational band on a three-quasineutron isomer in ^{127}Xe." *Phys. Rev. C* 97 (2018), p. 054311 (cit. on pp. 9, 134).

[21] P. Walker and G. Dracoulis. "Energy traps in atomic nuclei." *Nature* 399.6731 (1999), p. 35 (cit. on p. 8).

[22] N. J. Stone. "Table of nuclear magnetic dipole and electric quadrupole moments." *Atomic Data and Nuclear Data Tables* 90.1 (2005), pp. 75–176 (cit. on pp. 8, 12).

[23] S. Harissopulos et al. "Measurement of the magnetic moment of the 10^+ isomer in ^{132}Ba." *Phys. Rev. C* 52 (1995), pp. 1796–1800 (cit. on p. 8).

[24] J. J. Valiente-Dobón et al. "^{136}Ba studied via deep-inelastic collisions: Identification of the $(\nu_{11/2})^{-2}_{10+}$ isomer." *Phys. Rev. C* 69 (2004), p. 024316 (cit. on pp. 8, 14, 130).

[25] M. N. Tantawy et al. "Systematics of isomeric configurations in $N = 77$ odd-Z isotones near the proton drip line." *Phys. Rev. C* 73 (2006), p. 024316 (cit. on p. 8).

[26] H. F. Brinckmann et al. "Ein Hochangeregter isomerer kernzustand in ^{132}Xe." *Nucl. Phys. A* 96.2 (1967), pp. 318–326 (cit. on pp. 8, 12, 134).

[27] A. Vogt et al. "High-spin structures in ^{132}Xe and ^{133}Xe and evidence for isomers along the $N = 79$ isotones." *Phys. Rev. C* 96 (2017), p. 024321 (cit. on pp. 8–10, 12, 15, 130, 134).

[28] T. Matsuzawa et al. "Seniority isomerism in proton-rich $N = 82$ isotones and its indication to stiffness of the $Z = 64$ core." *Phys. Rev. C* 62 (2000), p. 054304 (cit. on p. 8).

[29] J. Genevey et al. "High spin isomers in ^{129}Sn and ^{130}Sb." *Phys. Rev. C* 65 (2002), p. 034322 (cit. on pp. 8, 10, 65).

[30] B. Fogelberg et al. "New high spin isomers obtained in thermal fission." *AIP Conf. Proc.* 447.1 (1998), pp. 191–195 (cit. on pp. 8, 10, 65, 130, 133).

[31] M. Ferraton et al. "Lifetime measurement of the six-quasiparticle isomer in ^{140}Nd and evidence for an isomer above the $19/2^+$ state in ^{139}Nd." *Eur. Phys. J. A* 35.2 (2008), pp. 167–170 (cit. on pp. 8, 10).

[32] J. A. Pinston et al. "Microsecond isomers in ^{125,127,129}Sn." *Phys. Rev. C* 61 (2000), p. 024312 (cit. on pp. 9–10, 111, 131).

[33] A. Kerek et al. "Two- and three-quasiparticle states in ^{132}Xe and ^{131}Xe." *Nucl. Phys. A* 172.3 (1971), pp. 603–617 (cit. on pp. 9–10, 14, 111, 131, 134).

[34] A. Zemel et al. "Magnetic Moment of the $19/2^+$ Isomer in ^{135}Ce." *Z. Phys. A* 304 (1982), p. 269 (cit. on pp. 9–10, 111, 131).

[35] J. Gizon et al. "Deformed states of neutron-deficient cerium and neodymium nuclei." *Nucl. Phys. A* 222.3 (1974), pp. 557–578 (cit. on pp. 10, 111–112, 131).

[36] J. Gizon et al. "Band structure in ^{131,132,133}Ba observed by (^{12}C,xn) reactions." *Nucl. Phys. A* 252.2 (1975), pp. 509–523 (cit. on pp. 10, 111, 131).

[37] R. H. Mayer et al. “New 19/2+ isomers in ^{119}Sn, ^{121}Sn and ^{123}Sn.” *Z. Phys. A* 342.2 (1992), pp. 247–248 (cit. on p. 8).

[38] S. Kumar et al. “Band structure and shape coexistence in $^{135}_{56}$Ba$_{79}$.” *Phys. Rev. C* 81 (2010), p. 067304 (cit. on p. 9).

[39] H. Gausemel et al. “Decay of ^{127}In and ^{129}In.” *Phys. Rev. C* 69 (2004), p. 054307 (cit. on p. 9).

[40] C. T. Zhang et al. “Yrast excitations in ^{129}Te.” *Z. Phys. A* 353.1 (1995), pp. 11–12 (cit. on p. 9).

[41] A. Astier et al. “High-spin structures of five $N = 82$ isotopes: $^{136}_{54}$Xe, $^{137}_{55}$Cs, $^{138}_{56}$Ba, $^{139}_{57}$La, and $^{140}_{58}$Ce.” *Phys. Rev. C* 85 (2012), p. 064316 (cit. on pp. 10, 17, 21).

[42] K. Li et al. “Identification and shell model calculation of high spin states in ^{137,138}Cs nuclei.” *Phys. Rev. C* 75 (2007), p. 044314 (cit. on pp. 10, 21).

[43] H.-K. Wang et al. “Large-scale shell-model study for excitations across the neutron $N = 82$ shell gap in $^{131-133}$Sb.” *Phys. Rev. C* 96 (2017), p. 054313 (cit. on pp. 10–11, 21).

[44] M. S. R. Laskar et al. “g-factor measurement of the 2738 keV isomer in ^{135}La.” *Phys. Rev. C* 99 (2019), p. 014308 (cit. on pp. 11, 22).

[45] R. Wyss et al. “Interplay between proton and neutron S-bands in the Xe-Ba-Ce-region.” *Nucl. Phys. A* 505.2 (1989), pp. 337–351 (cit. on p. 11).

[46] R. E. Peierls and D. J. Thouless. “Variational approach to collective motion.” *Nucl. Phys.* 38 (1962), pp. 154–176 (cit. on p. 11).

[47] R. Casten and R. F. Casten. Nuclear Structure from a Simple Perspective. Oxford science publications. Oxford University Press, 2000 (cit. on p. 11).

[48] H. Morinaga and N. L. Lark. “Collective excited states in even xenon isotopes.” *Nucl. Phys.* 67.2 (1965), pp. 315–320 (cit. on p. 11).

[49] A. Granderath et al. “Shapes and rotational structures of neutron $h_{11/2}$ configurations in the Xe-Ba-Ce region.” *Nucl. Phys. A* 597.3 (1996), pp. 427–471 (cit. on pp. 11, 17, 129).

[50] R. F. Casten and P. V. Brentano. “An extensive region of $O(6)$-like nuclei near $A = 130$.” *Phys. Lett. B* 152.1 (1985), pp. 22–28 (cit. on pp. 11, 17, 129).

[51] R. Wyss et al. “Highly deformed intruder bands in the $A \approx 130$ mass region.” *Phys. Lett. B* 215.2 (1988), pp. 211–217 (cit. on p. 11).

[52] E. S. Paul et al. “Shape coexistence in ^{132}Ba.” *Phys. Rev. C* 40 (1989), pp. 1255–1264 (cit. on p. 11).

[53] Y. Huang et al. “High-spin structures in the ^{129}Xe nucleus.” *Phys. Rev. C* 93 (2016), p. 064315 (cit. on pp. 11, 13, 17, 129, 133).

[54] R. S. Chakrawarthy. “$M1$ and $E2$ band structures in the Sn-Xe-Ba region.” *Pramana* 53.3 (1999), pp. 407–407 (cit. on p. 11).

[55] NuDat 2.7. https://www.nndc.bnl.gov/nudat2/ (cit. on p. 12).

[56] R. O. Sayer et al. “Rotational and quasirotational bands in even-even nuclei.” *Atomic Data and Nuclear Data Tables* 15.2 (1975), pp. 85–110 (cit. on p. 11).

[57] C. S. Purry et al. "Multi-quasiparticle isomers and rotational bands in ^{178}W." *Nucl. Phys. A* 632 (1998), pp. 229–274 (cit. on p. 11).

[58] A. Johnson et al. "Nuclear moment of inertia at high rotational frequencies." *Nucl. Phys. A* 179.3 (1972), pp. 753–768 (cit. on p. 11).

[59] A. Dewald et al. "10^+ yrast isomer in ^{132}Ba." *Phys. Rev. C* 37 (1988), pp. 289–291 (cit. on pp. 11, 133).

[60] S. E. A. Orrigo et al. "Direct Dark Matter search with XENON100." *Eur. Phys. J. Web of Conferences* 121 (2016), p. 06006 (cit. on p. 13).

[61] E. Aprile et al. "First Results on the Scalar WIMP-Pion Coupling, Using the XENON1T Experiment." *Phys. Rev. Lett.* 122 (2019), p. 071301 (cit. on p. 13).

[62] J. Angle et al. "Limits on Spin-Dependent WIMP-Nucleon Cross Sections from the XENON10 Experiment." *Phys. Rev. Lett.* 101 (2008), p. 091301 (cit. on p. 13).

[63] J. Menéndez et al. "Spin-dependent WIMP scattering off nuclei." *Phys. Rev. D* 86 (2012), p. 103511 (cit. on p. 13).

[64] P. Toivanen et al. "Large-scale shell-model calculations of elastic and inelastic scattering rates of lightest supersymmetric particles (LSP) on ^{127}I, ^{129}Xe, ^{131}Xe, and ^{133}Cs nuclei." *Phys. Rev. C* 79 (2009), p. 044302 (cit. on p. 13).

[65] M. T. Ressell and D. J. Dean. "Spin-dependent neutralino-nucleus scattering for $A \sim 127$ nuclei." *Phys. Rev. C* 56 (1997), pp. 535–546 (cit. on p. 13).

[66] E. Aprile et al. "Limits on Spin-Dependent WIMP-Nucleon Cross Sections from 225 Live Days of XENON100 Data." *Phys. Rev. Lett.* 111 (2013), p. 021301 (cit. on p. 13).

[67] T. Koike et al. "Systematic search of $\pi h_{11/2} \otimes \nu h_{11/2}$ chiral doublet bands and role of triaxiality in odd-odd $Z = 55$ isotopes: ^{128,130,132,134}Cs." *Phys. Rev. C* 67 (2003), p. 044319 (cit. on p. 14).

[68] H. Pai et al. "Structural change of the unique-parity $\pi h_{11/2} \otimes \nu h_{11/2}$ configuration in ^{134}Cs." *Phys. Rev. C* 84 (2011), p. 041301 (cit. on p. 14).

[69] A. Vogt et al. "Isomers and high-spin structures in the $N = 81$ isotones ^{135}Xe and ^{137}Ba." *Phys. Rev. C* 95 (2017), p. 024316 (cit. on pp. 14–15, 17, 135).

[70] L. Kaya. "High-spin properties of neutron-rich nuclei near the $N = 82$ and $Z = 50$ shell closures." Master Thesis. University of Cologne, 2017 (cit. on pp. 14, 129).

[71] A. Vogt. "Multinucleon-Transfer Reactions as a Gateway to Neutron-Rich Actinides and Nuclei near the $N = 82$ and $Z = 50$ Shell Closures." PhD thesis. Universität zu Köln, 2017 (cit. on pp. 14–15).

[72] A. Vogt et al. "Light and heavy transfer products in ^{136}Xe $+^{238}$ U multinucleon transfer reactions." *Phys. Rev. C* 92 (2015), p. 024619 (cit. on pp. 14–15).

[73] W. W. Wilcke et al. "Bombarding-energy dependence of the ^{209}Bi + ^{136}Xe reaction." *Phys. Rev. C* 22 (1980), pp. 128–147 (cit. on p. 14).

[74] J. S. Barrett et al. "^{136}Xe+^{208}Pb reaction: A test of models of multinucleon transfer reactions." *Phys. Rev. C* 91 (2015), p. 064615 (cit. on pp. 14, 138).

[75] Chart of Radioactive Ion Beams in Europe (CRIBE). https://u.ganil-spiral2.eu/chartbeams/ (cit. on p. 14).

[76] J. F. C. Cocks et al. “Spectroscopy of Rn, Ra and Th isotopes using multi-nucleon transfer reactions.” *Nucl. Phys. A* 645.1 (1999), pp. 61–91 (cit. on p. 14).

[77] A. Vogt et al. “High-spin structure of ^{134}Xe.” *Phys. Rev. C* 93 (2016), p. 054325 (cit. on pp. 14–15).

[78] A. M. Stefanini et al. “The heavy-ion magnetic spectrometer PRISMA.” *Nucl. Phys. A* 701.1–4 (2002), pp. 217–221 (cit. on p. 14).

[79] L. Corradi et al. “Multinucleon transfer reactions: Present status and perspectives.” *Nucl. Instrum. Meth. Phys. Res. B* 317, Part B (2013), pp. 743–751 (cit. on p. 14).

[80] S. Szilner et al. “Multinucleon transfer reactions in closed-shell nuclei.” *Phys. Rev. C* 76 (2007), p. 024604 (cit. on p. 14).

[81] S. Akkoyun et al. “AGATA – Advanced GAmma Tracking Array.” *Nucl. Instrum. Meth. Phys. Res. A* 668 (2012), p. 26 (cit. on p. 14).

[82] A. Gadea et al. “Conceptual design and infrastructure for the installation of the first AGATA sub-array at LNL.” *Nucl. Instrum. Meth. Phys. Res. A* 654.1 (2011), pp. 88–96 (cit. on pp. 14, 139).

[83] B. Birkenbach. “Gamma-ray tracking with the AGATA demonstrator – A novel approach for in-beam spectroscopy.” PhD thesis. Universität zu Köln, 2014 (cit. on pp. 14, 139).

[84] P.-A. Söderström et al. “Interaction position resolution simulations and in-beam measurements of the AGATA HPGe detectors.” *Nucl. Instrum. Meth. Phys. Res. B* 638.1 (2011), pp. 96–109 (cit. on p. 14).

[85] J. Litzinger et al. “Transition probabilities in neutron-rich ^{80,82}Se and the role of the $\nu g_{9/2}$ orbital.” *Phys. Rev. C* 97 (2018), p. 044323 (cit. on p. 15).

[86] E. Sahin et al. “Shell evolution beyond $N = 40$: ^{69,71,73}Cu.” *Phys. Rev. C* 91 (2015), p. 034302 (cit. on p. 15).

[87] P. R. John et al. “Shape evolution in the neutron-rich osmium isotopes: Prompt γ-ray spectroscopy of ^{196}Os.” *Phys. Rev. C* 90 (2014), p. 021301 (cit. on p. 15).

[88] B. H. Wildenthal. “Shell Model for $N = 82$ Nuclei.” *Phys. Rev. Lett.* 22 (1969), pp. 1118–1120 (cit. on p. 16).

[89] L. Coraggio et al. “Double-step truncation procedure for large-scale shell-model calculations.” *Phys. Rev. C* 93 (2016), p. 064328 (cit. on p. 16).

[90] E. Caurier et al. “The shell model as a unified view of nuclear structure.” *Rev. Mod. Phys.* 77 (2005), pp. 427–488 (cit. on pp. 16–17, 19).

[91] N. Shimizu. “Nuclear shell-model code for massive parallel computation, KSHELL.” *arXiv preprint arXiv:1310.5431* (2013) (cit. on p. 16).

[92] M. Queiser et al. “Cross-shell excitations from the fp shell: Lifetime measurements in ^{61}Zn.” *Phys. Rev. C* 96 (2017), p. 044313 (cit. on p. 16).

[93] W. Gropp et al. “Using MPI: portable parallel programming with the message-passing interface.” *MIT Press, Cambridge* (1994) (cit. on p. 16).

[94] B. H. Wildenthal. “Shell Model for $N = 82$ Nuclei.” *Phys. Rev. Lett.* 22 (1969), pp. 1118–1120 (cit. on p. 16).

[95] H. G. Kruse and B. H. Wildenthal. *Bull. Am. Phys. Soc.* 27.533 (1982), p. 27 (cit. on p. 16).

[96] W. J. Baldridge. “Shell-model studies for the ^{132}Sn region. I. Few proton cases.” *Phys. Rev. C* 18 (1978), pp. 530–538 (cit. on p. 16).

[97] F. Andreozzi et al. “Structure of neutron-rich nuclei around ^{132}Sn.” *Phys. Rev. C* 56 (1997), R16–R19 (cit. on p. 16).

[98] S. Sarkar and M. Saha Sarkar. “Shell model study of neutron-rich nuclei near ^{132}Sn.” *Phys. Rev. C* 64 (2001), p. 014312 (cit. on p. 16).

[99] W. T. Chou and E. K. Warburton. “Construction of shell-model interactions for $Z > 50, N < 82$ nuclei: Predictions for $A = 133$-134 β^- decays.” *Phys. Rev. C* 45 (1992), pp. 1720–1729 (cit. on p. 16).

[100] R. F. Casten and R. B. Cakirli. “The evolution of collectivity in nuclei and the proton-neutron interaction.” *Phys. Scr.* 91.3 (2016), p. 033004 (cit. on p. 17).

[101] Y. Utsuno et al. “Recent shell-model results for exotic nuclei.” *Eur. Phys. J. Web Conf.* 66 (2014). INPC 2013 - International Nuclear Physics Conference, p. 02106 (cit. on pp. 17, 22, 135).

[102] K. Tanabe and K. Sugawara-Tanabe. “Microscopic properties of the superdeformed rotational states in light rare-earth nuclei ^{132}Ce and ^{134,136}Nd.” *Phys. Lett. B* 259.1 (1991), pp. 12–18 (cit. on p. 17).

[103] K. Tanabe and K. Sugawara-Tanabe. “Shape coexistence at high spins in ^{158}Er and ^{160}Yb predicted by the self-consistent calculation.” *Phys. Lett. B* 135.5 (1984), pp. 353–357 (cit. on p. 17).

[104] E. Garrote et al. “Fingerprints of Reflection Asymmetry at High Angular Momentum in Atomic Nuclei.” *Phys. Rev. Lett.* 80 (1998), pp. 4398–4401 (cit. on p. 17).

[105] J. L. Egido and L. M. Robledo. “High-spin states in heavy nuclei with the density dependent Gogny force.” *Phys. Rev. Lett.* 70 (1993), pp. 2876–2879 (cit. on p. 17).

[106] N. Yoshida et al. “Description of high-spin states in the interacting boson model.” *Phys. Lett. B* 114.2 (1982), pp. 86–90 (cit. on pp. 17, 129).

[107] K. Nomura et al. “Shape-phase transitions in odd-mass γ-soft nuclei with mass $A \approx 130$.” *Phys. Rev. C* 96 (2017), p. 014304 (cit. on pp. 17, 129).

[108] L. M. Robledo et al. “Evolution of nuclear shapes in medium mass isotopes from a microscopic perspective.” *Phys. Rev. C* 78 (2008), p. 034314 (cit. on pp. 17, 129).

[109] C.-B. Moon et al. “Structure of the negative parity bands in ^{125}Xe.” *Phys. Rev. C* 76 (2007), p. 067301 (cit. on pp. 17, 129).

[110] E. Caurier et al. “Intrinsic vs Laboratory Frame Description of the Deformed Nucleus ^{48}Cr.” *Phys. Rev. Lett.* 75 (1995), pp. 2466–2469 (cit. on p. 17).

[111] G. Martínez-Pinedo et al. “Backbending in ^{50}Cr.” *Phys. Rev. C* 54 (1996), R2150–R2154 (cit. on p. 17).

[112] K. Higashiyama et al. “Shell model study of backbending phenomena in Xe isotopes.” *Phys. Rev. C* 65 (2002), p. 054317 (cit. on p. 17).

[113] Y. Lei and Z. Y. Xu. “$h^2_{11/2}$ alignments in neutron-rich ^{132}Ba with negative-parity pairs.” *Phys. Rev. C* 92 (2015), p. 014317 (cit. on p. 17).

[114] T. Takahashi et al. "Backbending phenomena in ^{132,134,136}Ce with a pair-truncated shell model." *Phys. Rev. C* 71 (2005), p. 014305 (cit. on p. 17).

[115] R. Machleidt et al. "Nonlocal nature of the nuclear force and its impact on nuclear structure." *Phys. Rev. C* 53 (1996), R1483–R1487 (cit. on pp. 17, 22).

[116] A. Astier et al. "High-spin states with seniority $v = 4$, 5, and 6 in $^{119-126}$Sn." *Phys. Rev. C* 85 (2012), p. 054316 (cit. on p. 17).

[117] M. Dufour and A. P. Zuker. "Realistic collective nuclear Hamiltonian." *Phys. Rev. C* 54 (1996), pp. 1641–1660 (cit. on pp. 17, 19).

[118] E. Caurier et al. "Collectivity in the light xenon isotopes: A shell model study." *Phys. Rev. C* 82 (2010), p. 064304 (cit. on pp. 17–18).

[119] E. Caurier et al. "Shell Model description of the $\beta\beta$ decay of ^{136}Xe." *Phys. Lett. B* 711.1 (2012), pp. 62–64 (cit. on pp. 17–18).

[120] M. Hjorth-Jensen et al. "Realistic effective interactions for nuclear systems." *Phys. Rep.* 261.3 (1995), pp. 125–270 (cit. on p. 17).

[121] M. Honma et al. "Effective interaction for pf-shell nuclei." *Phys. Rev. C* 65 (2002), p. 061301 (cit. on p. 17).

[122] K. Sieja et al. "Description of proton-neutron mixed-symmetry states near ^{132}Sn within a realistic large scale shell model." *Phys. Rev. C* 80 (2009), p. 054311 (cit. on p. 18).

[123] J. Menéndez et al. "Disassembling the nuclear matrix elements of the neutrinoless $\beta\beta$ decay." *Nucl. Phys. A* 818.3 (2009), pp. 139–151 (cit. on p. 18).

[124] A. Shrivastava et al. "Prompt γ-ray spectroscopy of isotopically identified fission fragments." *Phys. Rev. C* 80 (2009), p. 051305 (cit. on p. 18).

[125] S. Sarkar and M. S. Sarkar. "Structure of even-even $A = 138$ isobars and the yrast spectra of semi-magic Sn isotopes above the ^{132}Sn core." *Phys. Rev. C* 78 (2008), p. 024308 (cit. on p. 19).

[126] R. L. Lozeva et al. "New sub-μs isomers in ^{125,127,129}Sn and isomer systematics of $^{124\text{-}130}$Sn." *Phys. Rev. C* 77 (2008), p. 064313 (cit. on p. 19).

[127] V. Kumar et al. "Analysis of proton and neutron pair breakings: High-spin structures of $^{124-127}$Te isotopes." *Nucl. Phys. A* 942 (2015), pp. 1–17 (cit. on pp. 19, 21).

[128] E. Teruya et al. "Shell-model calculations of nuclei around mass 130." *Phys. Rev. C* 92 (2015), p. 034320 (cit. on pp. 19–22, 136).

[129] L. Coraggio et al. "Calculation of Gamow-Teller and two-neutrino double-β decay properties for ^{130}Te and ^{136}Xe with a realistic nucleon-nucleon potential." *Phys. Rev. C* 95 (2017), p. 064324 (cit. on pp. 19, 22).

[130] K. Suzuki and R. Okamoto. "Effective Operators in Time-Independent Approach." *Progress of Theoretical Physics* 93.5 (1995), pp. 905–917 (cit. on p. 19).

[131] Experimental Unevaluated Nuclear Data File (XUNDL). https://www.nndc.bnl.gov/xundl (cit. on pp. 21, 137).

[132] L. Coraggio et al. "Effective shell-model hamiltonians from realistic nucleon–nucleon potentials within a perturbative approach." *Annals of Physics* 327.9 (2012), pp. 2125–2151 (cit. on p. 22).

[133] L. Coraggio et al. “Shell-model calculations and realistic effective interactions.” *Progress in Particle and Nuclear Physics* 62.1 (2009), pp. 135–182 (cit. on p. 22).

[134] S. Bogner et al. “Low momentum nucleon-nucleon potential and shell model effective interactions.” *Phys. Rev. C* 65 (2002), p. 051301 (cit. on p. 22).

[135] M. Honma et al. *RIKEN Accel. Progr. Report* 49 (2015), p. 77 (cit. on p. 22).

[136] M. Honma et al. “Shell-model fits for Sn isotopes.” *RIKEN Accel. Prog. Rep.* 45 (2012), p. 35 (cit. on p. 22).

[137] Y. Utsuno et al. “Shape transitions in exotic Si and S isotopes and tensor-force-driven Jahn-Teller effect.” *Phys. Rev. C* 86 (2012), p. 051301 (cit. on p. 22).

[138] T. Otsuka et al. “Novel Features of Nuclear Forces and Shell Evolution in Exotic Nuclei.” *Phys. Rev. Lett.* 104 (2010), p. 012501 (cit. on p. 22).

[139] L. Kaya et al. “Millisecond $23/2^+$ isomers in the $N = 79$ isotones ^{133}Xe and ^{135}Ba.” *Phys. Rev. C* 98 (2018), p. 054312 (cit. on pp. 65, 133).

[140] M. Müller-Veggian et al. “Investigation of high-spin states in ^{138,139}Nd.” *Nucl. Phys. A* 344.1 (1980), pp. 89–108 (cit. on p. 65).

[141] M. Kortelahti et al. “Medium-Spin Levels in ^{137}Ce and the Prolate-Oblate Shape Transition in Ce Nuclei.” *Physica Scripta* 27.3 (1983), p. 166 (cit. on p. 65).

[142] E. A. Henry et al. “Systematic study of the structure of odd-mass lanthanum nuclei. I. Levels in ^{137}La from ^{137}Ce^{m+g} decay.” *Phys. Rev. C* 12 (1975), pp. 1314–1320 (cit. on p. 65).

[143] M. Müller-Veggian et al. “High-spin states and isomers in ^{136,137,138}Ce.” *Nucl. Phys. A* 304.1 (1978), pp. 1–28 (cit. on p. 65).

[144] G. T. Danby et al. “Successive Decays from Pr^{137} and Ce^{137m}: Decay of Adjacent Praseodymium Isotopes.” *Can. J. Phys.* 36.11 (1958), pp. 1487–1508 (cit. on p. 65).

[145] S. J. Zhu et al. “High spin states and a collective oblate band in ^{137}Ce.” *Phys. Rev. C* 62 (2000), p. 044310 (cit. on pp. 65–66).

[146] T. Bhattacharjee et al. “Multi-quasiparticle bands in ^{137}Ce.” *Phys. Rev. C* 78 (2008), p. 024304 (cit. on pp. 65–66).

[147] J. Ludziejewski and H. Arnold. “High-spin levels in ^{137,139}Ce and ^{139,141}Nd evidence for hole-core coupling.” *Z. Phys. A* 281.3 (1977), pp. 287–308 (cit. on p. 65).

[148] L. Netterdon et al. “The γ-ray spectrometer HORUS and its applications for nuclear astrophysics.” *Nucl. Instrum. Methods. Phys. Res. A* 754 (2014), pp. 94–100 (cit. on p. 67).

[149] J.-M. Régis et al. “On the time response of background obtained in γ-ray spectroscopy experiments using $LaBr_3$(Ce) detectors with different shielding.” *Nucl. Instr. Meth. Phys. Res. A* 811 (2016), pp. 42–48 (cit. on p. 67).

[150] J.-M. Régis et al. “The generalized centroid difference method for picosecond sensitive determination of lifetimes of nuclear excited states using large fast-timing arrays.” *Nucl. Instr. Meth. Phys. Res. A* 726 (2013), pp. 191–202 (cit. on p. 67).

[151] J.-M. Régis et al. “Reduced γ–γ time walk to below 50 ps using the multiplexed-start and multiplexed-stop fast-timing technique with $LaBr_3$(Ce) detectors.” *Nucl. Instr. Meth. Phys. Res. A* 823 (2016), pp. 72–82 (cit. on p. 67).

[152] A. Vancraeyenest et al. "Identification of new transitions feeding the high-spin isomers in ^{139}Nd and ^{140}Nd nuclei." *Phys. Rev. C* 87 (2013), p. 064303 (cit. on pp. 130, 133).

[153] P. Knoch. Master Thesis. University of Cologne, 2004 (cit. on p. 130).

[154] S. Juutinen et al. "Shape coexistence in the transitional ^{133}Ba nucleus." *Phys. Rev. C* 51 (1995), pp. 1699–1707 (cit. on p. 131).

[155] W. T. Cluff. "The High-Spin Structure of ^{134,135}Ba and ^{120}Te." PhD thesis. Florida State University, 2008 (cit. on p. 131).

[156] X. Che et al. "Level structure with high excitation states in ^{134}Ba." *Energy Phys. Nucl. Phys.* 31.7 (2007), pp. 621–624 (cit. on p. 131).

[157] T. Lönnroth et al. "Coexistence of Shapes in Transitional ^{132,133,134}Ba." *JYFL Ann. Rept. 1989-1990, p99* (1990) (cit. on p. 131).

[158] D. Husar et al. "Lifetimes of the yrast states of even Ce isotopes." *Nucl. Phys. A* 292.1 (1977), pp. 267–280 (cit. on p. 133).

[159] E. E. Peters et al. "Emerging collectivity from the nuclear structure of ^{132}Xe: Inelastic neutron scattering studies and shell-model calculations." *Phys. Rev. C* 99 (2019), p. 064321 (cit. on p. 134).

[160] A. A. Yousif et al. "Gamma-ray transition strengths and multipolarities in the doubly odd nucleus ^{132}I." *Journal of Physics G* 7.4 (1981), pp. 445–453 (cit. on p. 135).

[161] H. Watanabe et al. "Multi-quasiparticle isomers involving proton-particle and neutron-hole configurations in ^{131}I and ^{133}I." *Phys. Rev. C* 79 (2009), p. 064311 (cit. on p. 135).

[162] L. Kaya et al. "High-spin structure in the transitional nucleus ^{131}Xe: Competitive neutron and proton alignment in the vicinity of the $N = 82$ shell closure." *Phys. Rev. C* 98 (2018), p. 014309 (cit. on p. 135).

[163] L. Kaya et al. "Identification of high-spin proton configurations in ^{136}Ba and ^{137}Ba." *Phys. Rev. C* 99 (2019), p. 014301 (cit. on p. 135).

[164] C. W. Johnson et al. "BIGSTICK: A flexible configuration-interaction shell-model code." *arXiv preprint arXiv:1801.08432* (2018) (cit. on p. 135).

[165] S. Binder et al. "Ab initio path to heavy nuclei." *Phys. Lett. B* 736 (2014), pp. 119–123 (cit. on p. 136).

[166] D. J. Horen et al. "Isospin character of transitions to bound states in ^{204,206,208}Pb using inelastic scattering of ^{17}O ions." *Phys. Rev. C* 44 (1991), pp. 128–135 (cit. on p. 136).

[167] D. Goutte et al. "Determination of the Transition Charge Density of the Octupole Vibration in ^{208}Pb." *Phys. Rev. Lett.* 45 (1980), pp. 1618–1621 (cit. on p. 136).

[168] C. Ellegaard et al. "Inelastic scattering of deuterons, protons and tritons on ^{210}Po." *Nucl. Phys. A* 206.1 (1973), pp. 83–96 (cit. on p. 136).

[169] E. Caurier et al. "Large-scale shell model calculations for the $N = 126$ isotones Po–Pu." *Phys. Rev. C* 67 (2003), p. 054310 (cit. on p. 136).

[170] L. Coraggio et al. "Bonn potential and shell-model calculations for ^{206,205,204}Pb." *Phys. Rev. C* 58 (1998), pp. 3346–3350 (cit. on p. 136).

[171] A. Astier and M.-G. Porquet. “High-spin states in the five-valence-particle nucleus ^{213}Po.” *Phys. Rev. C* 83 (2011), p. 034302 (cit. on p. 136).

[172] A. Astier and M.-G. Porquet. “First observation of high-spin states in ^{214}Po: Probing the valence space beyond ^{208}Pb.” *Phys. Rev. C* 83 (2011), p. 014311 (cit. on pp. 136–137).

[173] E. K. Warburton. “Shell-model interpretation of the β^- decay of ^{212}Bi^g, ^{212}Bi^{m1}, and ^{212}Bi^{m2}.” *Phys. Rev. C* 44 (1991), pp. 261–267 (cit. on p. 136).

[174] E. Teruya et al. “Large-scale shell-model calculations of nuclei around mass 210.” *Phys. Rev. C* 93 (2016), p. 064327 (cit. on p. 136).

[175] K. Yanase et al. “Shell-model study of Pb, Bi, Po, At, Rn, and Fr isotopes with masses from 210 to 217.” *Phys. Rev. C* 98 (2018), p. 014308 (cit. on p. 136).

[176] A. R. Poletti et al. “High spin states in ^{210}Rn approaching the region of 3-particle-hole neutron excitations.” *Nucl. Phys. A* 756.1 (2005), pp. 83–117 (cit. on p. 137).

[177] M. E. Debray et al. “In-beam spectroscopy of ^{215}Rn$_{86}$.” *Phys. Rev. C* 86 (2012), p. 014326 (cit. on p. 137).

[178] J. F. C. Cocks et al. “Observation of Octupole Structures in Radon and Radium Isotopes and Their Contrasting Behavior at High Spin.” *Phys. Rev. Lett.* 78 (1997), pp. 2920–2923 (cit. on p. 137).

[179] G. J. Lane et al. “Structure of exotic nuclei near and above ^{208}Pb populated via deep-inelastic collisions.” *Nucl. Phys. A* 682.1 (2001), pp. 71–78 (cit. on p. 138).

[180] GRAZING-F. http://grazingf.oregonstate.edu/ (cit. on p. 138).

[181] GRAZING-9. http://personalpages.to.infn.it/ nanni/grazing/ (cit. on p. 138).

[182] V. I. Zagrebaev and W. Greiner. “Production of heavy and superheavy neutron-rich nuclei in transfer reactions.” *Phys. Rev. C* 83 (2011), p. 044618 (cit. on p. 138).

[183] V. I. Zagrebaev and W. Greiner. “Production of heavy trans-target nuclei in multinucleon transfer reactions.” *Phys. Rev. C* 87 (2013), p. 034608 (cit. on p. 138).

[184] V. F. Comas et al. “Study of multi-nucleon transfer reactions in ^{58,64}Ni + ^{207}Pb collisions at the velocity filter SHIP.” *Eur. Phys. J. A* 49.9 (2013), p. 112 (cit. on p. 138).

[185] Y. X. Watanabe et al. “Pathway for the Production of Neutron-Rich Isotopes around the $N = 126$ Shell Closure.” *Phys. Rev. Lett.* 115 (2015), p. 172503 (cit. on p. 138).

[186] E. Fioretto et al. “Sub-barrier transfer reactions studied with the magnetic spectrometer PRISMA.” *Journal of Physics: Conference Series* 533 (2014), p. 012006 (cit. on p. 139).

[187] F. Galtarossa et al. “Mass correlation between light and heavy reaction products in multinucleon transfer ^{197}Au $+^{130}$ Te collisions.” *Phys. Rev. C* 97 (2018), p. 054606 (cit. on p. 139).

List of figures

1 Arrangement of single-particle orbitals in the nuclear shell-model. 8

2 Partial nuclei chart showing all known $J^{\pi} = 19/2^{+}$, $23/2^{+}$, and 10^{+} isomers. 9

3 Evolution of excited states along the $N = 79$ and 77 chains. 10

4 E_{4^+}/E_{2^+} ratio in even-even nuclei northwest of ^{132}Sn. 12

5 Total aligned angular momentum along Xe, Ba, and Ce chains. 13

6 Shell-model comparison of even-even nuclei with $50 \leq Z, N \leq 82$. 18

7 Landscapes of calculated transition probabilities and effective charges. 20

8 Comparison between calculated and measured $B(E2)$ values. 21

9 Evolution of excited states along the $N = 79$ chain. 65

10 Experimental results of lifetime measurements in ^{137}Ce. 66

11 Fast-timing measurement of the $J^{\pi} = 19/2^{+}$ isomer in ^{137}Nd. 111

12 Gated spectra of ^{129}Xe from the Plunger test measurement. 133

13 AGATA γ-ray spectrum gated on ^{132}I. 135

14 Maximum observed excitation energies of nuclei around ^{208}Pb. 137

15 Calculated cross sections for MNT experiments with a ^{136}Xe beam. 138

List of publications

Publications in refereed journals

[1] A. Vogt, B. Birkenbach, P. Reiter, A. Blazhev, M. Siciliano, K. Hadyńska-Klęk, J. J. Valiente-Dobón, C. Wheldon, E. Teruya, N. Yoshinaga, K. Arnswald, D. Bazzacco, M. Bowry, A. Bracco, B. Bruyneel, R. S. Chakrawarthy, R. Chapman, D. Cline, L. Corradi, F. C. L. Crespi, M. Cromaz, G. de Angelis, J. Eberth, P. Fallon, E. Farnea, E. Fioretto, S. J. Freeman, B. Fu, A. Gadea, K. Geibel, W. Gelletly, A. Gengelbach, A. Giaz, A. Görgen, A. Gottardo, A. B. Hayes, H. Hess, R. Hirsch, H. Hua, P. R. John, J. Jolie, A. Jungclaus, L. Kaya, W. Korten, I. Y. Lee, S. Leoni, L. Lewandowski, X. Liang, S. Lunardi, A. O. Macchiavelli, R. Menegazzo, D. Mengoni, C. Michelagnoli, T. Mijatović, G. Montagnoli, D. Montanari, C. Müller-Gatermann, D. Napoli, C. J. Pearson, L. Pellegri, Z. Podolyák, G. Pollarolo, A. Pullia, M. Queiser, F. Radeck, F. Recchia, P. H. Regan, D. Rosiak, N. Saed-Samii, E. Şahin, F. Scarlassara, D. Schneiders, M. Seidlitz, B. Siebeck, G. Sletten, J. F. Smith, P.-A. Söderström, A. M. Stefanini, T. Steinbach, O. Stezowski, S. Szilner, B. Szpak, R. Teng, C. Ur, V. Vandone, D. D. Warner, A. Wiens, C. Y. Wu and K. O. Zell.
Isomers and high-spin structures in the $N = 81$ isotones ^{135}Xe and ^{137}Ba.
Phys. Rev. C 95 (15 Feb. 2017), p. 024316.

[2] L. Kaya, A. Vogt, P. Reiter, B. Birkenbach, R. Hirsch, K. Arnswald, H. Hess, M. Seidlitz, T. Steinbach, N. Warr, K. Wolf, C. Stahl, N. Pietralla, T. Limböck, K. Meerholz and R. Lutter.
Characterization and calibration of radiation-damaged double-sided silicon strip detectors.
Nucl. Instr. Meth. Phys. Res. A 855 (21 May 2017), pp. 109–117.

[3] A. Vogt, M. Siciliano, B. Birkenbach, P. Reiter, K. Hadyńska-Klęk, C. Wheldon, J. J. Valiente-Dobón, E. Teruya, N. Yoshinaga, K. Arnswald, D. Bazzacco, A. Blazhev, A. Bracco, B. Bruyneel, R. S. Chakrawarthy, R. Chapman, D. Cline, L. Corradi, F. C. L. Crespi, M. Cromaz, G. de Angelis, J. Eberth, P. Fallon, E. Farnea, E. Fioretto, C. Fransen, S. J. Freeman, B. Fu, A. Gadea, W. Gelletly, A. Giaz, A. Görgen, A. Gottardo, A. B. Hayes, H. Hess, R. Hetzenegger, R. Hirsch, H. Hua, P. R. John, J. Jolie, A. Jungclaus, V. Karayonchev, L. Kaya, W. Korten, I. Y. Lee, S. Leoni, X. Liang, S. Lunardi, A. O. Macchiavelli, R. Menegazzo, D. Mengoni, C. Michelagnoli, T. Mijatović, G. Montagnoli, D. Montanari, C. Müller-Gatermann, D. Napoli, C. J. Pearson, Z. Podolyák, G. Pollarolo, A. Pullia, M. Queiser, F. Recchia, P. H. Regan, J.-M. Régis, N. Saed-Samii, E. Şahin, F. Scarlassara, M. Seidlitz, B. Siebeck, G. Sletten, J. F. Smith, P.-A. Söderström, A. M. Stefanini, O. Stezowski, S. Szilner, B. Szpak, R. Teng, C. Ur, D. D. Warner, K. Wolf, C. Y. Wu and K. O. Zell.
High-spin structures in ^{132}Xe and ^{133}Xe and evidence for isomers along the $N = 79$ isotones.
Phys. Rev. C 96 (2 Aug. 2017), p. 024321.

[4] M. Queiser, A. Vogt, M. Seidlitz, P. Reiter, T. Togashi, N. Shimizu, Y. Utsuno, T. Otsuka, M. Honma, P. Petkov, K. Arnswald, R. Altenkirch, B. Birkenbach, A. Blazhev, T. Braunroth, A. Dewald, J. Eberth, C. Fransen, B. Fu, H. Hess, R. Hetzenegger, R. Hirsch, J. Jolie, V. Karayonchev, L. Kaya, L. Lewandowski, C. Müller-Gatermann, J.-M. Régis, D. Rosiak, D. Schneiders, B. Siebeck, T. Steinbach, K. Wolf and K.-O. Zell.
Cross-shell excitations from the fp shell: Lifetime measurements in ^{61}Zn.
Phys. Rev. C 96 (4 Oct. 2017), p. 044313.

[5] L. Kaya, A. Vogt, P. Reiter, M. Siciliano, B. Birkenbach, A. Blazhev, L. Coraggio, E. Teruya, N. Yoshinaga, K. Higashiyama, K. Arnswald, D. Bazzacco, A. Bracco, B. Bruyneel, L. Corradi, F. C. L. Crespi, G. de Angelis, J. Eberth, E. Farnea, E. Fioretto, C. Fransen, B. Fu, A. Gadea, A. Gargano, A. Giaz, A. Görgen, A. Gottardo, K. Hadyńska-Klęk, H. Hess, R. Hetzenegger, R. Hirsch, N. Itaco, P. R. John, J. Jolie, A. Jungclaus, W. Korten, S. Leoni, L. Lewandowski, S. Lunardi, R. Menegazzo, D. Mengoni, C. Michelagnoli, T. Mijatović, G. Montagnoli, D. Montanari, C. Müller-Gatermann, D. Napoli, Z. Podolyák, G. Pollarolo, A. Pullia, M. Queiser, F. Recchia, D. Rosiak, N. Saed-Samii, E. Şahin, F. Scarlassara, D. Schneiders, M. Seidlitz, B. Siebeck, J. F. Smith, P.-A. Söderström, A. M. Stefanini, T. Steinbach, O. Stezowski, S. Szilner, B. Szpak, C. Ur, J. J. Valiente-Dobón, K. Wolf and K. O. Zell.
High-spin structure in the transitional nucleus ^{131}Xe: Competitive neutron and proton alignment in the vicinity of the $N = 82$ shell closure.
Phys. Rev. C 98 (1 July 2018), p. 014309.

[6] L. Kaya, A. Vogt, P. Reiter, C. Müller-Gatermann, M. Siciliano, L. Coraggio, N. Itaco, A. Gargano, K. Arnswald, D. Bazzacco, B. Birkenbach, A. Blazhev, A. Bracco, B. Bruyneel, L. Corradi, F. C. L. Crespi, G. de Angelis, M. Droste, J. Eberth, E. Farnea, E. Fioretto, C. Fransen, A. Gadea, A. Giaz, A. Görgen, A. Gottardo, K. Hadyńska-Klęk, H. Hess, R. Hetzenegger, R. Hirsch, P. R. John, J. Jolie, A. Jungclaus, W. Korten, S. Leoni, L. Lewandowski, S. Lunardi, R. Menegazzo, D. Mengoni, C. Michelagnoli, T. Mijatović, G. Montagnoli, D. Montanari, D. Napoli, Z. Podolyák, G. Pollarolo, F. Recchia, D. Rosiak, N. Saed-Samii, E. Şahin, F. Scarlassara, M. Seidlitz, P.-A. Söderström, A. M. Stefanini, O. Stezowski, S. Szilner, B. Szpak, C. Ur, J. J. Valiente-Dobón, M. Weinert, K. Wolf and K. O. Zell.
Millisecond $23/2^{+}$ isomers in the $N = 79$ isotones ^{133}Xe and ^{135}Ba.
Phys. Rev. C 98 (5 Nov. 2018), p. 054312.

[7] D. Rosiak, M. Seidlitz, P. Reiter, H. Naïdja, Y. Tsunoda, T. Togashi, F. Nowacki, T. Otsuka, G. Colo, K. Arnswald, T. Berry, A. Blazhev, M. J. G. Borge, J. Cederkäll, D. M. Cox, H. De Witte, L. P. Gaffney, C. Henrich, R. Hirsch, M. Huyse, A. Illana, K. Johnston, L. Kaya, T. Kröll, M. L. L. Benito, J. Ojala, J. Pakarinen, M. Queiser, G. Rainovski, J. A. Rodriguez, B. Siebeck, E. Siesling, J. Snäll, P. Van Duppen, A. Vogt, M. von Schmid, N. Warr, F. Wenander and K. O. Zell.
Enhanced Quadrupole and Octupole Strength in Doubly Magic ^{132}Sn.
Phys. Rev. Lett. 121 (25 Dec. 2018), p. 252501.

[8] L. Kaya, A. Vogt, P. Reiter, C. Müller-Gatermann, A. Gargano, L. Coraggio, N. Itaco, A. Blazhev, K. Arnswald, D. Bazzacco, B. Birkenbach, A. Bracco, B. Bruyneel, L. Corradi, F. C. L. Crespi, G. de Angelis, M. Droste, J. Eberth, E. Farnea, E. Fioretto, C. Fransen, A. Gadea, A. Giaz, A. Görgen, A. Gottardo, K. Haadyńska-Klęk, H. Hess, R. Hetzenegger, R. Hirsch, P. R. John, J. Jolie, A. Jungclaus, W. Korten, S. Leoni, L. Lewandowski, S. Lunardi, R. Menegazzo, D. Mengoni, C. Michelagnoli, T. Mijatović, G. Montagnoli, D. Montanari, D. Napoli, Z. Podolyák, G. Pollarolo, F. Recchia, D. Rosiak, N. Saed-Samii, E. Şahin, M. Siciliano, F. Scarlassara, M. Seidlitz, P.-A. Söderström, A. M. Stefanini, O. Stezowski, S. Szilner, B. Szpak, C. Ur, J. J. Valiente-Dobón, M. Weinert, K. Wolf and K. O. Zell.
Identification of high-spin proton configurations in ^{136}Ba and ^{137}Ba.
Phys. Rev. C 99 (1 Jan. 2019), p. 014301.

[9] L. Kaya, A. Vogt, P. Reiter, M. Siciliano, N. Shimizu, Y. Utsuno, H.-K. Wang, A. Gargano, L. Coraggio, N. Itaco, K. Arnswald, D. Bazzacco, B. Birkenbach, A. Blazhev, A. Bracco, B. Bruyneel, L. Corradi, F. C. L. Crespi, G. de Angelis, M. Droste, J. Eberth, A. Esmaylzadeh, E. Farnea, E. Fioretto, C. Fransen, A. Gadea, A. Giaz, A. Görgen, A. Gottardo, K. Haadyńska-Klęk, H. Hess, R. Hirsch, P. R. John, J. Jolie, A. Jungclaus, V. Karayonchev, L. Kornwebel,

W. Korten, S. Leoni, L. Lewandowski, S. Lunardi, R. Menegazzo, D. Mengoni, C. Michelagnoli, T. Mijatović, G. Montagnoli, D. Montanari, C. Müller-Gatermann, D. Napoli, Z. Podolyák, G. Pollarolo, F. Recchia, J.-M. Régis, N. Saed-Samii, E. Şahin, F. Scarlassara, K. Schomacker, M. Seidlitz, B. Siebeck, P.-A. Söderström, A. M. Stefanini, O. Stezowski, S. Szilner, B. Szpak, E. Teruya, C. Ur, J. J. Valiente-Dobón, K. Wolf, K. Yanase, N. Yoshinaga and K. O. Zell.
Isomer spectroscopy in ^{133}Ba and high-spin structure of ^{134}Ba.
Phys. Rev. C 100 (2 Aug. 2019), p. 024323.

Acknowledgements – *Danksagung*

Ich danke Herrn Prof. Dr. Peter Reiter für die Vergabe des vielseitigen und interessanten Promotionsthemas und für die Möglichkeit diese Arbeit in seiner Arbeitsgruppe am Institut für Kernphysik durchführen zu können. Ich bedanke mich für die vielfältige wissenschaftliche und methodische Unterstützung während der gesamten Bearbeitungsphase meiner Dissertation.

Ich danke weiterhin herzlich Herrn Prof. Dr. Andreas Zilges für die Übernahme des Koreferats sowie Herrn Prof. Dr Andreas Schadschneider für die Übernahme des Vorsitzes der Prüfungskommission. Ich danke herzlich Herrn Prof. Dr. Thorsten Kröll für die Übernahme des Drittgutachtens.

Mein besonderer Dank geht an Herrn Dr. Andreas Vogt, der mir stets mit viel Engagement und Tatkraft zur Seite stand und mir somit einen idealen Einstieg in die Bearbeitungsphase meiner Dissertation ermöglichte. Ich danke für die gemeinsame Arbeit und die vielen Anregungen zur Interpretation der erzielten Ergebnisse.

I also wish to thank Dr. Marco Siciliano from the Université de Saclay-Paris, France, Prof. Dr. Zolt Podolyák from the University of Surrey, United Kingdom, and Irene Zanon from the Laboratori Nazionali di Legnaro, Italy, for providing the $^{136}\mathrm{Xe} + {}^{208}\mathrm{Pb}$ dataset and all the discussions and the great collaboration on the different papers.

I owe special thanks to Dr. Eri Teruya and Prof. Dr. Naotaka Yoshinaga from Saitama University, Japan, for performing calculations with the PQM130 interaction on several Xe and Ba isotopes.

Furthermore, I would like to thank Dr. Han-Kui Wang from the College of Physics and Telecommunication Engineering Zhoukou, China, for his cross-shell calculations. Moreover, I also wish to thank Prof. Dr. Noritaka Shimizu and Prof. Dr. Yutaka Utsuno from the University of Tokyo, Japan, for valuable discussions and the results of the SNV interaction.

A very special thanks goes to Dr. Andrey Blazhev und Prof. Dr. Alfredo Poves from the University of Madrid, Spain, for the detailed help and their great and constructive collaborations.

In ganz besonderem Maße danke ich Herrn Dr. Claus Müller-Gatermann für die produktive und ergiebige Zusammenarbeit bei den gemeinsam durchgeführten Experimenten. Des Weiteren danke ich Herrn Konrad Arnswald, Herrn Dr. Jürgen Eberth, Herrn Dr. Christoph Fransen, Herrn Dr. Philipp John von der TU Darmstadt, Herrn Dr. Jean-Marc Régis, und Herrn Dr. Michael Seidlitz für viele anregende Diskussionen und konstruktive Hilfestellungen.

Ein großer Dank geht an Herrn Arwin Esmaylzadeh, Herrn Max Droste, Herrn Dr. Herbert Hess, Herrn Rouven Hirsch, Herrn Vasil Karayonchev, Herrn Lars Lewandowski, Herrn Nima Saed-Samii, und Herrn Dr. Nigel Warr für die enge Zusammenarbeit, Hilfe und Unterstützung in vielen Projekten und Experimenten. Ich danke weiterhin Frau Alina Goldkuhle, Frau Sarah Prill, Herrn Burkhard Siebeck, Herrn Michael Weinert, Herrn David Werner, und Herrn Kai Wolf für viele anregende Diskussionen und die Übernahme von Strahlzeitschichten während der Durchführung der Experimente.

Ein großer Dank geht an die Operateure des IKP Tandembeschleunigers, die für einen reibungslosen Strahlbetrieb bei unseren Experimenten sorgten. Ich danke der Feinmechanikwerkstatt des IKP unter der Leitung von Herrn Stefan Thiel und der Elektronikwerkstatt des IKP unter der Leitung von Herrn Christoph Görgen für die großartige Zusammenarbeit.

Großer Dank gebührt meinen Eltern und meiner Frau, die mich auf meinem Weg durch das Studium und durch die anschließende Promotion tatkräftig unterstützt haben.

Contribution to publications essential for this thesis

Publication I:
High-spin structure in the transitional nucleus ^{131}Xe: Competitive neutron and proton alignment in the vicinity of the $N = 82$ shell closure

- L. Kaya and A. Vogt commissioned the DSSSD setup at the HORUS array
- L. Kaya and A. Vogt planned and carried out the Cologne experiment
- L. Kaya performed the data analysis of the Cologne experiment
- A. Vogt and B. Birkenbach carried out the channel selection of the Xe channel of the experiment LNL 11.22; L. Kaya performed the analysis of the ^{131}Xe data
- M. Siciliano and K. Hadyńska-Klęk carried out the channel selection of experiment LNL 10.26; L. Kaya performed the analysis of the ^{131}Xe data
- L. Kaya performed the truncated and untruncated SN100PN, GCN50:82, and SN100-KTH shell-model calculations; pair-truncated shell-model calculations (PQM130) were provided by E. Teruya and N. Yoshinaga; results of the Relalistic SM were provided by A. Gargano
- L. Kaya and A. Vogt conceptualized the theoretical part of the paper and confronted the experimental observables with theory
- L. Kaya wrote the paper, A. Vogt co-wrote the paper

Publication II:
Millisecond $23/2^{+}$ isomers in the $N = 79$ isotones ^{133}Xe and ^{135}Ba

- L. Kaya commissioned the millisecond-pulsing setup at the 10-MeV tandem accelerator
- L. Kaya and C. Müller-Gatermann planned and carried out the Cologne experiment
- L. Kaya performed the data analysis of the Cologne experiment
- M. Siciliano and K. Hadyńska-Klęk carried out the channel selection of experiment LNL 10.26; L. Kaya performed the analysis of the ^{135}Ba data
- L. Kaya performed the SN100PN, SN100-KTH and GCN50:82 shell-model calculations; pair-truncated shell-model calculations (PQM130) were provided by E. Teruya and N. Yoshinaga; results of the Relalistic SM were provided by A. Gargano
- L. Kaya wrote the paper, A. Vogt co-wrote the paper

Publication III:
Identification of high-spin proton configurations in ^{136}Ba and ^{137}Ba

- L. Kaya planned and carried out the Cologne experiments
- L. Kaya performed the data analysis of the Cologne experiments
- A. Vogt carried out the channel selection of the Ba channel of the experiment LNL 11.22; L. Kaya performed the analysis of the ^{136}Ba data

- L. Kaya performed the SN100PN and GCN50:82 shell-model calculations; pair-truncated shell-model calculations (PQM130) were provided by E. Teruya and N. Yoshinaga; results of the Relalistic SM were provided by A. Gargano
- L. Kaya wrote the paper

Publication IV:
Isomer spectroscopy in ^{133}Ba and high-spin structure of ^{134}Ba

- L. Kaya planned and carried out the Cologne experiment
- L. Kaya, A. Esmaylzadeh, V. Karayonchev, L. Kornwebel, J.-M. Régis and K. Schomaker commissioned the fast-timing setup
- L. Kaya performed the data analysis of the Cologne experiment
- M. Siciliano and K. Hadyńska-Klęk carried out the channel selection of experiment LNL 10.26; L. Kaya performed the analysis of the ^{134}Ba data
- L. Kaya performed the truncated and untruncated SN100PN and GCN50:82 shell-model calculations; pair-truncated shell-model calculations (PQM130) were provided by E. Teruya and N. Yoshinaga; results of the Relalistic SM were provided by A. Gargano; N. Shimizu and Y. Utsuno performed the SNV calculations; cross-shell calulations with EPQQM were performed by H.-K. Wang
- L. Kaya wrote the paper

Manuscript I:
Excited states in doubly-odd ^{130}I

- L. Kaya, C. Müller-Gatermann and C. Fransen planned and carried out the Cologne experiment
- L. Kaya performed the data analysis of the Cologne experiment
- A. Vogt and B. Birkenbach carried out the channel selection of the I channel of the experiment LNL 11.22; L. Kaya performed the analysis of the ^{130}I data
- M. Siciliano and K. Hadyńska-Klęk carried out the channel selection of experiment LNL 10.26; L. Kaya performed the analysis of the ^{130}I data
- L. Kaya performed the truncated and SN100PN and GCN50:82 shell-model calculations; results of the Relalistic SM were provided by A. Gargano and G. De Gregorio; calulations with EPQQM were performed by H.-K. Wang
- L. Kaya wrote the manuscript

Curriculum vitae

Persönliche Daten

Name:	Levent Kaya
Anschrift:	Frankfurter Straße 324, 51103 Köln
Geburtsdatum:	23. Februar 1991
Geburtsort:	Mutlangen
Nationalität:	deutsch
Familienstand:	verheiratet mit Jenny Kaya-Schneider, 1 Kind

Hochschulstudium und Promotion

2018-2020	Promotion an der Universität zu Köln im Fach Experimentalphysik
2015-2017	Studium der Physik an der Universität zu Köln (M.Sc. Physik)
2012-2015	Studium der Physik an der Universität zu Köln (B.Sc. Physik)

Arbeitsverhältnisse

seit 2018	Wissenschaftlicher Mitarbeiter am Institut für Kernphysik der Universität zu Köln
2014-2017	Studentische Hilfskraft am Institut für Kernphysik der Universität zu Köln
2010	Elektroniker Fachrichtung Automatisierungstechnik bei der Daimler AG im Mercedes-Benz Werk Sindelfingen

Berufsausbildung

2007-2010	Berufsausbildung zum Elektroniker Fachrichtung Automatisierungstechnik bei der Daimler AG im Mercedes-Benz Werk Sindelfingen

Schulbildung

2010-2012	Technische Oberschule Stuttgart, Stuttgart
2007-2010	Gottlieb-Daimler-Berufschule, Sindelfingen
2001-2007	Adalbert-Stifter-Realschule, Schwäbisch Gmünd

Erklärung zur Dissertation

Ich versichere, dass ich die von mir vorgelegte Dissertation selbständig angefertigt, die benutzten Quellen und Hilfsmittel vollständig angegeben und die Stellen der Arbeit – einschließlich Tabellen, Karten und Abbildungen –, die anderen Werken im Wortlaut oder dem Sinn nach entnommen sind, in jedem Einzelfall als Entlehnung kenntlich gemacht habe; dass diese Dissertation noch keiner anderen Fakultät oder Universität zur Prüfung vorgelegen hat; dass sie – abgesehen von unten angegebenen Teilpublikationen – noch nicht veröffentlicht worden ist, sowie, dass ich eine solche Veröffentlichung vor Abschluss des Promotionsverfahrens nicht vornehmen werde. Die Bestimmungen der Promotionsordnung sind mir bekannt. Die von mir vorgelegte Dissertation ist von Prof. Dr. Peter Reiter betreut worden.

Teilpublikationen

- L. Kaya *et al.* "High-spin structure in the transitional nucleus ^{131}Xe: Competitive neutron and proton alignment in the vicinity of the $N = 82$ shell closure".
  Phys. Rev. C 98, 014309 (2018)
- L. Kaya *et al.* "Millisecond $23/2^{+}$ isomers in the $N = 79$ isotones ^{133}Xe and ^{135}Ba".
  Phys. Rev. C 98, 054312 (2018)
- L. Kaya *et al.* "Identification of high-spin proton configurations in ^{136}Ba and ^{137}Ba".
  Phys. Rev. C 99, 014301 (2019)
- L. Kaya *et al.* "Isomer spectroscopy in ^{133}Ba and high-spin structure of ^{134}Ba".
  Phys. Rev. C 100, 024323 (2019)

Köln, den 14. April 2020

____

(Levent Kaya)